Synthesis and Complexation of Nitrogen-rich Materials

Elena Sebastiao

Supervisor: Professor Muralee Murugesu

Department of Chemistry
Faculty of Science
University of Ottawa

A thesis submitted to the Faculty of Graduate and Postdoctoral Studies in partial fulfillment of the requirements for the M.Sc. degree in Chemistry

Abstract

Nitrogen-rich materials are of increasing interests for the development of a wide variety of applications. These compounds are prime candidates for ligands used in the complexation of metals since they possess several lone pairs. Resulting complexes have also exhibited a wide variety of interesting properties, ranging from magnetism to gas absorption to energetic properties. This thesis describes the synthesis and characterisation of new metallic complexes with the known energetic ligands: hydrazine and H_3bta, as well as that of a new nitrogen-rich compound: H_4ttp. Chapter 2 outlines a series of chains bridged by hydrazine and their potential as initiatory compounds. Mononuclear lanthanide H_3bta complexes are presented in Chapter 3. The development of the new nitrogen-rich, tetrazole-based H_4ttp ligand is described in Chapter 4. This new ligand was used to synthesise various lanthanide complexes through hydrothermal reactions.

Forward

First and foremost, I wish to express my deepest gratitude towards my supervisor, Dr. Muralee Murugesu, for approaching me and offering me the opportunity to work with him on these nitrogen-rich projects. The field of energetic materials has long been a passion of mine and I sincerely appreciated being given the opportunity to explore it from a research and development perspective. Muralee's mentorship and guidance have been invaluable over the last couple years. His encouragement and constructive advice allowed for a safe environment to explore and improve my professional skills. I also appreciate the trust you emplaced on me regarding mentoring one of your summer students, Benjamin Bouny. I very much enjoyed working with him on the hydrazine project.

I would also like to thank Dr. Serge Desgreniers, with whom we collaborated on these projects. Serge and his graduate student Dominique Laniel collected Raman spectra and performed high pressure measurements on our nitrogen-rich materials. Funding for our nitrogen-rich projects was graciously provided by the Defense Threat Reduction Agency.

The work provided herein was greatly aided by the support of two important department staff members: Dr. Glenn Facey and Dr. Ilia Korobkov. Glenn's NMR expertise and his help in performing all ^{15}N NMR and CPAS experiments were essential for the characterisation of H_4ttp. Likewise, Ilia's work regarding the collection of single crystal x-ray data and the resolution of all my crystal structures was invaluable. I also greatly appreciate the time they both spent ensuring that I had comprehended all the relevant information. I must also thank Dr. Simon Teat from the Lawrence Berkeley National Lab for collecting single crystal x-ray data for two complexes which were too small for collection on the equipment available to the department.

As anyone who has worked within a research lab would know, postdocs are one of the lab's best resources. I owe a great deal of gratitude to Dr. Cyril Cook, Dr. Amélie Pialat, and Dr. Tomoko Aharen for their guidance, mentorship, and patience. In addition to your specific expertise, which you generously shared with all group members, you are all fantastic people which made for a great working environment. Cyril and Amélie deserve an additional mention for their collaborations on the development of nitrogen-rich materials and for having to share their fume hood with me.

The Murugesu Group is a colourful group with members that came from around the world. It was a pleasure to work alongside Dr. Judith Caballero from Mexico, Dr. Irina Keuhne from Germany, Maykon Lemes from Brazil, Yuting Jiang from China, Dr. Tomoko Aharen from Japan, and our French summer students, which included Benjamin Bouny. I greatly enjoyed all the language lessons that were exchanged during coffee or lunch breaks, as well as all the delicious treats you all shared at group gatherings. Other fantastic group members which also made the last couple years memorable are Katie Harriman, Dr. Fatemah Habib, Becky Holmberg, Dr. Jen LeRoy, Gabe Brunet, and A-J Hutchings. It really was an amazing experience to have all of you as labmates. You all played an important part in the completion of this thesis, whether scientifically, morally, or both.

Lastly, but not least, I would like to thank my friends and family for their support and patience. This thesis required the bulk of my time and I appreciate their understanding in my absence.

Table of Contents

Table of Contents (cont.)

Table of Contents (cont.)

Table of Contents (cont.)

List of Tables

List of Tables (cont.)

List of Figures

List of Figures (cont.)

List of Figures (cont.)

List of Figures (cont.)

List of Figures (cont.)

List of Figures (cont.)

List of Figures (cont.)

List of Schemes

List of Schemes (cont.)

List of Abbreviations

Physical properties

T_m	melting temperature	ESD	electrostatic discharge sensitivity
T_d	decomposition temperature	FS	friction sensitivity
T_{ign}	thermal ignition temperature	IS	impact sensitivity
T_{det}	detonation temperature	N	% nitrogen content
ρ	density	OB	oxygen balance: for $C_aH_bN_cO_d$ to be converted to CO_2 and H_2O (without crystal water) OB (%) = 1600[(d-2a-b/2)/M_w] where M_w is the molecular weight
ΔH_f	enthalpy of formation		
ΔH_{det}	enthalpy of detonation		
Q_{exp}	heat of explosion		
P_{det}	detonation pressure		
ν_{det}	detonation velocity		

Energetic chemical abbreviations

AN (**4**)	ammonium nitrate	NG (**6**)	*nitroglycerin:* 1,2,3-trinitroxypropane
BP (**1**)	blackpowder	NHN (**87**)	*nickel hydrazinium nitrate*
CL-20 (**17**) HNIW	*hexanitrohexaazaisowurtzitane:* 2,4,6,8,10,12-hexanitro-2,4,6,8,10,12-hexaazaisowurtzitane	NQ (**8**)	nitroguaninine
DMAZ (**19**)	2-azido-N,N-dimethylethanamine	PETN (**13**)	*pentaerythritol tetranitrate:* [3-nitrooxy-2,2-*bis*(nitrooxymethyl) propyl] nitrate
Fox-7 (**20**) DADNE	2,2-dinitroethene-1,1-diamine	RDX (**14**)	*research department explosive/ hexogen/cyclonite/cyclomethylene-trinitramine:* 1,3,5-trinitro-1,3,5-triazacyclohexane
HMX (**15**)	*high melting explosive/ octogen:* octahydro-1,3,5,7-tetranitro-1,3,5,7-tetrazocine	TATB (**10**)	*triaminotrinitrobenzene:* 2,4,6-triamino-1,3,5-trinitrobenzene
HNS (**16**)	*hexanitrostilbene:* 1,3,5-trinitro-2-[2-(2,4,6-trinitro phenyl)ethenyl]benzene	Tetryl (**9**)	*nitramine:* N-methyl-N,2,4,6-tetranitroaniline
MF (**3**)	mercury fulminate	TNAZ (**18**)	1,3,3-trinitroazetidine
NC (**6**)	nitrocellulose	TNT (**7**)	*trinitrotoluene:* 2-methyl-1,3,5-trinitrobenzene

List of Abbreviations (cont.)

Chemical abbreviations

acac	acetylacetonate	*i*-PrOH	isopropanol
ATCP	aminotricyanopyrazine	MeOH	methanol
DAMN	diaminomaleonitrile	*m*-bdtH_2 (**117**)	1,3-benzeneditetrazol-5-yl
DDQ	2,3-dichloro-5,6-dicyano-1,4-benzoquinone	TCP	tetracyanopyrazine
DISN	diiminosuccinonitrile	terpy (**122**)	2,6-bis(2-pyridyl)pyridine
DMACl	dimethylammonium chloride	TFA	trifluoroacetic acid
DMF	dimethylformamide	THF	tetrahydrofuran
DMSO	dimethyl sulfoxide	TMS	trimethylsilyl
EtOH	ethanol	TMS	tetramethylsilane (NMR reference)
H_3bta (**106**)	5,5'-bis(1*H*-tetrazolyl)amine	tppz (**113**)	tetra-2-pyridylpyrazine
H_4ttp (**114**)	2,3,5,6-tetra(1*H*-tetrazol-5-yl) pyrazine		

General abbreviations

CPMAS	cross polarization magic angle spinning	IR	infrared
CVD	chemical vapour deposition	MOF	metal organic framework
DSC	differential scanning calorimetry	MS	mass spectrometry
EA	elemental analysis	NMR	nuclear magnetic resonance
EM	energetic material	PPE	personal protective equipment
ESI	electrospray ionization	PXRD	powder x-ray diffraction
HEDM	high-energy density material	TGA	thermogravimetric analysis
HEM	high-energy material	UV	ultra violet

1 Introduction

1.1 Energetic materials

In order to be considered an energetic material (EM), the compound in question must chemically store a large amount of energy, and be able to release it very quickly.[1] EMs are classified as a subset of combustible materials, differing slightly from the general classification as they contain both oxidizer and fuel within their molecular composition.[2] The combustion process of such substances is defined as a self-sustaining exothermic rapid redox reaction, in which the decomposition of chemical bonds generates a considerable amount of gases, such as CO_2, H_2O and N_2, which act as thermodynamic sinks.[2,3] Since these gases are liberated at high temperatures, their rapid expansion is what generates an EM's power.[3] The resulting pressures may allow for sustained combustion without the presence of oxygen.[2] Despite the common misconception that EMs are mainly used for military purposes, more EMs are actually consumed in peaceful applications, mainly in industrial applications.[4] They have become indispensable to our modern life, in great part due to modern advances.[4]

The application of EMs, or high-energy materials (HEMs), is dependent on their energy releasing process.[4,5] This class of compounds decomposes by one of two major pathways: deflagration or detonation (Table 1.1).[4,5] Deflagration is a thermal process where the compound releases its stored energy in the form of hot gas evolving over a given time frame, ranging from milliseconds to seconds.[2,4-5] Compounds following this pathway are referred to as deflagrating explosive or propellants, due to the force that can be generated by the evolved gases. The most common use for propellants is for fuel-like purposes which include driving turbines, moving pistons, and

starting aircraft engines, as well as pumping fluids and shearing bolts and wires.[2,5] Military specific applications focus on the launching of projectiles, such as: bullets, rockets and missiles, in addition to ejecting pilots.[2,5]

Table 1.1 : Reaction types for an energetic material with Q_{ex} = 4187 kg^{-3}

Reaction type	Combustion	Deflagration	Detonation
Reaction speed ($m\ s^{-1}$)	10^{-3} - 10^{-2}	10^{2}	10^{4}
Mass flow ($m^3\ s^{-1}$)	10^{-3} - 10^{-2}	10^{2}	10^{4}
Gaseous products ($m^3\ s^{-1}$)	1 - 10	10^{5}	10^{7}
Reaction time ($s\ m^{-3}$)	10^{2} - 10^{3}	10^{-2}	10^{-4}

Reproduction of a table presented by Klapötke.[7]

What are commonly referred to as “explosives” [i] are compounds defined as undergoing a detonation. This pathway employs a different mechanism in which the compound decomposes through a shockwave at supersonic speeds.[5,6] Various industries are increasingly employing these materials for a variety of applications which include: blasting, mining, cratering, and the manipulation of metals by either cutting, welding, forming or fragmentation.[4,5] The detonation properties of these explosives are also used in shaped charges for military applications.[5] There are two classes within which explosive are classified: primary and secondary explosives (Table 1.2).[7] Primary explosives are inherently very sensitive to various initiation stimuli and will detonate regardless of their confinement conditions.[6] Conversely, secondary explosives tend to be less sensitive to stimuli but are more powerful than primary explosives.[6] The aforementioned applications will employ secondary explosives for the explosive power and generally use a primary explosive to initiate them. However, the boundary between the two classes is not absolute:

[i] Though the term “explosive” is colloquially interchanged for describing both propellants, and EMs which detonate, this document will use the term exclusively for refereeing to EMs which detonate, as per the proper definition.

Table 1.2 : Typical sensitivity and performance data for primary and secondary explosives

Properties	Primary explosives	Secondary explosives
IS (J)	≤ 4	≥ 4
FS (N)	≤ 10	≥ 50
ESD (J)	0.002 - 0.020	≥ 0.1
Q_{det} (kJ kg^{-1})	1000 - 200	5000 - 6000
P_{det} (GPa)	---	21 - 39
v_{det} (m s^{-1})	3500 - 5500	6500 - 9000

Reproduction of a table presented by Klapötke.[7]

Table 1.3 : Common explosives and their properties

	TNT[7-11] (7)	**Tetryl[6,11] (9)**	**RDX[7-9,11] (14)**	**PETN[6,7,11] (13)**	**CL20[11-15] (17)**	**Lead azide[6,7,11] (12)**
T_m (°C)	80.4	129.5	204.1	143	167	---
T_d (°C)	295	162	213	202	213	190
T_{ign} (°C)	300	187	210	202	---	327 - 360
T_{det} (°C)	3471	---	4081	4076	---	---
ρ (g cm^{-3})	1.65	1.73	1.80	1.76	2.044	4.8
OB	–73.96	–47.36	–21.61	–10.12	–10.95	–5.49
N	18.5	24.4	37.8	17.7	38.4	28.9
ΔH_f (kJ mol^{-1})	–62.07	33.89	70.29	–530.53	372.00	468.61
ΔH_f (kJ kg^{-1})	–273.28	118.02	316.45	–1678.16	848.95	1609.02
ΔH_{det} (kJ mol^{-1})	–929.34	–1246.35	–1127.36	–1838.37	–2609.59	–469.00
Q_{exp} (kJ kg^{-1})	4091.63	4340.50	5075.50	5815.08	5955.43	1610.36
P_{det} (GPa)[c]	21.0,[b] 20.2 [a]	---	37.5,[b] 34.5 [a]	31.5,[b] 31.1 [a]	48.23	34.3
V_{det} (m s^{-1})	6950,[b] 7150 [a]	7080	8750,[b] 8920 [a]	8270,[b] 8660 [a]	9620[b]	5500
IS (J)	15	3	7.4	3	2 - 4	2.4 - 4
FS (N)	> 353	> 353	120	60	48	< 1
ESD (J)	0.46 - 0.57	---	0.15 - 0.20	0.19	---	0.005

[a] calculated value, [b] experimental value, [c] original value has been converted to units employed within this thesis for clearer comparison. Oxygen balance (OB) represents how much oxygen is required for complete combustion, resulting in 100% conversion to CO_2, H_2O, metal oxide and/or non-metal oxide (without crystal water). For a molecule with formula $C_aH_bN_cO_dB_eP_fF_gM_h$, OB (%) = 1600[(d – 2a – (b–g)/2 – 3e/2 – 5f/2 – 3h/2)/M_w] where M_w is the molecular weight (%)and M is any metal). A value of zero represents a system that has enough oxygen content for auto combustion, and is the desired value.

under the right conditions, many propellants are known to detonate.[5] Physical properties of commonly referenced explosives are provided in Table 1.3. Within these examples, only lead azide is characterised as a primary explosive.

1.1.1 History

The first account of a manmade explosive compound is that of the accidental discovery of blackpowder (BP, 1) (Scheme 1.1, p. 11).[11] Though there are conflicting sources, it is generally accepted that its discovery occurred in 220 BC by Chinese alchemists.[7,11] Akhavan suggests that, in efforts to separate silver from a gold ore, these alchemists added saltpetre (potassium nitrate) and sulfur to their furnace, but forgot to add charcoal in the first step.[11] Attempting to rectify this mistake, they added the charcoal in a subsequent step, which resulted in a large explosion due to the formation of blackpowder within the furnace.[11] By 1045 AD, the Wu-Ching Tsung-Yao (*Complete Compendium of Military Classics*), the first document containing formulas for gunpowder along with its use in warfare, was published in limited editions by the scholars Zeng Gongliang (the chief editor), Ding Du, and Yang Weide in China.[16]

It was not until two centuries later that BP was introduced to the western world, with its introduction to Europe in the middle of the 13th century being credited to the English monk Roger Bacon.[7,11] The German monk Berthold Schwarz is said to have studied Bacon's writings as early as 1320, and further researched the properties of BP.[7,11] By the end of the 13th century, BP was being employed as an aid in military conquests to breach castles and city walls throughout most of Europe.[11] Since BP consists of a mixture of powdered charcoal, sulfur and potassium nitrate, the degree of mixing between the fuels and oxidizer plays a large role in its efficiency.

Due to poor mixing, early composites were considerably unreliable.[7,11] It wasn't until 1425 that Corning developed a grinding process, using heavy wheels to mix the three components, which significantly improved the production of BP, and rendered it useful as a propellant charge for small calibre guns.[7,11] By the 16th century, blackpowder was being employed in large calibre guns, and it began its first use in civil engineering applications.[7,11] By the 17th century, its use in mining applications was common place.[11]

The 17th century was rich in new discoveries regarding the identification or synthesis of chemicals. The next significant energetic compound, ammonium nitrate (AN, 2) (Scheme 1.1, p. 11), was first identified by Glauber in 1654. However, its potential as an explosive was not recognised until Grindel and Robin suggested its use as a replacement for potassium nitrate in BP at the beginning of the 19th century.[11] In 1849, evidence supporting Grindel and Robin's suggested use of AN was provided when an explosion resulted from heating a mixture of ammonium nitrate and charcoal.[11] Despite reports of several small scale incidents, ammonium nitrate was not regarded as an explosive.[11] It was not until 1947, when three ships carrying fertiliser grade AN were destroyed by massive explosions; the SS Grandchamp, the SS Highflyer and the SS Ocean Liberty.[11] With investigations into the cause of these separate incidences determining that AN was the cause, rigid regulations regarding its storage, loading and transportation have since been implemented in numerous countries worldwide.[11]

Another inorganic explosive first reported in the 17th century, which followed in the tradition of the Chinese and was discovered by Swedish-German alchemist Baron Johann Kunkel von Löwenstern, is mercury fulminate (MF, 3) (Scheme 1.1, p. 11).[7,11] Due to his inability to find a useful application, this explosive was forgotten until it was rediscovered at the turn

of the 19th century by an Englishman, Edward Howard.[11] In studying its properties, Howard proposed its potential as a percussion initiator.[11] Such a device was patented by the Scottish Clergyman Alexander Forsyth in 1807, and a metal blasting cap using MF was invented by Alfred Nobel in 1864.[11]

Glauber is also accredited in providing the first written accounts of picric acid (PA, 4) (Scheme 1.1, p. 11).[7,11] This is the earliest known nitrophenol, and was originally used as a fast dye for silk and wool in the second half of the 19th century.[11] PA was first suggested as an explosive in 1830 by Welter.[11] It was also suggested by Designolle and Brugère that its salts could be used as propellants.[11] This was reinforced by Abel in 1871 who proposed ammonium picrate as an explosive.[11] In 1873, Sprengel was able to demonstrate PA's ability to detonate.[11] Twelve years later, Turpin found PA to be a suitable replace for BP and started to fill munitions shells with the compound.[7,11] By 1885, the British had replaced BP by PA, under the name Liddite.[7,11] Panpushko developed PA for the Russians in 1894, quickly noticing its explosive potential.[11] PA soon became the standard military explosive across Europe.[11] Though it exhibited better performance than BP, it required high temperatures, along with long times, for it to be melt casted into munitions.[11] Furthermore, if the shells were exposed to water, corrosion occurred, and the resulting salts were very sensitive.[11]

The 19th century saw great progress in the development of EMs, with the discovery of some of the most famous EMs. The nitration of starch by Braconnot in 1833 led to the formation of nitrocellulose (NC, 5) (Scheme 1.1, p. 11), also known as guncotton.[11] In continuation of these experiments, Pelouze nitrated paper and cotton, among other materials, unknowingly discovering NC in 1838.[11] From 1845 and 1847, several researchers were known to be working on the development of NC.[11] Despite published literature

at the time, credit for its discovery was allotted to Schönbien and Böttger in 1846.[11] Several accidents due to the unexpected detonation of NC were reported, including the destruction of at least three manufacturing plants.[11] As a result, investigations into stabilising NC were undertaken and in 1865, Sir Frederick Abel published his process of pulping, boiling and washing, which led to significant sensitivity reduction.[11] In 1868, Abel's assistant, E. A. Brown discovered that dry NC could be initiated with a MF detonator, while wet NC could be initiated with a small quantity of dry NC, rendering the use of NC comparatively much safer.[11] This led to the use of NC as both a military and commercial explosive.[11]

The next significant milestone was the development of a small scale synthesis of nitroglycerine (NG, 6) (Scheme 1.1, p. 11) by the Italian chemist Ascanio Sobrero in 1846.[7,11] Though Sobrero discontinued his investigations into **NG** upon discovering its explosive nature, the Swedish inventor Immanuel Nobel, Alfred Nobel's father, soon developed an industrial scale process, and opened up the first small scale manufacturing plant in 1863.[11] Since NG combines both the fuel and the oxidizer at the molecular level, it proved to be a much more potent explosive than BP. Unfortunately, this energetic material is quite sensitive and led to many premature or unanticipated detonations.[7,11] In order to address this issue, Alfred Nobel added an absorbent clay named "Kieselguhr" (25%) to his family's NG (75%) recipe, and patented the resulting product, "Ghur Dynamite", in 1867.[7,11] Though dynamite failed to have any significant military applications, it was readily used throughout the civil sector.[7] In 1875 Alfred Nobel discovered that he could form a gel by mixing NG with NC.[7] This led to the production of blasting gelatine, gelatine dynamite, and ballistite (1888 – mixture of NC, NG, benzene and camphor) which was the first smokeless powder product.[7,11]

The most iconic explosive, TNT or 2,4,6-trinitrotoluene (7) (Scheme 1.1, p. 11), was first synthesised by Wilbrand in 1863.[11] A more complete study was performed by Beilstein and Kuhlberh in 1870 where-by they identified the 2,4,5-isomer.[11] Ten years later, Hepp was finally able to isolate the pure 2,4,6-isomer, which is the preferred isomer for military purposes, and its structure was determined by Claus and Becker in 1883.[7,11] By 1902, both the British and the Germans had experimented with TNT and had begun to replace PA with it.[7,11] Within 10 years, the US had also replace PA with TNT.[11] Once WWI broke out, TNT was the explosive of choice on all fronts.[7,11] Its manufacturing, however was limited to the availability of toluene, which was extracted from coal tar.[11] As supplies began to run low during the war, TNT was diluted with AN, and given the name amatol.[11] The incorporation of aluminum metal within this mixture gave aminal, which was used as an underwater explosive.[11] One of the main drawbacks of TNT was the sensitivity associated to its cast charges.[7] This was eventually mitigated by the use of binders.[7] TNT is still an important blasting explosive today and one of the most common standards used to asses new explosives.[7]

Nitroguanidine (NQ, 8) (Scheme 1.1, p. 11) was first developed by Jousselin in 1877, but its properties were investigated by Vieille in 1901.[7,11] Though not widely used, NQ was employed during WWI and WWII.[7,11] It could be found in mixed composition in grenades for mortars (with AN),[7] and in bursting charges (mixed with NC).[11] Unfortunately, NQ would react with NC upon long term storage.[11] NQ was best known for its use in triple-based propellants systems, where it reduced the muzzle flash, and lowered the combustion temperatures, resulting in a longer lifetime for the barrel.[7,11] 1877 also saw the development of Tetryl (**9**) (Scheme 1.1, p. 11) by Mertens, though structure was determined the same year as TNT by Romburgh.[11]

Tetryl is the first example of a nitroamino-type explosive.[7] Its use as an explosive started in 1906, it was often used as a base charge in blasting caps.[11]

The next nitro-benzene-based explosive to be developed was triaminotrinitrobenzene (TATB, **10**) (Scheme 1.1, p. 11) in 1888 by Jackson and Wing.[7] TATB exhibits the highest thermal and shock stability in comparison to other EMs with comparable performance.[11] Thus, after commercial production commenced in 1978 with Adkins' and Norris' synthetic method, it has been employed for hot deep oil drilling applications.[7] TATB is also often used by the Navy and has been mixed with other EMs to obtain a safer product.

One of the most widely use liquid propellants, hydrazine (**11**) (Scheme 1.1, p. 11) was first described by Curtis in 1889.[11,17] Hydrazine can be used as both a mono- or bipropellant and is commonly used in rocket fuel. Though its primary use is as a propellant, it has been shown that hydrazine is very capable of detonation.[18] Unfortunately, hydrazine exhibits several undesirable properties, such as high volatility and carcinogenic vapors.[5] In more recent years, much effort has been allocated towards developing replacements which are safer and more environmentally friendly. Another EM which stimulated research towards finding a suitable replacement is the primary explosive lead azide (**12**) (Scheme 1.1, p. 11), which was first described in 1891 by Curtius.[19] Lead azide was used by Alfred Nobel to replace MF in his blasting caps, as it was comparably safer to handle.[7] Unfortunately the long-term use of these initiators led to heavy-metal contamination of military sites.[7]

Three years after the initial reporting of lead azide, nitritation of pentaerythritol lead to the preparation of PETN (**13**) (Scheme 1.1, p. 11).[11]

Despite being a powerful explosive, its early use was limited by lack of availability of formaldehyde and acetaldehyde.[11] It was not until about a decade before WWII that PETN became readily available.[11] PETN was commonly used throughout WWII, though not as much as RDX due to its high sensitivities.[7] Its uses included grenades, blasting caps, detonation cords, and booters.[7] Due to its high sensitivity, it was often mixed with other compounds. One composition of note was pentolite, a 50:50 mixture of PETN and TNT, which was used to fill hand and anti-tank grenades, as well as detonators.[7,11]

Today's most utilized explosive was developed over a hundred years ago. The Research Department Explosive (RDX, **14**) (Scheme 1.1, p. 11) was first synthesised by the German Henning in 1899.[7,11] Its original intended use was for medicinal purposed.[7] Nitric oxides (NO_x), the product of nitrate esters metabolised by mitochondrial aldehyde dehydrogenase, are natural vasodilators.[7] Other explosive nitrate esters, such as NG and PETN, are also used for treating angia pectoris.[7] RDX's explosive potential was not characterized until 1920, when Herz synthesised this product through direct nitration of hexamethylene tetramine.[7,11] This route, however was low yielding. Improvements to the synthetic route were performed by Hale, Meissner, Ross and Schiessler, until Bachmann developed the manufacturing process in 1940.[11] These processes all produced a secondary product, which is an explosive in its own right, given the name High Melting Explosive (HMX, **15**).[7,11] HMX became more readily available after WWII and is still one of the EMs of choice for modern day militaries.

Though most of the explosives used today were first developed prior to the 20th century, considerable efforts have been invested towards developing new EMs which meet the growing demands for performance, while adhering

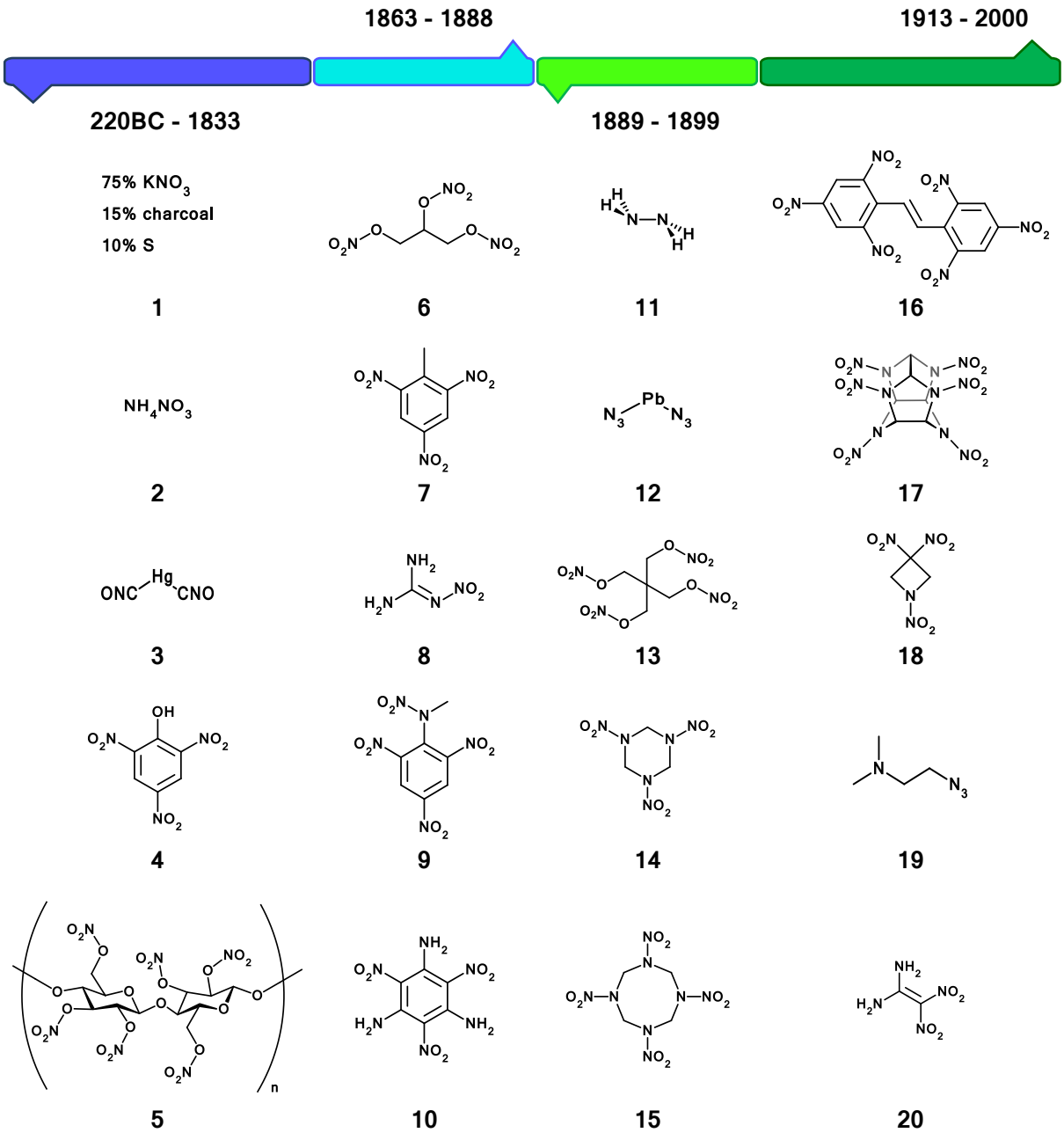

Scheme 1.1 : The chronological evolution of common EMs.

to growing concerns towards safety. At the turn of the century, the insensitive hexanitrostilbene (HNS, **16**) (Scheme 1.1, p. 11) was developed.[7] HNS is comparable to TATB in terms of sensitivity and also has a high melting point. Near the end of the 20th century, EM developers moved away from

the traditional designs and successful new EMs, such as hexanitrohexaazaisowurtzitane (CL-20, **17**) and 1,3,3-trinitroazetidine (TNAZ, **18**) (Scheme 1.1, p. 11), were achieved using ring or cage strain motifs.[7,11] CL-20 is considered to be the most powerful explosive currently in existence, though its costly synthesis and sensitivities have kept it from replacing RDX as the most common EM for the military.[7] Another avenue explored was that of organic azides, with 2-dimethylaminoethylazide (DMAZ, **19**) (Scheme 1.1, p. 11) as a prime example.[20] Another notable EM is a derivative of NQ, diaminodinitroethene (FOX-7, **20**) (Scheme 1.1, p. 11), which was developed by the Swedish defence agency FOI in the late 1990's.[7] Despite having the same C/H/N/O ratio as RDX, FOX-7 is a less powerful EM.[7]

1.1.2 Modern trends

As EMs have been developed and improved, society has increasingly incorporated their use within numerous civilian industries. This, along with the never-ending desire for military might, has stimulated vast interest world-wide for the development of more powerful EMs or high-energy density materials (HEDMs).[1,4] HEDMs are targeted for their high performance and/or insensitivities towards undesirable stimuli, such as thermal shock, friction, impact, and electrostatic discharge.[1] There are two main approaches employed for the design and synthesis of modern HEDMs: (i) targeting new molecules with high positive heats of formation, namely nitrogen-rich compounds; and (ii) targeting new molecules that derived their energy from the oxidation of their carbon backbone, as with traditional EMs.[1] In regards to the second avenue, physical attributes, such as cage strain, have been incorporated into the designs for improved performance. Regardless of the avenue taken, focus has been placed on obtaining materials with higher densities. The densities of EMs have been found to be directionally proportional to its detonation velocity

and thus, increasing its density improved performance without introducing increased instability.[3]

1.1.2.1 Nitrogen-rich EMs

Designing new nitrogen-rich compounds is currently one of the most popular routes for developing HEDMs. This class of EMs relies on possessing large positive heats of formation, rather than heats of combustion, to store its energy.[1] The inherently energetic N–N and C–N bonds lead to very high heats of formation, which in turn results in a considerable amount of released energy upon their decomposition.[1] When comparing heterocyclic-based compounds with their carbocyclic analogues in the context of an energetic role, the heterocyclic compounds benefit from higher heats of formation, higher densities, and better oxygen balance.[1] These systems have the added benefit of mainly decomposing into dinitrogen gas, and thus are considered more environmentally friendly. In reducing the carbon content in exchange for nitrogen, many of these N-rich compounds are being investigated as smokeless EMs; smoke being primarily caused by the incomplete combustion of the carbon content.

Nitrogen-rich compounds are not exclusively of interest for the EMs community. Novel high-pressure forms of nitrogen have been the object of research for physicist for several decades.[1,21-31] The high-pressure physics community has been placing dinitrogen gas under high pressures (on the order of 10^1 - 10^2 GPa) in order to rearrange or completely destroy covalent bonds, in attempts to isolate new forms of nitrogen.[1] Due to the complexity of dinitrogen's triple bond, pressure-induced transformations were expected to go through the formation of intermediate polymeric networks before losing covalency at higher pressures.[1] Experimental verification of such high-pressure non-molecular phases of nitrogen was only recently obtained, along with

several molecular phases which have been determined.[1,21-32] Several non-molecular structures have been predicted to be obtainable at pressures corresponding to molecular phases by theoretical studies.[1,33-41] One such structure is the cubic gauche (CG) structure, which would correspond to the nitrogen diamond analog, a fully coordinated three-dimensional structure, for which experimental evidence has recently been provided.[1,31] CG polynitrogen has been predicted to be the best HEDM to date, but remains unattainable at ambient conditions.[1] In hopes of finding new avenues for forming CG polynitrogen, along with other high-pressure phases, or a hybrid carbon-nitrogen analogue, high-pressure physicists have turned to using nitrogen-rich compounds as precursors to their experiments. Table 1.4 lists key all-nitrogen species which have been isolated.

Table 1.4 : Isolated all-nitrogen species

All-nitrogen species	Name	Comments	Refs.
Neutral compounds			
N_2	Dinitrogen	Thermodynamically stable form of nitrogen; not energetic	42
CG-N_x	Cubic polynitrogen	Prepared from N_2 in diamond anvil cell at 200 K and 110 GPa; metastable only above 42 GPa	31,43,44
Ionic species			
N_3^-	Azide anion	Suitable energetic anion (or covalent azide group R–NNN)	42
N_5^+	Pentanitrogen cation	Metastable salts only with large counter anions ($Sb_2F_{11}^-$ etc.)	45-47
N_5^-	Pentanitrogen anion	Only detected in gas phase (mass spectrometry)	48,49

Reproduction of a table presented by Klapötke[1]

When considering the synthesis of new nitrogen-rich material, 5- and 6-membered heterocycles are often favoured as a starting point due to the intrinsic stability offered by their aromaticity. In comparing the heats of formation for the two series, one may observe that higher heats of formation are obtained for consecutively linked nitrogen atoms (Figure 1.1). Pentazole (**26**), the azole ring consisting purely of nitrogen, has the highest heat of formation within the series. Though it would appear to be the best choice in terms of energetic perforce, pentazole has yet to be isolated, and its derivatives, consisting of bulky substituents, are unstable above −10°C.[53] Thus,

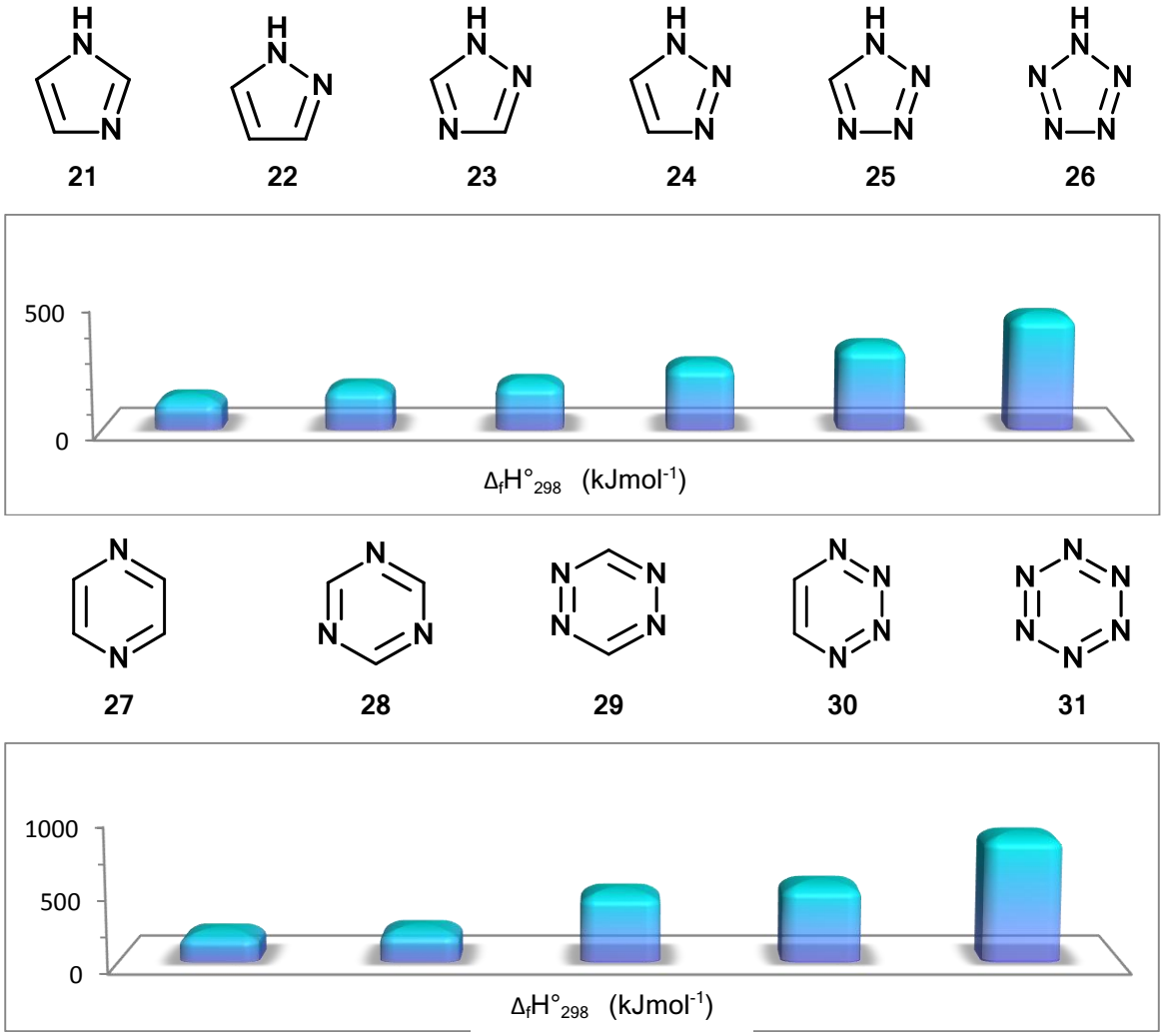

Figure 1.1: Enthalpies of formation for the azole[50,51] and azine[52] series.

tetrazoles, with four consecutive nitrogen atoms, offer the best compromise between energetic performance and stability. In considering the 6-membered cyclic azine series, pentazine (**31**), similarly to pentazole, is still a theoretical compound. Comparing the azole series with the 6-membered cyclic azine series, the two tetrazine isomers (**29** and **30**) have a lower nitrogen content than tetrazole (68.27% and 79.98% respectively). Thus tetrazoles are the ideal building block for the synthesis of new nitrogen-rich EMs.

1.2 Tetrazoles

Due to their optimal balance between stability and energetic performance, tetrazole-based compounds have been chosen as the focus of this work. More specifically, 5-substituted tetrazoles have been pursued due to their ease of synthesis.

1.2.1 Properties

1.2.1.1 Tautomers and isomerisation of tetrazoles:

There are three main tautomers of tetrazole (Scheme 1.2), of which two are stable under ambient conditions (**25** and **33**). The 2*H* form (**33**) has been found to be the dominant species in the gas phase, while the 1*H* form (**25**) is dominant in solution due to solvation effects.[54] Tetrazoles also have the ability for ring-chain isomerisation (Scheme 1.3). At higher temperatures,

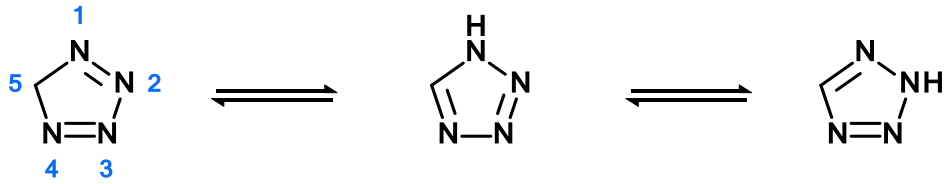

32 **25** **33**

Scheme 1.2: Tetrazole tautomers along with identification of atom numbering for nomenclature.[54]

the azido form (**35**) is in equilibrium with the closed ring (**34**).[54] It is therefore possible to obtain tetrazoles upon heating an appropriate organic azide precursor. Opening of the tetrazole ring, due to this isomerisation, is responsible for the Dimroth rearrangement of 5-substituted aminotetrazoles.[54] In the case of the Dimroth rearrangement, where one of the R groups is and amino group, the azido intermediate will cyclise onto the imino nitrogen with the strongest electron-donation substituent.[54]

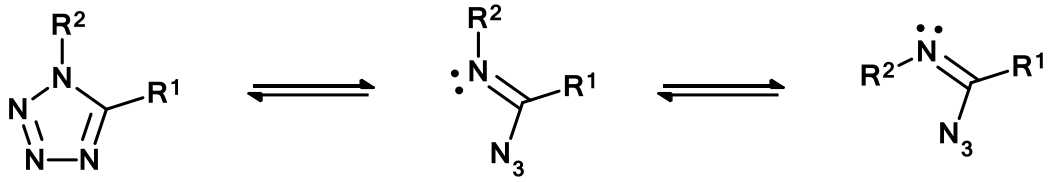

34 **35** **36**

Scheme 1.3: Ring-chain isomerism for 1,5-di-substitued tetrazole.[54]

1.2.1.2 Acidity of tetrazoles:

Of all the azoles, tetrazoles are the weakest bases; as can be seen by the protonation energies presented in Scheme 1.4.[54] Despite the difference of approximately 80 kcalmol^{-1} between the different calculation methods, both data sets exhibit a reverse order to the sigma ionization potentials.[54] The protonation energy of azoles is therefore thought to be related to the energy required for ionizing an electron from its sigma-framework.[54]

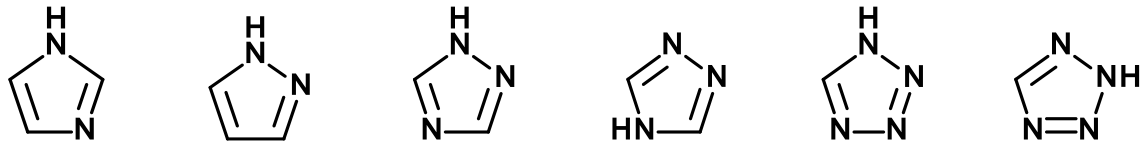

21 **23** **24** **37** **25** **33**

240.1 (318) **227.0 (312)** **225.1 (300)** **231.8 (307)** **213.4 (293)** **209.6 (294)**

Scheme 1.4 Protonation energies from *ab initio* calculations at 6-31G*//6-31G[55] for imidazole, pyrazole, 1*H*-1,2,4-triazole, 4*H*-1,2,4-triazole, 1*H*-tetrazole, and 2*H*-tetrazole (kcalmol^{-1}). Values in parentheses are from INDO calculations.[54,56]

Compounds consisting primarily of a 5-substituted tetrazole functional group are also referred to as tetrazolic acids (RCN_4H), since they are the nitrogen isosteres of carboxylic acids (RCO_2H).[54] Given their structural similarity to their carbon analogs, 5-substituted tetrazoles have very similar pK_a values, though often slightly lower due to their aromaticity's ability of to stabilise the negative charge (Scheme 1.5).[54]

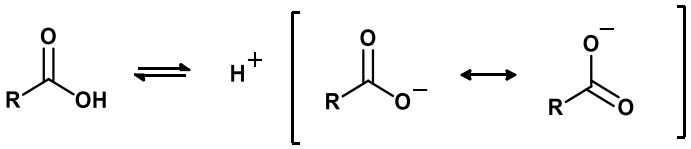

38

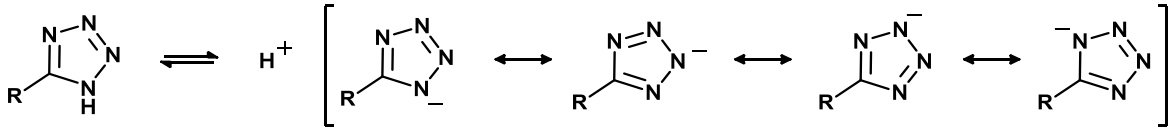

39

Scheme 1.5: Resonance structure comparison of carboxylic acids and tetrazolic acids.[54]

1.2.2 Heterocyclic synthesis

Tetrazoles are synthesised according to two major synthetic strategies: either through the formation of one bond in a five-atom component or through the formation of two bonds from 3 + 2 atom components.[54]

1.2.2.1 Formation of One Bond in a Five-atom Component

1.2.2.1.1 Tetrazole from imidoyl azides

A major route in the synthesis of 5-, 1-, and 1,5-substituted tetrazoles is the cyclisation of imidoyl azides (**41**); which may be derived from imidoyl halides (**40**).[54] For the cyclisation to occur, the imidoyl azide must conform to two structural requirements: (i) a *cis* conformation between the imino lone pair and the azido group, and (ii) an R group that allows sufficient electron

density to remain on the imino group (Scheme 1.6).[54] Since the resulting aromatic ring would be electron withdrawing, the electron-donating azido group will not cyclise if the R groups are too electron-withdrawing.[54] In the case where an intermediate imidoyl azide is derived from a carbodiimide, two potential cyclisation sites are present (Scheme 1.7). The site consisting of the strongest electron-donating substituents will be the site of cyclisation.[54] In general, cyclisation is favoured by low temperatures and basic conditions, while the opposite conditions, especially ones which protonate the imine, favour the azido form.[54] However, spontaneous cyclisation generally occurs once the once the imidoyl azide has been formed.[54]

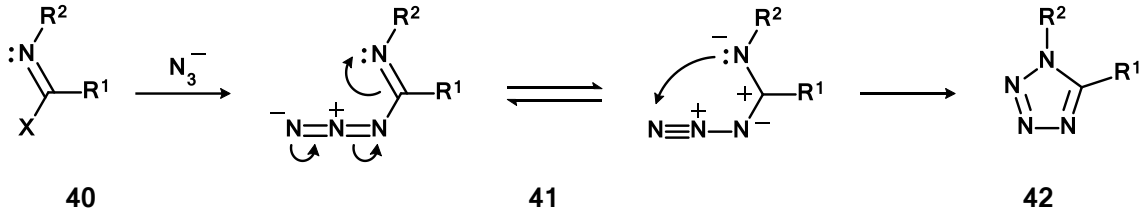

Scheme 1.6: Tetrazole synthesis from imidoyl azides.[54]

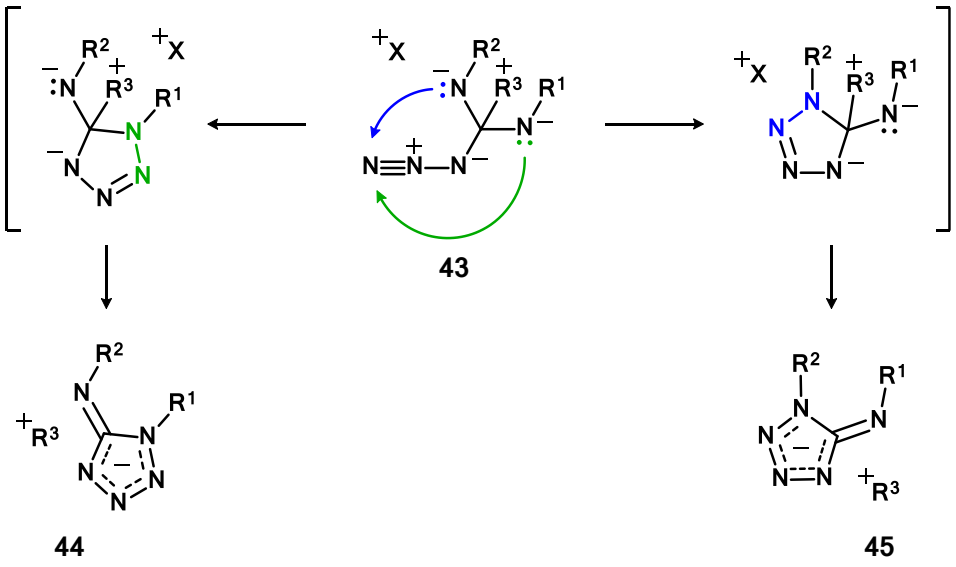

Scheme 1.7: Tetrazole synthesis from imidoyl azides derived from carbodiimides.[54,57]

1.2.2.1.2 Tetrazole from 1,1,-diazido compounds

Another route for the synthesis of 1,5-disubstituted tetrazoles is achieved using *gem*-diazido compounds (examples: **48**, **49**, **50**) as precusors.[54] This route is thought to pass through an imidoyl azide intermediate, from a 1,2-C→N shift either through an azido nitrene intermediate or related structure with the loss of N_2 gas from one of the azide groups (as in **49**), which cyclises (Scheme 1.8).[54] In the case where diazidomalonates (**50**, Scheme 1.9) are used as precursors, it has been shown that a complicated chain process, including an intermolecular methyl transfer, is responsible for the process.[54]

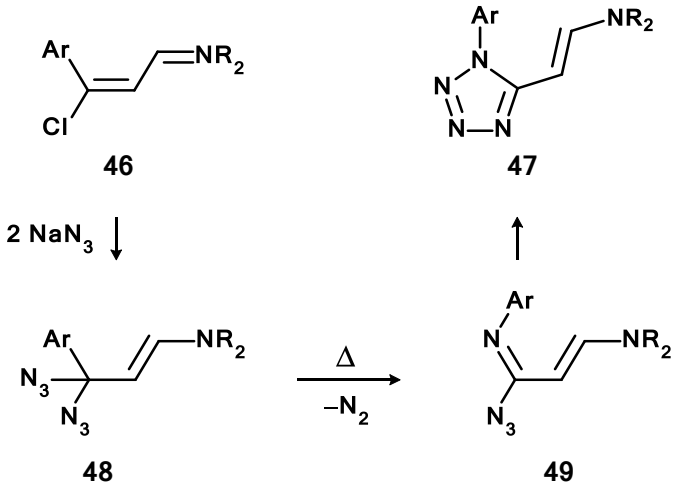

Scheme 1.8: Tetrazole synthesis from *gem*-diazido compounds.[54]

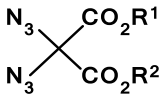

Scheme 1.9: *Gem*-diazido compounds - diazidomalonates.[54]

For geminal vinyl azides (**51**), one of the azido groups is replaced by either NH_3 or RNH_2 to give an aminovinyl azide (**52**).[54] By employing a base,

such as Et_3N, followed by an acidic workup, one obtains the corresponding 4,5,-dihydro-1h-tetrazol-5-ylidene (**53**) (Scheme 1.10).[54]

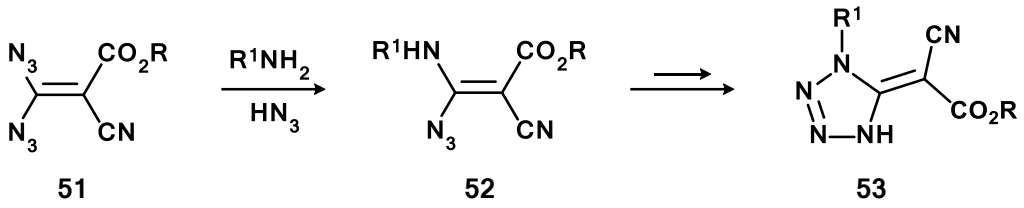

51 **52** **53**

Scheme 1.10: Tetrazole synthesis from geminal vinyl azides.[54]

1.2.2.1.3 Tetrazoles from cyclisation of tetrazenes, triazenes, and formazans

Imidoyl azides are not the only acyclic systems which have been found to form tetrazoles.[54] The coupling of aryl diazonium salts with hydrazides leads to the formation of tetrazenes with an α-carbonyl group.[54] The dehydration of such tetrazenes (**54**) will provide tetrazoles, such as (**55**), in yields as high as 80% (Scheme 1.11).[54] Another system capable of forming tetrazoles is triazenes.[54] These are oxidatively cyclised to form tetrazoles.[54] Precursors of the same type as (**57**), obtained by displacement of a cyanide group from (**56**), are not the best candidates as they, themselves, are hard to synthesise, and the cyclisation is low yielding (Scheme 1.12).[54] Other precursors, consisting of the motif in (**59**), will provide fused azolotetrazoles (**60**) or tetrazoloazinium salts (**61**), depending on the substrate.[54] Oxidative cyclisation of formazans, such as (**62**), may also be employed to form

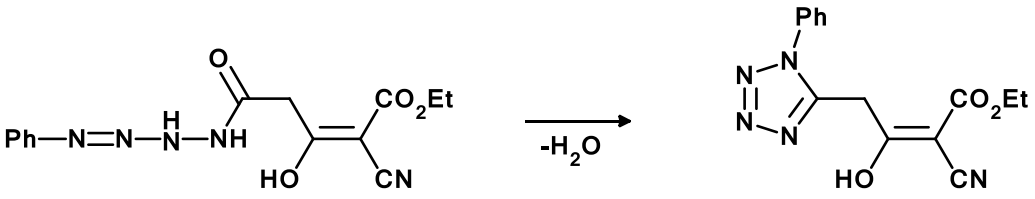

54 **55**

Scheme 1.11: Cyclisation of tetrazenes.[54]

tetrazoles (Scheme 1.13).[54] This is one of the standard synthetic routes for obtaining tetrazolium salts (**63**).[54] 2,5-Diaryltetrazoles (**64**) may also be easily obtained by treatment with a strong base of formazans consisting of an arylsulfonyl group on one of the nitrogens, in a Bamford-Stevens-type reaction.[54]

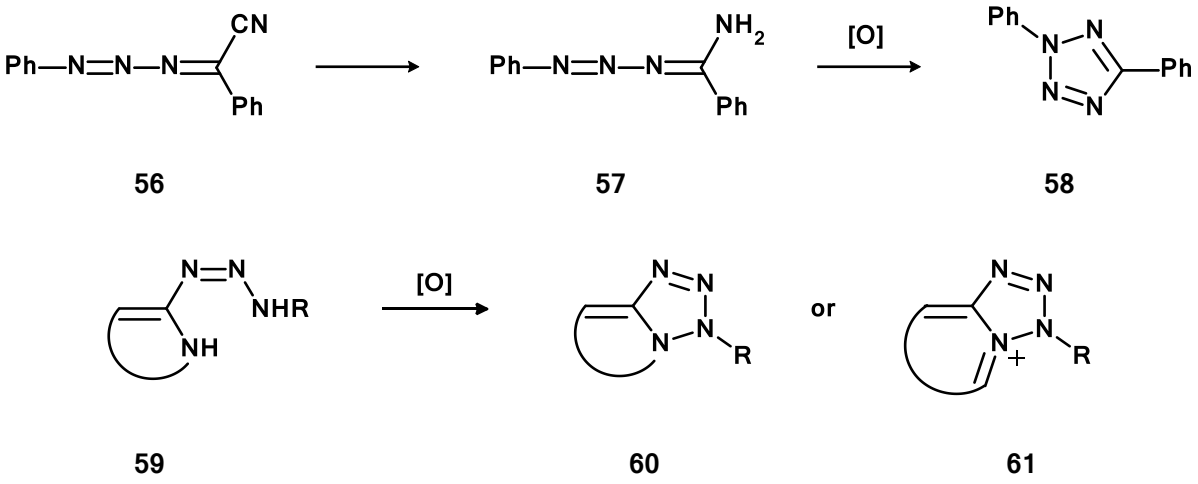

Scheme 1.12: Cyclisation of triazenes.[54]

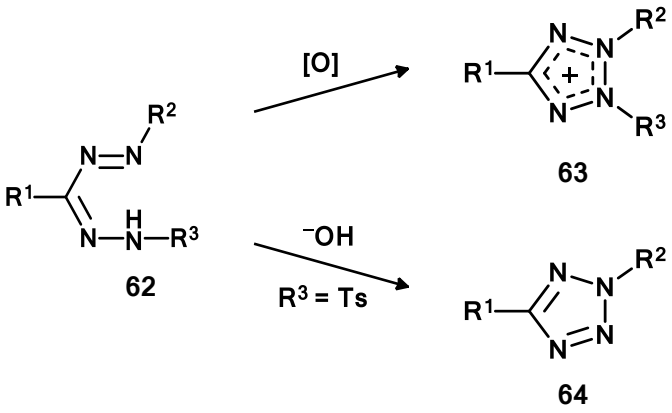

Scheme 1.13: Cyclisation of formazans.[54]

1.2.2.2 Formation of Two bonds from 3 + 2 atom Components

1.2.2.2.1 Addition of Azide ions and metal azides to nitriles and nitrilium ions

The most utilised synthetic route to form 5-substituted tetrazoles is, without a doubt, the addition of azide ions to nitriles.[54] This synthetic approach is thought to pass through a complexed imidoyl azide intermediate (**66**) that undergoes a rapid nitrogen inversion, followed by ring closure.[54] An acidic workup provides the final tetrazole compound (**39**) (Scheme 1.14).[54] Originally, acid was added to a refluxing mixture of sodium azide and nitrile precursor (**65**), generating HN_3 *in situ*.[54] One of the earliest procedures, developed by Herbst *et al.*, consisted of refluxing, for 50 h, the desired nitrile and sodium azide within an acetic acid - butanol mixture.[54] Tetrazole synthesis has also been achieved using ammonium chloride along ammonium azide salts at 120 °C.[54] Much effort has been allocated towards lowering the required temperatures and reaction times.[54] The use of dipolar aprotic solvents, such as DMF and DMSO, has proven to be effective.[54,58]

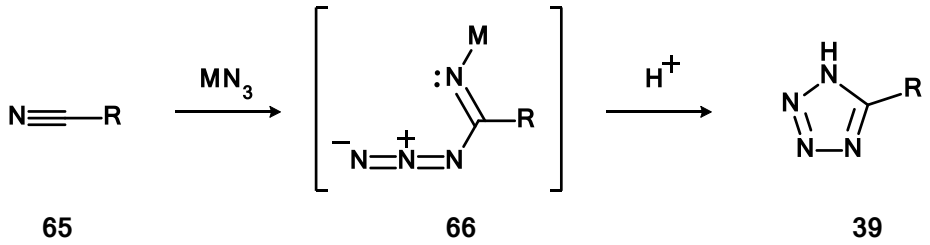

65 **66** **39**

Scheme 1.14: Tetrazole synthesis from nitriles and metal azides. M = must be a metal Lewis acid or addition of acid (H^+) is also required.

The use of nitrilium ions as precursors will provide 1,5-disubstituded tetrazoles.[54] Similarly to the nitrile reactions, nucleophilic addition of an azide ion to the nitrilium ion is thought to provide an imidoyl azide intermediate (**41a**).[54] Upon a nitrogen inversion (**41**), the imidoyl azide will spontaneously cyclise to provide the tetrazole (**42**).[54] It is worth noting that a mechanism

involving a concerted cycloaddition has also been proposed, but the general opinion supports the 2-step process; along with semi-empirical and *ab initio* calculations.[54]

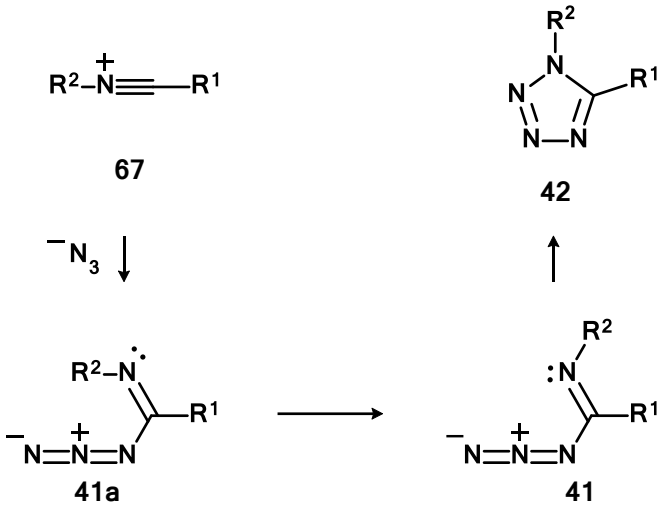

Scheme 1.15: Tetrazole synthesis from nitrilium ions and metal azides.[54]

An example of improvements to 1,5-disubstituted tetrazole synthesis comes to us from the work performed by Amer and Booth.[59] They showed that the use of N-methyl nitrilium trifluoromethanesulfonate salts in dry nitromethane at 25-40 °C provided 1-methyl-5-substituted tetrazoles in yields ranging from 88-92%, depending on R.[59] Variations on the nitrilium ion synthetic route include the Beckmann reactions of oximes (Scheme 1.16) and the Schmidt reaction of ketones, where both utilise HN_3 as the source of azides.[54] Here the nitrilium ion is an intermediate. Use of the Schmidt reaction (Scheme 1.17), reacting carbonyls with HN_3 in the presence of mineral acids, has been a desirable route for the synthesis of tetrazoles since its first reporting.[54] The Schmidt reaction has also been employed to generate a series of steroidal tetrazole, whereby the ring on cyclic-α,β-unsaturated ketones was expanded using excess HN_3 or trimethylsilylazide and trimethylsilyl triflate.[54] It has been suggested, however, that this reaction might

proceed through diazido intermediates, rather than a nitrilium ion intermediate.[54] Other variations on this reaction include the use of Lewis acids, such as $SnCl_2$ with TMS-N_3, $ToCl_4$ with NaN_3, or excess HN_3 in the presence of $BF{\cdot}Et_2O$.[54] The use of isocyanides as precursors, with the acid-catalysed addition of azides, is another example which is thought to go through a nitrilium ion intermediate.[54]

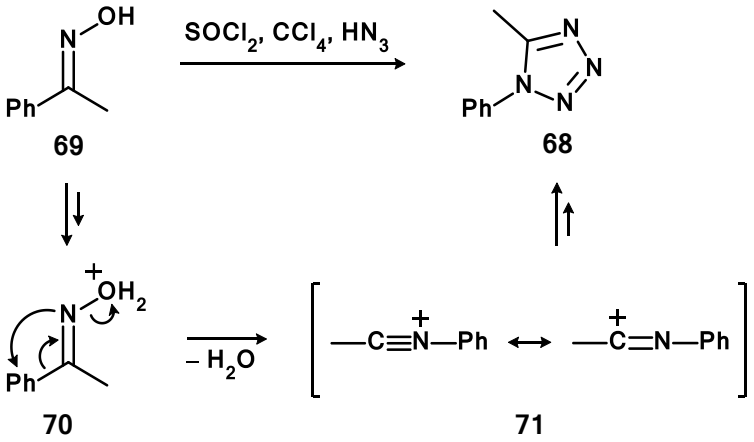

Scheme 1.16: Trapping of Beckmann intermediate with azide ion.[60]

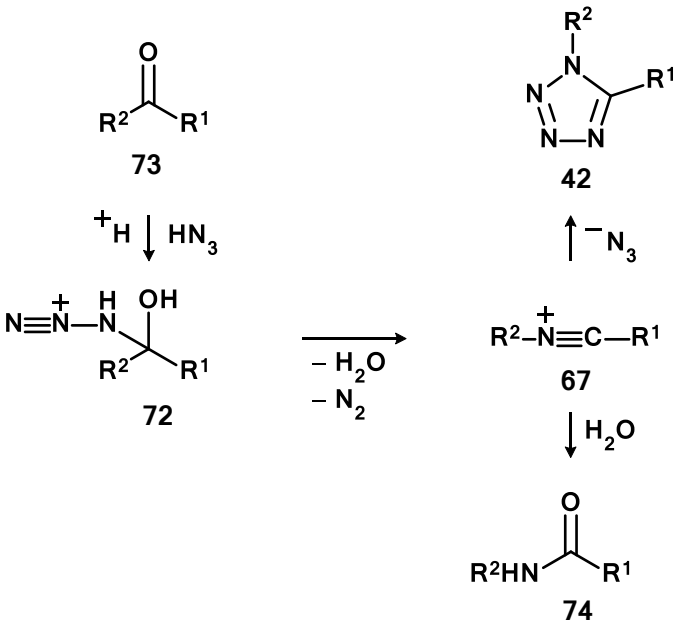

Scheme 1.17: Tetrazoles from Schmidt reaction with nitrilium ion intermediate.[54]

1.2.3 Characterisation of Tetrazoles

Tetrazoles are characterised by standard spectroscopic techniques for organic compounds. In addition to structural characterisation, however, it is also important to identify energetic properties for safe handling.

1.2.3.1 IR Spectroscopy

Though not sufficient for characterising tetrazoles independently, infrared spectroscopy is especially useful for analysing corresponding metal complexes.[54] As suggested by *ab initio* analyses, the stretching-deformation vibrations of the tetrazole ring, namely the cyclic C–N=N and N–N=N fragments,[59] characteristically occur between 900-1100 cm^{-1}.[54] Upon complexation with a given metal source, significant changes are observed in this region, allowing to easily identify successful complexation.[54] Many tetrazoles will also exhibit weak to medium intensity bands in the 1200-1300 cm^{-1} region due to N–N bond vibrations.[61] Another indication of metal complexation is the intensification of these bands.[54]

1.2.3.2 Mass Spectrometry

Tetrazoles are known to undergo three major pathways during mass spectral fragmentation (Scheme 1.18).[54,62-65] The most prominent pathway consists of the loss of N_2, from either the 1,2- or 3,4- positions, especially for 5-substistuted tetrazoles. For the second pathway, a radical species is lost. In the case of 5-methyl tetrazole, the loss of a $HN_2\cdot$ radial leaves a $MeCN_2^+$ fragment, while for 1-phenyl-5-(2'-dimethylaminovinyl)tetrazole, the loss of a $N_3\cdot$ radical gives a nitrilium fragment. The last major pathway consists of the loss of a neutral azide to provide a nitrile species. This third pathway is a characteristic feature, especially for 5-substituted tetrazoles.[54]

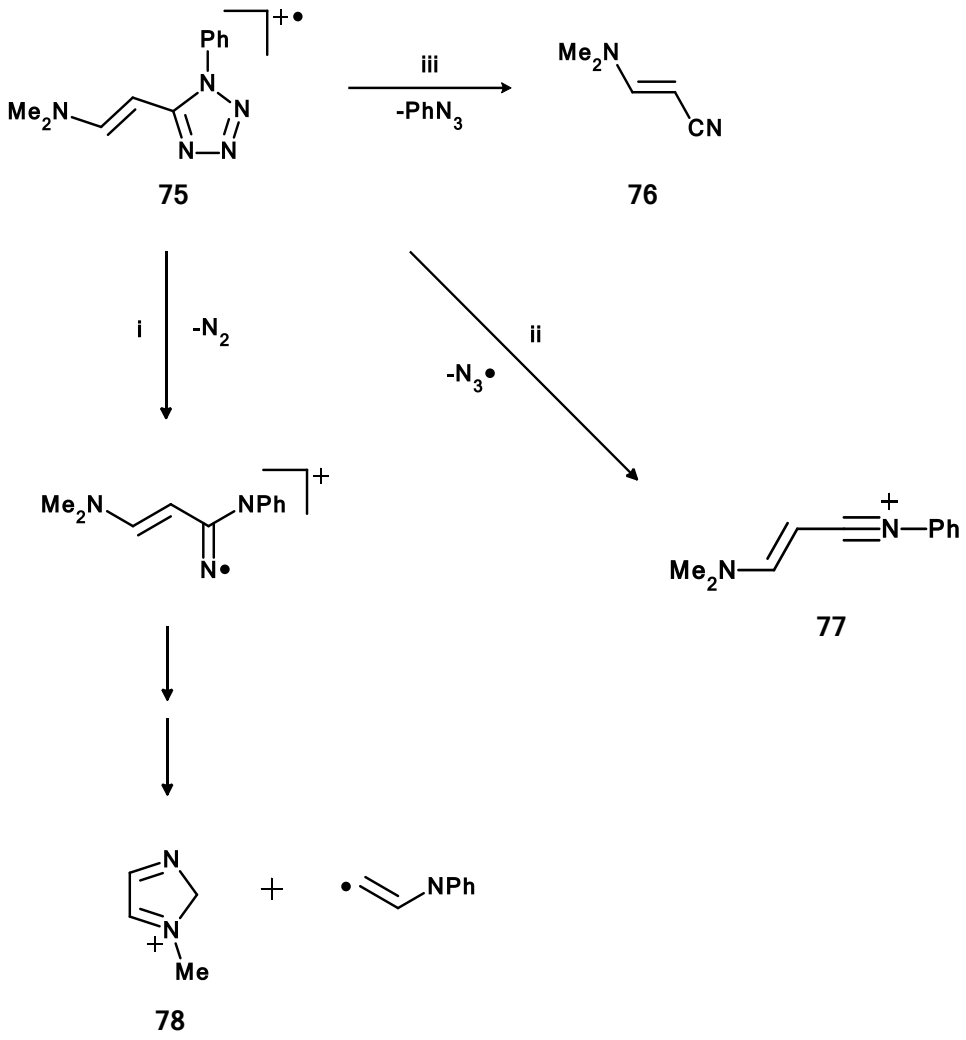

Scheme 1.18: Main MS fragmentation pathways for 1-phenyl-5-(2'-dimethylaminovinyl) tetrazole.[54]

1.2.3.3 NMR Spectroscopy

Since the 1980's, the main characterisation technique for the structure of tetrazoles has been NMR spectroscopy.[54] Due to the high concentration of nitrogen atoms within the chemical formula of these compounds, ^{15}N NMR, or sometimes ^{14}N NMR is used in addition to the typical ^{13}C and ^{1}H isotopes for a complete study.

1.2.3.3.1 ^{15}N NMR Spectroscopy

Due to the nature of tetrazoles, which unsubstituted have a 79.98% nitrogen content, ^{15}N NMR, as well as ^{14}N NMR, are essential characterisation techniques. Furthermore, nitrogen NMR has a very wide chemical shift range, allowing for distinctive assignment. Though the ^{15}N isotope is less abundant then the ^{14}N isotope, it exhibits sharper NMR signals which allow for the extrapolation of more data, such as spin-spin coupling, relaxation information, substitution effects, complexation, and tautomerism (Scheme 1.19).[66,67] For 5-substituted tetrazoles, one can obtain anywhere from 3 to 4 peaks for the tetrazole ring. The pyrrole-type singly-bound nitrogen within substituted rings

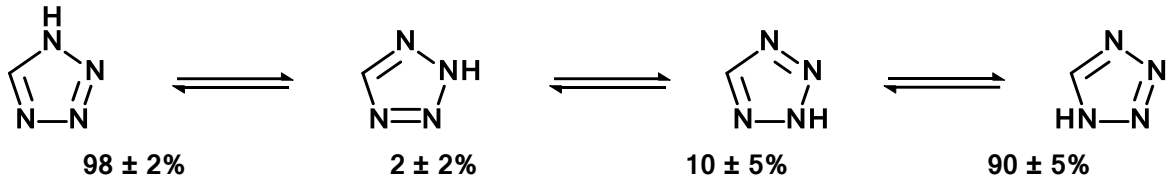

Scheme 1.19: Estimates of tautomeric equilibria for tetrazole in DMSO. Reproduction of Witanowski *et al.*[66]

has the highest π density, resulting in its exhibiting the greatest upfield shift.[54] The higher π density can be understood by electron-distribution theories, where pyrrole-type atoms provide two electrons to the delocalised π-electron system of an azole, while pyridine-type nitrogen atoms, whose lone-pair electron are considered as part of the σ-bond system, will contribute only one electron (Scheme 1.20).[66] As a result, the protonation or quaternisation of tetrazoles leads to an upfield shift.[54] Usually occurring at the N4 position, the upfield shifts may be as high as 100 ppm for the respective N-atom, while adjacent nitrogen atoms exhibit a shift ranging between 15-25 ppm.[54,66]

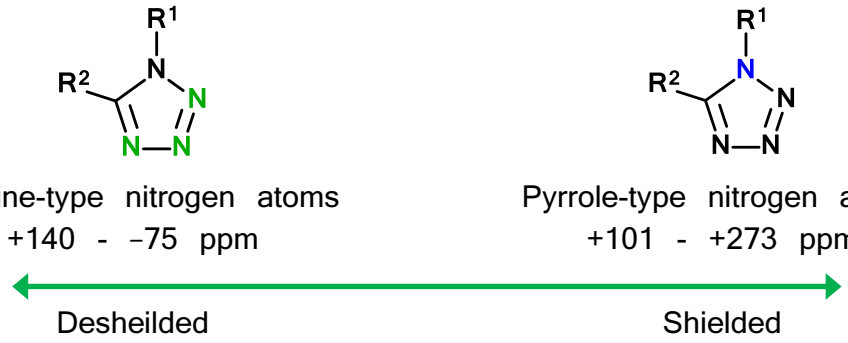

Scheme 1.20: Nitrogen shielding[66]

1.2.3.3.2 ^{13}C NMR Spectroscopy

Despite only having one carbon atom within the ring, ^{13}C NMR is still a vital tool for characterising tetrazoles. The C5 position is very sensitive to the location of substituents on the nitrogen ring, and proves useful in distinguishing isomers.[54] For example, 2,5-disubstituted derivatives are generally desheilded approximately 10 ppm from their 1,5-disubstrituted counterpart.[54] A further experiment that can be used to distinguish between 1,5- and 2,5-disubstituted tetrazole isomers is by irradiation of alkyl groups on the nitrogen ring. Alkyl groups located on N1 will give a nuclear Overhauser enhancement in signals for protons at or near C5, where as a very weak effect, if any, will occur for N2 alkyl substitutents.[54] CPMAS ^{13}C NMR experiments have also proved to be an important tool for providing information regarding the tautomerism in the solid state. Tautomeric investigations into the solid tetrazole compared to 1-methyl-tetrazole found that the 1-NH form was most likely the major tautomer due to similar chemical shifts (144.0 ppm and 143.4 ppm respectively).[54] This was further supported by X-ray studies.

1.2.3.4 Energetic Characterisation

When a new EM is produced, determining its stability towards various stimuli is imperative. Though the power produced by EMs can be of great

benefit when applied towards specific applications, it can also be destructive when not handled appropriately. Determining the parameters within which the risks associated to working with EMs are first assessed with four safety tests. Once the parameters for their manipulation are outlined, they are further studied by various calorimetric experiments.

1.2.3.4.1 Impact sensitivity

The standard for impact safety testing, recognised by the UN Recommendations on the Transportation of Dangerous Goods, is the BAM Drop Hammer test.[68] This test essentially consists of dropping a weight from a given height onto a sample of the EM in question. Knowing the mass of the weight, the height from which it was dropped and its acceleration (gravity), the impact energy can be calculated.[7] This test is repeated until the minimum impact energy required for the initiation of one out of five samples is determined.[7] Parameters for this test generally consists of a sample mass of approximately 40 mg, and a hammer whose mass and height vary from 0.1–10 kg and 0.1–1 m respectively.[7] In the absence of equipment required to perform this type of test, hitting the sample (≤0.5 mg) with a traditional hammer can provide the operator with a rough qualitative estimate of the compound's impact sensitivity, though this is not sufficient for publication.

1.2.3.4.2 Friction sensitivity

Friction sensitivity tests were originally performed with ceramic mortar and pestle.[69] This method however was not accurate at determining the sensitivity of loose materials.[69] The BAM friction tester was developed to replace this technique in the 1950's.[69] The pestle was replaced by a static porcelain peg attached to a lever, to which a weight can be applied.[7] The mortar was replaced by a ceramic plate located on a moving platform.[7] Thus in varying the weight applied and the distance upon which it is placed on

the lever, friction forces in the range of 0.5–360 N can be applied to the sample (located between the plate and peg).[7] Ignition, colour change, generation of crackling sound or denotation is considered a failed experiment. One out of six attempts displaying either of these reactions is considered a failed friction force. Without access to this equipment, scratching a small sample (≤0.5 mg) with a metal spatula over a metal plate can provide the operator with a rough qualitative estimate of the compound's friction sensitivity, though this is not sufficient for publication. Crystals of cyanuric triazide submerged in mother liquor have been known to detonate upon being disturbed by a metal spatula.[70]

1.2.3.4.3 Electrostatic discharge sensitivity

One of the most common sources of accidental initiation of EMs is through electrostatic discharge.[7] Since the operator can be the source, knowing the sensitivity to this property is very important to the safe handling of EMs.[7] ESD test apparatus, which emit spark energies ranging from 0.001–20 J, are used to determine the electrostatic sensitivity.[7] It has been found that particle size has a significant impact on this property and thus samples with the smallest particle size should be used when conducting this test.[7]

1.2.3.4.4 Thermal sensitivity

Thermal stability consists mainly in identifying the decomposition temperature of EMs under no confinements. This is best achieved using TGA and DSC experiments.[7] TGA will provide valuable information regarding the decomposition step(s), while DSC will quantify the energy produced by the decomposition. DSC pans for experiments with suspected EMs should be carefully selected for compatibility. Other thermal stability tests, such as the Koenen or steel-sleeve test is used to determine the critical diameter, at

which the heated sample detonated and destroys the steel sleeve, for transport safety.[7] When confined, certain EMs are more prone to detonation due to the increased pressure imposed by the container. Several other calorimetric experiments can also be performed such as: accelerating rate calorimetry, heat flux calorimetry, thermal conductivity analysis, etc.

1.2.3.4.5 Combustion of tetrazoles

As candidates for EMs, and their corresponding applications, the thermal decomposition of tetrazoles is important to understand. However, it is a complicated process.[54] Their predominant decomposition pathway is the release of dinitrogen gas, which is eliminated from an acyclic azide in its liquid state and from a 2-NH tautomer in the gaseous state.[54] The large release of dinitrogen gas is one of the more attractive decomposition products, as it is environmentally benign and useful in propulsion applications. Within the melted state, approximately 5% of the tetrazole will decompose into HN_3, which is itself an explosive compound at ambient conditions.[54] Common decomposition intermediates include nitrenes and nitrilimines, which themselves decompose to give HCN, H_2, cyanamide polymers, or more N_2 gas.[71-73] Other observed intermediates include 1,2,4,5-tetrazines and 1,2,4-triazoles.[74,75]

1.2.4 Applications

Tetrazoles have been found to be useful for a wide variety of applications, other than the apparent EMs applications. Various photographic products have been improved due to tetrazole based additives: 5-substituted tetrazoles help to prevent fogging of silver halide materials upon storage, 1-aryl-5-thiotetrazoles derivatives improve the sharpness, colour grain and colour reproduction of silver halide colour photographic materials, and the reduction

of tetrazolium salts has also proved to be useful in the intensification of silver-based photographic materials.[54]

Due to its similar properties and improved bioavailability in comparison to carboxylic acids, tetrazoles have become common place in several biologically related applications.[54] Drug applications include antihypertensive activity/angiotensin II antagonists, such as (**79**), which are said to treat congestive heart failure and prevent cardiac hypertrophy, as well as antihistamines, such as (**82**, **80**, **81**), which are often found to be more effective than their carboxylic analog (Scheme 1.21).[54]

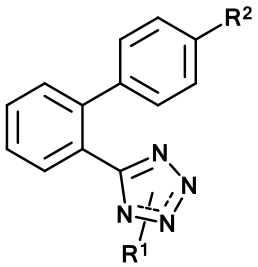

79

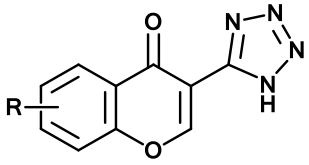

80

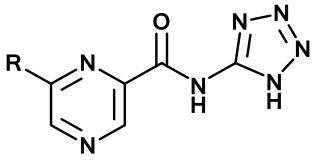

81

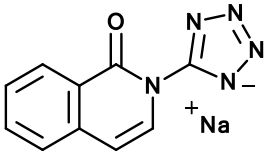

82

Scheme 1.21: Tetrazole based drugs.[54]

Tetrazoles have also been employed in the agricultural sector as plant growth regulators (**83**, **84**), herbicides, and fungicides (**85**) (Scheme 1.22).[54]

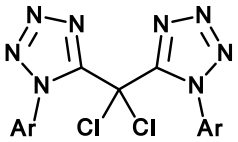

83

Growth inhibitor for oats

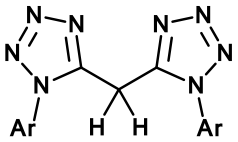

84

Growth stimulant

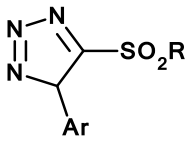

85

Fungicide for plasmopara viticola

Scheme 1.22: Tetrazoles employed in the agricultural sector.[54]

Tetrazoles have even found their way into food chemistry, where they have been used as sweeteners.[54] Some tetrazoyl guanidines (**86**) exhibit a potency as high as 3000 times that of a 2% sucrose solution (Scheme 1.23).[54] Though some derivatives are effective sweeteners, depending on the R and Ar groups, some exhibit no sweetness.[54]

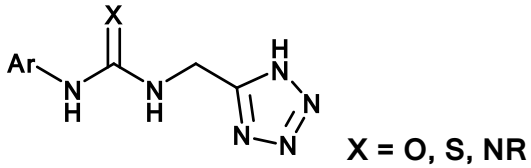

86

Scheme 1.23: Tetrazoyl guanidines uses as sweeteners.[54]

Tetrazoles have long been considered as viable components of explosives and rocket fuels.[54] Examples include the use of 5-nitrotetrazole and azotetrazole (along with their metallic salts) as the main constituent of detonators and primers, along with the several patents for the non-toxic explosives used in air-bags, as well as for the use of fatty amido-derivatives of 5-, 1-, and 2-aminotetrazoles as anticorrosion additives in gasoline-ethanol fuel mixtures.[54] More recently, nitrogen-rich tetrazole-based ligands have been used in metal complexation. Tetrazole-based complexes have been reported as candidates for pyrotechnic products. They have been proposed as colouring alternatives to the toxic barium salts used for green effects, as well as for the production of smokeless products.

1.3 Complexation of nitrogen-rich materials

Since hetero-atoms are ideal for complexation with metal ions, due to the availability of their lone pairs, nitrogen-rich materials make ideal ligands. Research into the development of new explosives consisting of coordination compounds was a thriving avenue in the 1950s and 1960s.[76] The resulting

complexes, however, were found to be extremely sensitive, resulting in a decline in this field.[76]

1.3.1 Roles of hydrazine in complexation

Hydrazine has been found to act as both ligand and redox-reagent in complexation reactions.[77] Both one- and two-electron redox-reactions have been identified with transitional metal complexes.[77] As a ligand, hydrazine has three possible coordination modes: unidentate, bidentate, and bridging.[78] The use of hydrazine as ligand in coordination compounds saw a revival in the 1980s, and new primary explosives, such as nickel hydrazinium nitrate (NHN) and di-(4-amino-3-hydrazino-1,2,3-triazole)-copper(II) perchlorate, have since been produced.[76,79,80] Hydrazine-based complexes have also been shown to exhibit interesting magnetic properties.[81]

1.3.2 Roles of tetrazoles in complexation

Tetrazole based-complexes have been described by several reviews.[82-86] Since there are three pyridine-type nitrogens, each possessing an available lone-pair, within the tetrazole ring, tetrazoles are very versatile ligands.[54] Their binding mode thus includes, unidentate, bidentate, and various bridging modes such as μ2,3, μ2,4, μ3,4 and μ2,3,4.[82] Tetrazole-based ligands have been included in coordination compounds which include: cubic clusters,[87] chains,[88-95] 2D networks,[95-98] 3D networks,[91,95,99-116] and MOFs.[117-124] These have exhibited properties such as gas absorption,[117,118,120,121] photoluminescence,[91,98,101,103,115,116,119,122,123,125,126] and various magnetic behaviours,[88,90-98,101,109,112,116,123,127-131] in addition to energetic behaviour.[126,132-134]

1.4 Thesis overview and research objectives

With aim of developing new EMs, this thesis outlines the synthesis and characterisation of new nitrogen-rich complexes. The work described herein

consists of three separate projects, as described by their respective chapters. The overall goal of this thesis was to design new nitrogen-rich complexes which would be good candidates for various energetic applications, but that could also posses interesting magnetic properties. In addition to the added density that complexation would bring to these potential new EMs, complexation to metal centres which can respond to an applied magnetic field might lead to new and interesting EM applications. The first project focused on developing new hydrazine-based transition metals complexes for possible initiatory applications. The next project was meant to expand on the work performed by a previous group member. This project consisted in using the tetrazole-based H_3bta ligand to form complexes with transitional metals. A homoleptic Fe^{III} complex was found to exhibit high-temperature spin cross over behaviour.[135] Continuation of this project had the aim to develop analogous lanthanide complexes and further study their magnetic properties in conjunction to their energetic properties. The final project, conceived by this author, consisted in developing a new tetrazole-based ligand system: the nitrogen-rich H_4ttp ligand, to serve as an alternate ligand for H_3bta. This ligand was then successfully coordinated to lanthanide metals through hydrothermal reactions. These three respective ligands were chosen for this work due to their high nitrogen content and their known or implied energetic properties.

1.5 References

1. *High Energy Density Materials*; Klapötke, T. M., Ed.; Structure and Bonding; Springer Berlin Heidelberg: **2007**; Vol. 125.

2. Linder, V. in *Propellants*; Seidel, A., Bickford, M., Eds.; Kirk-Othmer Encyclopedia of Chemical Technology; John Wiley & Sons, Inc.: **2000**; Vol. 9, pp 1-47.

3. Bushuyev, O. S.; Brown, P.; Maiti, A.; Gee, R. H.; Peterson, G. R.; Weeks, B. L.; Hope-Weeks, L. J.; J. Am. Chem. Soc. **2012**, 134, pp 1422-1425.

4. Singh, R. P.; Verma, R. D.; Meshri, D. T.; Shreeve, J. M.; Angew. Chem., Int. Ed. **2006**, 45, pp 3584-3601.

5. Sebastiao, E.; Cook, C.; Hu, A.; Murugesu, M. J. Mater. Chem. A **2014**, 2, pp 8153-8173.

6. Akhavan, J. in *Explosives and Propellants*; Seidel, A., Bickford, M., Eds.; Kirk-Othmer Encyclopedia of Chemical Technology; John Wiley & Sons, Inc.: **2004**; Vol. 10, pp 719-744.

7. Klapötke, T. M. *Chemistry of High-Energy Materials*; Walter de Gruyter Gmbh & Co. KG: Berlin, **2011**.

8. Lin, Q.; Li, Y.; Li, Y.; Wang, Z.; Liu, W.; Qi, C.; Pang, S.; J. Mater. Chem. **2012**, 22, pp 666-674.

9. Klapötke, T. M.; Stierstorfer, J.; Jenkins, H. D. B.; van Eldik, R.; Schmeisser, M.; Z. Anorg. Allg. Chem. **2011**, 637, pp 1308-1313.

10. Zang, Y.; Guo, Y.; Joo, Y.; Parrish, D. A.; Shreeve, J. M.; Chem. Eur. J. **2010**, 16, pp 10778-10784.

11. Akhavan, J. *The Chemistry of Explosives*; RSC Publishing: 2011.

12. Zeman, S. J. Energ. Mater. **1999**, 17, pp 305-329.

13. *Explosive Charges & Additives* Business Unit. http://www.eurenco.com.

14. Meyer, R.; Kohler, J.; Homberg, A.; *Explosives*; Wiley-VCH Verlag Gmbh: Weinheim, **2007**.

15. Krause, H. H. in *Ch. 1 - New Energetic Materials; Energetic Materials*: Particle Processing and Characterization; Wiley-VCH Verlag GmbH: Weinheim, **2005**; pp 25.

16. Winter, F. H.; Neufeld, M. J.; Dougherty, K. Acta Astronaut. **2012**, 77, pp 131-137.

17. Curtis, T.; J. Prakt. Chem. **1889**, 39, pp 107.

18. Vasil'ev, A. A.; Valishev, A. I.; Vasil'ev, V. A.; Panfilova, L. V.; Combust., Explos., Shock Waves **2000**, 36, 358-373.

19. Boileau, J.; Fauquignon, C.; Hueber, B.; Meyer, H. H. in *Explosives*; Ullmann's Encyclopedia of Industrial Chemistry; John Wiley & Sons: New York, **2009**; Vol. 13, pp 621-654.

20. McQuaid, M. J. *Computational Characterization of 2-Azidocycloalkanamines: Notional Variations on the Hypergol 2-Azido-N,N-Dimethylethanamine (DMAZ).* 2002, ARL-TR-2806.

21. Schuch, A. F.; Mills, R. L.; J. Chem. Phys. **1970**, 52, pp 6000.

22. Reichlin, R.; Schiferl, D.; Martin, S.; Vanderborgh, C.; Mills, R. L.; Phys. Rev. Lett. **1985**, 55, pp 1464.

23. Mills, R. L.; Olinger, B.; Cromer, D. T.; J. Chem. Phys. **1986**, 84, pp 2837.

24. Olijnyk, H.; J. Chem. Phys. **1990**, 93, pp 8968.

25. Olijnyk, H.; Jephcoat, A. P.; Phys. Rev. Lett. **1999**, 83, pp 332.

26. Bini, R.; Ulivi, L.; Kreutz, J.; Jodl, H. J.; J. Chem. Phys. **2000**, 112, pp 8522.

27. Goncharov, A. F.; Gregoryanz, E.; Mao, H.; Liu, Z.; Hemley, R. J.; Phys. Rev. Lett. **2000**, 85, pp 1262.

28. Eremets, M. I.; Hemley, R. J.; Mao, H.; Gregoryanz, E.; Nature **2001**, 411, pp 170.

29. Gregoryanz, E.; Goncharov, A. F.; Hemley, R. J.; Mao, H.; Phys. Rev. B **2001**, 64, pp 052103.

30. Gregoryanz, E.; Goncharov, A. F.; Hemley, R. J.; Mao, H.; Somayazulu, M.; Shen, G.; Phys. Rev. B **2002**, 66, pp 224108.

31. Eremets, M. I.; Gavriliuk, A. G.; Trojan, I. A.; Dzivenko, D. A.; Boehler, R.; Nat. Mater. **2004**, 3, pp 558-563.

32. LeSar, R.; J. Chem. Phys. **1984**, 81, pp 5104.

33. Mitáš, L.; Martin, R. M.; Phys. Rev. Lett. **1994**, 72, pp 2438.

34. McMahan, A. K.; LeSar, R.; Phys. Rev. Lett. **1985**, 54, pp 1929.

35. Martin, R. M.; Needs, R. J.; Phys. Rev. B **1986**, 34, pp 5082.

36. Lewis, S. P.; Cohen, M. L.; Phys. Rev. B **1992**, 46, pp 11117.

37. Mailhiot, C.; Yang, L. H.; McMahan, A. K.; Phys. Rev. B **1992**, 46, pp 14419.

38. Barbee III, T. W. in *Phonons and metastability in compressed nitrogen; AIP Conference Proceedings - High-pressure science and technology*; **1993**; Vol. 309.

39. Alemany, M. M. G.; Martins, J. L.; Phys. Rev. B **2003**, 68, pp 024110.

40. Mattson, W. D.; Sanchez-Portal, D.; Chiesa, S.; Martin, R. M.; Phys. Rev. Lett. **2004**, 93, pp 125501.

41. Yu, H. L.; Yang, G. W.; Yan, X. H.; Xiao, Y.; Mao, Y. L.; Yang, Y. R.; Cheng, M. X.; Phys. Rev. B **2006**, 76, pp 012101.

42. Klapötke, T. M. in *Nichtmetallchemie*; Riedel, E., Ed.; Moderne Anorganische Chemie; Walter de Gruyter: Berlin, 2007.

43. Eremets, M. I.; Gavriliuk, A. G.; Serebryanaya, N. R.; Trojan, I. A.; Dzivenko, D. A.; Boehler, R.; Mao, H. K.; Hemley, R. J.; J. Chem. Phys. **2004**, 121, pp 11296.

44. Eremets, M. I.; Popov, M. Y.; Trojan, I. A.; Denisov, V. N.; Boehler, R.; Hemley, R. J.; J. Chem. Phys. **2004**, 120, pp 10618.

45. Christe, K. O.; Wilson, W. W.; Sheehy, J. A.; Boatz, J. A.; Angew. Chem., Int. Ed. **1999**, 38, pp 2004-2009.

46. Vij, A.; Wilson, W. W.; Vij, V.; Tham, F. S.; Sheehy, J. A.; Christe, K. O.; J. Am. Chem. Soc. **2001**, 123, pp 6308-6313.

47. Klapötke, T. M.; Angew. Chem. **1999**, 111, pp 2694.

48. Schroer, T.; Haiges, R.; Schneider, S.; Christe, K. O.; Chem. Commun. **2005**, 2005, pp 1607-1609.

49. Vij, A.; Pavlovich, J. G.; Wilson, W. W.; Vij, V.; Christe, K. O.; Angew. Chem., Int. Ed. **2002**, 41, pp 3051.

50. da Silva, G.; Bozzelli, J. W.; J. Org. Chem. **2008**, 73, pp 1343-1353.

51. *Green Energetic Materials*; John Wiley & Sons Ltd: 2014.

52. Cheng, M.; Ho, H.; Lam, C.; Li, W.; J. Serb. Chem. Soc. **2002**, 67, pp 257-264.

53. Geiger, U.; Elyashiv, A.; Fraenkel, R.; Zilberg, S.; Haas, Y.; Chem. Phys. Lett. **2013**, 556, pp 127-131.

54. Butler, R. N. in *Tetrazoles*; Storr, R. C., Ed.; Comprehensive Heterocyclic Chemistry II - A Review of the Literature 1982-1995; Elsevier Science Ltd.: Glasgow, UK, 1996; Vol. 4 - Five-Membered Rings with more than Two Heteroatoms and Fused Carbocyclic Derivatives, pp 621-679.

55. Mo, O.; De Paz, J. L. G; Yanez, M.; J. Phys. Chem. **1986**, 90, pp 5597-5604.

56. Jano, I.; J. Phys. Chem. **1991**, 95, pp 7694-7699.

57. Yagupolskii, L. M.; Shelyazhenko, S. V.; Maletina, I. I.; Petrik, V. N.; Rusanov, E. B.; Chernega, A. N.; Eur. J. Org. Chem. **2001**, 2001, pp 1225-1233.

58. Tisseh, Z. N.; Dabiri, M.; Nobahar, M.; Soorki, A. A.; Bazgir, A.; Tetrahedron **2012**, 68, pp 3351-3356.

59. Amer, M. I. K.; Booth, B. L.; J. Chem. Res. Synop. **1993**, 1, pp 4-5.

60. Craig, D. in *Oxidation of C-C Bonds: The Beckmann and Related Reactions*; Trost, B. M., Fleming, I., Eds.; Comprehensive Organic Synthesis - Selectivity, Strategy & Efficiency in Modern Organic Chemistry; Elsevier Ltd.: Oxford, UK, **2005**; Vol. 7, pp 689-703.

61. Sokolova, M. M.; Melnikov, V. V.; Ostrovskii, V. A.; Zh. Org. Khim. **1975**, 11, pp 1744-1749.

62. Ražyńska, A.; Tempczyk, A.; Maliński, E.; Szafranek, J.; Grzonka, Z.; Hermann, P.; J. Chem. Soc., Perkin Trans. **1983**, 2, pp 379-383.

63. Butler, R. N. in *Tetrazoles; Comprehensive Heterocyclic Chemistry*; Elsevier Science Ltd.: **1984**; Vol. 5, pp 791-838.

64. Herrmann, M.; Fischer, G. W.; Org. Mass Spectrom. **1989**, 24, pp 823-829.

65. Fischer, G. W.; Herrmann, M.; J. Heterocycl. Chem. **1996**, 33, pp 815-823.

66. Witanowski, M.; Stefaniak, L.; Webb, G. A.; Annu. Rep. NMR Spectro. **1987**, 18, pp 1-211.

67. Naumenko, V. N.; Koren, A. O.; Gaponik, P. N.; Magn. Reson. Chem. **1992**, 30, pp 558-564.

68. United Nations UN Recommendations on the Transport of Dangerous Goods: Manual of Tests and Criteria. 2009.

69. Harris, J. *Friction Sensitivity of Primary Explosives*. 1982, AD A11 9982.

70. Matyáš, R.; Pachman, J. *Primary Explosives*; Springer: Heidelberg, 2013.

71. Lesnikovich, A. I.; Ivashkevich, O. A.; Lyutsko, V. A.; Printsev, G. V.; Kovalenko, K. K.; Gaponik, P. N.; Levchik, S. V.; Thermochim. Acta **1989**, 145, pp 195-202.

72. Vyazovkin, S. V.; Lesnikovich, A. I.; Lyutsko, V. A.; Thermochim. Acta **1990**, 165, pp 17-22.

73. Lesnikovich, A. I.; Ivashkevich, O. A.; Printsev, G. V.; Gaponik, P. N.; Levchik, S. V.; Thermochim. Acta **1990**, 171, pp 207-213.

74. Feist, M.; Csongár, C.; Adler, L.; J. Therm. Anal. Calorim. **1987**, 32, pp 1957-1967.

75. Feist, M.; Adler, L.; Csongár, C.; J. Therm. Anal. Calorim. **1988**, 33, pp 1201-1206.

76. Wojewódka, A.; Bełzowski, J.; Chemik Int. Ed. **2011**, 65, pp 20-27.

77. Bottomley, F.; Q. Rev., Chem. Soc. **1970**, 24, pp 617-638.

78. Heaton, B. T.; Jacob, C.; Page, P.; Coord. Chem. Rev. **1996**, 154, pp 193-229.

79. Shunguan, Z.; Youchen, W.; Wenyi, Z.; Jingyan, M.; Propellants, Explos., Pyrotech. **1997**, 22, pp 317-320.

80. Chernai, A. V.; Sobolev, V. V.; Chernai, V. A.; Ilyushin, M. A.; Dlugashek, A.; Combust., Explos., Shock Waves **2003**, 39, pp 335-339.

81. Patil, K. C.; Govindarajan, S.; Soundararajan, R.; Verneker, V. R.; Proc. Indian Acad. Sci. (Chem. Sci.) **1981**, 90, pp 421-426.

82. Aromí, G.; Barrios, L. A.; Roubeau, O.; Gamez, P.; Coord. Chem. Rev. 2011, 255, pp 485-546.

83. Popova, E. A.; Trifonov, R. E.; Ostrovskii, V. A.; Arkivoc **2012**, 2012, pp 45-65.

84. Gao, H.; Shreeve, J. M.; Chem. Rev. **2011**, 111, pp 7377-7436.

85. Zhao, H.; Qu, Z.; Ye, H.; Xiong, R.; Chem. Soc. Rev. **2008**, 37, pp 87-100.

86. Gaponik, P. N.; Voitekhovich, S. V.; Ivashkevich, O. A.; Usp. Khim. **2006**, 75, pp 569-603.

87. Dinca, M.; Harris, T. D.; Iavarone, A. T.; Long, J. R.; J. Mol. Struct. **2008**, 890, pp 139-143.

88. Shvedenkov, Y. G.; Virovets, A. V.; Lavrenova, L. G.; Russ. Chem. Bull. **2003**, 52, pp 1353-1357.

89. Zhao, H.; Ye, Q.; Wu, Q.; Song, Y.; Liu, Y.; Xiong, R.; Z. Anorg. Allg. Chem. **2004**, 360, pp 1367-1370.

90. Friedrich, M.; Gálvez-Ruiz, J. C.; Klapötke, T. M.; Mayer, P.; Weber, B.; Weigand, J. J.; Inorg. Chem. **2005**, 44, pp 8044-8052.

91. Absmeier, A.; Bartel, M.; Carbonera, C.; Jameson, G.; Weinberger, P.; Caneschi, A.; Mereiter, K.; Letard, J.; Linert, W.; Chem. Eur. J. **2006**, 12, pp 2235-2243.

92. Quesada, M.; Kooijman, H.; Gamez, P.; Costa, J. S.; van Koningsbruggen, P. J.; Weinberger, P.; Reissner, M.; Spek, A. L.; Haasnoot, J. G.; Dalton Trans. **2007**, pp 5434-5440.

93. Rodriguez-Dieguez, A.; Mota, A. J.; Cano, J.; Ruiz, J.; Choquesillo-Lazarte, D.; Colacio, E.; Dalton Trans. **2009**, pp 6335-6344.

94. Herchel, R.; Sindelar, Z.; Travnicek, Z.; Zboril, R.; Vanco, J.; Dalton Trans. **2009**, pp 9870-9880.

95. Hu, T.; Tao, Y.; Chang, Z.; Bu, X.; Inorg. Chem. **2011**, 50, pp 10994-11003.

96. Keene, T. D.; Deng, Y.; Li, F.; Ding, Y.; Wu, B.; Liu, S.; Ambrus, C.; Waldmann, O.; Decurtins, S.; Yang, X.; Inorg. Chim. Acta **2009**, 362, pp 2265-2269.

97. Liu, P.; Wang, Y.; Tian, C.; Peng, H.; Gao, E.; J. Mol. Struct. **2009**, 920, pp 459-465.

98. Wu, X.; Dong, P.; Yu, R.; Zhang, Q.; Kuang, X.; Chen, S.; Lin, Q.; Lu, C.; Cryst. Eng. Comm. **2011**, 13, pp 3686-3688.

99. Hill, M. S.; Mahon, M. F.; Molloy, K. C.; J. Chem. Soc. Dalton Trans. **1996**, pp 1857-1865.

100. Hill, M. S.; Mahon, M. F.; McGinley, J.; Molloy, K. C.; J. Chem. Soc. Dalton Trans. **1996**, pp 835-845.

101. Stassen, A.; Kooijman, H.; Spek, A.; Haasnoot, J.; Reedijk, J.; J. Chem. Crystallogr. **2001**, 31, pp 307-314.

102. Tao, J.; Ma, Z.; Huang, R.; Zheng, L.; Inorg. Chem. **2004**, 43, pp 6133-6135.

103. Jiang, C.; Yu, Z.; Jiao, C.; Wang, S.; Li, J.; Wang, Z.; Cui, Y.; Euro. J. Inorg. Chem. **2004**, 2004, pp 4669-4674.

104. Dong, Wen-Wen, Zhao, Jun; Xu, L.; J. Solid State Chem. **2008**, 181, pp 1149-1154.

105. Dong, W.; Zhao, J.; Xu, L.; Cryst. Growth Des. **2008**, 8, pp 2882-2886.

106. Jiang, T.; Zhang, X.; Cryst. Growth Des. **2008**, 8, pp 3077-3083.

107. Kostakis, G. E.; Abbas, G.; Anson, C. E.; Powell, A. K.; Cryst. Eng. Comm. **2008**, 10, pp 1117-1119.

108. Bondar, O. A.; Lukashuk, L. V.; Lysenko, A. B.; Krautscheid, H.; Rusanov, E. B.; Chernega, A. N.; Domasevitch, K. V.; Cryst. Eng. Comm. **2008**, 10, pp 1216-1226.

109. Li Ru-Yin; Gao Song; Chin. J. Inorg. Chem **2008**, 24, pp 1229-1236.

110. Kostakis, G. E.; Mondal, K. C.; Anson, C. E.; Powell, A. K.; Polyhedron **2010**, 29, pp 24-29.

111. Tao, Y.; Li, J.; Chang, Z.; Bu, X.; Cryst. Growth Des. **2010**, 10, pp 564-574.

112. Yang, E.; Liu, Z.; Wu, X.; Chang, H.; Wang, E.; Zhao, X.; Dalton Trans. **2011**, 40, pp 10082-10089.

113. Li, Y.; Tao, Y.; Wang, L.; Hu, T.; Bu, X.; RSC Adv. **2012**, 2, pp 4348-4352.

114. Liang, L.; Li, G.; Sun, L.; Lan, G.; Zhang, L.; Yang, C.; Ma, Y.; Deng, H.; Inorg. Chem. Commun. **2012**, 20, pp 295-298.

115. Song, W.; Li, S.; Miao, D.; Ji, L.; Ng, S. W.; Tiekink, E. R. T.; Ma, D.; Inorg. Chem. Commun. **2012**, 17, pp 91-94.

116. Liang, L.; Peng, G.; Ma, L.; Sun, L.; Deng, H.; Li, H.; Li, W.; Cryst. Growth Des. **2012**, 12, pp 1151-1158.

117. Dinca, M.; Dailly, A.; Liu, Y.; Brown, C. M.; Neumann, D. A.; Long, J. R.; J. Am. Chem. Soc. **2006**, 128, pp 16876-16883.

118. Dincă, M.; Yu, A. F.; Long, J. R.; J. Am. Chem. Soc. **2006**, 128, pp 8904-8913.

119. Wang, X.; Chen, J.; Liu, J.; Cryst. Growth Des. **2007**, 7, pp 1227-1229.

120. Dinca, M.; Dailly, A.; Tsay, C.; Long, J. R.; Inorg. Chem. **2008**, 47, pp 11-13.

121. Li, J.; Tao, Y.; Yu, Q.; Bu, X.; Sakamoto, H.; Kitagawa, S.; Chem. Eur. J. **2008**, 14, pp 2771-2776.

122. Zheng, L.; Li, H.; Leng, J.; Wang, J.; Tong, M.; Eur. J. Inorg. Chem. **2008**, 2008, pp 213-217.

123. Liang, X.; Jia, J.; Wu, T.; Li, D.; Liu, L.; Tsolmon; Zhu, G.; Cryst. Eng. Comm. **2010**, 12, pp 3499-3501.

124. Yan, Z.; Li, M.; Gao, H.; Huang, X.; Li, D.; Chem. Commun. **2012**, 48, pp 3960-3962.

125. Andreiadis, E. S.; Demadrille, R.; Imbert, D.; Pecaut, J.; Mazzanti, M.; Chem. Eur. J. **2009**, 15, pp 9458-9476.

126. Wang, S.; Zheng, F.; Zhang, M.; Liu, Z.; Chen, J.; Xiao, Y.; Wu, A.; Guo, G.; Huang, J.; Inorg. Chem. **2013**, 52, pp 10096-10104.

127. Shvedenkov, Y.; Virovets, A.; Lavrenova, L.; Russ. Chem. Bull. **2003**, 52, pp 1353-1357.

128. Shvedenkov, Y.; Ikorskii, V.; Lavrenova, L.; J. Phys. IV **2004**, 114, pp 649-650.

129. Li, R.; Wang, X.; Liu, T.; Xu, H.; Zhao, F.; Wang, Z.; Gao, S.; Inorg. Chem. **2008**, 47, pp 8134-8142.

130. Rodriguez-Dieguez, A.; Palacios, M. A.; Sironi, A.; Colacio, E.; Dalton Trans. **2008**, pp 2887-2893.

131. Yao, R.; Qin, Y.; Ji, F.; Zhao, Y.; Zhang, X.; Dalton Trans. **2013**, 42, pp 6611-6618.

132. Hiskey, M. A.; Chavez, D.; Naud, D. US Patent US6214139 B1, 2001.

133. Steinhauser, G.; Klapötke, T. M.; Angew. Chem., Int. Ed. **2008**, 47, pp 3330-3347.

134. Karaghiosoff, K.; Klapoetke, T. M.; Sabate, C. M.; Eur. J. Inorg. Chem. **2009**, 2009, pp 238-250.

135. Cook, C.; Habib, F.; Aharen, T.; Rodolphe, C.; Hu, A.; Murugesu, M.; Inorg. Chem. **2013**, 52, pp 1825-1831.

Chapter 2

Hydrazine ligand system

2.1 Introduction

Though traditional energetic salts and complexes, such as lead azide and mercury fulminate (MF), exhibit densities which far exceed those of regular organic explosives, these are typically less powerful and classified as primary explosives. There are two main reasons why the high density general rule (higher density leads to better energetic performance) fails to apply for these compounds. Firstly, metal–ligand bonds tend to be lower in energy than organic bonds, and thus less energy is released upon their decomposition.[1] Furthermore, metals will generally form oxides upon decomposition, rather than generating gaseous products, such as CO_2, N_2, and H_2O, whose presence and rapid production is required to cause the pressure necessary to induce a detonation.[1] A simple improvement, would be to synthesise higher gas-generating energetic metal complexes, as generating more gas would allow for higher power output. Hydrazine-based complexes are prime candidates due to hydrazine's use as a rocket fuel.

Hydrazine's use as a ligand in metal complexes has long been known, with examples dating as far back as 1894.[2,3,4] These, along with more recent examples,[5,6,7,8,9,10,11] exhibited a mixture of hydrazine and corresponding counter ions within the coordination sphere. Hydrazine-based metal complexes have been shown to exhibit catalytic,[12] and antibiotic behaviour.[13] Interesting one and three dimensional magnetic interactions have also been observed for hydrazinium metal sulphates, which exhibit linear-chain antiferromagnet behaviour.[8]

However, it wasn't until the 1960's that evidence of a homoleptic hydrazine complex, hexahydrazinecobalt dichloride $[Co(N_2H_4)_6]Cl_2$, was provided by Nicholls *et al.*[6] Nickel hydrazinium nitrate (NHN, **87**), was one of the next homoleptic hydrazine complexes to be identified. Originally reported by

Shunguan *et al.*,[14] this compound, was only characterised by IR spectroscopy; in addition to studies regarding its energetic performance; which proved to be of great intrigue (a detonation velocity of 7000 m/s at maximum density of 1.7 g/cm^3). This prompted subsequent groups to further investigate its potential as an initiatory compound in addition to synthesising analogous complexes.[15,16] Unfortunately, no crystal structures were provided to support the proposed structures (Table 2.1).

Table 2.1: Mononuclear Hydrazine Complexes reported by Wojewódka *et al.*[16]

Proposed structure	Nitrate analogues		Perchlorate analogues	
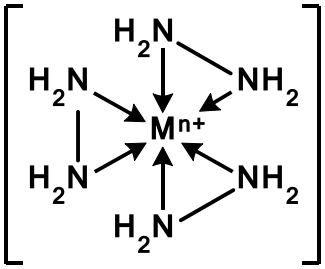 $(X^-)_n$	$[Ni(H_4N_2)_3](NO_3)_2$	**87**		
	$[Zn(H_4N_2)_3](NO_3)_2$	**88**	$[Zn(H_4N_2)_3](ClO_4)_2$	**89**
	$[Co(H_4N_2)_3](NO_3)_3$	**90**	$[Co(H_4N_2)_3](ClO_4)_3$	**91**
	$[Cr(H_4N_2)_3](NO_3)_3$	**92**	$[Cr(H_4N_2)_3](ClO_4)_3$	**93**
$X^- = NO_3^-, ClO_4^-$	$[Cd(H_4N_2)_3](NO_3)_2$	**94**	$[Cd(H_4N_2)_3](ClO_4)_2$	**95**

Complexes were characterized by elemental analysis, IR spectroscopy, and X-ray fluorescence spectroscopy (EDXRF), as well as sensitivity tests.

Further investigations regarding the improvement of complex **87**, led to the synthesis of ionic hydrazine-based polymers (Figure 2.1).[1] These ionic hydrazine-based polymers were the first homoleptic hydrazine complexes for which crystal structures have been provided. Compound **96** is predicted to have a heat of detonation comparable to TNT, while compounds **97** and **98** are predicted to be more comparable to HMX.[1] Presented as compounds suitable for use in microcharges, these ionic hydrazine-based polymers were the inspiration for the work in this chapter.

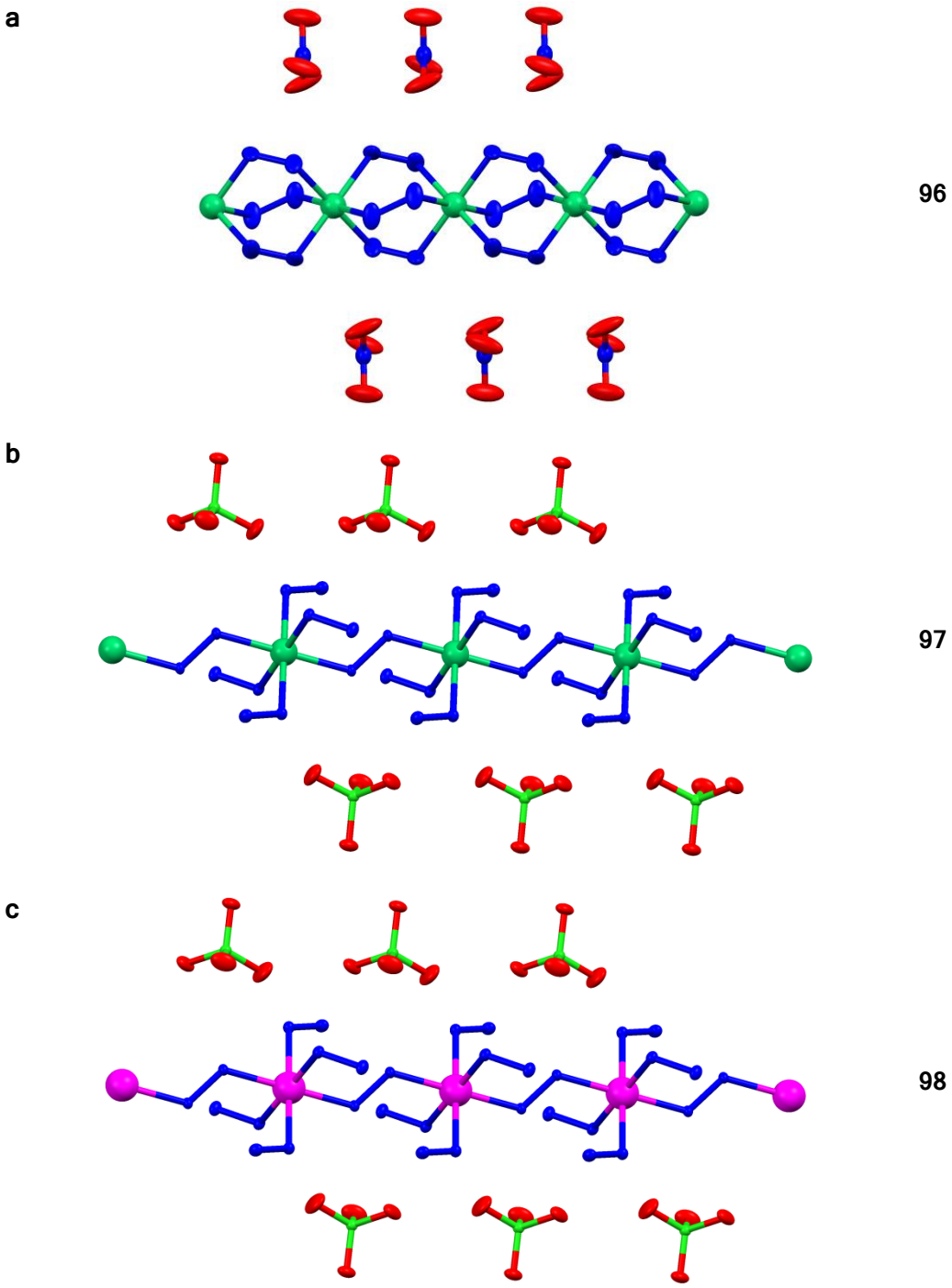

Figure 2.1: Hydrazine-based ionic polymers presented by Bushuyev *et al.*[1]: a) nickel hydrazine nitrate $[Ni(H_4N_2)_3](NO_3)_2$, b) nickel hydrazine perchlorate $[Ni(H_4N_2)_3](ClO_4)_2$, c) cobalt hydrazine perchlorate $[Co(H_4N_2)_3](ClO_4)_2$. Ellipsoids shown at 50 % with metal centers shown using the ball and stick representation. Colour code: teal green (Ni), pink (Co), blue (N), red (O), lime green (Cl). Hydrogens are omitted for clarity.

2.2 Results and Discussion

2.2.1 Structures

2.2.1.1 Chain structures

2.2.1.1.1 $[Co(\mu\text{-}N_2H_4)_2(NO_3)_2]_n$

In examining the work published by Bushuyev *et al.*,[1] the first objective was to synthesise analogues of the triply-bridged nickel complex **96**. Given that a cobalt analogue **98** of singly-bridged nickel complex **97** had been reported, but none for **96**, the first attempts were focused towards acquiring the cobalt analogue. However, catena-bis-μ-hydrazine(N,N')-dinitratocobalt(II,II) (**99**), was isolated instead of obtaining an analogous complex of **96** (Figure 2.2).

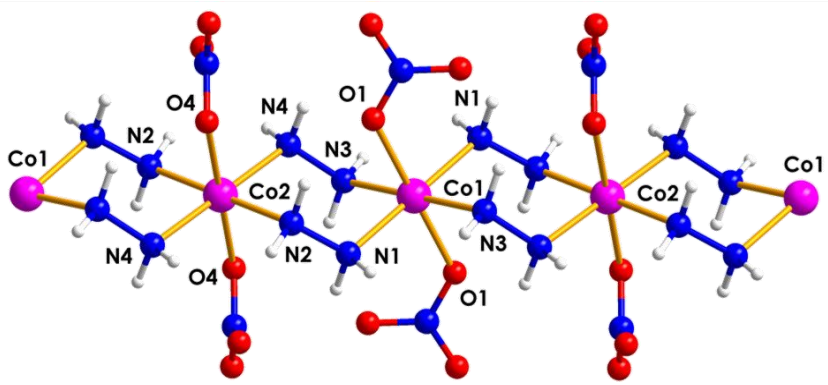

99

Figure 2.2: Labeled molecular structure showing a chain fragment of complex $[Co(\mu\text{-}N_2H_4)_2(NO_3)_2]_n$ (**99**). Ball and stick representation. Colour code: pink (Co), blue (N), red (O), white (H).

This 1D chain complex consists of two crystallographically unique cobalt metal centers, which can be easily identified by the orientation of the coordinated nitrate ions; either parallel (O1) or perpendicular (O4) to the plane of the chain. Both metal centers consist of slightly distorted octahedral geometry, exhibiting a Jahn-Teller elongation along the *z* axis (Figure 2.3, Table 2.2). This distortion is to be expected as the *z* axis ligands (nitrates)

are different from the bridging hydrazine ligands, and thus removing the degeneracy of the *d*-orbitals becomes favourable. The Co2 has a more pronounced Jahn-Teller elongation than Co1. The intrametallic distance of 4.14 Å of this chain complex is within the range reported for other octahedral 1D Co^{II} chains: a mixed azide and tetrazolate bridged 1D Co^{II} chain (3.63 Å),[17] and an end to end azide bridged 1D Co^{II} chain (5.38 Å).[18] The closest intermetallic distance of 6.83 Å is shorter than what has been reported for the end to end azide bridged 1D Co^{II} chain (8.28 Å),[18] though this complex has coordinated pyridines, which are considerably larger, at its axial positions. The two metal centers are bridged by two hydrazine molecules, which exhibit torsion angles of -71.29° and 77.11° for N1-N2 and N3-N4 respectively. In addition to a greater torsion angle, N3-N4 also exhibits a longer N-N bond (Table 2.2).

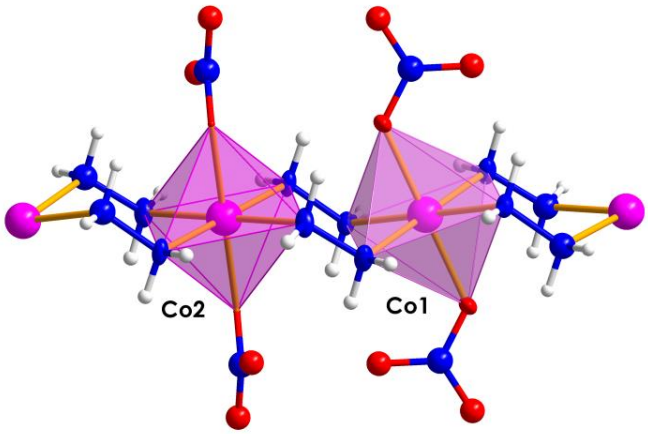

Figure 2.3: Coordination sphere polyhedra for complex **99**. Ellipsoid representation at 50% and ball and stick representation for the metal center. Colour code: pink (Co), blue (N), red (O), white (H).

Complex **99** crystallises in the triclinic P-1 space group. The 1D chains pack together such that the nitrate groups are pointed towards each other (Figure 2.4). Coordinated nitrate ions of the same orientation are staggered with respects to the ions in the rows above and below as seen along axis

b. Though the metal centers overlap nicely when viewed along axis *c*, the indication of the presence of two different metal centers can be seen by the imperfect overlap of hydrazine bridges.

Table 2.2: Selected distances and angles for complex **99**.

Distances (Å)			
Co1-N1	2.15	Co2-N2	2.16
Co1-N3	2.14	Co2-N4	2.16
Co1-O1	2.16	Co2-O2	2.17
O1-N5	1.26	O2-N6	1.27
N1-N2	1.45	N3-N4	1.46
Co1-Co2 (intra)	4.14	Co1-Co2 (inter)	6.83
Angles (°)			
N1-Co1-N3 (bridge)	88.38	N2-Co2-N4 (bridge)	91.19
N1-Co1-N3	91.62	N2-Co2-N4	88.81
N1-Co1-O1	95.35	N2-Co2-O1	80.94
Co1-N1-N2-Co2	-71.29	Co1-N3-N4-Co2	77.11

To gauge the stimuli sensitivity of this complex, rudimentary impact and friction tests were undertaken prior to manipulation for analyses. This consisted of hitting a small sample (1-3 crystals) with a hammer over a metal surface, and scratching the sample with a metal spatula. These tests were performed within the fume hood behind a blast shield, while wearing Kevlar sleeves, Kevlar gloves under thick leather gloves, and polycarbonate face shield (in addition to standard laboratory PPE such as lab coat and safety glasses). Complex **99** showed no signs of reactivity to these stimuli. In order to determine its sensitivity towards heat, a fresh sample was placed in an aluminium boat atop a hot plate located behind the blast shield. Around 200 °C, the pink crystals started to hop, accompanied by a soft popping noise, and soon appeared to vanish, leaving behind a thin dark grey residue.

Though this decomposition was quite rapid, no loud sounds or shock waves, characteristic of detonations, were noticed.

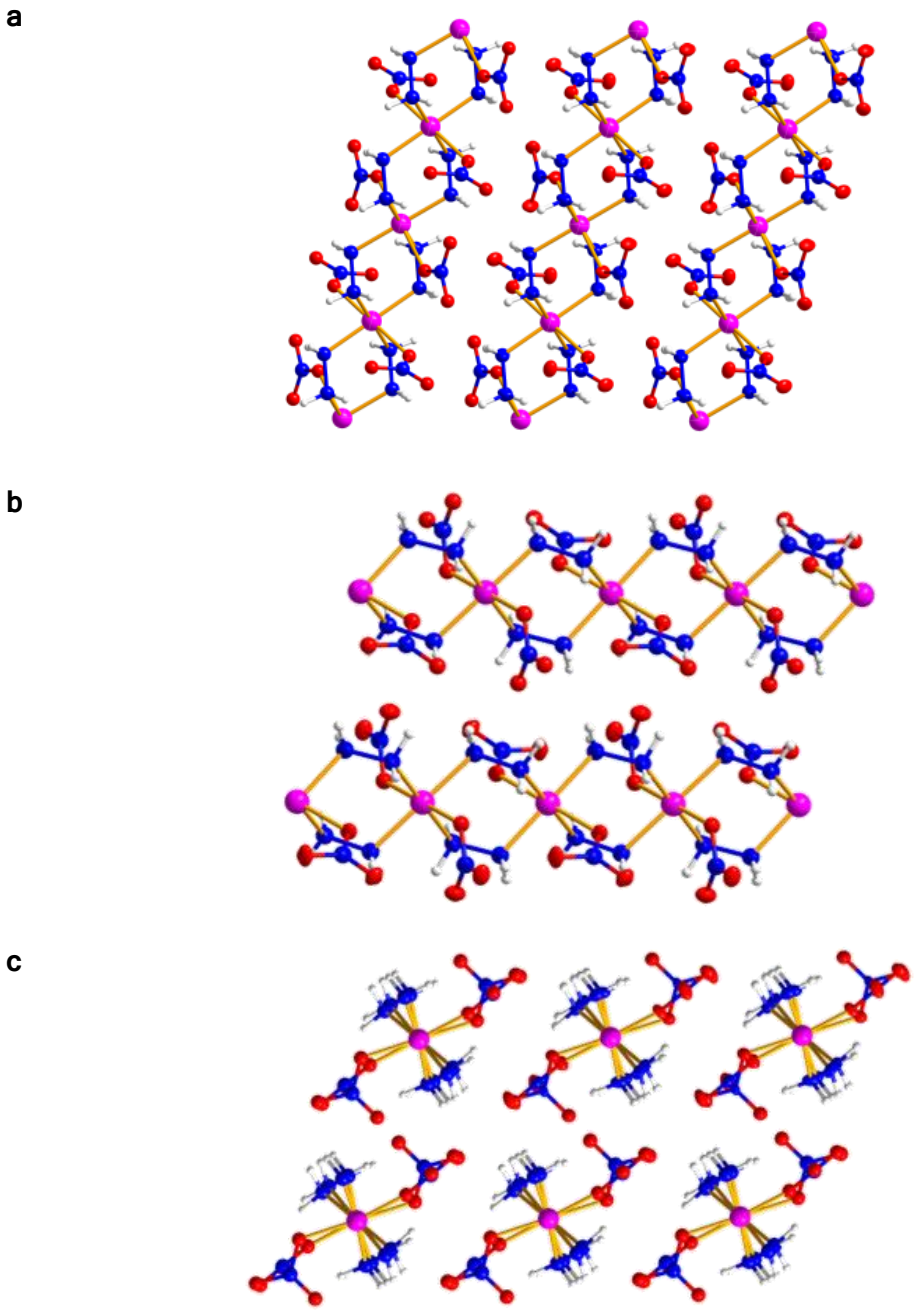

Figure 2.4: Packing arrangement for a 2x2x2 cell of complex **99**. a) Viewed along axis *a*. b) Viewed along axis *b*. c) Viewed along axis *c*. Ellipsoid representation at 50% and ball and stick representation for the metal center. Colour code: pink (Co), blue (N), red (O), white (H).

To further investigate the decomposition of complex **99** under ambient conditions, a TGA experiment was undertaken under oxidizing atmosphere (Figure 2.5). Apart from a 0.7% mass loss occurring around 65 °C, which could have been due to residual mother liquor, **99** is stable below 100 °C. Past 150 °C, with an inflection point at 178.35 °C, the first major mass loss (20.00%) occurs. This corresponds roughly to the loss of three hydrazine molecules. Though the onset of this step has a very shallow slope (-0.03 %/°C), past 175 °C two successive vertical drops are observed; for which the overall slope is -1.30 %/°C. The second major step accounts for a 56.25% mass loss and also exhibits a considerably steep slope (-1.80 %/°C). This corresponds roughly to the loss of the last hydrazine molecule and the four nitrate ions. The remaining 23.04% corresponds very closely with the cobalt metal's mass. By 250 °C, complex **99** has completely decomposed. With such a sharp TGA profile, complex **99** is comparable to a tetrazole derivative of **20** known as $(NH_4)_2$DNMT (**100**) (Scheme 2.1). $(NH_4)_2$DNMT was characterised

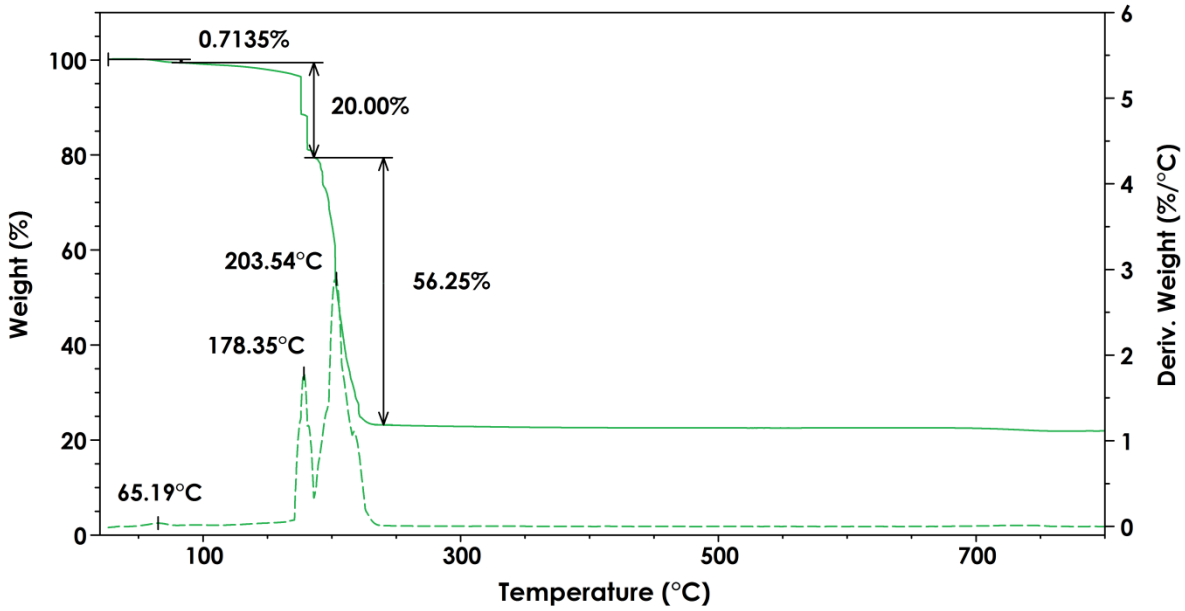

Figure 2.5: TGA plot (solid green) and weight derivative (dashed green) for complex **99**. The experiment was conducted at a heating rate of 10 °Cmin^{-1} under an oxidizing atmosphere with a sample size of 2.53 mg.

as having good energetic performance.[19] Furthermore, **99**'s TGA profile is sharper than that reported for $[Cd_2(N_2H_4)_2(N_3)_4]_n$, whose three decomposition steps span over 150 °C.[9] Its TGA profile also greatly resembles that of **90**, as reported by Chhabra *et al.*[15] Since complex **90** was suggested as a viable candidate for eco-friendly initiatory charges in detonators, complex **99** could also be an alternative candidate; though more calorimetric experiments and calculations would be required to confirm this.

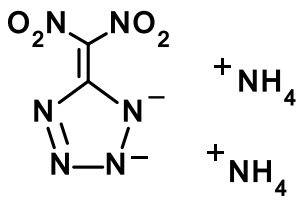

100

Scheme 2.1: Structure of $(NH_4)_2$DNMT (**100**).[19]

2.2.1.1.2 $[Co(\mu\text{-}N_2H_4)_2(\mu\text{-}OH)]_n(BF_4)_n \cdot nH_2O$

Having failed to obtain a trihydrazine-bridged complex with cobalt nitrate as a precursor, our attention was turned to non-coordinating anions. Using cobalt tetrafluoroborate with the same synthetic method used to prepare complex **99**, pink needles were obtained after two weeks. X-ray diffraction of these crystals revealed that another dihydrazine-bridged chain complex had been synthesised (Figure 2.6). Complex **101** crystallises in the monoclinic $P2_1/n$ space group and is a linear chain consisting of one cryptographically unique cobalt metal center bridged by a hydroxide and two hydrazines. There is also one lattice water molecule for every metal center. Similarly to complex **99**, complex **101** consists of a distorted octahedral coordination geometry (Figure 2.7). However, in this case the metal center experiences a Jahn-Teller compression as opposed to the elongation seen in **99** (Table 2.3).

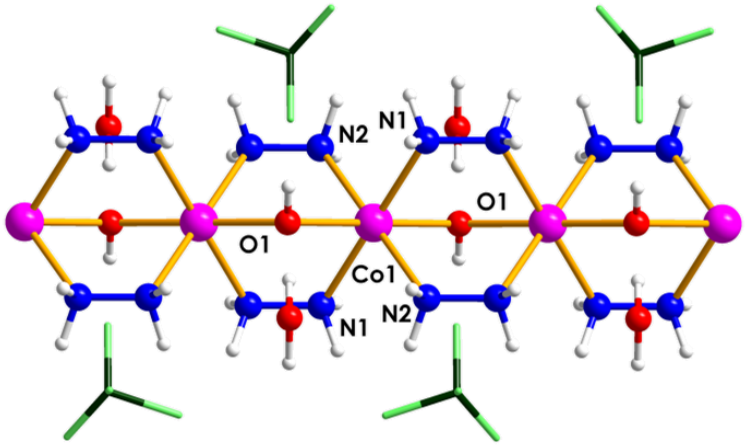

101

Figure 2.6: Labeled molecular structure showing a chain fragment of complex $[Co(\mu\text{-}N_2H_4)_2(\mu\text{-}OH)(BF_4)]_n{\cdot}H_2O$ **101**. Ball and stick representation for the chain and wire representation for the BF_4 counter ions for clarity. Colour code: pink (Co), blue (N), red (O), white (H), dark green (B), light green (F).

The axial hydroxides are also tilted slightly with respect to the equatorial plane. Unlike **99**, complex **101** does not exhibit a torsion angle along the hydrazine bridges. The hydroxide bridges have a bite angle of 110.50°, and their hydrogen atoms point in opposite directions with respect to the opposing axial position. These are pointing away from the lattice water molecule and towards the closest BF_4^- anion, with hydrogen bonds connecting all three species. All BF_4^- anions experience disorder throughout the lattice (Figure 2.8). Along axis *b*, the disorder for these ions can scarcely be identified. The disorder is attributed to competing hydrogen bonding from the hydrazine and water hydrogens to the fluorines on the BF_4^- anions. Along axis *c*, the chains stack one on top on the other so that they form a closed zipper pattern with the hydrazine bridges. These are, however, separated by the lattice water and anions. Along this axis, it appears as though the water molecules align in a straight line parallel to the chains. Along the *a* axis,

this straight row of water molecules separates into two rows, one on each side of the chain.

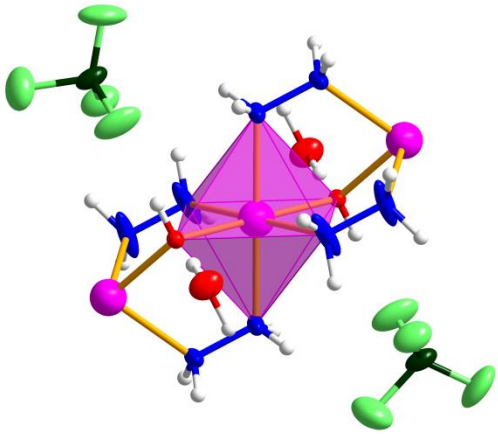

Figure 2.7: Coordination sphere polyhedra for complex **101**. Ellipsoid representation at 50% and ball and stick representation for the metal center. Colour code: pink (Co), blue (N), red (O), white (H), dark green (B), light green (F).

Table 2.3: Selected distances and angles for complex **101**.

Distances (Å)		
Co-N hydrazine	Co1-N1	2.18
	Co1-N2	2.19
Co-O hydroxide	Co1-O1	2.05
N-N hydrazine	N1-N1	1.41
	N2-N2	1.36
Intramolecular	Co1-Co1	3.37
Intermolecular	Co1-Co1	7.16
Angles (°)		
Hydroxide bridge	O1-Co1-O1	110.50
Axial O to equatorial N	O1-Co1-N1	85.68
		94.32
	O1-Co1-N2	92.40
		87.60
Hydrazine bridge torsion	Co1-N1-N1-Co1	0.00
	Co1-N2-N2-Co1	0.00
Hydrazine torsion	H1A-N1-N1-H1A	0.00
	H2A-N2-N2-H2A	0.00

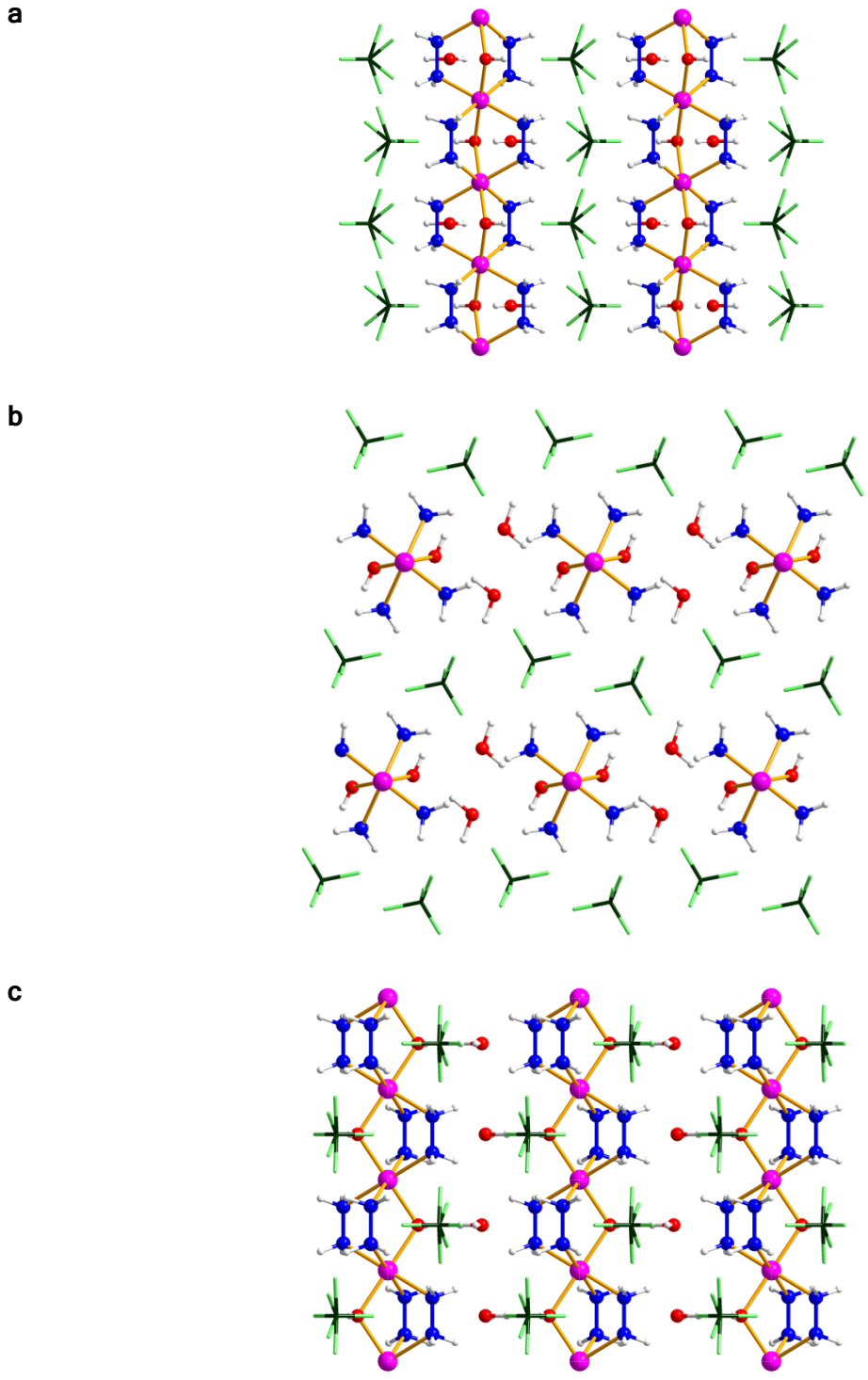

Figure 2.8: Packing arrangement for a 2x2x2 cell of complex **101**. a) Viewed along axis *a*. b) Viewed along axis *b*. c) Viewed along axis *c*. Wireframe representation for BF_4^- anions and ball and stick representation for remaining atoms. Colour code: pink (Co), blue (N), red (O), white (H), dark green (B), light green (F).

Rudimentary impact and friction tests on complex **101** failed to initiate any reaction. The TGA experiment revealed this compound to have a much broader profile with respect to complex **99** (Figure 2.9). Furthermore, **101**'s decomposition is considerably more complicated, with at least eight discernible steps. The first two steps add up to just under the mass of the lattice water. The following steps cannot be assigned to a particular remaining molecule or ion. With a residual mass of 38.41%, the remaining substance is likely a metal oxide. Regardless, it is clear that the hydroxide bridges and presence of water within the lattice greatly reduced the energetic potential of this compound.

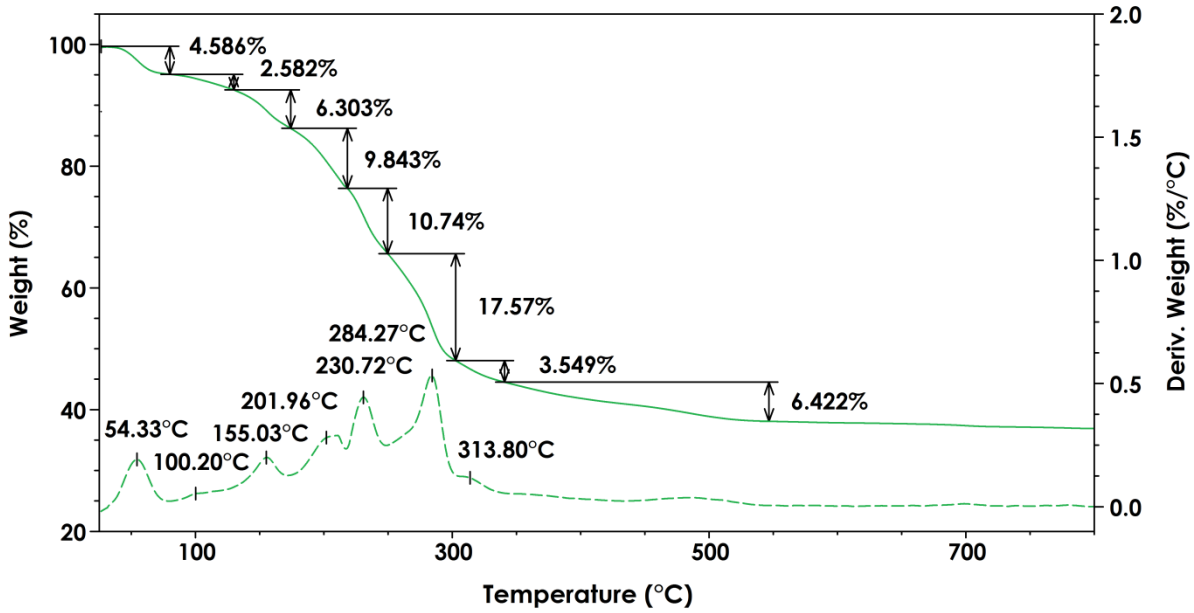

Figure 2.9: TGA plot (solid green) and weight derivative (dashed green) for complex **101**. The experiment was conducted at a heating rate of 10 °Cmin^{-1} under an oxidizing atmosphere with a sample size of 1.30 mg.

2.2.1.1.3 $[Co(\mu\text{-}N_2H_4)_2(N_2H_4)_2]_n(BF_4)_{2n}$

Since the use of water as a solvent in the synthesis of complex **101** led to a hydrated lattice and hydroxide bridges, the same reaction was repeated in an alcoholic mixture (EtOH : *i*-PrOH). This resulted in the growth

of orange block crystals (Figure 2.10). The change in solvent resulted in the successful synthesis of the tetrafluoroborate analogue (**102**) of complex **98**. In comparing the unit cell dimensions of **97** and **98** with **102**, complex **102** has a slightly smaller cell volume (699.86 $Å^3$, 712.79 $Å^3$, and 689.23 $Å^3$ for **97**, **98**, and **102** respectively) but a larger β angle (100.49°, 100.74°, and 101.03 ° for **97**, **98**, and **102** respectively).[1] Like its reported analogues, complex **102** forms chains linked by a single hydrazine bridge, with the remaining coordination sites occupied by four singly bound hydrazine molecules. Co^{II} metal centers thus exhibit a slightly distorted octahedral geometry (Figure 2.11).

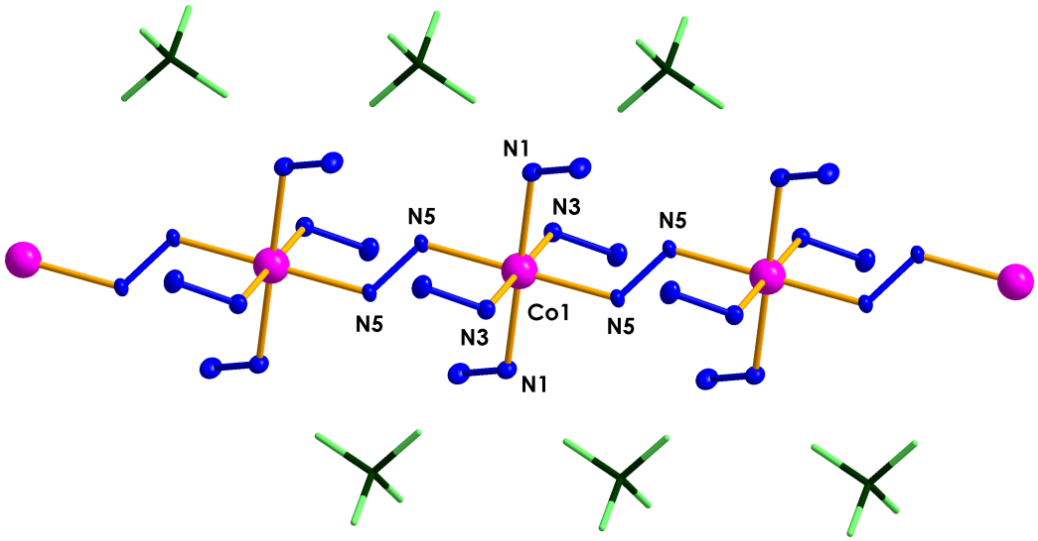

102

Figure 2.10: Labeled molecular structure showing a chain fragment of complex **102**. Ellipsoid representation for the chain with Hydrogens omitted for clarity, ball and stick representation for the metal center, and wire representation for the BF_4 counter ions. Colour code: pink (Co), blue (N), dark green (B), light green (F).

Similarly to **101**, complex **102** experiences a Jahn-Teller compression, with the axial positions defined as the bridging hydrazines (Table 2.4). Though the bond lengths are shortened between the metal centers (N5–Co1),

these bridges experience a slight elongation of their N–N bonds (N5–N5 1.47 Å) with respects to the singly bound hydrazines (N1–N2 1.45 Å, N3-N4 1.45 Å). The pivot angles at which the equatorial hydrazines are bound are 115.70° and 115.11° for N1–N2 and N3–N4 respectively, while the axial bridging hydrazines are bound at 117.43°. The equatorial hydrazines also experience torsion angles of ± 61.8°, while the axial hydrazines have a torsion angle of 180.00°. Thus the equatorial hydrazines are in the lower-energy *gauche* conformation, while the axial hydrazines consist of a *trans*-staggered conformation. This allows for the lone pairs to participate in the bridges' coordination along a straight line with respects to the 0° and 360° vectors of the Neumann projection.[20]

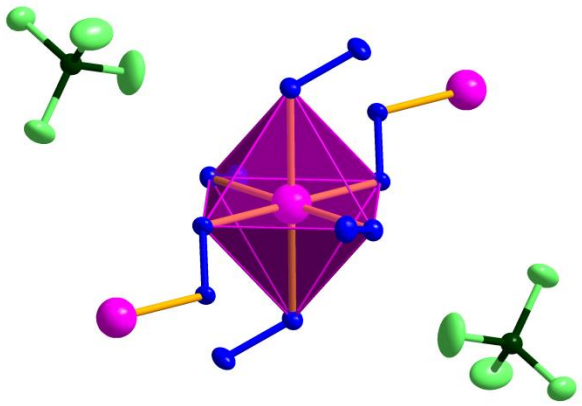

Figure 2.11: Coordination sphere polyhedra for complex **102**. Ellipsoid representation at 50% and ball and stick representation for the metal center. Colour code: pink (Co), blue (N), red (O), white (H), dark green (B), light green (F).

Complex **102** crystallises in the monoclinic $P2_1/n$ space group. Viewed along axis *a* (top view of 1D chains), the chains pack in a staggered fashion, with BF_4^- anions surrounding each chain. The chains appear to pack in two alternating vertical rows, where each row has chains which are orientated differently. Chains within these vertical rows possess the shortest

intermolecular Co–Co distances (8.49 Å). This shortest intermolecular distance is further cemented by the fact that chains in the neighboring, oppositely orientated row are staggered along the *b* axis. Though slightly crowded, viewing this complex along axis *b* also shows that the 1D chains form a step-like motif.

Table 2.4: Selected distances and angles for complex **102**.

Distances (Å)		
Co-N hydrazine bridge	Co1–N5	2.14
Co-N hydrazine	Co1–N1	2.19
	Co1–N3	2.23
N-N hydrazine	N1–N2	1.45
	N3–N4	1.45
	N5–N5	1.47
Intramolecular	Co1–Co1	5.14
Intermolecular	Co1–Co1	8.49
Angles (°)		
Axial O to equatorial N	N5–Co1–N1	88.92
		91.08
	N5–Co1–N3	87.70
		92.30
Hydrazine bridge torsion	Co1–N5–N5–Co1	180.00
Hydrazine torsion	H1C–N5–N5–H1D	180.0
	H1A–N1–N2–H2B	61.85
	H3A–N3–N4–H4B	–61.84
Pivot angle of coordinated hydrazines	Co1–N5–N5	117.43
	Co1–N1–N2	115.70
	Co1–N3–N4	115.11

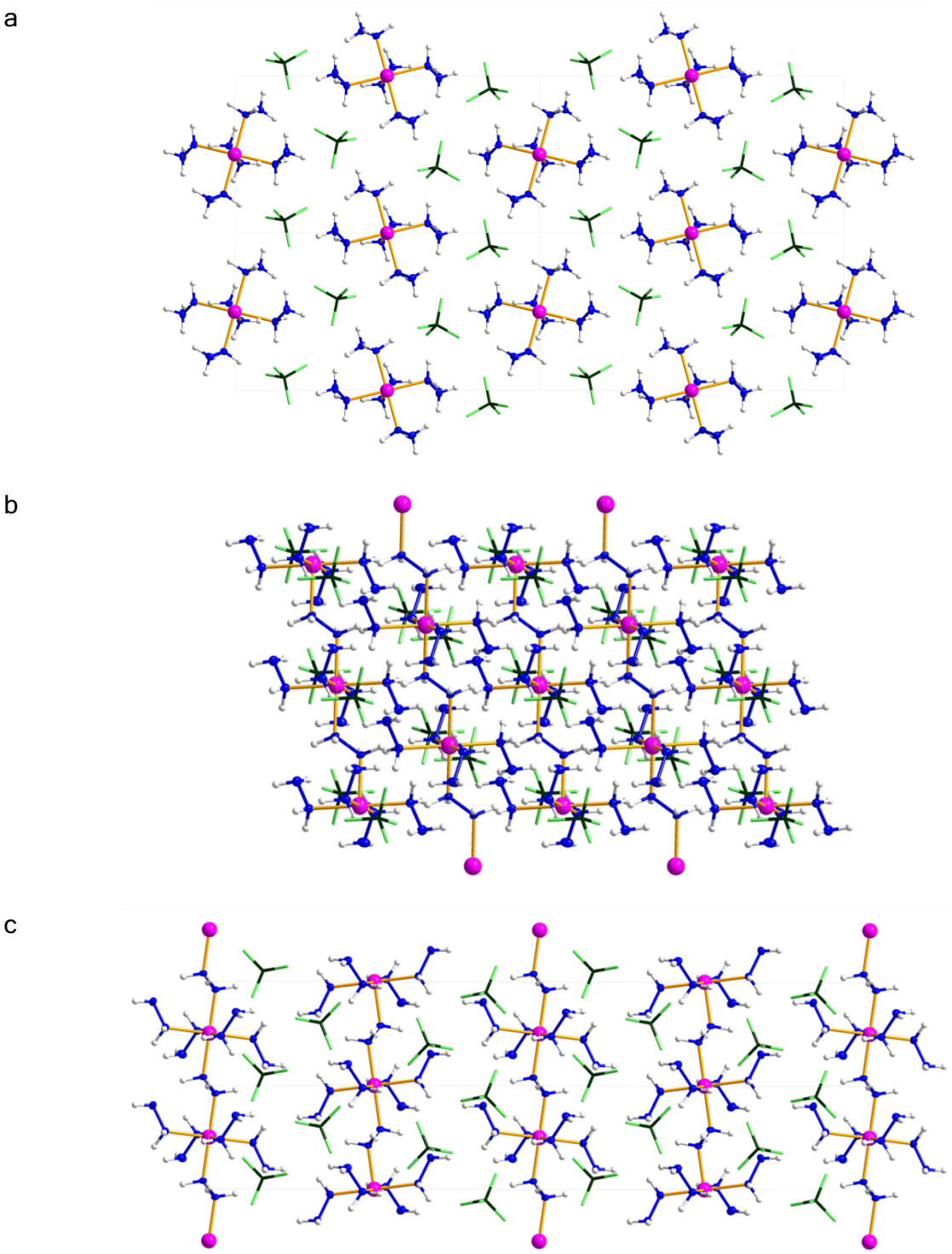

Figure 2.12: Packing arrangement for a 2x2x2 cell of complex **102**. a) Viewed along axis *a*. b) Viewed along axis *b*. c) Viewed along axis *c*. Ellipsoid representation at 50% and ball and stick representation for the metal center. Colour code: pink (Co), blue (N), red (O), white (H), dark green (B), light green (F).

The same rudimentary impact and friction tests performed on complexes **99** and **101** were also performed on **102**, for which no observable reactions were noted. This was followed by TGA experiments (Figure 2.13). Since energetic properties for complex **102**'s analogues were estimated using DFT calculations,[1] a more thorough calorimetric study was performed for **102**. Experiments were performed under air (oxidizing environment) so as to observe its decomposition under ambient conditions, as well as under a N_2 environment to observe the complex's pyrolysis. The first TGA experiment was performed in an oxidizing environment at a heating rate of 10 °Cmin^{-1} and revealed three decomposition steps. This is a stark difference in comparison to the TGA curve obtained for complex **101**. The profile of **101**'s thermogram is more rounded, with a gradual decomposition whose main features end past

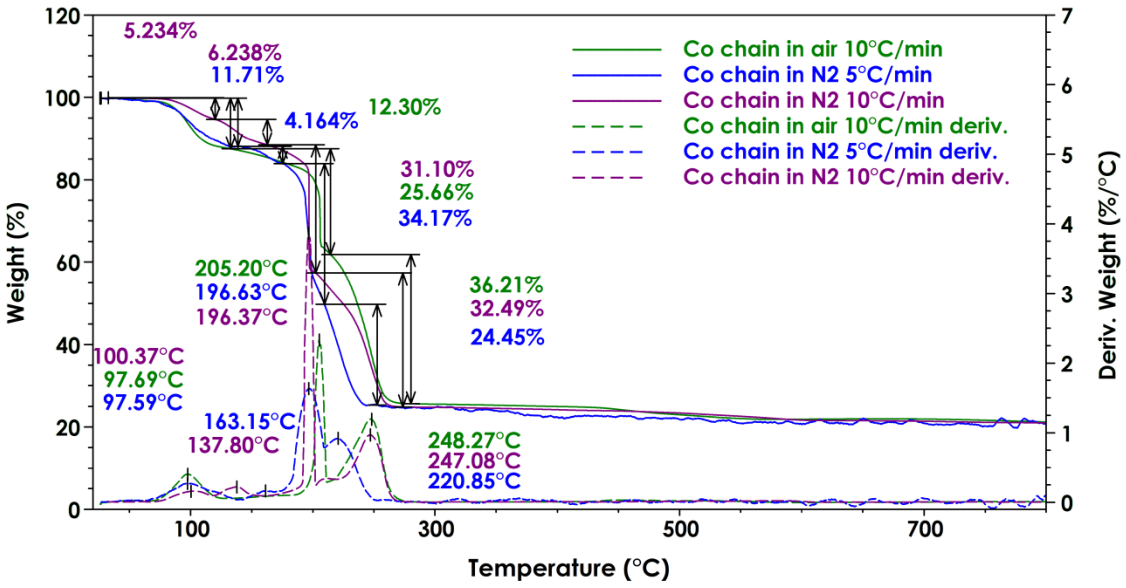

Figure 2.13: TGA experiments conducted on complex **102**. The experiments were conducted at a heating rate of 10 °Cmin^{-1} under oxidizing atmosphere (2.81 mg), and under nitrogen atmosphere (2.91 mg) as well as at a heating rate of 5 °Cmin^{-1} under nitrogen atmosphere (2.87 mg). The experiment conducted under nitrogen at a heating rate of 5 °Cmin^{-1} was compromised by a constant unknown source of vibrations. The data presented here was treated with a line smoothing application within the TA Universal software with a smoothing region width of 5 °C.

300 °C, while **102** has much sharper features which end well under 300 °C. Complex **102** starts to lose mass gradually after 50 °C, with the first step's inflection point just below 100 °C. This 12.30% mass loss could account for one hydrazine molecule and half a hydrazine molecule or ammonia. The next step has a vertical drop around 200 °C, where the 25.66% mass loss could correspond to the remaining hydrazines. This step is similar to those seen on complex **99**'s thermogram, and even occurs roughly at the same temperature as its second step. The third step is still quite steep and corresponds to a 36.21% mass loss. However, this loss does not account for the whole mass of the tetrafluoroborate counter ions. Furthermore, the remaining mass percent does not appear to correspond to one of cobalt's oxides.

The experiment was repeated under a nitrogen atmosphere. Since this experiment has the same final mass percent as the experiment conducted in an oxidizing atmosphere, it lends further support that the final product is not a cobalt oxide. New features were also identified. Without the oxidizing atmosphere, the initial step separates in two. This first step still corresponds nicely to the first step under oxidizing atmosphere, while the second step occurs with inflection point at 137.80 °C. These are both gradual steps which add up to 11.47% mass loss. The third step is a vertical drop corresponding to 31.10% mass loss, and occurs roughly 10 °C earlier than under oxidizing atmosphere. The last decomposition step (32.49% mass loss) is more gradual than its oxidizing atmosphere counterpart, yet its inflection point occurs at nearly the same temperature.

Interested in how the heating rate would affect the thermograms, the experiment under nitrogen atmosphere was repeated at a heating rate of 5 °Cmin^{-1}. Though the thermogram of both experiments conducted under inert atmosphere share the same number of steps, the profile of the 5 °Cmin^{-1}

heating rate experiment more closely resembles that of the experiment conducted under oxidizing atmosphere. Its second and last step, however, are shifted with respects to both the other thermograms; with the inflection point of the second step occurring 25 °C after the corresponding step from the 10 °Cmin^{-1} thermogram, and the inflection point of the last step occurring roughly 25 °C before both other thermograms. Decreasing the heating rate for the nitrogen experiment affected the first two decomposition steps (attributed to the loss of some hydrazines) and significantly affected the last decomposition step (attributed to the tetrafluoroborate ions), but had no effect on the third decomposition step where the remaining hydrazines are lost. Increases in heating rates generally result in higher decomposition temperatures as a result of the rate of heat conduction into the sample. Only the first and last steps follow this trend. Though tetrafluoroborate ions have been incorporated into energetic ionic liquids with adequate energetic performances,[21] this counter ion is non oxidizing. As such, complexes **97** and **98** are expected to have better performances than complex **102**.[1]

2.2.1.1.4 $[Mn(\mu N_2H_4)_3]_n(NO_3)_{2n}$

Having been unsuccessful at synthesising the cobalt analogue of complex **96**,[1] complexation reactions with other transition metal nitrates precursors were also performed. Colourless blocks were obtained from reactions with manganese nitrate. X-ray diffraction of these crystals revealed that the manganese analogue of complex **96** had been achieved (Figure 2.14). Similarly to its reported analogue, complex **103** forms linear chains linked by three hydrazine bridges, bound to the metal center in a nearly perfect octahedral geometry (Figure 2.15). All metal–nitrogen distances are 2.28 Å but axial to equatorial angles vary by +0.52° or –0.48° from a perfect right angle (Table 2.5). This metal–nitrogen distance is longer than what was

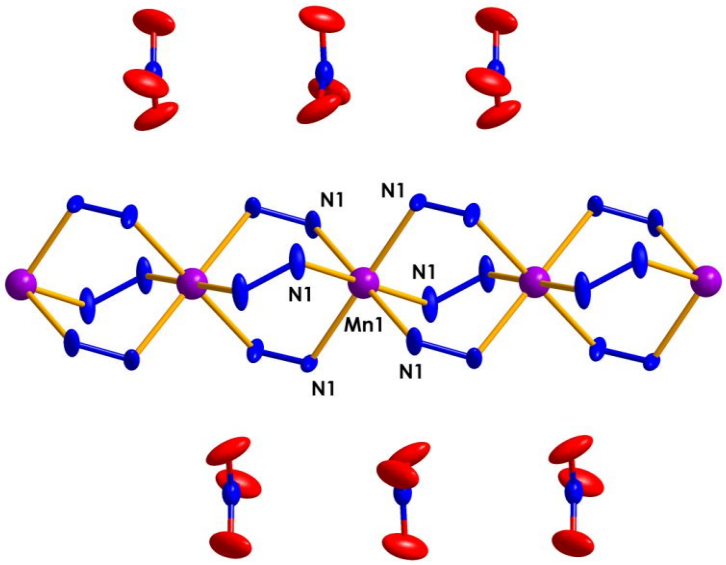

103

Figure 2.14: Labeled molecular structure showing a chain fragment of complex **103**. Ball and stick representation for the metal center and ellipsoid representation at 50% for remaining atoms. Hydrogens are omitted for clarity. Colour code: purple (Mn), blue (N), red (O).

reported for **96** (2.12 Å), and is likely a result of six coordinate octahedral Mn^{2+} ions having a larger ionic radius than six coordinate octahedral Ni^{2+} ions (0.81 Å and 0.70 Å for Mn^{2+} and Ni^{2+} ions respectively).[1,22] The hydrazine bridges experience a higher degree of torsion (–2.72° more for Mn1–N1–N1–Mn1) with respect to **96**, yet the N1–N1 bond lengths are slightly shorter (1.46 Å and 1.47 Å for **103** and **96** respectively).[1] Unlike complex **102**, the hydrazine bridges in **103** exhibit the lower-energy *gauche* conformation,[20] with **103** possessing a dihedral angle of –52.50°. This angle differs by –1.13° from that observed in **96**.[1] The intrametallic distance for complex **103** is also longer than that reported for **96** (3.91 Å and 3.76 Å for **103** and **96** respectively),[1] but is considerably shorter than the distance for singly-bridged **102** (3.91 Å versus 5.14 Å for **103** and **102** respectively). A similar trend is also observed for the intermetallic distances of **96**, **103**, and **102** (8.11 Å, 8.20 Å, and 8.49 Å respectively), though the difference between

103 and **102** is significantly smaller than that observed for intrametallic distances.

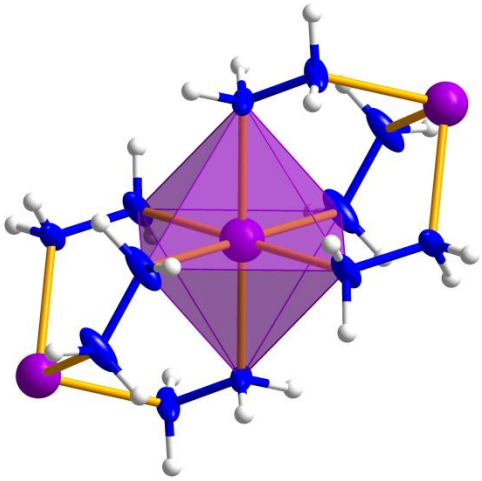

Figure 2.15: Coordination sphere polyhedra for complex **103**. Ellipsoid representation at 50% and ball and stick representation for the metal center. Colour code: purple (Mn), blue (N), red (O), white (H).

Table 2.5: Selected distances and angles for complex **103**.

Distances (Å)		
Co-N hydrazine bridge	Mn1–N1	2.28
N-N hydrazine	N1–N1	1.46
Intramolecular	Mn1–Mn1	3.91
Intermolecular	Mn1–Mn1	8.20
Angles (°)		
Axial N to equatorial N	N1–Mn1–N1	89.48 90.52
Hydrazine bridge torsion	Mn1–N1–N1–Mn1	–52.49
Hydrazine torsion	H1A–N1–N1–H1B	–52.50
Pivot angle of coordinated hydrazine bridges	Co1–N1–N1	115.95

Complex **103** crystallises in the trigonal P-3c1 space group (Figure 2.16), and is thus the complex with the highest number of symmetry

operators (12 versus 8, 4, 4, and 2 for complexes **103**, **104**, **101**, **102**, and **99** respectively) for the hydrazine complexes presented within this work. Comparison of the unit cell dimensions between **103** and the reported analogue **96**, reveals that complex **103** has a slightly lager cell volume (429.70 $Å^3$ and 456.02 $Å^3$ respectively).[1] Furthermore, the lower density obtained for **103** (2.15 gcm^{-3} and 2.00 gcm^{-3} for **96** and **103** respectively) is consistent with the difference in cell volume and the lower atomic weight of manganese.[1] Viewing complex **103** along the *a* and *b* axis shows the linear chains separated by the nitrate anions. Manganese ions are lined up with the neighbouring chains, while the nitrate anions between are staggered. The unit cell forms a diamond shape when viewed along the *c* axis, with the metal centers indicating the corners. From this view, the chains appear to form spoked wheels. The rows of chains are staggered from one another, and are separated by a horizontal zigzag row of nitrate ions.

Rudimentary impact and friction tests were performed on complex **103** with no notable observations. Attempts to produce more crystals of **103** were unsuccessful. As a result TGA experiments were not performed due to insufficient sample. However, considering that complex **103** consists of three hydrazine bridges in the lower-energy *gauche* conformation, whereas complex **102** and its reported analogues are singly bridged with the higher energy *trans*-staggered conformation, it would not be unreasonable to predict that **103** would have milder energetic performances than **97** and **98** like its reported analogue **96**. Whether **103** would have better performances than **102**, however, would be harder to predict as tetrafluoroborate is not an oxidizing anion.

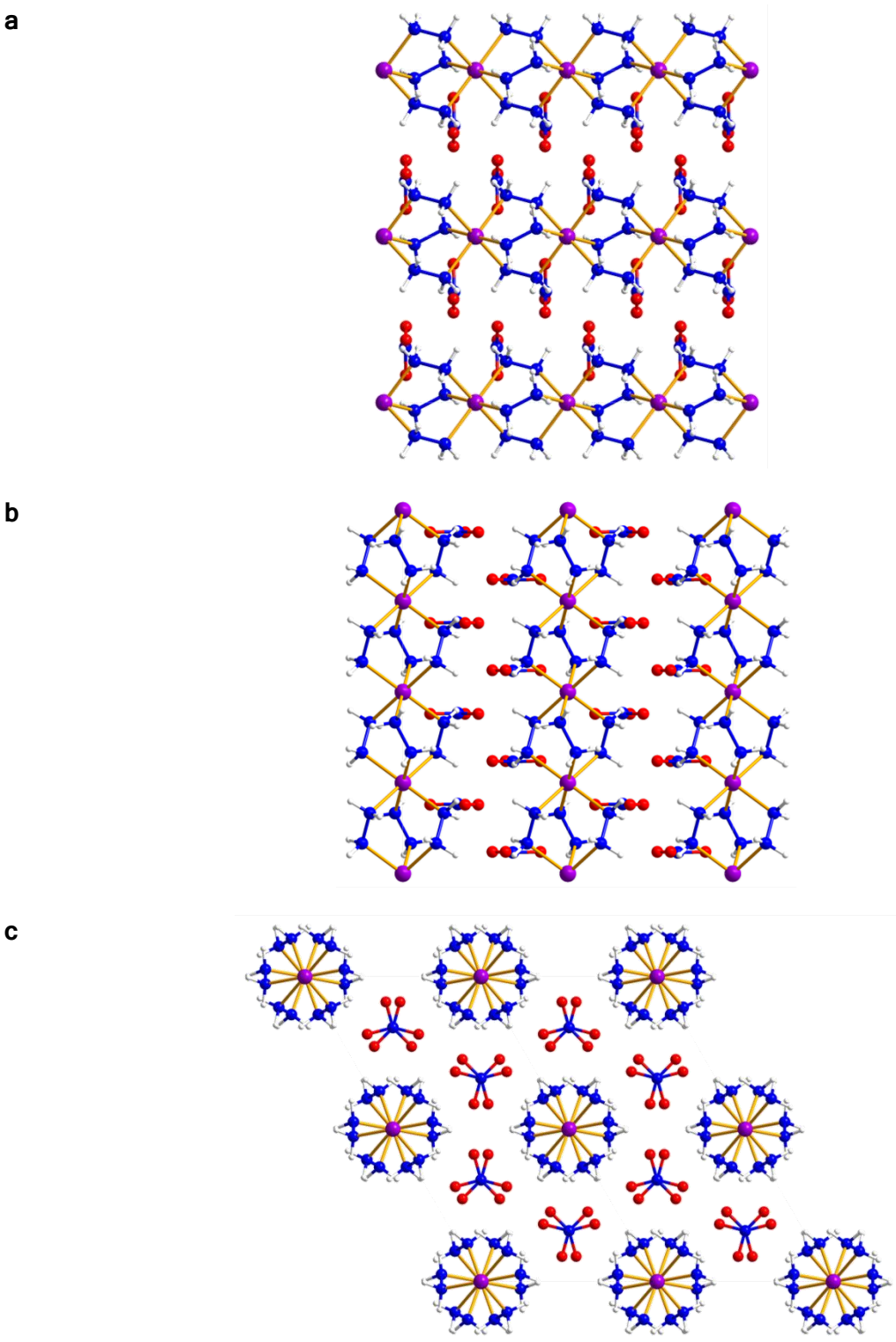

Figure 2.16: Packing arrangement for a 2x2x2 cell of complex **103**. a) Viewed along axis *a*. b) Viewed along axis *b*. c) Viewed along axis *c*. Ball and stick representation for all atoms. Colour code: purple (Mn), blue (N), red (O), white (H).

2.2.1.2 Monomeric structures

2.2.1.2.1 [(Co(acac)$_2$)$_2$ (μ-N$_2$H$_4$)$_2$] and secondary product

Given that there were difficulties obtaining crystalline product for many of the metal nitrates and perchlorates used to synthesise analogues of complexes **96**, **97** and **98**, focus was turned towards more soluble counter ions. Thus far, all complexes obtained formed insoluble chains which could not be re-crystallised. Metal acac salts were selected as precursors for their solubility in water miscible solvents. Though Hacac is not considered to be energetic (OB = −191.78 %) and has a lower molar enthalpy of combustion than TNT (−2687.0 kJmol^{-1} and −3406 kJmol^{-1} for Hacac and TNT respectively), in terms of weight, its enthalpy of combustion is more exothermic (−26.8 kJg^{-1} and −15.0 kJg^{-1} for Hacac and TNT respectively).[23,24] Thus incorporating acac counter ions could provide a carbon fuel source to burn after a nitrogen-rich material is initiated. Since diffusion reactions with metal acac salts failed to produce crystalline materials, their solubility in acetonitrile was used to perform layered reactions.

The layering of Co^{II}acac$_2$ in acetonitrile over an aqueous hydrazine solution led to the rapid growth (20 minutes) of pink needles (**104**) at the interface. However, if these pink crystals were to fall to the bottom of the reaction vial, or if the vial was left undisturbed for three days, the pink needles turned an intense purple colour (**105**). X-ray diffraction of the pink needles revealed that a dimer had been produced (Figure 2.17). This dimer consists of two crystallographically identical Co^{II} metal centers, bridged by two hydrazine molecules. The coordination sphere is completed with two κ^2-acac ligands which inhibit the formation of a chain. The metal centers thus exhibit a distorted octahedral geometry (Figure 2.18).

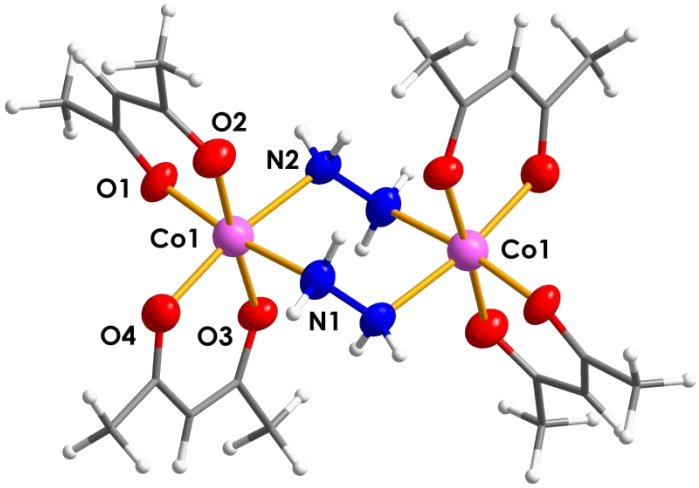

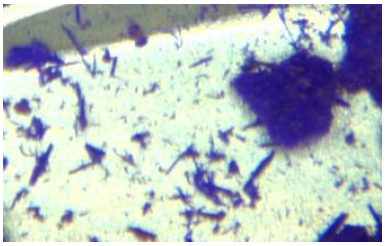

104 **105**

Figure 2.17: Complexes obtained from $Co^{II}acac_2$ hydrazine reactions. Pink needles formed in the early stages of the reaction are identified as the acac dimer complex **104**. Ellipsoid representation at 50% for the heteroatoms, wire representation for the carbon chain, and ball and stick representation for the metal center and hydrogen atoms. Colour code: pink (Co), blue (N), red (O), grey (C), white (H). Purple needles collected at the end of the reaction were not suitable for single crystal diffraction but are designated as complex **105**.

In relation to the aforementioned octahedral cobalt metal centers, complex **104**'s geometry is the most distorted; wherein none of the opposing vertices form a 180° angle (

Table 2.6). The equatorial atoms also exhibit the greatest variance in bond lengths (2.03 Å - 2.19 Å). These variations are accredited to the rigidity of the acac ligand. The metal centers and hydrazine bridges form a 6-membered ring in a chair conformation, whose intrametallic distance is 4.23 Å. The hydrazine bridges exhibit an average N–N bond length in comparison to complexes presented herein, and consist of a *gauche*-staggered

conformation. The hydrazine hydrogens arranged such that they are pointing away from the ring.

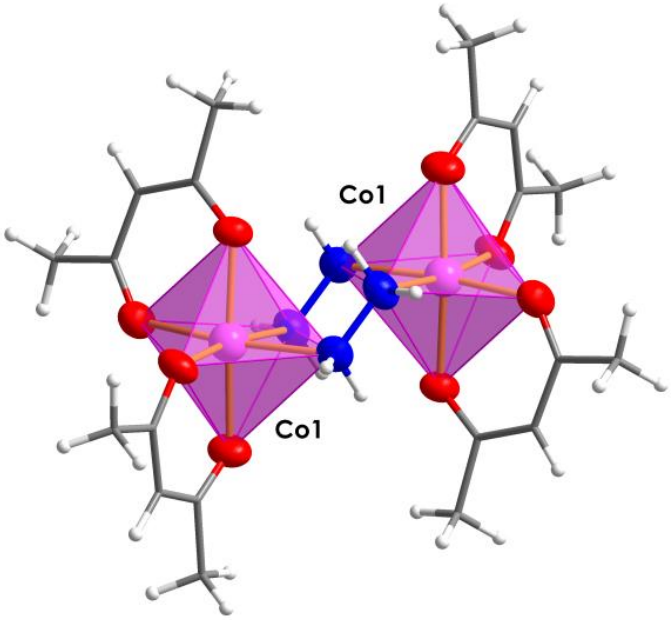

Figure 2.18: Coordination sphere polyhedra for complex **104**. Ellipsoid representation at 50% for the heteroatoms, wire representation for the carbon chain, and ball and stick representation for the metal center. Colour code: pink (Co), blue (N), red (O), grey (C), white (H).

Complex **104** crystallises in the monoclinic C2/c space group, and packs in staggered columns whose diamond-shaped cross section can be seen along axis *c* (Figure 2.19 and Figure 2.20). Within the columns, molecules of **104** are rotated 90° with respects to the corresponding molecules above and below. The closest intermetallic distance between metal centers is 5.50 Å, and occurs between dimers within the same column. Hydrogen bonding also occurs between hydrazine hydrogens and acac's oxygen atoms within the same column. Observing the packing structure along axis *a* shows that the metal clusters are aligned with those in the neighbouring columns. Within these cross-column rows, the rotation of the molecules is the same and is opposite to the rows above and below.

Table 2.6: Selected distances and angles for complex **104**.

Distances (Å)		
Co-N hydrazine bridge	Co1–N1	2.17
	Co1–N2	2.19
Co-O acac	Co1–O1	2.03
	Co1–O2	2.04
	Co1–O3	2.06
	Co1–O4	2.06
Hydrazine	N1–N2	1.44
Intramolecular	Co1–Co1	4.23
Intermolecular	Co1–Co1	5.50
Angles (°)		
Axial O to equatorial atoms	O2–Co1–O1*	88.72
	O2–Co1–O4	94.53
	O2–Co1–N1	85.44
	O2–Co1–N2	89.59
Axial N to equatorial atoms	O3–Co1–O1	92.75
	O3–Co1–O4*	87.59
	O3–Co1–N1	92.88
	O3–Co1–N2	88.06
Hydrazine bridge torsion	Co1–N1–N2–Co1	–83.16
Hydrazine torsion	H1A–N1–N2–H2A	–83.38
Pivot angle of coordinated hydrazine bridges	Co1–N1–N2	114.70
	Co1–N2–N1	115.84

*acac bite angles

a

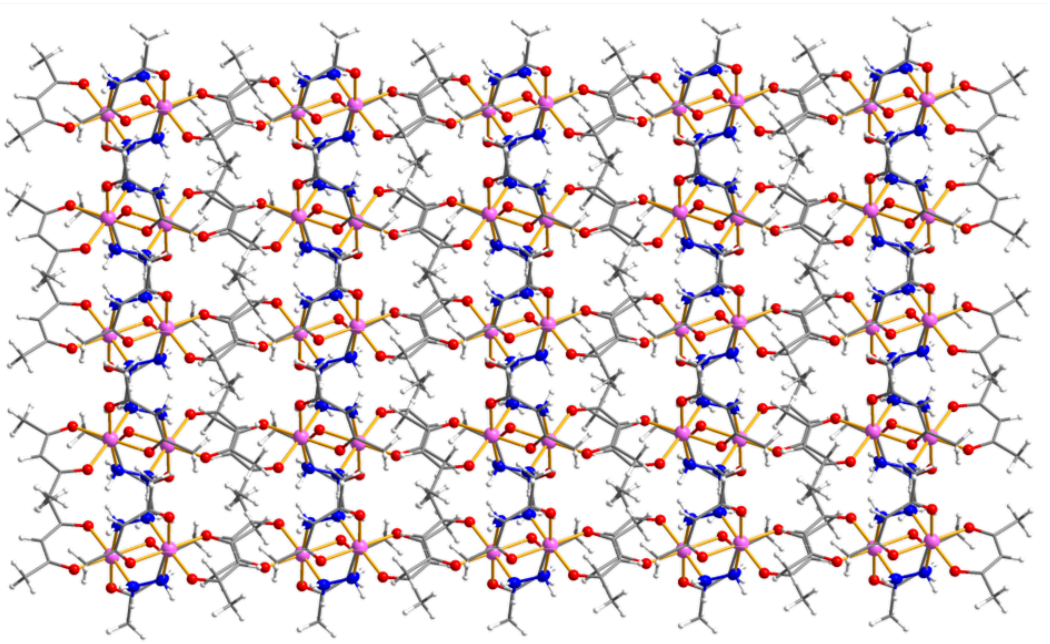

b

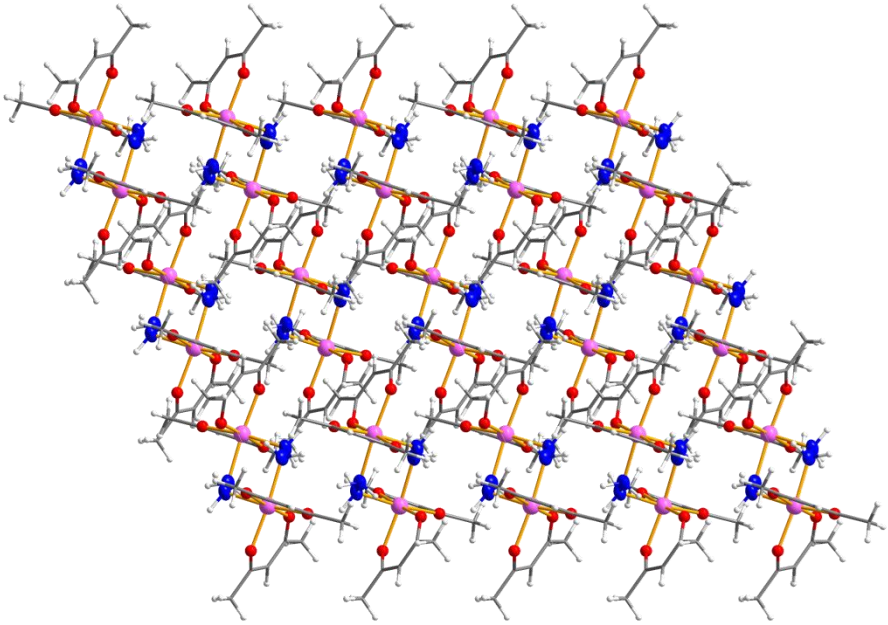

Figure 2.19: Packing arrangement for a 2x2x2 cell of complex **104**. a) Viewed along axis *a*. b) Viewed along axis *b*. Ellipsoid representation at 50% for the heteroatoms, wire representation for the carbon chain, and ball and stick representation for the metal center. Colour code: pink (Co), blue (N), red (O), grey (C), white (H).

c

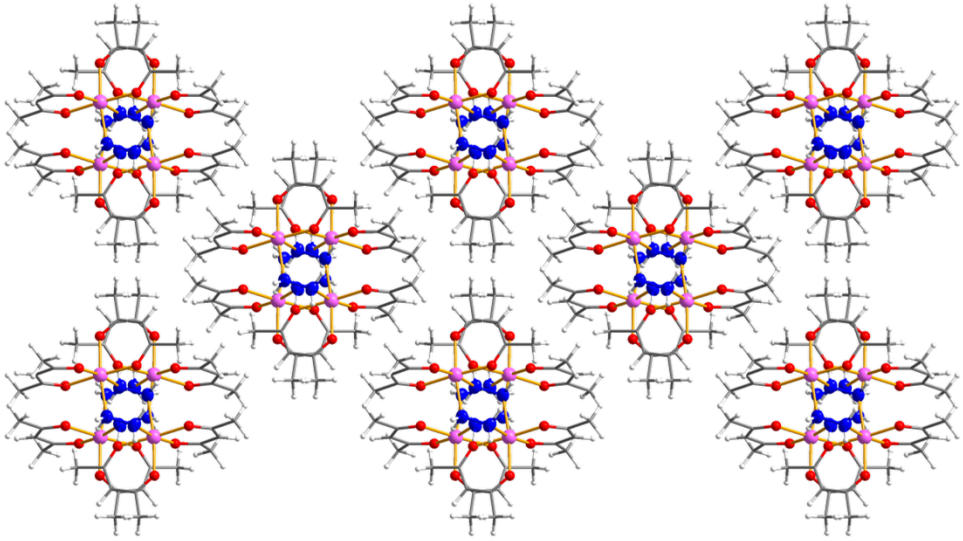

d

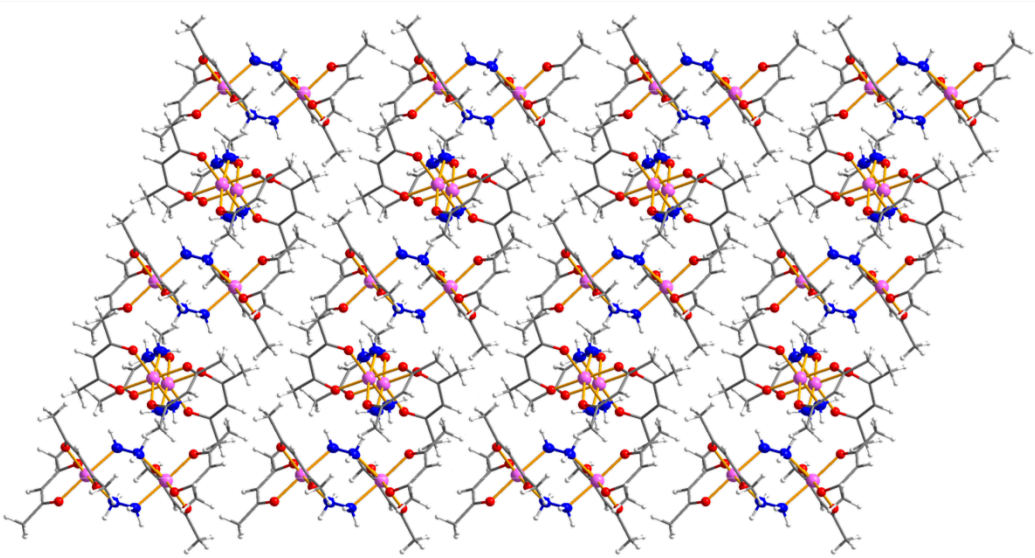

Figure 2.20: Packing arrangement for a 2x2x2 cell of complex **104**. c) Viewed along axis *c*. d) Viewed along x = -90, y = 40.3, z = 0. Ellipsoid representation at 50% for the heteroatoms, wire representation for the carbon chain, and ball and stick representation for the metal center. Colour code: pink (Co), blue (N), red (O), grey (C), white (H).

After no noticeable reactions were observed for the impact and friction tests performed on complex **104**, TGA experiments were undertaken (Figure 2.21). Under oxidizing atmosphere at a rate of 10 °Cmin^{-1}, **104** decomposes in four major steps. The complex appears stable below 100 °C, with the first

step occurring as a vertical drop at 113 °C. This accounts roughly for the loss of a hydrazine and acac ligand. The following step, with an inflection point at 155.52 °C, is significantly less steep and could account for approximately two acac ligands. The last two steps account roughly for the remaining hydrazine and acac ligands, however the final mass is 3.04% less than what would be expected for the remaining cobalt.

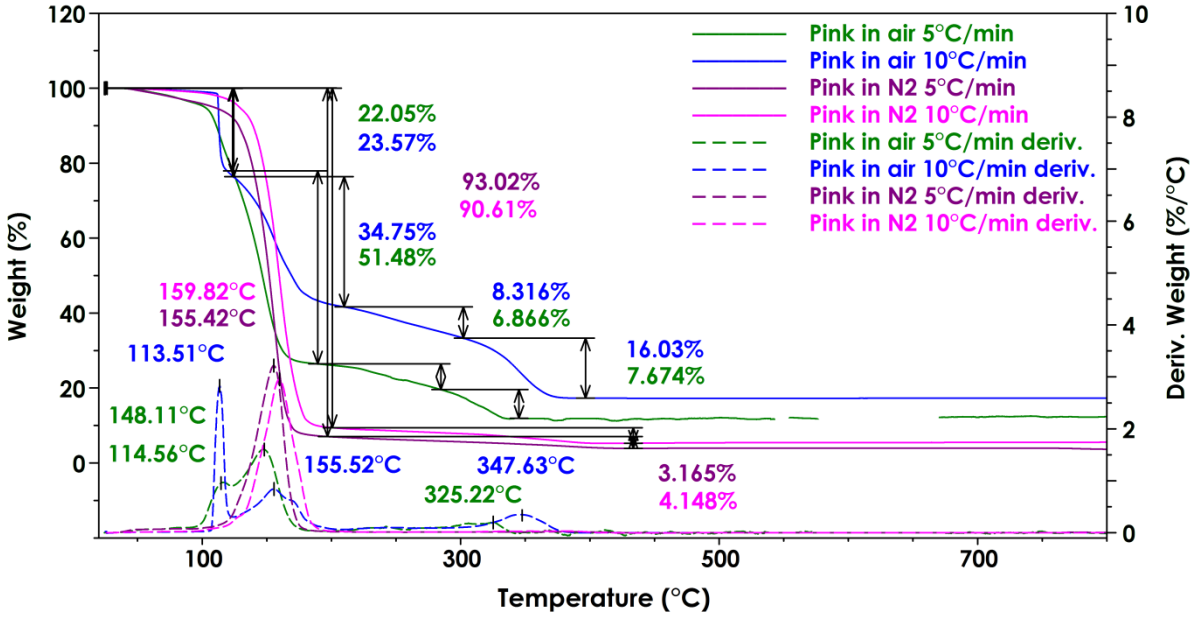

Figure 2.21: TGA experiments conducted on complex **104**. The experiments were conducted at a heating rate of 10 °Cmin^{-1} under oxidizing atmosphere (4.59 mg), and under nitrogen atmosphere (2.92 mg) as well as at a heating rate of 5 °Cmin^{-1} under oxidizing atmosphere (2.59 mg), and under nitrogen atmosphere (2.48 mg). The experiment conducted in air at a heating rate of 5 °Cmin^{-1} was compromised by an unknown source of vibrations past 300 °C. The data presented here was treated with a line smoothing application within the TA Universal software with a smoothing region width of 10 °C. Data which could not be smooth was not included in the plot.

Repeating the experiment at a heating rate of 5 °Cmin^{-1} essentially merges the first two steps, for which the onset of the decomposition starts at 50 °C, and accounts roughly for the four acac ligands and one of hydrazine. The last two steps parallel the profile of the last two steps from

the 10 °Cmin^{-1} thermogram, but end below 350 °C, and result in a lower mass percent (8.45% less than expected for the remaining cobalt content). Performing these experiments under nitrogen atmosphere results in one major decomposition step (90.61% and 93.02% mass loss for heating rates of 10 °Cmin^{-1} and 5 °Cmin^{-1} respectively). The onset temperatures for the nitrogen thermograms follow those of their corresponding heating rates under oxidizing atmosphere. The final mass percent of these are both less than 10.19%, the equivalent of one cobalt (5.24% and 3.82% final mass percent for heating rates of 10 °Cmin^{-1} and 5 °Cmin^{-1} respectively). There are two possible ways to explain the lower final mass percent obtained for these experiments. The first explanation, and the most likely, is that the sample used had begun to convert to the purple complex **105** and was not pure, thus skewing the observed percent mass loss. Alternatively, complex **104** may be a prime candidate for the chemical vapour deposition (CVD) of cobalt or cobalt oxide. The literature shows examples of precursors such as $Co_2(CO)_8$ which has deposition temperatures in the range of 50 °C to 300 °C.[25] Cobalt acetate has also been used to deposited cobalt oxide at temperatures above 300 °C.[26] More elaborate precursors, such as $HCo[P(OR)_3]_4$, where R = methyl, ethyl, *i*-propyl, and *n*-butyl, have also shown to produce high-purity cobalt films at temperatures as low as 300 °C.[27] Since these compounds are adequate CVD agents at atmospheric pressure within the temperature range of **104**'s decomposition, perhaps the missing percent mass is due to sublimation. Future inquiries should be geared towards determining whether **104** is indeed a candidate for CVD precursors.

Despite numerous attempts, which included varying the layer concentrations and adding various buffer layers to slow down the crystallization process, single crystals suitable for x-ray diffraction could not be

obtained for purple complex **105**. However, a powder x-ray diffraction spectrum was collected and clearly demonstrates that **104** and **105** are two different compounds (Figure 2.22). Furthermore, their IR spectra demonstrate the stark structural differences between the two complexes. Complex **104**'s IR spectrum resembles that of $Co^{II}acac_2$ very closely in the 500–1000 region, unlike **105** which has much fewer bands. The profile of the 500–750 region in **105**'s IR spectrum has the shape of hydrazine's spectrum while exhibiting peaks corresponding to $Co^{II}acac_2$. Given that **105**'s IR spectrum resembles $Co^{II}acac_2$'s spectrum less than **104**'s, and since **105** forms when **104** is exposed to a greater concentration of hydrazine, it would be reasonable to deduce that **105** contains more hydrazine in its structure. The inability to obtain single crystals for x-ray diffraction further suggest that a substantial change occurs, whose rearrangement causes fracturing within the needles.

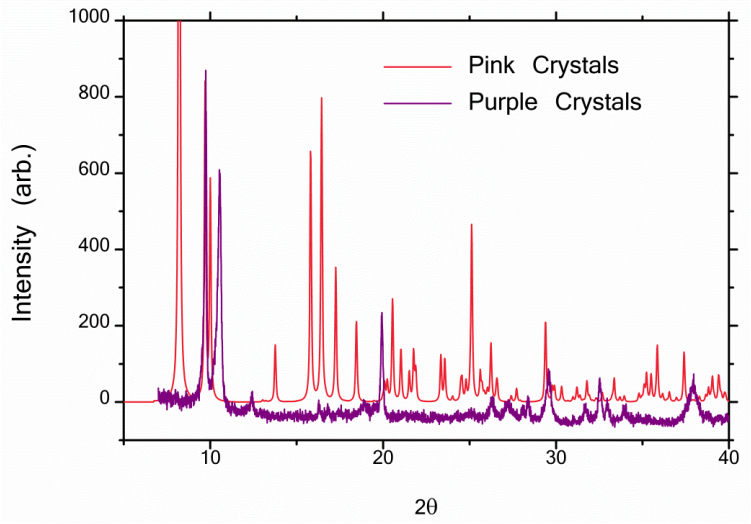

Figure 2.22: PXRD patterns for cobalt acac reactions. The calculated powder pattern for complex **104** (pink) is compared to the collected pattern for complex **105** (purple). The plot for **105** has been increased by a factor of 1.2 and offset by 80 arbitrary intensity units.

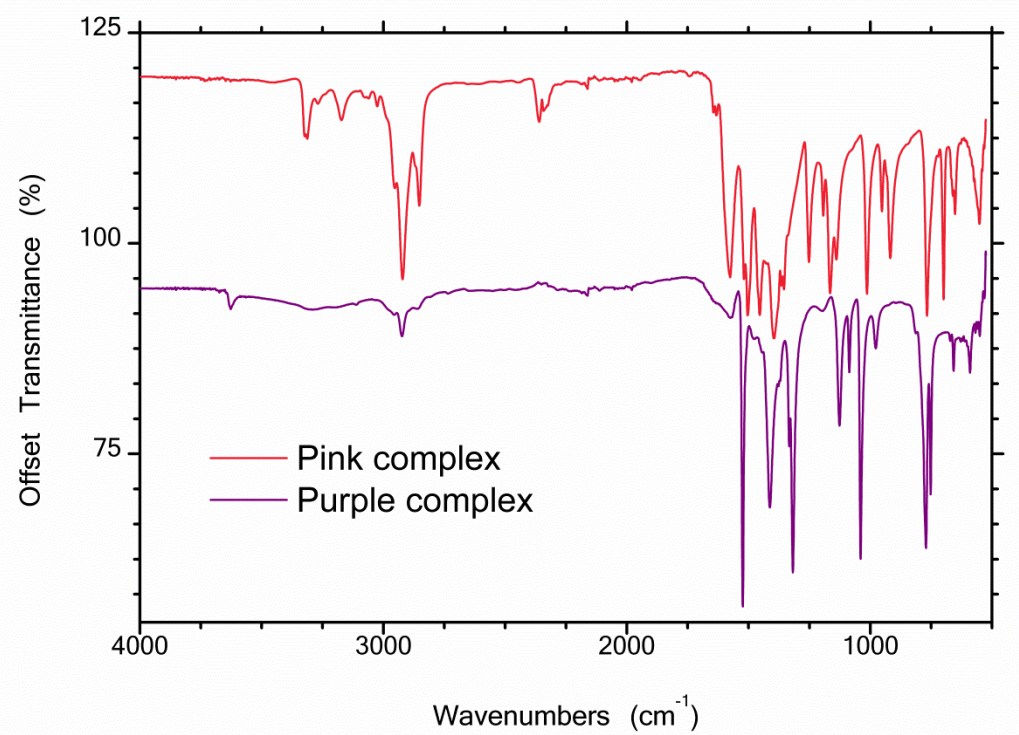

Figure 2.23: IR spectra of cobalt acac reaction products: complexes **104** (pink) and **105** (purple). The plot for complex **105** is offset by 22%.

Having passed the rudimentary sensitivity tests performed on previous crystals, complex **105** was subject to TGA experiments (Figure 2.24). With a quick overview of the thermograms, **105** appears to be more thermally resistant then its precursor. Under both heating rates and atmospheres, **105** is stable below 100 °C. The first decomposition step occurs between 160 °C and 200 °C, accounting for a 4.83% to 8.57% mass loss for 10 °Cmin^{-1} experiments under nitrogen and air respectively. The major decomposition step occurs between 300 °C and 450 °C and accounts for 55.40% to 59.22% mass loss for experiments under air at a heating rate of 10 °Cmin^{-1} and under nitrogen at a heating rate of 5 °Cmin^{-1} respectively. Experiments conducted under an oxidizing atmosphere had decomposed below 350 °C while those conducted under nitrogen loss the majority of their mass past 350 °C and had decomposed completely by 475 °C. Experiments conducted

under an oxidizing atmosphere also experienced vertical drops reminiscent of decomposition steps observed for complexes **99** and **102**. While the final mass percent for experiments performed in air and under nitrogen at a heating rate of 5 °Cmin^{-1} range between 33.7–35.9%, the final mass percent for the experiment performed under air at a heating rate of 10 °Cmin^{-1} is considerably lower (27.3%). Unfortunately, due to lack of information regarding the formula or the structure of **105**, no more information can be extrapolated from these experiments. Future work regarding complex **105** should include elemental analysis and other studies which could provide further information regarding its structure.

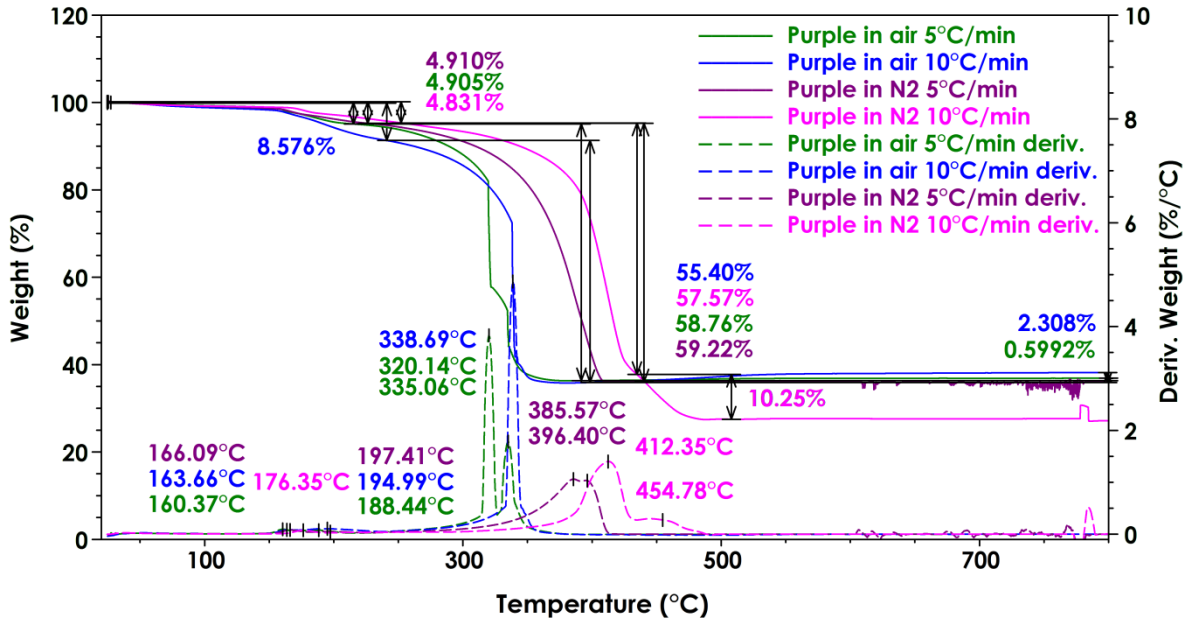

Figure 2.24: TGA experiments conducted on complex **105**. The experiments were conducted at a heating rate of 10 °Cmin^{-1} under oxidizing atmosphere (1.12 mg), and under nitrogen atmosphere (2.16 mg) as well as at a heating rate of 5 °Cmin^{-1} under oxidizing atmosphere (2.57 mg), and under nitrogen atmosphere (2.29 mg).

2.2.2 Conclusion

Five hydrazine-based complexes, four 1D chains and one dimer, were synthesised and characterised by x-ray diffraction. These complexes exhibited both bridging and singly bound hydrazine ligands whose conformations ranged from *trans*-staggered, to *gauche*-staggered to eclipsed. Analogues of the reported complexes **96**, **97**, and **98** were successful achieved: complexes **102** and **103**. Though complex **102** is not expected to perform as well as its reported analogues (**97**, and **98**), complex **103** is likely comparable and should be subject to further energetic testing. Rather than obtaining the cobalt analogue of **96**, a new energetic chain motif was achieved with complex **99**. Given that its TGA thermogram's profile greatly resembles that of reported complex **90**, a viable candidate for eco-friendly initiatory charges in detonators, further testing should be performed on complex **99** to quantify its potential. In regards to the acac complexes **104** and **105**, new efforts should be aimed at determining the structure of **105**. Future work on this project should include further calorimetric characterisation, such as DSC, in order to quantify the energetic performance of each complex presented. It should also include magnetic measurements on the presented complexes, as single chain magnets are an interesting sub-class of magnetic materials. Furthermore, there should be an expansion on the metals used for complexation; mainly 1st row transition metals. These should be targeted so as to maximise the number of unpaired electrons present on the metal center for magnetic properties, while minimizing costs and maximizing energetic performance. Though it would be difficult to control the reaction conditions so as to avoid precipitating very sensitive metal azides, another possible future avenue for this work would be to target the motifs of complexes **97**, **98** and **99**, but replace the oxidizing nitrate and perchlorate anions with azides. Rather than acting as oxidizing

agents, these counter ions could contribute directly to the gas generation and work output. The safest route for this avenue would probably be through ion exchange reactions.

2.3 Experimental

2.3.1 Instrumentation

IR spectra were recorded using a Diamond ATR Thermo Scientific Nicolet 6700 spectrometer. Thermogravimetric experiments were performed on a TA Q5000 TGA instrument. Single crystals x-ray diffraction data was collected using a Bruker AXS SMART single crystal diffractometer equipped with a sealed Mo tube APEX II CCD detector (λ = 0.71073 Å). Powder x-ray diffraction data was collected using a RIGAKU Ultima IV, equipped with a Cu-Kα radiation source (λ = 1.541836 Å), and a graphite monochromator. Scanning of the 2θ range was performed from 5-40°. In order to assign the peaks corresponding to particular crystalline phases, PDXL software equipped with the RIGAKU apparatus was used with the ICDD database.

2.3.2 General considerations

Nitrogen-rich materials are potentially explosive and should be handled with care. The use of polycarbonate face shield, Kevlar sleeves, Kevlar gloves under thick leather gloves, ear protection, and blast shield (in addition to standard laboratory PPE such as lab coat and safety glasses), should be common practice when working with these materials.

2.3.3 Complex Synthesis

2.3.3.1 Reagents and Methods

Hydrazine monohydrate was purchased from Sigma Aldrich. Metal salts were purchased from either Sigma Aldrich, Alfa Aesar or Stem Chemicals.

Alcoholic solvents were purchased from Fisher Scientific. All reagents were used as received. Diffusion reactions were performed by placing the dissolved metal salt in a small vial, which was placed in a larger sealed vial containing hydrazine monohydrate, and left to stand at room temperature behind a blast shield in a fume hood.

2.3.3.2 Chain Structures

2.3.3.2.1 $[Co(\mu\text{-}N_2H_4)_2(NO_3)_2]_n$ - (99)

Hydrazine monohydrate (100 μL, 2.06 mmol) was diffused into an aqueous solution (300 μL) of $Co(NO_3)_2{\cdot}6H_2O$ (37.4 mg, 0.13 mmol). After 1-2 weeks orange blocks had formed (33% yield).

2.3.3.2.2 $[Co(\mu\text{-}N_2H_4)_2(\mu\text{-}OH)]_n (BF_4)_{2n} \cdot nH_2O$ - (101)

Hydrazine monohydrate (100 μL, 2.06 mmol) was diffused into an aqueous solution (300 μL) of $Co(BF_4)_2{\cdot}4H_2O$ (37.5 mg, 0.11 mmol). After 1-2 weeks orange plates had formed (28% yield).

2.3.3.2.3 $[Co(\mu\text{-}N_2H_4)_1(N_2H_4)_4]_n (BF_4)_{2n}$ - (102)

Hydrazine monohydrate (100 μL, 2.06 mmol) was diffused into an alcoholic solution (1:1 EtOH and *i*-PrOH, 300 μL) of $Co(BF_4)_2{\cdot}4H_2O$ (37.5 mg, 0.11 mmol). After 1-2 weeks orange plates had formed (33% yield).

2.3.3.2.4 $[Mn(\mu\text{-}N_2H_4)_3]_n (NO_3)_{2n}$ - (103)

Hydrazine monohydrate (100 μL, 2.06 mmol) was diffused into an aqueous solution (300 μL) of $Mn(NO_3)_2{\cdot}6H_2O$ (19.7 mg, 0.08 mmol). After 1-2 weeks orange blocks had formed (31% yield).

2.3.3.3 Monomeric Structures

2.3.3.3.1 . [(Co(acac)$_2$)$_2$ (μ-N$_2$H$_4$)$_2$] - (104), and secondary product - (105)

Hydrazine monohydrate (100 μL, 2.06 mmol) was first dissolved in a skinny test tube with distilled water (1 mL) and then placed in the fridge until cold to the touch. Room temperature acetonitrile (1mL) was then layered on top and the vessel was chilled again. This step is necessary to slow down the diffusion rate for crystal growth. As a third layer, cobalt (II) acac (28.3 mg, 0.11 mmol) dissolved in acetonitrile (2 mL) was added and the reaction test tube was left to stand alone at room temperature. Within 20 minutes, thin bright pink needles (**104)** can be observed. If the reaction vessel is left undisturbed for 3 days, or if the pink crystals fall to the bottom of the vessel, these turn a deep purple colour. As such, depending on when the crystals are removed from the vessel, and how much the solution is disturbed, the yield for [(Co(acac)$_2$)$_2$(μ-N$_2$H$_4$)$_2$] ranges from 10-50%, while up to 80 % of the purple complex may be obtained.

2.3.4 Supplemental Information

2.3.4.1 IR Spectra for Hydrazine-Based Complexes

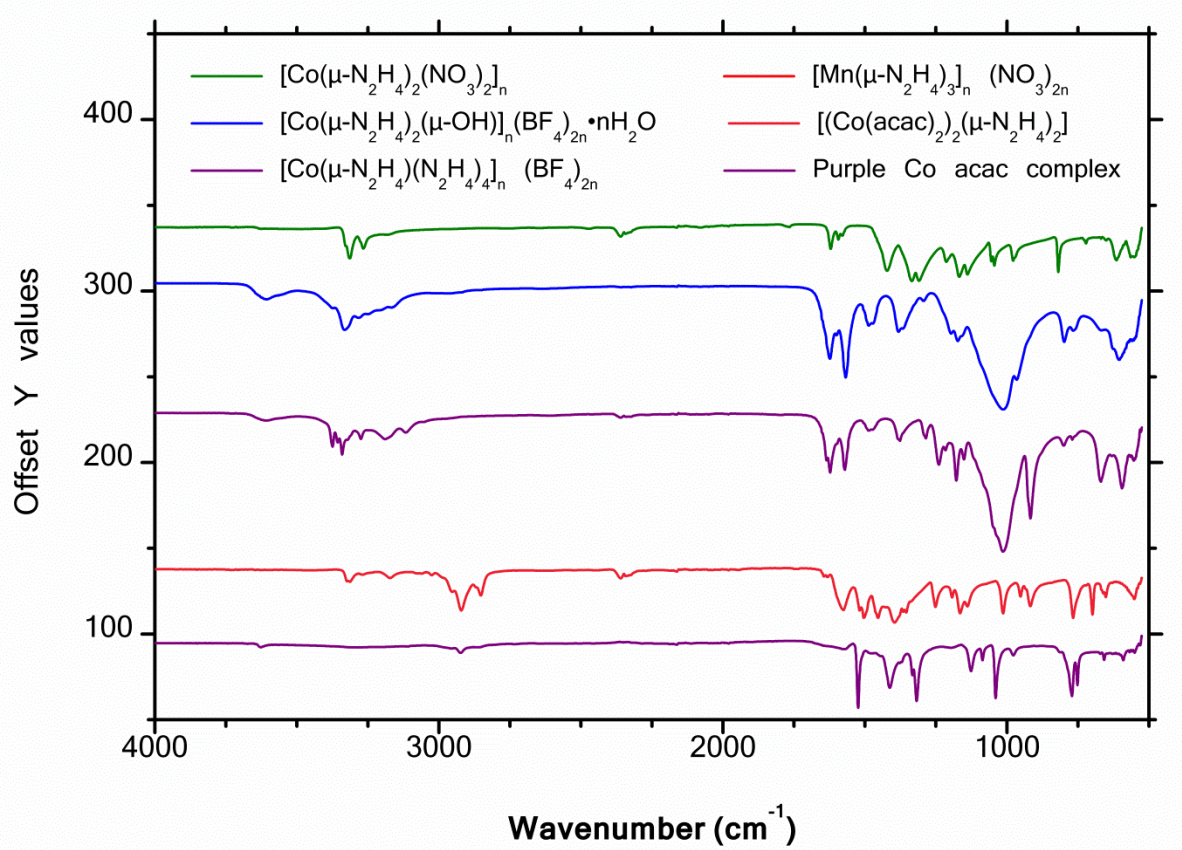

Figure 2.25: IR Spectra for Hydrazine-Based Complexes.

2.3.4.2 Crystallographic Data Tables for Hydrazine-Based Complexes

Table 2.7: Crystallographic data for nitrate chain complexes

Compound		99	103
Empirical formula		H_{16} Co_2 N_{12} O_{12}	H_{12} Mn N_8 O_6
Formula weight (g/mol)		494.11	275.12
Space group		Triclinic	Trigonal
Crystal system		P-1	P-3c1
Unit cell dimensions	a (Å)	7.4119(17)	8.2062(2)
	b (Å)	7.4193(17)	8.2062(2)
	c (Å)	8.2919(19)	7.8194(2)
	α (°)	65.471(9)	90
	β (°)	65.530(9)	90
	γ (°)	63.395(9)	120
V (Å^3)		356.00(15)	456.02(3)
Z		1	2
ρ_{calc} (g cm^{-3})		2.305	2.004
Absorption coefficient (mm^{-1})		2.431	1.482
F(000)		250	282
λ (Mo Kα) (Å)		0.71073	0.71073
Crystal size (mm)		0.13 x 0.11 x 0.08	0.17 x 0.11 x 0.08
θ Range (°)		2.81 - 28.28	3.87 - 28.30
Reflections collected		1991	4544
T_{min} / T_{max}		0.530188 , 0.745685	0.5710 , 0.7457
Goodness of fit		1.047	1.030
R1		0.0674	0.0346
wR2		0.2014	0.1026
Reflections with I>2σ(I)		1565	362

These structures were collected at 200(2) K. Crystals were orange blocks and colourless blocks for **99** and **103** respectively.

Table 2.8: Crystallographic data for tetrafluoroborate chain complexes

Compound		101	102
Empirical formula		H_{11} B Co F_4 N_4 O_2	H_{20} B_2 Co F_8 N_{10}
Formula weight (g/mol)		244.87	392.81
Space group		Monoclinic	Monoclinic
Crystal system		$P2_1/m$	$P2_1/n$
Unit cell dimensions	a (Å)	7.1644(2)	5.1436(4)
	b (Å)	6.7521(2)	16.0763(13)
	c (Å)	8.3546(3)	8.4920(8)
	α (°)	90	90
	β (°)	95.6914(15)	101.031(4)
	γ (°)	90	90
V (Å^3)		402.16(2)	689.23(10)
Z		2	2
ρ_{calc} (g cm^{-3})		2.022	1.893
Absorption coefficient (mm^{-1})		2.175	1.348
F(000)		246	398
λ (Mo Kα) (Å)		0.71073	0.71073
Crystal size (mm)		0.20 x 0.08 x 0.06	0.22 x 0.21 x 0.20
θ Range (°)		3.89 - 28.23	2.44 - 28.31
Reflections collected		6903	7821
T_{min} / T_{max}		0.5637 , 0.7457	0.5780 , 0.7457
Goodness of fit		1.026	1.063
R1		0.0296	0.0237
wR2		0.0901	0.0644
Reflections with I>2σ(I)		983	1608

These structures were collected at 200(2) K. Crystals were orange plates for both 101 and 102.

Table 2.9: Crystallographic data for acac complexes

Compound		104	105
Empirical formula		C_{20} H_{36} Co_2 N_4 O_8	---
Formula weight (g/mol)		578.39	---
Space group		Monoclinic	---
Crystal system		C2/c	---
Unit cell dimensions	**a (Å)**	14.9794(7)	---
	b (Å)	17.6709(8)	---
	c (Å)	11.3285(6)	---
	α (°)	90	---
	β (°)	115.003(3)	---
	γ (°)	90	---
V (Å^3)		2717.6(2)	---
Z		4	---
ρ_{calc} (g cm^{-3})		1.414	---
Absorption coefficient (mm^{-1})		1.267	---
F(000)		1208	---
λ (Mo Kα) (Å)		0.71073	---
Crystal size (mm)		0.26 x 0.05 x 0.02	---
θ Range (°)		2.24 - 27.15	---
Reflections collected		18032	---
T_{min} / T_{max}		0.5920 , 0.7457	---
Goodness of fit		1.026	---
R1		0.0385	---
wR2		0.0956	---
Reflections with I>2σ(I)		2379	---

The structure for complex **104** was collected at 200(2) K. Collections for complex **105** were attempted several times unsuccessfully. Crystals were pink needles and purple needles for complexes **104** and **105** respectively.

2.4 References

1. Bushuyev, O. S.; Brown, P.; Maiti, A.; Gee, R. H.; Peterson, G. R.; Weeks, B. L.; Hope-Weeks, L. J.; J. Am. Chem. Soc. **2012**, 134, pp 1422-1425.

2. Curtius, T.; Schrader, F.; J. Prakt. Chem. **1894**, 50, pp 311-346.

3. Franzen, H.; von Mayer, O.; Z. Anorg. Chem. **1908**, 60, pp 247-291.

4. Franzen, H.; Lucking, H. L.; Z. Anorg. Chem. **1911**, 70, pp 145-156.

5. Braibanti, A.; Bigliardi, G.; Manottilanfredi, A. M.; Tiripicchio, A.; Nature **1966**, 211, pp 1174-1175.

6. Nicholls, D.; Rowley, M.; Swindells, R.; J. Chem. Soc. A **1966**, 1966, pp 950-952.

7. Nicholls, D.; Swindells, R.; J. Inorg. Nucl. Chem. **1968**, 30, pp 2211-2217.

8. Patil, K. C.; Govindarajan, S.; Soundararajan, R.; Verneker, V. R.; Proc. Indian Acad. Sci. (Chem. Sci.) **1981**, 90, pp 421-426.

9. Liu, Z.; Zhang, T.; Zhang, J.; Wang, S.; J. Hazard. Mater. **2008**, 154, pp 832-832.

10. Arunadevi, N.; Vairam, S.; JEC&AS **2012**, 1, pp 1-8.

11. Bai, E. H. P.; Vairam, S.; J. Chem. **2013**, 2013, pp 1-10.

12. Field, L. D.; Li, H. L.; Dalgarno, S. J.; McIntosh, R. D.; Inorg. Chem. **2013**, 52, pp 1570-1583.

13. Salawu, O. W.; Abdulsalam, A. O.; Pharma Chem. **2011**, 3, pp 298-304.

14. Shunguan, Z.; Youchen, W.; Wenyi, Z.; Jingyan, M.; Propellants, Explos., Pyrotech. **1997**, 22, pp 317-320.

15. Chhabra, J. S.; Talawar, M. B.; Makashir, P. S.; Asthana, S. N.; Singh, H.; J. Hazard. Mater. **2003**, 99, pp 225-239.

16. Wojewódka, A.; Bełzowski, J.; Chemik Int. Ed. **2011**, 65, pp 20-27.

17. Li, X.; Zhuang, G.; Wang, X.; Wang, K.; Gao, E.; Chem. Commun. **2013**, 49, pp 1814-1816.

18. Abu-Youssef, M. A. M.; Mautner, F. A.; Vicente, R.; Inorg. Chem. **2007**, 46, pp 4654-4659.

19. Xu, K.; Zhang, H.; Lui, P.; Huang, J.; Ren, Y.; Wang, B.; Zhao, F. Propellants, Explos., Pyrotech. **2012**, 37, pp 653-661.

20. Chapter XIV. *The Nitrogen Group 1.2.3 Hydrazine*; Holleman, A. F., Wilberg, N., Eds.; Inorganic Chemistry; Academic Press, Walter de Gruyter GmbH & Co.: Berlin, **2001**; pp 618-623.

21. Zhang, Y.; Shreeve, J. M.; Angew. Chem. **2011**, 123, pp 965-967.

22. Shannon, R. D.; Acta Cryst. **1976**, A32, pp 751-767.

23. Nicholson, G. R.; J. Chem. Soc. **1957**, pp 2431-2432.

24. Rouse, P. E. J.; J. Chem. Eng. Data **1976**, 21, pp 16-20.

25. Ye, D.; Pimanpang, S.; Jezewski, C.; Tang, F.; Senkevich, J. J.; Wang, G.; Lu, T.; Thin Solid Films **2005**, 485, pp 95-100.

26. Maruyama, T.; Nakai, T.; Sol. Energy Mater. **1991**, 23, pp 25-29.

27. Choi, H.; Park, S.; Jang, H. G.; J. Mater. Res. **2002**, 17, pp 267-270.

Chapter 3

H_3bta ligand system

3.1 Introduction

The nitrogen-rich 5,5'-bis(1*H*-tetrazolyl)amine (H_3bta, Scheme 3.1) was first reported by Norris *et al.* in 1964, where it was characterised by elemental analysis.[1] A more thorough characterisation, including crystal structure and energetic performances, was reported four decades later by Klapötke *et al.*[2] H_3bta was shown to provide higher detonation pressures and velocities than TNT, even in its monohydrate form.[2] Furthermore, organic salts consisting of $Hbta^{2-}$ anions have calculated energetic parameters which are comparable to the range between TNT's to RDX's detonation pressures and velocities.[3,4] In the last decade, there have been various examples of H_3bta's use as a ligand in coordination chemistry.[5-8] These complexes exhibit diverse properties which include magnetic behaviour,[9-11] photoluminescent MOFs,[6,12] as well as energetic performances which could lead to their use as pyrotechnic additives.[13-16]

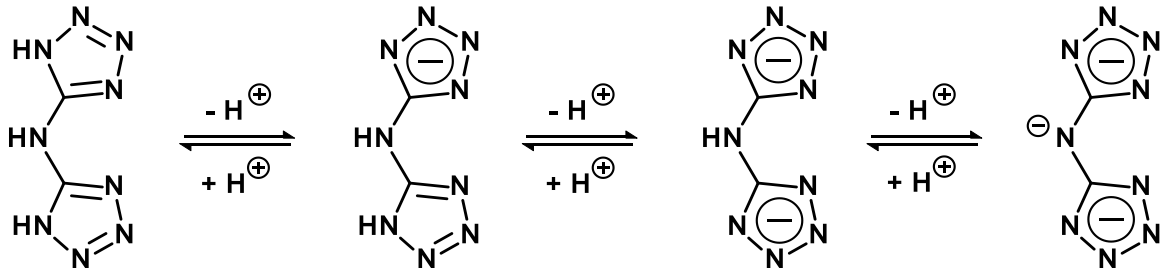

106

Scheme 3.1: Schematic representation of the H_3bta ligand (**106**) and its deprotonated forms.

Previous work by Dr. Cyril Cook, a former Murugesu group member, led to the synthesis of $Na_2NH_4[Fe(Hbta)_3]\cdot 3DMF\cdot 2H_2O$ (**107**) (Figure 3.1).[11] The anionic homoleptic octahedral Fe^{III} complex, paired with solvated 1D Na^+ chains, was found to exhibit high-temperature spin crossover behaviour.[11] The next step for this project was to further expand studies regarding the

magnetic properties of H_3bta-based complexes, in conjunction to their energetic properties. Since lanthanides have a larger number of unpaired electrons comparatively to transition metals, due to their *f*-orbitals, and have been shown to exhibit interesting magnetic behaviours, focus was geared towards the synthesis of lanthanide complexes.

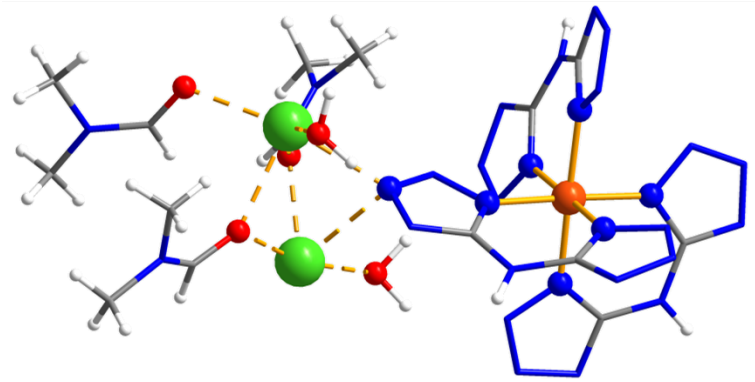

107

Figure 3.1: Crystal Structure of complex $Na_2NH_4[Fe^{III}(Hbta)_3]\cdot 3DMF\cdot 2H_2O$ (**107**).[11] Ball and stick representation for the metal centers and coordinated atoms, and wire frame representation for organic moieties. Colour code: orange (Fe), light green (Na), blue (N), red (O), grey (C), white (H).

3.2 Results and Discussion

First attempts at coordinating H_3bta to various lanthanide salts were performed according to the procedure used to obtain **107**.[11] This one-pot reaction technique, where the metal salt solution and ligand solution are mixed together, gave insoluble powders which crashed out of solution immediately upon addition of the metal salt. With the aim of slowing down the complexation rate, so as to obtain single crystals suitable for further characterisation, the coordination procedure was changed to the use of layering reactions. Unfortunately, the use of organic solvents, regardless of combination, systematically led to insoluble powders. The use of a buffer

layer, an intermittent layer between the ligand layer and metal salt layer used to further reduce the diffusion rate, also failed to inhibit the formation of insoluble powders.

3.2.1 Synthesis of bta-based Ln complexes

As a result of the difficulties experienced with organic solvent systems, focus was turned towards the use of aqueous systems. The metal salts were dissolved in distilled water within long test tubes and placed in the fridge until cold. A buffer layer of room temperature distilled water was then added, with the deprotonated ligand MeOH/water solution layered on top. This procedure, once the total volume of solvent was increased to 13 mL for 0.05 mmol reaction scales (with respects to the metal salts), led to the formation of small needle clusters for the $La(NO_3)_3{\cdot}6H_2O$, $Gd(NO_3)_3{\cdot}6H_2O$, $Dy(NO_3)_3{\cdot}6H_2O$ and $Ho(NO_3)_3{\cdot}6H_2O$ precursors. The lanthanum and gadolinium crystals were suitable for single crystal x-ray diffraction but the dysprosium and holmium crystals were too small for the Bruker AXS SMART single crystal diffractometer available to the University of Ottawa's chemistry department. These were thus sent to the Advanced Light Source Synchrotron in order to obtain their crystal structures.

3.2.1.1 Mononuclear ammonium salt

The x-ray diffraction of crystals obtained from the $La(NO_3)_3{\cdot}6H_2O$ coordination reaction led to the formation of the mononuclear ammonium salt: $NH_4[La(Hbta)_2(H_2O)_5]{\cdot}2H_2O$ (**108**) (Figure 3.2). This anionic complex consists of two deprotonated Hbta ligands coordinated to the metal center in a bidentate mode. The nine-coordinate metal center exhibits a slightly distorted capped square antiprism geometry, with the remaining five coordination sites occupied by water molecules (Figure 3.3). The La–N bond lengths for the coordinated

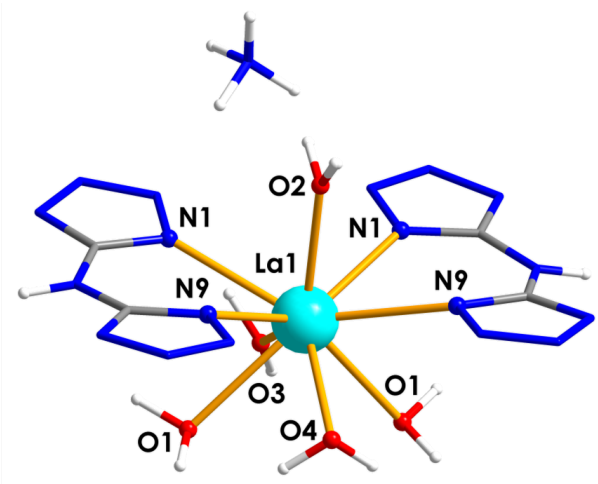

108

Figure 3.2: Labelled molecular structure of complex $NH_4[La(Hbta)_2(H_2O)_5]\cdot 2H_2O$ (**108**). Ball and stick representation for the metal centers and coordinated atoms, wire frame representation for remaining organic components. Lattice water omitted for clarity. Colour code: light blue (La), blue (N), red (O), grey (C), white (H).

Hbta ligands, ranging from 2.66 Å to 2.69 Å, are slightly longer on average than the La–O bonds of coordinated water, which range from 2.49 Å to 2.67 Å (Table 3.1). The top four vertices of the antiprism, relating to the two bidentate Hbta ligands, all lie within a plane. The slightly distorted rectangle formed between these four nitrogen atoms (2.91 Å and 4.32 Å between N atoms within the same Hbta molecule and between opposing Hbta molecules respectively) has corner angles of 87.05° and 92.95°. However the polyhedron is most distorted at the four lower vertices of the antiprism. Oxygen atoms O3 and O4 lie 0.21 Å above the average plane of all four atoms, while oxygen atoms O1 and O2 lie 0.42 Å below the plane. Furthermore, atoms O3 and O4 experience some disorder throughout the lattice, whereby their positions are shifted 0.059 and 0.129 respectively (Table 3.1). The bottom of the antiprism base therefore exhibits a 32.48° deviation from planarity.

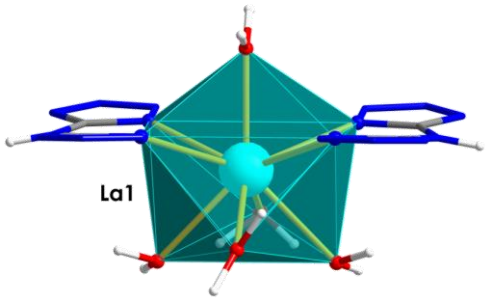

Figure 3.3: Coordination sphere polyhedral for complex **108**. Ball and stick representation for the metal centers and coordinated atoms, wire frame representation for remaining organic components. Colour code: light blue (La), blue (N), red (O), grey (C), white (H).

Table 3.1: Selected distances and angles for complexes **108**.

	Distances (Å)	**108**
Ln–N Tetrazole	Ln1–N1	2.66
	Ln1–N9	2.69
Ln–OH_2	Ln1–O1	2.67
	Ln1–O2	2.49
	Ln1–O3	2.53
	Ln1–O4	2.52
Disorder in water molecules (shift)	O3–O3	0.05
	O4–O4	0.12
Intermetallic distance	Ln1–Ln1	7.71
Tetrazole planes (a ◤)	N1,N2,N3,N4,C1–N1,N2,N3,N4,C1	3.23
	C2,N6,N7,N8,N9–C2,N6,N7,N8,N9	3.42
Tetrazole centroids (c ◤)	N1,N2,N3,N4,C1–N1,N2,N3,N4,C1	3.39
	C2,N6,N7,N8,N9–C2,N6,N7,N8,N9	3.65
Parallel displacement of tetrazoles (b ◤)	N1,N2,N3,N4,C1–N1,N2,N3,N4,C1	1.03
	C2,N6,N7,N8,N9–C2,N6,N7,N8,N9	1.25
	Angles (°)	
Tetrazole N-bite	N1–Ln1–N9	65.85
Opposing Tetrazole	N1–Ln1–N9	143.41
Opposing water molecules	O1–Ln1–N1	89.09
	O3–Ln1–N4	118.79
Cap tilt	O2–Ln1–N1	72.56
	O2–Ln1–N9	71.23
Hbta bend angle (tetrazole planes)	N1,N2,N3,N4,C1–C2,N6,N7,N8,N9	10.63
Tetrazole plane displacement	N1,N2,N3,N4,C1–N1,N2,N3,N4,C1	65.222
	C2,N6,N7,N8,N9–C2,N6,N7,N8,N9	61.84

◤ refers to the right angle triangle used to characterise parallel-displaced π–π interactions

Complex **108** crystallises in the monoclinic $P2_1/m$ space group (Figure 3.4). Viewed along the *b* axis, the complexed anions form diagonal rows. The orientations of the anions are alternated within each row such that the caps of the polyhedra are facing the row above or below. The ammonium cations, as well as the lattice water molecules, are located between these rows in the spaces created by two anions whose caps are facing the opposite rows. Alternating anions within the diagonal rows experience parallel displaced π–π interactions. This overlap is best viewed along axes *a* and *c*. Along these axes, the rows are zigzagged, rather than straight, with the metal centers forming the corners. The π–π interactions occur between tetrazoles consisting of the same labelled atoms. The N9 tetrazoles are separated by a distance of 3.42 Å and are parallel displaced by 1.25 Å. The N1 tetrazoles are separated by a distance of 3.23 Å and are parallel displaced by 1.03 Å, thus providing a better overlap than the N9 tetrazoles. The interplanar distance for the N1 tetrazoles are also below those generally reported (3.3–3.8 Å).[17] Due to these π–π interactions, the complexes anions from a 1D network along the perceived diagonal rows. This network is further expanded through extensive hydrogen bonding. Hydrogen bonding between anions of two rows with ammonium (N2–H10D and O1–H10B) expands the network vertically into 2D. Competition for hydrogen bonding between the two O1 atoms with the ammonium's H10B as well as the two N2 atoms with the ammonium's H10D leads to disorder within ammonium's hydrogens. The ammonium also experiences hydrogen bonding with one of the lattice water molecules (O5–H10A). This water molecule is further hydrogen bonded to the next row of anions behind it. Complex **108** thus forms a 3D network through its hydrogen bonding and π–π interactions.

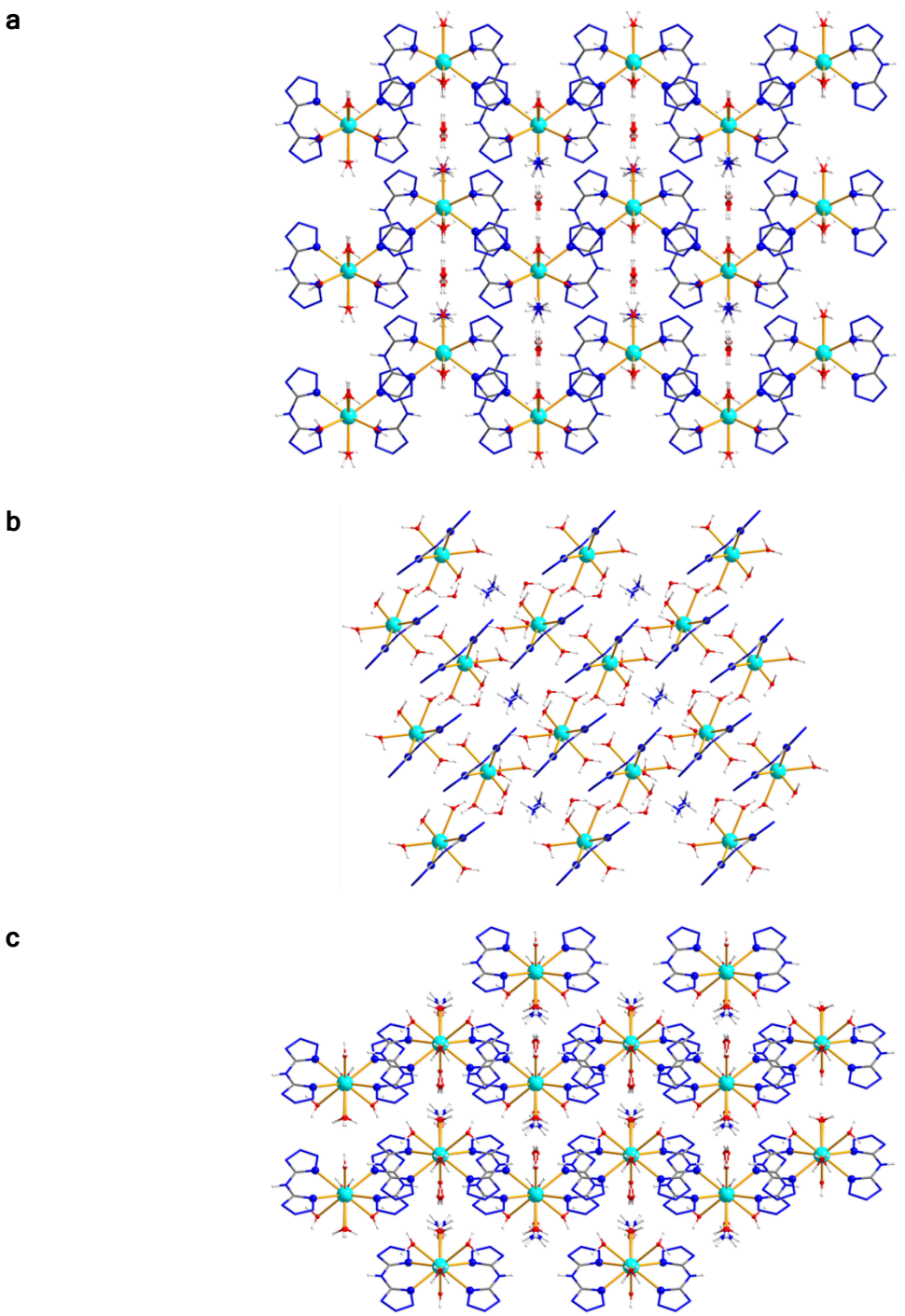

Figure 3.4: Packing for a 2x2x2 cell of complex **108**. a) Viewed along axis *a*. b) Viewed along axis *b*. c) Viewed along axis *c*. Wire frame representation for organic ligands, and ball and stick representation for coordinated atoms, for metal centers and hydrogen atoms. Lattice water omitted for clarity. Colour code: light blue (La), blue (N), red (O), grey (C), white (H).

3.2.1.2 Analogous complexed salts

The x-ray diffraction of crystals obtained from the $Gd(NO_3)_3{\cdot}6H_2O$, $Dy(NO_3)_3{\cdot}6H_2O$, and $Ho(NO_3)_3{\cdot}6H_2O$ coordination reactions led to the formation of the mononuclear complexes: $[Gd(Hbta)(H_2O)_6][Dy(Hbta)_2(H_2O)_4]{\cdot}3.2H_2O{\cdot}0.2H_4O_2$ (**109**), $[Dy(Hbta)(H_2O)_6][Dy(Hbta)_2(H_2O)_4]{\cdot}4.25H_2O$ (**110**), and $[Ho(Hbta)(H_2O)_6][Ho(Hbta)_2(H_2O)_4]{\cdot}4.25H_2O$ (**111**) (Figure 3.5, Figure 3.6, and Figure 3.7 respectively). These are comprised of a complexed cation (Ln2), consisting of a bidentate Hbta ligand and five coordinated water molecules, and a complexed anion (Ln1), consisting of two bidentate Hbta ligands and four coordinated water molecules. Though all three complexes are structural analogues, complex **109** bears some differences from **110** and **111**. Firstly, complex **109** contains more lattice water than complexes **110** and **111**. The orientation of its cation and distortions of its coordination environments also differ with respects to complexes **110** and **111**.

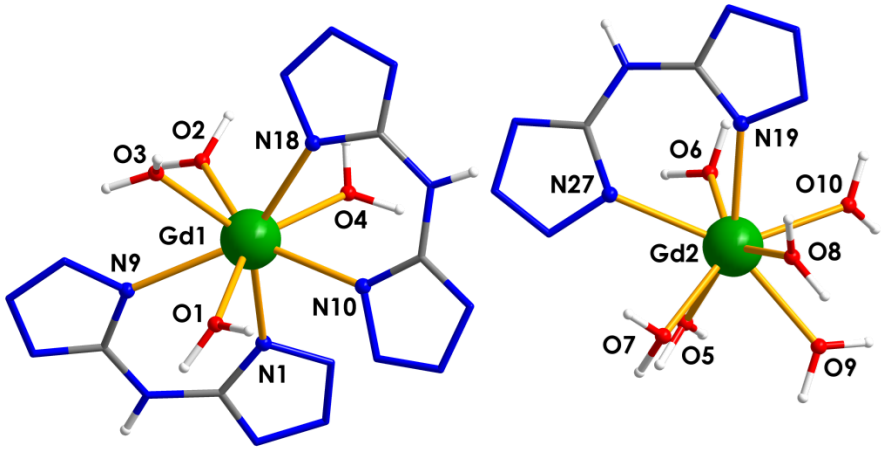

109

Figure 3.5: Labelled molecular structure of complex $[Gd(Hbta)(H_2O)_6][Gd(Hbta)_2(H_2O)_4]{\cdot}3.2H_2O{\cdot}0.2H_4O_2$ (**109**). Ball and stick representation for the metal centers and coordinated atoms, wire frame representation for remaining organic components. Colour code: green (Gd), blue (N), red (O), grey (C), white (H).

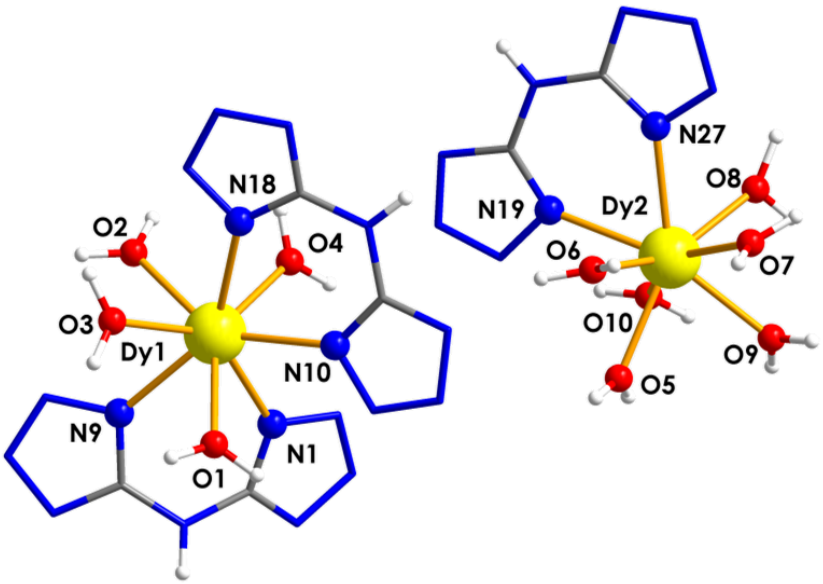

110

Figure 3.6: Labelled molecular structure of complex $[Dy(Hbta)(H_2O)_6][Dy(Hbta)_2(H_2O)_4]\cdot 4.25H_2O$ (**110**). Ball and stick representation for the metal centers and coordinated atoms, wire frame representation for remaining organic components. Colour code: yellow (Dy), blue (N), red (O), grey (C), white (H).

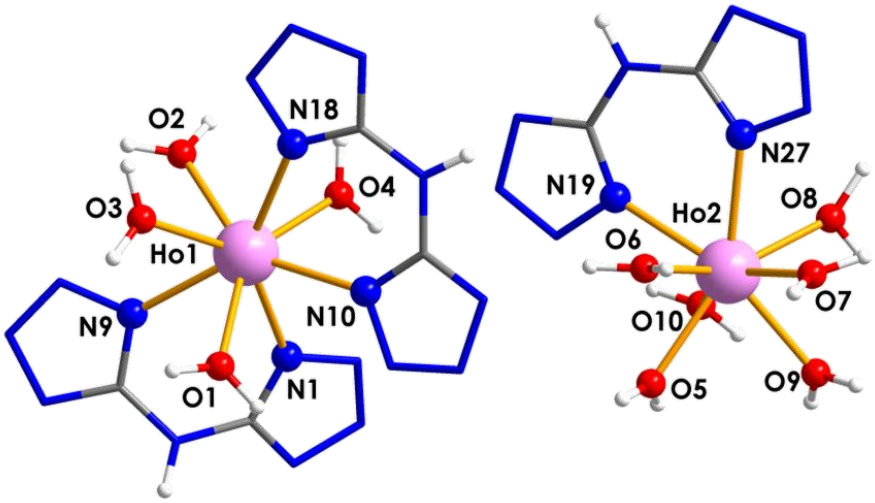

111

Figure 3.7: Labelled molecular structure of complex $[Ho(Hbta)(H_2O)_6][Ho(Hbta)_2(H_2O)_4]\cdot 4.25H_2O$ (**111**). Ball and stick representation for the metal centers and coordinated atoms, wire frame representation for remaining organic components. Colour code: pink (Ho), blue (N), red (O), grey (C), white (H).

Regardless, all three complexes consist of two 8-coordinate metal centers exhibiting square antiprism geometry (Figure 3.8). The Ln1 metal centers of the complexed anions are significantly more distorted than there corresponding cations for the Gd analogue, while the reverse is true for the Dy and Ho analogues. These complexes adhere to a decreasing bond length trend from Gd to Ho (2.33–2.59, 2.34–2.49, and 2.33–2.47 for **109**,

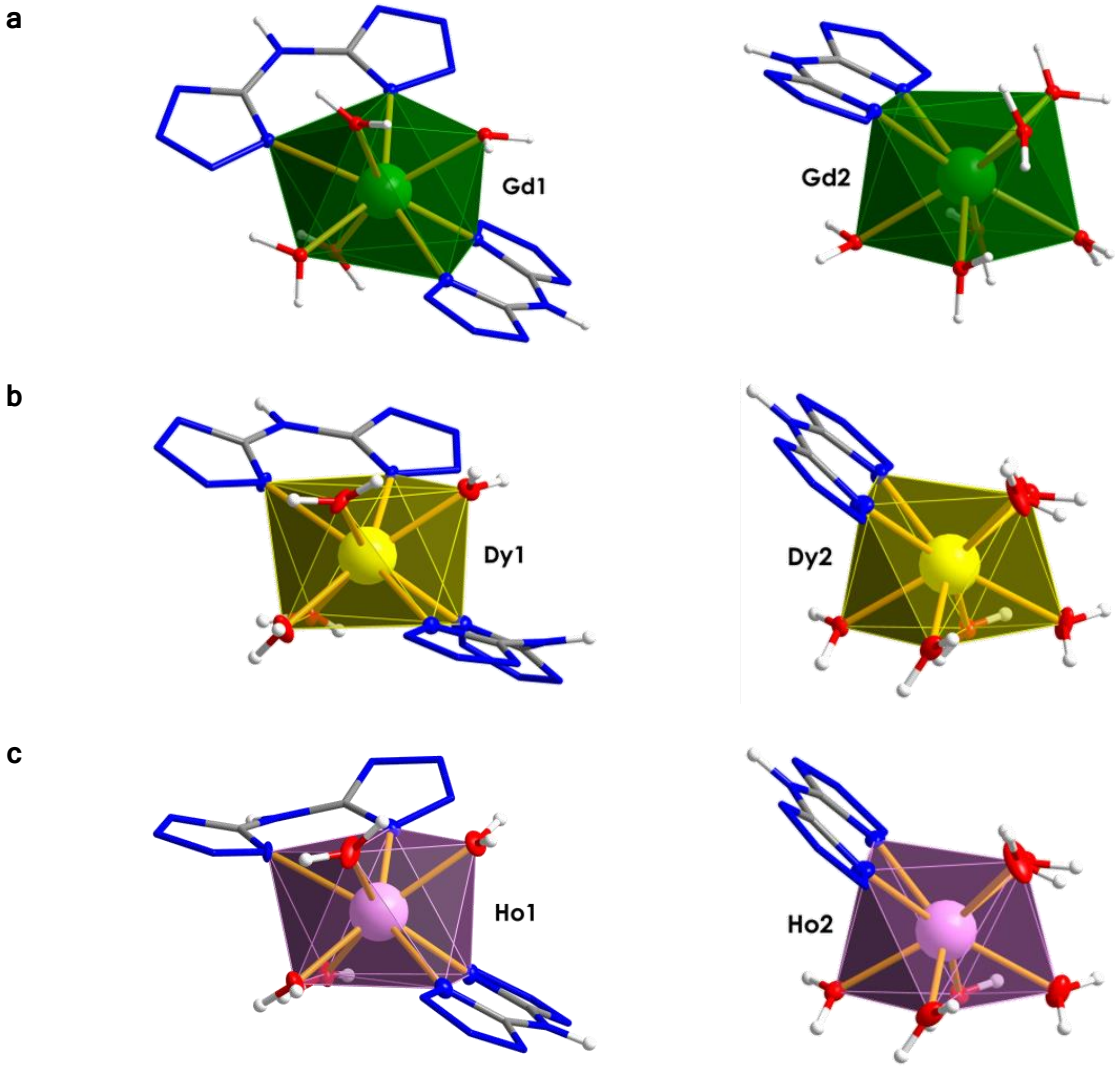

Figure 3.8: Coordination sphere polyhedral for analogous complexes: a) **109**, b) **110**, and c) **111**. Ball and stick representation for the metal centers, ellipsoid representation for coordinated atoms, and wire frame representation for remaining organic components. Colour code: green (Gd), yellow (Dy), light pink (Ho), blue (N), red (O), grey (C), white (H).

110, and **111** respectively), with the exception of the Ln2–O5 bond (Table 3.2). In this case, the Gd analogue has a shorter bond length than the Dy and Ho analogues which follow the trend. This trend is consistent with the lanthanide contraction, where the 4*f* electrons fail to shield the outer shell electrons, resulting in a more effective nuclear charge and a smaller ionic radius and the ionic number increases. Thus the smaller metal ions can fit more tightly into the coordination pocket.

Conversely, a wider Hbta bite angle is observed from the Gd analogue to the Ho analogue (Table 3.3). It is interesting to note that the Hbta ligand coordinated to the Ln1 metal centers through N1 and N9 experiences a significant bend between the two tetrazolate functional groups for complexes **110** and **111** (30.28°, and 29.91° respectively). While the similarly labelled ligand in complex **109** also experiences a slight bend (2.40°), it is closer to the degree of bending observed for the Hbta ligand bound to the Ln2 metal center through N19 and N27 in complexes **110** and **111**. The corresponding Hbta ligand in complex **109** experiences approximately four times the degree of bending seen in complexes **110** and **111** (12.93°, 2.93°, and 3.14° respectively), but halve of the degree of bending seen for the Hbta ligand coordinated to the Ln1 metal center through N1 and N9. Bending though the Hbta ligand, coordinated to the Ln1 metal centers through N10 and N18, follows a trend which increases by approximately 2° from complex **109** to complex **111** (7.86°, 9.78°, and 10.22° respectively). All three complexes also exhibit a mixture of two optical isomers for the anions (Figure 3.9), but no optical isomerism is experienced for the cations.

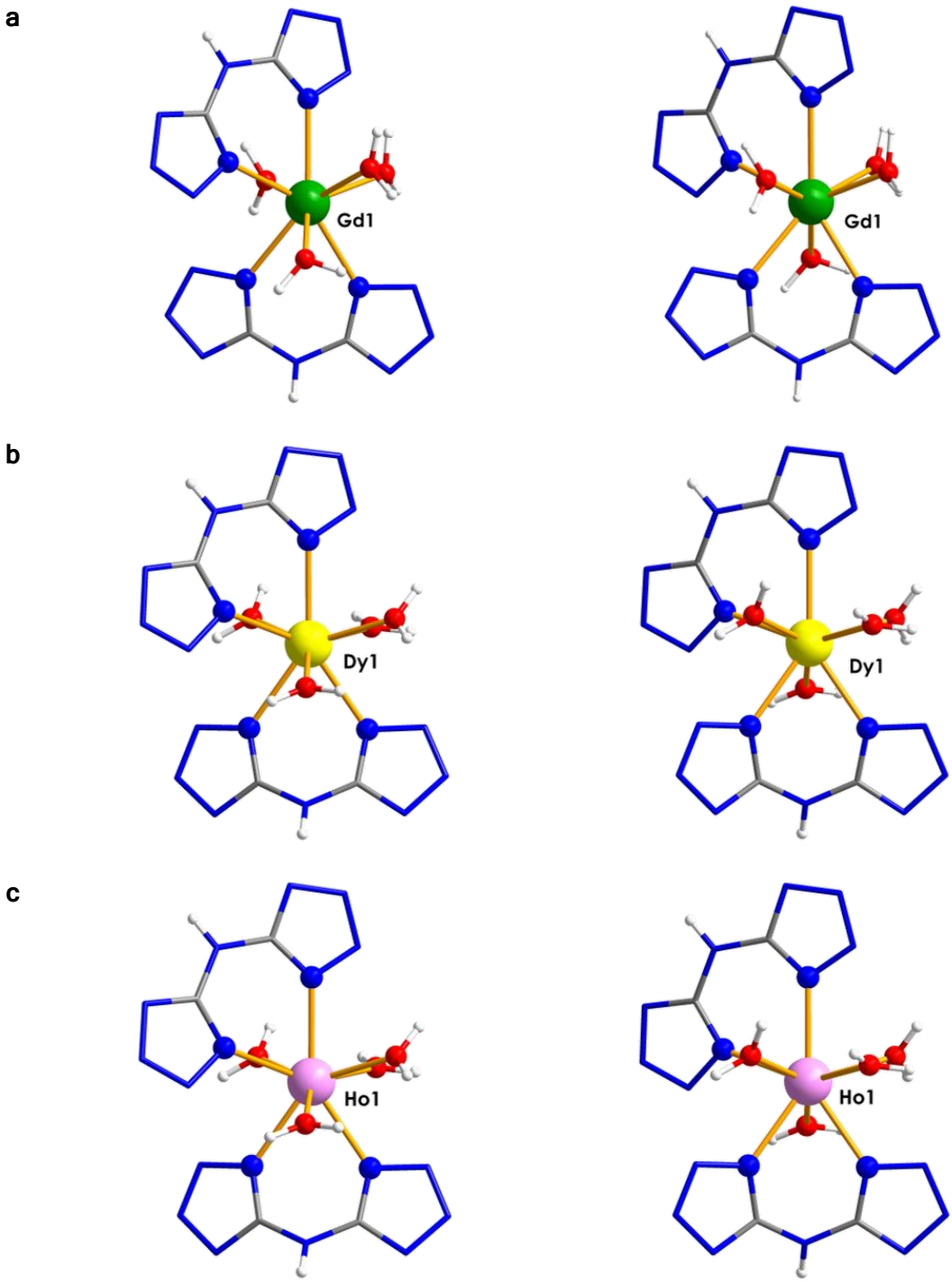

Figure 3.9: Comparison of anionic enantiomers for complexes: a) **109**, b) **110**, and c) **111**. Wire frame representation for organic ligands, and ball and stick representation for coordinated atoms, for metal centers and hydrogen atoms. Colour code: green (Gd), yellow (Dy), light pink (Ho), blue (N), red (O), grey (C), white (H).

Table 3.2: Selected distances for complexes **109**, **110**, and **111**.

	Distances (Å)	109	110	111
Ln–N Tetrazole	Ln1–N1	2.52	2.49	2.47
	Ln1–N9	2.59	2.48	2.46
	Ln1–N10	2.53	2.47	2.47
	Ln1–N18	2.51	2.48	2.46
	Ln2–N19	2.49	2.47	2.46
	Ln2–N27	2.52	2.45	2.44
Ln–OH_2	Ln1–O1	2.42	2.39	2.37
	Ln1–O2	2.43	2.37	2.35
	Ln1–O3	2.44	2.37	2.36
	Ln1–O4	2.51	2.36	2.35
	Ln2–O5	2.35	2.37	2.36
	Ln2–O6	2.48	2.39	2.39
	Ln2–O7	2.44	2.37	2.37
	Ln2–O8	2.41	2.37	2.36
	Ln2–O9	2.46	2.40	2.37
	Ln2–10	2.42	2.34	2.33
Intermetallic distances	Ln1–Ln2	7.19	6.95	6.95
	Ln1–Ln1	6.86	6.63	6.62
	Ln2–Ln2	6.86	6.63	6.62
Tetrazole planes (a ◤)*	C1,N1,N2,N3,N4–C2,N6,N7,N8,N9	3.13	---	---
	C2,N6,N7,N8,N9–C2,N6,N7,N8,N9	3.16	3.26	3.27
		3.12	3.06	3.06
	N10,N11,N12,N13,C3–C6,N24,N25,N26,N27	2.93	3.24	3.25
	N15,N16,N17,N18,C4–C5,N19,N20,N21,N22	3.45	3.33	3.33
Tetrazole centroids (c ◤)	C1,N1,N2,N3,N4–C2,N6,N7,N8,N9	3.55	---	---
	C2,N6,N7,N8,N9–C2,N6,N7,N8,N9	5.33	3.42	3.41
		3.65	3.21	3.21
	N10,N11,N12,N13,C3–C6,N24,N25,N26,N27	4.36	3.77	3.77
	N15,N16,N17,N18,C4–C5,N19,N20,N21,N22	3.76	3.66	3.75
Parallel displacement of tetrazoles (b ◤)	C1,N1,N2,N3,N4–C2,N6,N7,N8,N9	1.68	---	---
	C2,N6,N7,N8,N9–C2,N6,N7,N8,N9	4.29	1.02	0.97
		1.89	0.97	0.96
	N10,N11,N12,N13,C3–C6,N24,N25,N26,N27	3.23	1.92	1.91
	N15,N16,N17,N18,C4–C5,N19,N20,N21,N22	1.50	1.53	1.73

* the tetrazole planes between the cation and the anions (N10,N11,N12,N13,C3 and C6,N24,N25,N26,N27 as well as N15,N16,N17,N18,C4 and C5,N19,N20,N21,N22) were not parallel. Therefore the interplanar distances were measured using the centroid of the anion and the plane of the cation.

◤ refers to the right angle triangle used to characterise parallel-displaced π–π interactions

Table 3.3: Selected angles for complexes **109**, **110**, and **111**.

	Angles (°)	109	110	111
Tetrazole N-bite	N1–Ln1–N9	68.75	69.13	69.37
	N10–Ln1–N18	68.26	69.94	70.06
	N19–Ln2–N27	69.44	69.84	70.18
Opposing Tetrazole	N1–Ln1–N18	146.73	144.19	144.03
	N9–Ln1–N10	136.62	139.24	139.52
Opposing polyhedra vertices	O1–Ln1–O3	78.99	74.81	74.86
	O2–Ln1–N1	92.06	110.55	109.96
	O4–Ln1–N9	128.07	117.90	117.97
	O5–Ln2–O10	107.34	108.60	108.49
	O6–Ln2–O9	119.08	123.67	123.23
	O7–Ln2–O8	75.56	75.32	74.74
Hbta bend angle (tetrazole planes)	N1,N2,N3,N4,C1–C2,N6,N7,N8,N9	2.40	30.28	29.91
	N10,N11,N12,N13,C3–C4,N15,N16,N17,N18	7.86	9.78	10.22
	N19,N20,N21,N22,C5–C6,N24,N25,N26,N27	12.93	2.92	3.14
Tetrazole plane displacement	C1,N1,N2,N3,N4–C2,N6,N7,N8,N9	50.93	---	---
	C2,N6,N7,N8,N9–C2,N6,N7,N8,N9	20.57	65.67	66.63
		47.08	65.36	65.51
	N10,N11,N12,N13,C3–C6,N24,N25,N26,N27	26.81	47.78	47.95
	N15,N16,N17,N18,C4–C5,N19,N20,N21,N22	57.17	55.51	51.82

Complexes **109**, **110**, and **111** crystallise in the triclinic P–1 space group (Figure 3.10, Figure 3.11, and Figure 3.12). Viewing these structures from axis *a*, two distinctive diagonal rows can be identified. The first row is comprised of sets of Δ and Λ anions which overlap both their N9 tetrazoles. These sets are joined to each other through the Hbta ligands of two cations which are orientated perpendicularly to the row, on opposite sides, with their metal centers pointed outwards. The Hbta ligands of Δ and Λ anions and the two cations form a pinwheel motif. Subsequent rows are shifted with respects to one another such that the pinwheel motif is staggered. The second row is comprised of the metals centers and lattice solvent. These two rows therefore give the packing structure, viewed along axis *a*, an appearance of alternating red and blue diagonal stripes. One notable difference between complex **109**,

and its analogous Dy and Ho complexes, is that the N9 tetrazole overlap is significantly shifted with respects to complexes **110**, and **111**. This in turn, causes the distance between the rows to be significantly shorter in **109**; resulting in less space to accommodate lattice solvent. This may explain why complexes **110** and **111** accommodate more lattice solvent than **109**.

Viewing all three complexes through axes *b* and *c*, the vertical stacking of the tetrazolate functional groups is apparent. This leads to a considerable amount of paralleled displaced π–π interactions. The N9 tetrazoles from both anionic enantiomers in complexes **110** and **111** exhibit the greatest degree of overlap; with parallel displacements ranging from 0.96 Å to 1.02 Å, and interplanar distances ranging from 3.06 Å to 3.27 Å. Complex **109**, however, shows considerably less overlap with parallel displacements of 3.65 Å and 5.33 Å, as well as interplanar distances of 3.12 Å and 3.16 Å respectively. In this case, better overlap is achieved through the N1 and N9 tetrazoles of opposing enantiomers (parallel displacement of 1.68 Å and interplanar distance of 3.13 Å). There are also π–π interactions occurring within the pinwheel motif for all three complexes. Interactions between the N10 and N27 tetrazoles, as well as the N18 and N19 tetrazoles exhibit parallel displacements ranging from 1.91 Å to 3.22 Å and 1.50 Å to 1.73 Å, as well as interplanar distances ranging from 2.93 Å to 3.25 Å and 3.33 Å to 3.45 Å respectively. In addition to the π–π interactions, there is an extensive network of hydrogen-bonding occurring between the solvated metal centers, which expands perpendicularly to the π–π interactions. Thus, these analogous metal complexes form 3D networks.

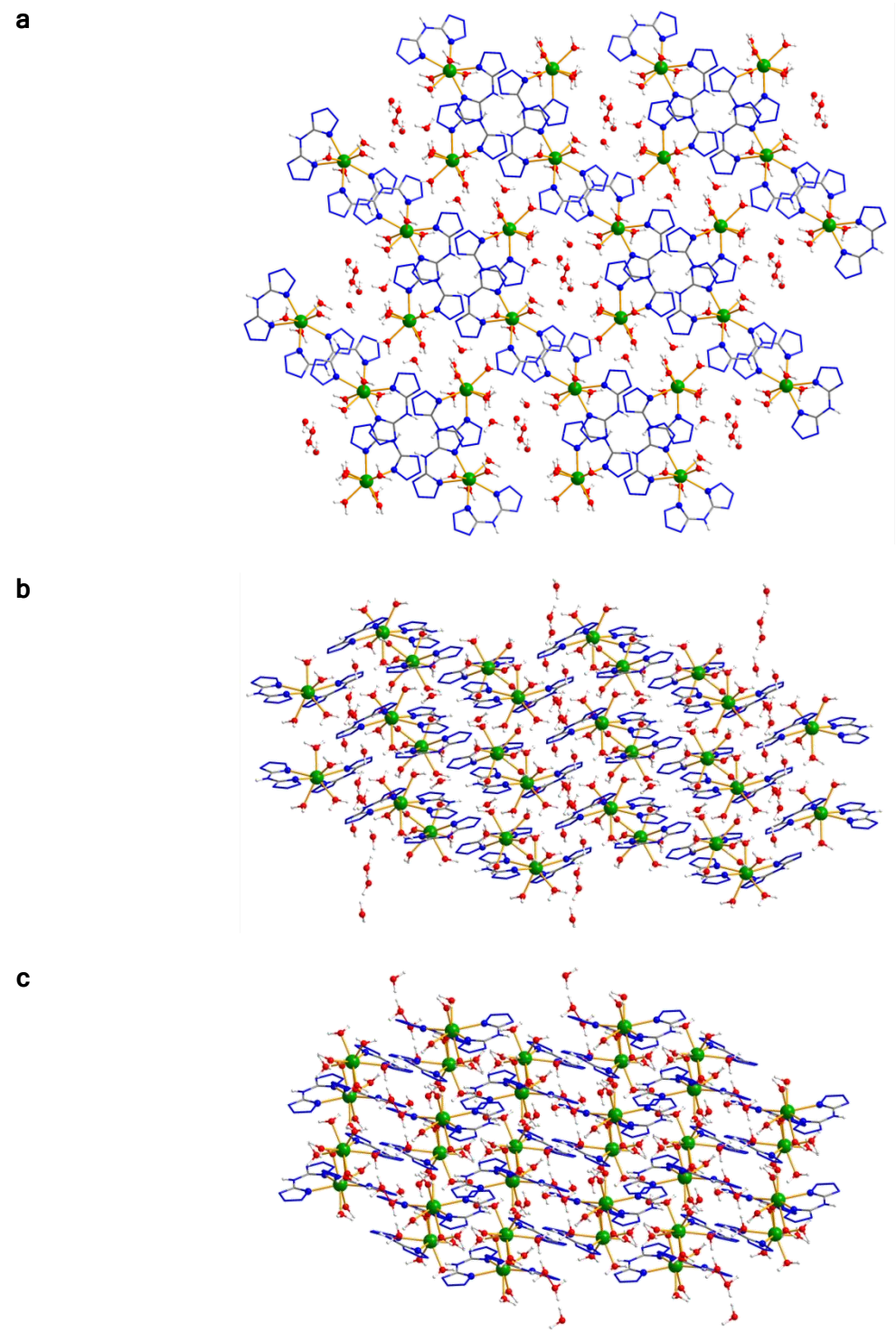

Figure 3.10: Packing for a 2x2x2 cell of complex **109**. a) Viewed along axis *a*. b) Viewed along axis *b*. c) Viewed along axis *c*. Wire frame representation for organic ligands, and ball and stick representation for coordinated atoms, for metal centers and hydrogen atoms. Colour code: green (Gd), blue (N), red (O), grey (C), white (H).

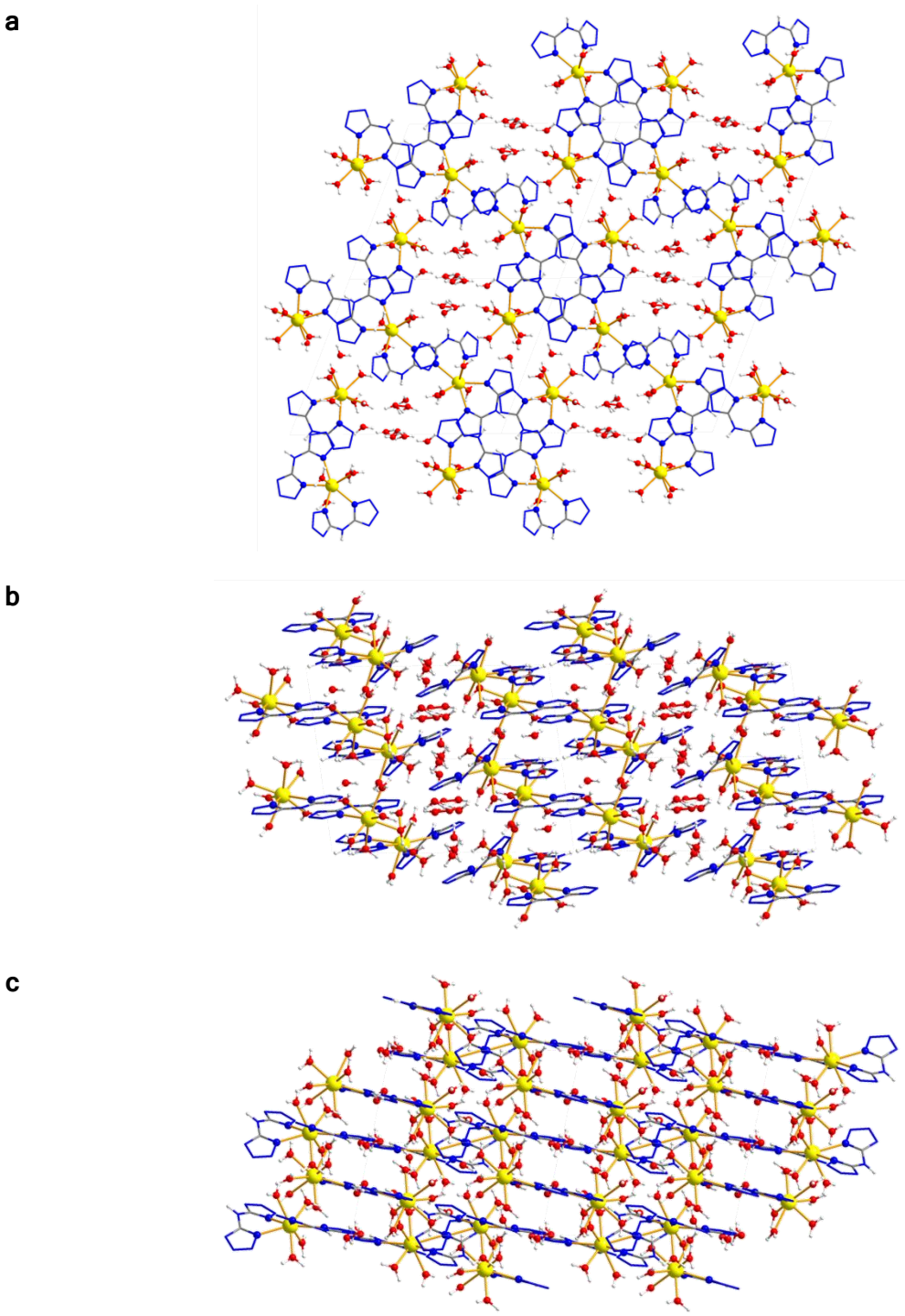

Figure 3.11: Packing for a 2x2x2 cell of complex **110**, with lattice water omitted for clarity. a) Viewed along axis *a*. b) Viewed along axis *b*. c) Viewed along axis *c*. Wire frame representation for organic ligands, and ball and stick representation for coordinated atoms, for metal centers and hydrogen atoms. Colour code: yellow (Dy), blue (N), red (O), grey (C), white (H).

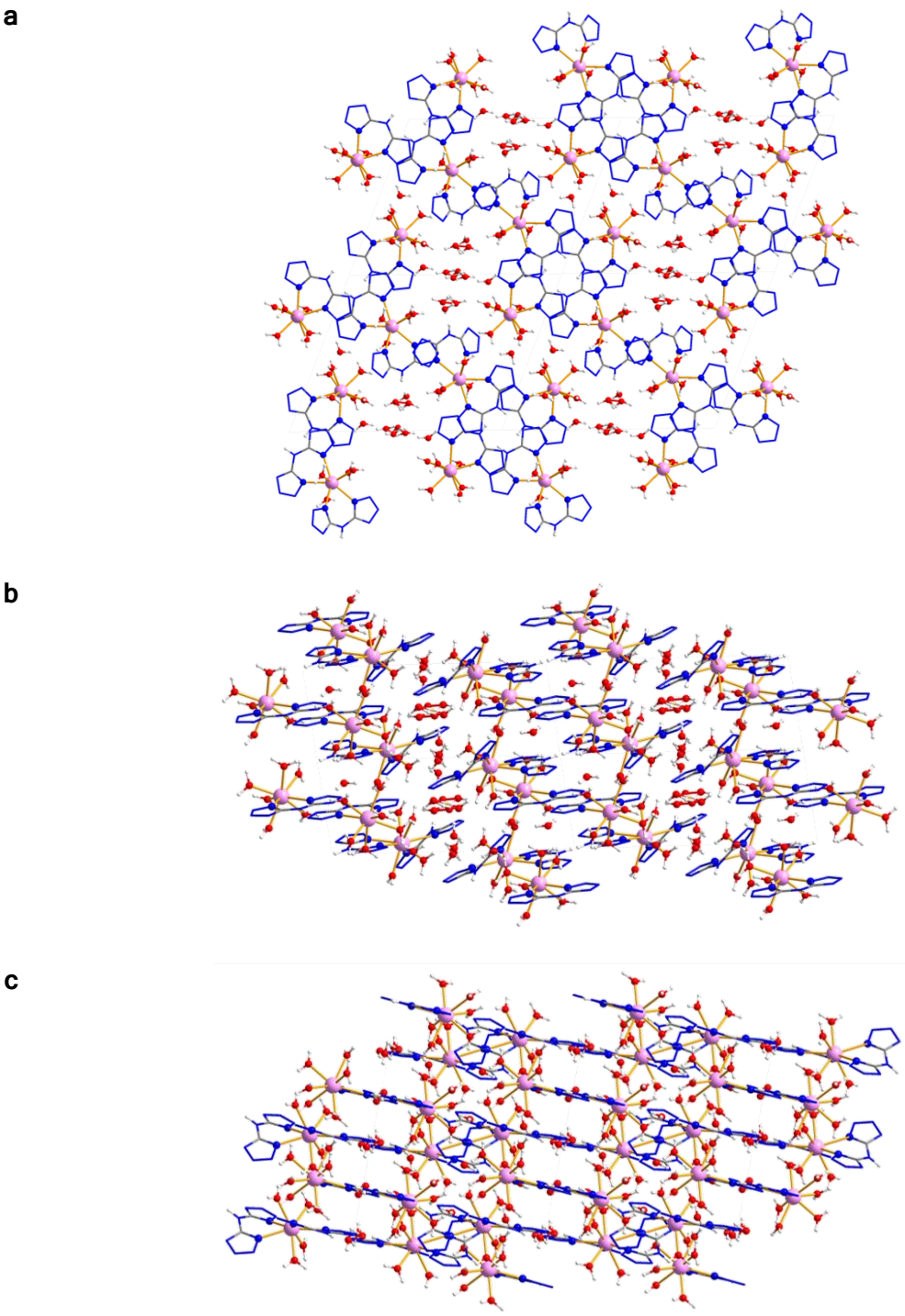

Figure 3.12: Packing for a 2x2x2 cell of complex **111**, with lattice water omitted for clarity. a) Viewed along axis *a*. b) Viewed along axis *b*. c) Viewed along axis *c*. Wire frame representation for organic ligands, and ball and stick representation for coordinated atoms, for metal centers and hydrogen atoms. Colour code: light pink (Ho), blue (N), red (O), grey (C), white (H).

Rudimentary impact and friction tests were performed on all three complexes with no visible reactions. A TGA experiment was performed for complex **109** (Figure 3.13). The thermogram depicts four major decomposition steps which have a gradual profile. The first two steps, with inflection points at 73.10 °C and 134.92 °C, correlate to the loss of lattice solvent, followed by most of the coordinated water molecules. The last two major steps add up roughly to the mass loss of Hbta ligands. The remaining 35.08% corresponds to more than the weight of the gadolinium metal ions. Since this experiment was conducted under inert atmosphere, the additional remaining mass percent might correlate to a graphitic residue from incomplete decomposition of some of the Hbta ligands. Comparing the profile of this thermogram with those obtained for the hydrazine complexes presented in Chapter 2, it is clear that the decomposition of **109** is a significantly more gradual process. The extensive coordination of water molecules appears to have inhibited the energetic potential of this bta-based complex.

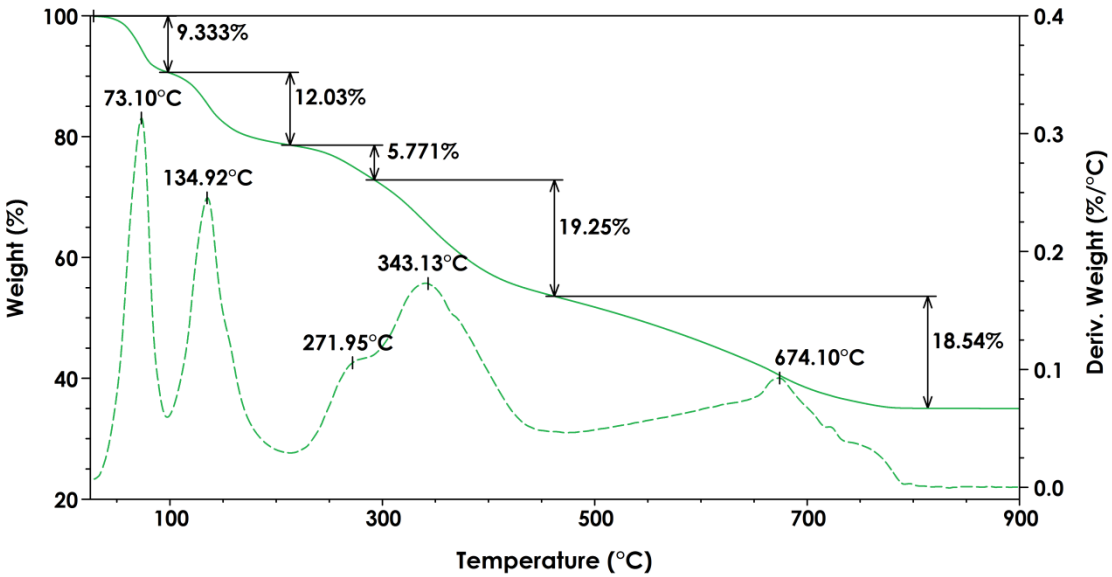

Figure 3.13: TGA plot (solid green) and weight derivative (dashed green) for complex **109**. The experiment was conducted at a heating rate of 10 °Cmin^{-1} under a nitrogen atmosphere with a sample size of 8.34 mg.

3.2.2 Conclusion

Using dilute, layered complexation reactions with an aqueous solvent system, four new lanthanide Hbta-based complexes have been synthesised: complexes **108**, **109**, **110**, and **111**. Due to the oxophilic nature of lanthanides, the coordination environments were severely hydrated and the desired analogous lanthanide homoleptic bta complexes of **107** were not achieved. Complex **108** consists of an ammonium salt with a symmetric *bis*-bta complexed anion, while the remaining complexes were analogous salts comprised of two complexed ions. The anions of complexes **109**, **110**, and **111** consisted of a racemic mixture of optical isomers. All four complexes exhibited various parallel displaced π–π interactions through the tetrazole functional groups. In addition to the extensive hydrogen bonding, promoted by the large content of water molecules, these complexes form 3D networks. A TGA experiment was also performed on complex **109** and revealed that its decomposition was comparatively slow to the hydrazine complexes presented in Chapter 2. Magnetic measurements were not performed on these due to their high degree of hydration. Water is a weak-field ligand and would not contribute significantly to the energy splitting of the electronic states, comparatively to the spin-orbit coupling and interelectronic repulsion inherent to the lanthanide ions. Thus the resulting magnetic performance would not be significantly improved over the metal ion's inherent properties. The high degree of hydration of these complexes hindered both the intended magnetic properties as well as the desired energetic properties. Future work should therefore focus on establishing a procedure which would allow for the inclusion of less water. A possible avenue to consider would be Teflon bomb reactions. Under the right pressures and temperatures, the solubility issues which lead to the use of water as solvent might be overcome.

3.3 Experimental

IR spectra were recorded using a Diamond ATR Thermo Scientific Nicolet 6700 spectrometer. Calorimetric studies were performed on a TA Q2000 DSC and with a TA Q5000 TGA instrument. Single crystals x-ray diffraction data was collected using a Bruker AXS SMART single crystal diffractometer equipped with a sealed Mo tube APEX II CCD detector (Mo radiation wavelength of 0.71073 Å), or at the Advanced Light Source synchrotron facilities at Lawrence Berkeley National Laboratory.

3.3.1 General considerations

Nitrogen-rich materials are potentially explosive and should be handled with care. The use of polycarbonate face shield, Kevlar sleeves, Kevlar gloves under thick leather gloves, ear protection, and blast shield (in addition to standard laboratory PPE such as lab coat and safety glasses), should be common practice when working with these materials.

3.3.2 Ligand Synthesis

The ligand $H_3bta{\cdot}H_2O$ was synthesised according to the literature procedure.[2] A solution of 2N HCl (45 mL, 90.00 mmol) was added drop wise over 3h to a refluxing clear, colourless solution of $NaN(CN)_2$ (2.6714 g, 27.25 mmol) and NaN_3 (3.9014g, 60.01 mmol) in a mixture of $EtOH/H_2O$ (1.5:1 75 mL). The resulting reaction mixture was refluxed for an additional 48h and then allowed cooled to room temperature. The mixture was further cooled in an ice bath. Drop wise addition of 36% concentrated HCl (13 mL, 151.45 mmol) to the chilled reaction solution produced a white precipitate. The product was filtered out and washed with ample chilled water (30-50 mL). The resulting product was a fluffy white powder (yield of 88.9%). Collection of ^1H NMR provided two NH peaks: one at 11.98 ppm for the two tetrazoyl

hydrogens and one at 3.43 ppm for the amine hydrogen. ^{13}C NMR provided one peak at 153.39 ppm for the tetrazoyl carbon. An IR spectrum was also collected and compared to literature spectra: 687.47, 736.20, 787.19, 814.81, 895.35, 974.01, 1001.76, 1035.43, 1070.97, 1108.46, 1261.78, 1281.65, 1335.92, 1351.31, 1451.41, 1553.80, 1611.06, 1640.05.

3.3.3 Complex Synthesis

3.3.3.1 Mononuclear ammonium salt

3.3.3.1.1 $NH4[La(Hbta)_2(H_2O)_5]\cdot 2H_2O$ - (108)

In a long test tube, $La(NO_3)_3\cdot 6H_2O$ (21.2 mg, 0.05 mmol) was dissolved in 2 mL of distilled water and placed in the fridge for 1 hour. Meanwhile, $H_3bta\cdot H_2O$ (0.0301 g, 0.18 mmol), was dissolved into 6 mL of a 1:1 MeOH/water and deprotonated using NH_4OH (21 μL, 0.53 mmol). Once the metal aqueous solution had been in the fridge for 1 hour, a 2 mL layer of room temperature distilled water was to the test tube, followed by the ligand layer. After 2-3 weeks, colourless needles formed within the test tube (≈ 25%).

3.3.3.2 Analogous complexed salts

3.3.3.2.1 $[Gd(Hbta)(H_2O)_6][Gd(Hbta)_2(H_2O)_4]\cdot 3.2H_2O\cdot 0.2H_4O_2$ - (109)

In a long test tube, $Gd(NO_3)_3\cdot 6H_2O$ (23.9 mg, 0.05 mmol) was dissolved in 2 mL of distilled water and placed in the fridge for 1 hour. Meanwhile, $H_3bta\cdot H_2O$ (0.0300 g, 0.18 mmol), was dissolved into 6 mL of a 1:1 MeOH/water and deprotonated using NH_4OH (21 μL, 0.53 mmol). Once the metal aqueous solution had been in the fridge for 1 hour, a 2 mL layer of room temperature distilled water was to the test tube, followed by the ligand layer. After 2-3 weeks, colourless needles formed within the test tube (≈ 25%).

3.3.3.2.2 $[Dy(Hbta)(H_2O)_6][Dy(Hbta)_2(H_2O)_4]\cdot 4.25H_2O$ - (110)

In a long test tube, $Dy(NO_3)_3\cdot 6H_2O$ (26.8 mg, 0.06 mmol) was dissolved in 2 mL of distilled water and placed in the fridge for 1 hour. Meanwhile, $H_3bta\cdot H_2O$ (0.0301 g, 0.18 mmol), was dissolved into 6 mL of a 1:1 MeOH/water and deprotonated using NH_4OH (21 μL, 0.53 mmol). Once the metal aqueous solution had been in the fridge for 1 hour, a 2 mL layer of room temperature distilled water was to the test tube, followed by the ligand layer. After 2-3 weeks, colourless needles formed within the test tube (≈ 25%).

3.3.3.2.3 $[Ho(Hbta)(H_2O)_6][Ho(Hbta)_2(H_2O)_4]\cdot 4.25H_2O$ - (111)

In a long test tube, $Ho(NO_3)_3\cdot 6H_2O$ (20.4 mg, 0.04 mmol) was dissolved in 2 mL of distilled water and placed in the fridge for 1 hour. Meanwhile, $H_3bta\cdot H_2O$ (0.0299 g, 0.18 mmol), was dissolved into 6 mL of a 1:1 MeOH/water and deprotonated using NH_4OH (21 μL, 0.53 mmol). Once the metal aqueous solution had been in the fridge for 1 hour, a 2 mL layer of room temperature distilled water was to the test tube, followed by the ligand layer. After 2-3 weeks, light pink needles formed within the test tube (≈ 25%).

3.3.4 Supplemental Information

3.3.4.1 IR Spectra for bta-based complexes

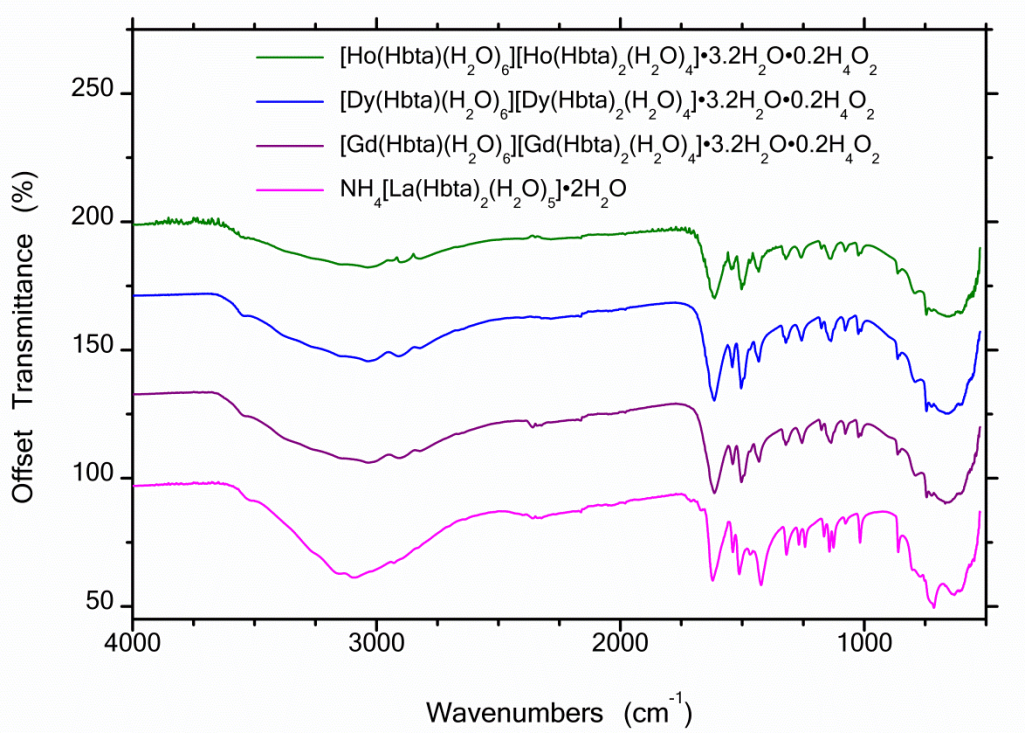

Figure 3.14: IR Spectra for Hydrazine-Based Complexes.

3.3.4.2 Crystallographic data tables for bta-based complexes

3.3.4.2.1 . Mononuclear ammonium salt

Table 3.4: Crystallographic Data for $NH_4[La(Hbta)_2(H_2O)_5]\cdot 2H_2O$

Compound		**108**
Empirical formula		$C_4\ H_{20}\ La\ N_{19}\ O_7$
Formula weight (g/mol)		585.30
Space group		Monoclinic
Crystal system		$P2_1/m$
Unit cell dimensions	**a (Å)**	7.71400(10)
	b (Å)	12.9192(2)
	c (Å)	10.0820(2)
	α (°)	90.00
	β (°)	101.8680(10)
	γ (°)	90.00
V (Å^3)		983.281
Z		2
ρ_{calc} (g cm^{-3})		1.977
Absorption coefficient (mm^{-1})		2.249
F(000)		580
λ (Mo Kα) (Å)		0.71073
Crystal size (mm)		0.19 x 0.06 x 0.04
θ Range (°)		2.06 - 30.51
Reflections collected		4773
T_{min} / T_{max}		0.6745, 0.9154
Goodness of fit		1.012
R1		0.0533
wR2		0.1767

This structure was collected at 200(2) K. Crystals were colourless needles.

3.3.4.2.2 Analogous complexed salts

Table 3.5: Crystallographic Data for analogous complexes **109**, **110**, and **111**

Compound		**109**	**110**	**111**
Empirical formula		C_6 $H_{30.2}$ Gd_2 N_{27} $O_{13.6}$	C_6 $H_{31.5}$ Dy_2 N_{27} $O_{14.25}$	C_6 $H_{31.5}$ Ho_2 N_{27} $O_{14.25}$
Formula weight (g/mol)		1012.87	1034.99	1039.85
Space group		Triclinic	Triclinic	Triclinic
Crystal system		P-1	P-1	P-1
Unit cell dimensions	**a (Å)**	6.861(3)	6.6390(17)	6.6252(13)
	b (Å)	13.698(6)	14.266(4)	14.235(3)
	c (Å)	17.416(8)	17.874(5)	17.886(4)
	α (°)	105.092(11)	110.393(3)	110.512(3)
	β (°)	95.691(12)	93.501(4)	93.531(3)
	γ (°)	95.396(12)	99.803(4)	99.720(3)
V (Å^3)		1560.3	1550.27	1543.82
Z		2	2	2
ρ_{calc} (g cm^{-3})		2.156	2.221	2.246
Absorption coefficient (mm^{-1})		4.315	9.02	9.59
F(000)		984	960	966
λ (Mo Kα) (Å)		0.71073	---	---
Crystal size (mm)		0.12 x 0.09 x 0.06	0.30 x 0.04 x 0.01	0.22 x 0.01 x 0.01
θ Range (°)		1.69 - 28.37	6.32 - 67.19	6.33 - 67.42
Reflections collected		15878	21872	16821
T_{min} / T_{max}		0.7818, 0.6255	0.5859, 0.7466	0.3815, 0.7466
Goodness of fit		1.048	0.864	0.769
R1		0.0345	0.0386	0.0420
wR2		0.0900	0.1231	0.1209

These structures were collected at 200(2) K for complex 109, and 100 K for complexes 110 and 111. Crystals were colourless needles, except for 111 which had light pink needles.

3.4 References

1. Norris, W. P.; Henry, R. A.; J. Org. Chem. **1964**, 29, pp 650-660.
2. Klapötke, T. M.; Mayer, P.; Stierstorfer, J.; Weigand, J. J.; J. Mater. Chem. **2008**, 18, pp 5248-5258.
3. Guo, Y.; Gao, H.; Twamley, B.; Shreeve, J. M.; Adv. Mater. **2007**, 19, pp 2884-2888.
4. Guo, Y.; Tao, G.; Zeng, Z.; Gao, H.; Parrish, D. A.; Shreeve, J. M.; Chem. Eur. J. **2010**, 16, pp 3753-3762.
5. Guan, Y.; Wang, D.; Dong, W.; Acta Cryst. **2007**, E63, pp m3150.
6. Jiang, T.; Zhang, X.; Cryst. Growth Des. **2008**, 8, pp 3077-3083.
7. Lin, J.; Huang, B.; Guan, Y.; Liu, Z.; Wang, D.; Dong, W.; Cryst. Eng. Comm. **2009**, 11, pp 329-336.
8. Xue, B.; Yang, Q.; Chen, S.; Gao, S. J. Therm. Anal. Calorim. **2010**, 101, pp 997-1002.
9. Gao, E.; Lui, N.; Cheng, A.; Gao, S. Chem. Commun. **2007**, 2007, pp 2470-2472.
10. Lu, Y.; Wang, M.; Zhou, W.; Xu, G.; Guo, G.; Huang, J.; Inorg. Chem. **2008**, 47, pp 8935-8942.
11. Cook, C.; Habib, F.; Aharen, T.; Rodolphe, C.; Hu, A.; Murugesu, M.; Inorg. Chem. **2013**, 52, pp 1825-1831.
12. Zheng, L.; Li, H.; Leng, J.; Wang, J.; Tong, M.; Eur. J. Inorg. Chem. **2008**, **2008**, pp 213-217.
13. Hiskey, M. A.; Chavez, D.; Naud, D. US Patent US6214139 B1, **2001**.
14. Friedrich, M.; Gálvez-Ruiz, J. C.; Klapötke, T. M.; Mayer, P.; Weber, B.; Weigand, J. J.; Inorg. Chem. **2005**, 44, pp 8044-8052.
15. Steinhauser, G.; Klapötke, T. M.; Angew. Chem., Int. Ed. **2008**, 47, pp 3330-3347.
16. Wang, W.; Chen, S.; Gao, S.; Eur. J. Inorg. Chem. **2009**, 2009, pp 3475-3480.
17. Janiak, C.; Dalton Trans. **2000**, pp 3885-3896.

Chapter 4

H_4ttp ligand system

4.1 Introduction

The well known neutral ligand 2,6-bis(2-pyridyl)pyridine (terpy, **112**) has been employed to make numerous metal complexes with wide-spread applications.[1] Its tridentate coordination pocket is a motif which efficiently binds to most metals. This includes transition metals such as: Fe, Co, Ni, Cu, Zn, Ru, Cd, and Y, as well as lanthanides and actinides such as: Yb, Ce, Nd, and U.[1,2] Incorporating the terpy motif into a bridging ligand gives tetra-2-pyridylpyrazine (tppz, **113**), which has been employed to form a wide variety of complexes, including coordination polymers,[3-8] and mixed valence complexes.[9-16] Replacing the pyridine rings on tppz with tetrazoles gives the more nitrogen-rich pyrazine analogue: 2,3,5,6-tetra(1*H*-tetrazol-5-yl)pyrazine (H_4ttp, **114**) (Scheme 4.1).

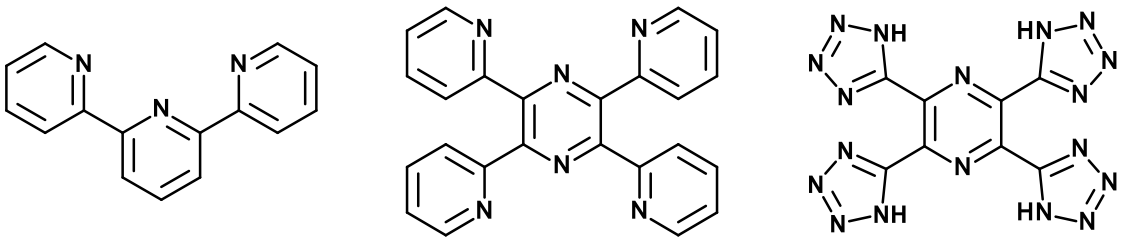

112 $C_{15}H_{11}N_3$ N18.01%

113 $C_{24}H_{16}N_6$ N21.64%

114 $C_8H_4N_{18}$ N71.58%

Scheme 4.1: Ligand structures along with their respective nitrogen content (mass %): terpy (**112**), tppz (**113**), and H_4ttp (**114**)

Tetrazole-based molecules have been increasingly employed as ligands in a vast variety of complexes due to their versatility.[17] Since the turn of the 21st century, one of the most pursued fields in supramolecular chemistry and crystal engineering is the development of 5-substituted 1H-tetrazoles.[18] Their novel structural architectures and topologies have led to potential applications in coordination chemistry, medicinal chemistry, and materials science.[18] Based

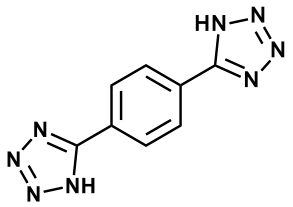

115

$C_8H_6N_8$
N52.32%

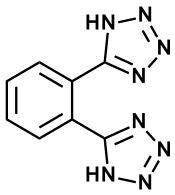

116

$C_8H_6N_8$
N52.32%

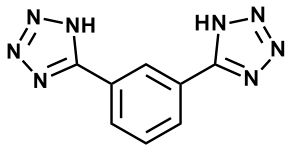

117

$C_8H_6N_8$
N52.32%

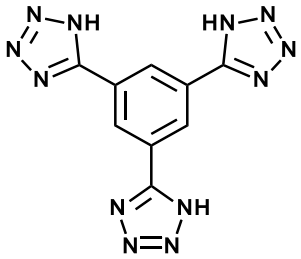

118

$C_9H_6N_{12}$
N59.56%

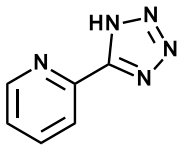

119

$C_6H_5N_5$
N47.60%

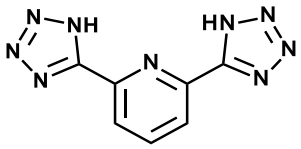

120

$C_7H_5N_9$
N58.58%

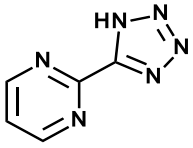

121

$C_5H_4N_6$
N56.74%

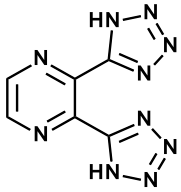

122

$C_6H_4N_{10}$
N64.80%

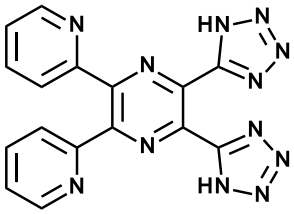

123

$C_{16}H_{10}N_{12}$
N45.39%

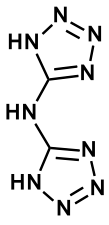

106

$C_2H_3N_9$
N82.34%

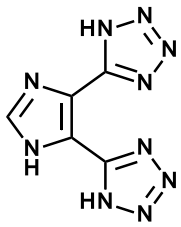

124

$C_5H_4N_{10}$
N68.61%

Scheme 4.2: Selection of known tetrazole-based ligands used in complexation, along with their respective nitrogen content (mass %). Corresponding references for each ligand: **115**,[19-21] **116**,[22] **117**,[22-26] **118**,[27] **119**,[28,29] **120**,[30] **121**,[31] **122**,[32,33] **123**,[34,35] **106**,[36] **124**.[37,38]

solely on the tetrazole-based ligands provided in Scheme 4.2, structures such as H-bonded networks,[19,20,22-24,32] 1D frameworks,[34,37] 2D frameworks,[26,28,29,31] MOFs,[21,27,33-35] and cubic metal clusters have been obtained.[38] Furthermore, these exhibit properties such as gas absoption,[21,27,33,35] luminescence,[26,30,34] mixed valence states,[38] as well as magnetic properties such as spin canting,[28,31] metamagnetism,[28] and frustrated magnets.[29] Combining the terpy motif with tetrazole rings adds the ability to incorporate an anionic charge to further strengthen the motif's binding affinity by allowing the creation of a σ-type coordination bond. Furthermore, the addition of tetrazoles to the terpy motif introduces new binding modes with the introduction of more heteroatoms whose lone pairs are available for π-type coordination binding (Scheme 4.3 and Scheme 4.4).

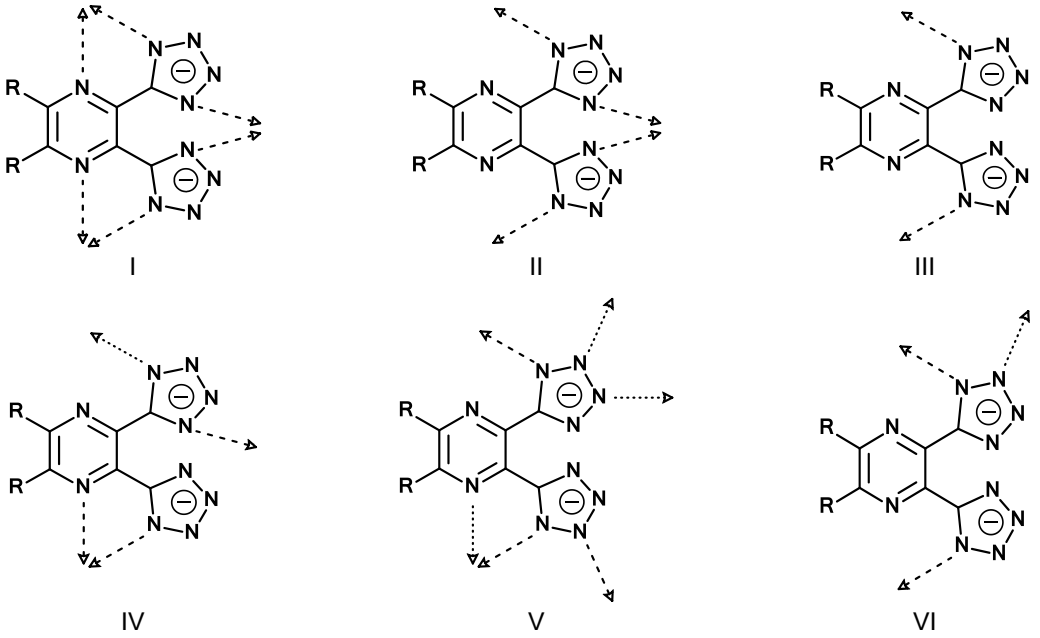

Scheme 4.3: Selected coordination modes of 2,3-substituted-5,6-di-(1*H*-tetrazol-5-yl)pyrazine ligand (**122** for R = H).[32]

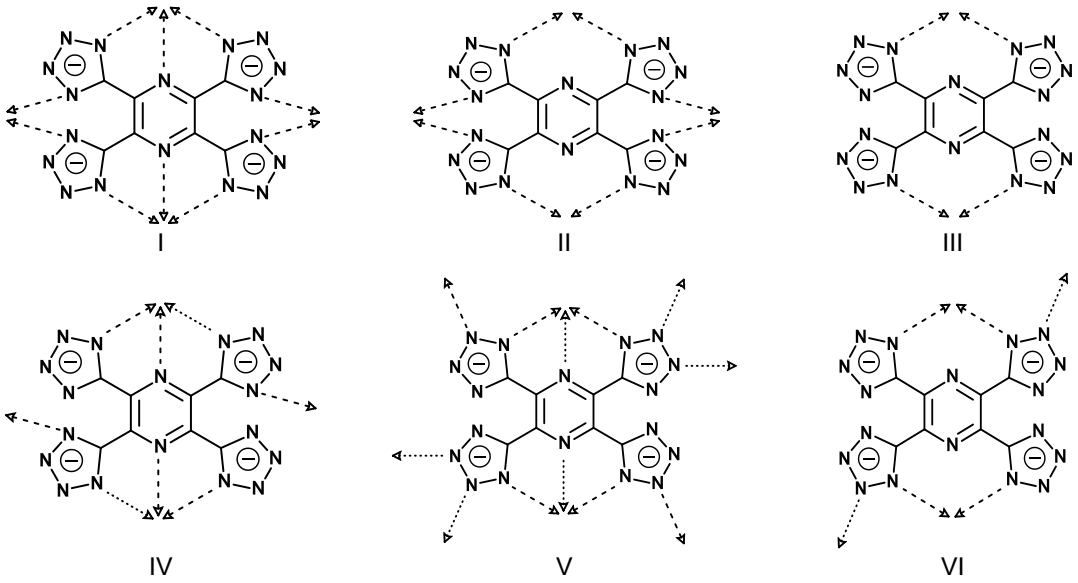

Scheme 4.4: Extension of selected possible coordination modes of 2,3-substituted-5,6-di-(1*H*-tetrazol-5-yl)pyrazine ligand[32] for the ttp ligand (**114**).

4.2 Results and Discussion

4.2.1 First Reported Synthesis of H_4ttp ligand

Having worked with the known H_3bta (**106**) (Chapter 3), the next objective was to synthesise a new tetrazole-based nitrogen-rich compound which would have a similar coordination pocket as H_3bta, could act as a bridging ligand, and would have a desirable packing motif to optimise its density. Inspiration for designing the never previously reported 2,3,5,6-tetra(1*H*-tetrazol-5-yl)pyrazine (H_4ttp, Scheme 4.5) came from thorough bibliographic research of hydrogen cyanide chemistry and finding tetracyanopyrazine (TCP) which presented as a good precursor to multi-tetrazole ramified compounds.[39,40] Given that TCP decomposes in acidic aqueous media, the synthetic procedure for H_3bta could not be used.[41] Several attempts to use a procedure consisting of $Et_3N{\cdot}HCl$ as catalyst in toluene were unsuccessful at converting all four nitrile groups to tetrazoles.[42] Further literature inquiries for non-aqueous tetrazole procedures lead to a paper by Tisseh *et al.* where various mono-

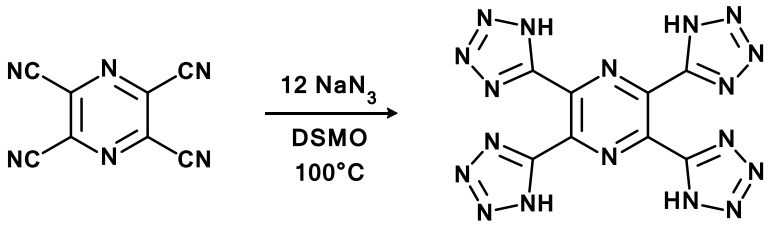

125 114

Scheme 4.5: Optimized synthesis of 2,3,5,6-tetra(1*H*-tetrazol-5-yl)pyrazine (H_4ttp)

and bis-tetrazoyl pyrazine-based compounds were successfully synthesised using only DMSO as both solvent and catalyst, followed by acidic workup.[43] The use of a more polar solvent allowed for the dissociation of the azide salt and the polarisation of the nitrile bond. Modifying the number of NaN_3 equivalents in this procedure to accommodate for the four nitrile groups on TCP, led to the successful synthesis of the H_4ttp molecule. This was first confirmed by ^1H, ^{13}C and ^{15}N NMR experiments (Table 4.1).

Table 4.1: Results from NMR experiments

^1H NMR					
Assignment	**Tetrazole H**				
Liquid state	12.55				
^{13}C NMR					
Assignment	**Pyrazine C**			**Tetrazole C**	
Liquid state	140.50			154.08	
Solid state	136.57			153.01	
^{15}N NMR					
Assignment	**N3**	**N2**	**N5**	**N4**	**N1**
Liquid state	-3.93		-48.92	-87.29	
Solid state	7.12	-9.77	-58.34	-65.73	-142.81

The ^1H NMR spectrum, as well as a ^{15}N NMR spectrum were acquired from a dry DMF-d_7 solution and loaded in a glove box, while the ^{13}C NMR spectrum was acquired from a DMSO-d_6 solution. ^1H and ^{13}C experiments were referenced to TMS, and ^{15}N experiments were referenced to NH_4Cl; which was assigned a chemical shift of -341.2 ppm.[44]

The proton NMR experiments were originally carried out in DMSO-d_6 (Supplemental: Figure 4.31), but there was only one broad peak observed apart from the solvent peak. This peak was shifted too far downfield to be water, but too far upfield to be the protons on the tetrazole groups. Similar broad peaks had been observed for proton NMR spectra of unsuccessful toluene syntheses, though these peaks never appeared at the same positions. It was thought that this broad peak might be caused by the rapid exchange of protons between the tetrazole groups and water present within DMSO or the sample. The position of the peak would therefore be dependent on the concentration of both species. Given that DMSO has a melting point just below room temperature, variable temperature experiments used to slow down proton exchange and separate the two peaks could not be undertaken. Instead, a qualitative test was performed, whereby drop of water was added to a measured sample and a new spectrum was collected. As expected, the peak shifted upfield, closer to the expected position for water. This confirmed that proton exchange was indeed occurring between the tetrazoles and water molecules. In order to obtain the true NMR shift for the tetrazole protons, a sample of H_4ttp was dried under vacuum with a P_2O_5 trap for 24 h and brought into a glove box where it was dissolved in dry DMF-d_7. The proton shift for H_4ttp was thus determined to be 12.55 ppm (Supplemental: Figure 4.32).

Though the proton NMR experiments carried out in DMSO-d_6 were not conclusive, the ^{13}C NMR experiments were found to be strait forward (Supplemental: Figure 4.33). Although H_4ttp has eight carbons, due to the symmetry of the molecule, only two spectroscopically unique carbons are observed: the pyrazine carbons and the tetrazole carbons. Apart from the solvent peak, two peaks appear on the spectrum. The pyrazine carbons are

assigned to the peak at 140.50 ppm,[45,46] while the tetrazole carbons are assigned to the peak further downfield at 154.08 ppm.[30,45,47-55] Solid state ^{13}C NMR experiments using cross polarization magic angle spinning (CPMAS) also exhibit two peaks for H_4ttp: 136.57 ppm for pyrazine carbons,[56] and 153.01 ppm for tetrazole carbons (Supplemental: Figure 4.34).[57] Both peaks show an upfield shift comparatively to liquid state measurements. These differences are most likely due to translational and rotational restrictions in the solid state and due to solvent shifts.

In regards to the ^{15}N NMR experiments, there are five nitrogens with unique electronic environments with H_4ttp (Scheme 4.6). However, the ^{15}N NMR spectrum for H_4ttp in DMF-d_7 exhibits three peaks (Supplemental: Figure 4.35). This discrepancy could be due to either rotational freedom between the pyrazine-tetrazole C–C bond, or a 1,3–proton shift. Thus, there is one peak representing the average of each electronic environment observed for N1 and N4 as well as N2 and N3. Within the tetrazole ring, substituted nitrogens experience the most shielding,[45,47-64] and thus the peak at –87.29 ppm is assigned to N1 and N4. Conversely, N2 and N3 are assigned to the peak at –3.93 ppm. The peak at –48.92 ppm is consistent with literature values for substituted pyrazine.[45,46,58,59,65-67] In order to provide more evidence to support the rationalisation of the three peaks observed for the solution measurements, an ^{15}N CPMAS NMR measurement was also collected (Supplemental: Figure 4.36). In this spectrum, five peaks are observed as expected. The pyrazine peak is shifted upfield to –58.34 ppm.[56] The additional shielding of N5 with respects to the solution measurement might be explained as a result of a closer proximity to N1 in the solid state. In regards to the tetrazole, N1 is assigned a chemical shift of –142.81 ppm, N4 –65.73 ppm, N2 –9.77 ppm, and N3 7.12 ppm.[57]

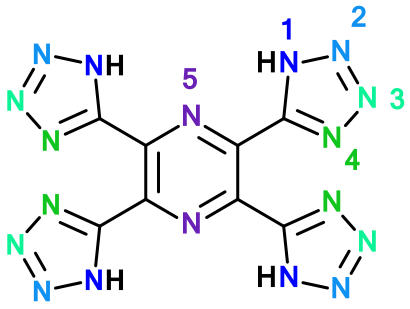

114

Scheme 4.7 Labelled H_4ttp molecule for ^{15}N NMR assignments.

Upon confirming by NMR that the compound was successfully synthesised, rudimentary energetic safety tests were undertaken to ensure safe handling. A small sample (less than 5 mg) was placed on a metallic plate within the fume hood behind a blast shield. Wearing Kevlar sleeves, Kevlar gloves under thick leather gloves, and polycarbonate face shield (in addition to standard laboratory PPE such as lab coat and safety glasses), the sample was scratched with a metal spatula to test for sensitivity to friction. At first, slow gentle strokes were applied to the sample, and with no evident changes. The speed and pressure applied were then gradually increased until the sample became too dispersed. The sample was then regrouped and stuck with force by a metal hammer (the metal hammer was secured to a metal rod, allowing further distance between the sample and the operator's gloved hand). With the sample exhibiting no noticeable change, the impact test was repeated five times. The sample failed to exhibit any notable changes. In order to test its sensitivity to heat, the yellow sample was place in an aluminum tray atop a heating plate, and then set to maximum setting. As the sample reached its decomposition temperature, a thin mist was observed leaving the sample as it started turning white. Within very little time, the sample's mass appeared to vanish and all that was left was a very small

dark grey residue. No violent reaction was observed. Assessing that the material was relatively safe to handle, further characterisations were performed.

To supply additional evidence in support of the successful synthesis of H_4ttp, mass spectrometry experiments were conducted. The sample was prepared by dissolving H_4ttp in acetonitrile, with the help of a couple drops of DMF. Using electrospray ionisation, H_4ttp was found to produce positive ions whose indentified species are presented in Table 4.2. The third highest peak, with an ion count of 3944, is that of an H_4ttp and sodium ion species. The second highest peak, with an ion count of 5509, is that of an H_4ttp dimer and sodium ion species. Agglomerated species of H_4ttp as high as of the order of pentamers are identified within the spectrum. Furthermore, all species, with the exception of the pentamer, have a corresponding isotopic peak. These results suggest that H_4ttp is quite stable under MS conditions and that it has strong intermolecular interactions, which likely include hydrogen bonding and π–π interactions.

Table 4.2: Identified species from electrospray ionization mass spectrometry experiments

Species	Peak	Isotopic peak
M + Na	375.01	376.01
Dimer + Na	727.04	728.04
Trimer + Na	1079.06	1080.06
Tetramer + Na	1431.10	1432.10
Pentamer + Na	1784.39	

M = molecule of H_4ttp

The vibrational spectrum of H_4ttp further supports the successful cyclisation of all four nitriles in the TCP precursor. Firstly, the nitrile peak in the vibrational spectrum of TCP at 2252 cm^{-1} is not present in the vibrational spectrum of H_4ttp (Figure 4.1). Moreover, several peaks can be identified as tetrazole peaks: the peaks at 1027 cm^{-1} and 1065 cm^{-1} are

consistent with tetrazole stretching deformation vibrations, the peaks at 1221 cm^{-1} and 1288 cm^{-1} can be identified as of C–N and N–N bond stretching vibrations, the peak at 1414 cm^{-1} is in agreement with known N=N bond stretching vibrations, and the peaks 1538 cm^{-1} and 1556 cm^{-1} are typical of C=C bond stretching vibrations.[68] The broad peak at 3389 cm^{-1} with shoulder at 3498 cm^{-1} is assigned to the tetrazole's N–H stretches.[69] In regards to the pyrazine ring portion of the molecule, the peak at 1185 cm^{-1} is consistent with stretching and/or in-plane bending of the ring, and the peak at 1341 cm^{-1} could also be pyrazine ring stretching; as these peaks are similar to those seen in the TCP spectrum and those seen for 2-chloropyrazine and 2,6-dichloropyrazine.[70] Other peaks associated to the pyrazine ring stretching and or its in-plane bending are 663 cm^{-1} and 782 cm^{-1}, the peak at 1474 cm^{-1} only to ring stretching, and out-of-plane bending is associated to 583 cm^{-1} and 742 cm^{-1}.[70]

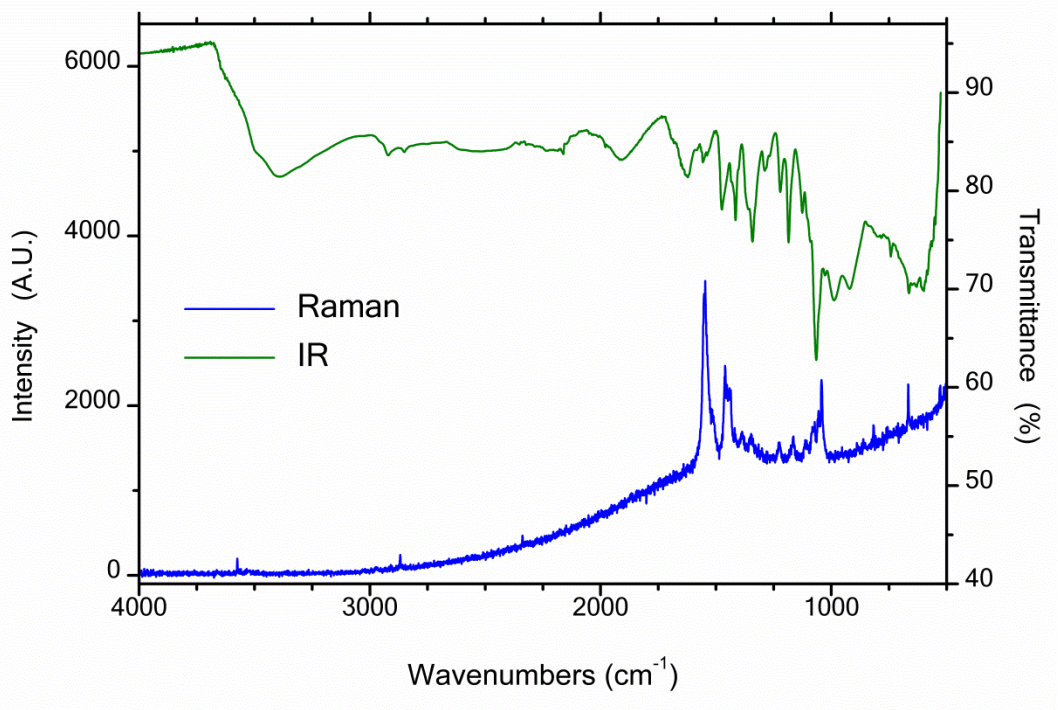

Figure 4.1: Vibrational spectra for H_4ttp. IR spectrum in green and Raman (785 nm) spectrum in blue.

Measuring the Raman spectrum for H_4ttp initially proved to be challenging as it was being obscured by too much fluorescence. As such, the electronic spectrum, followed by its fluorescence spectrum was measured (Figure 4.2). Once the fluorescence profile was identified, a laser of 785 nm was chosen to generate the Raman spectrum.

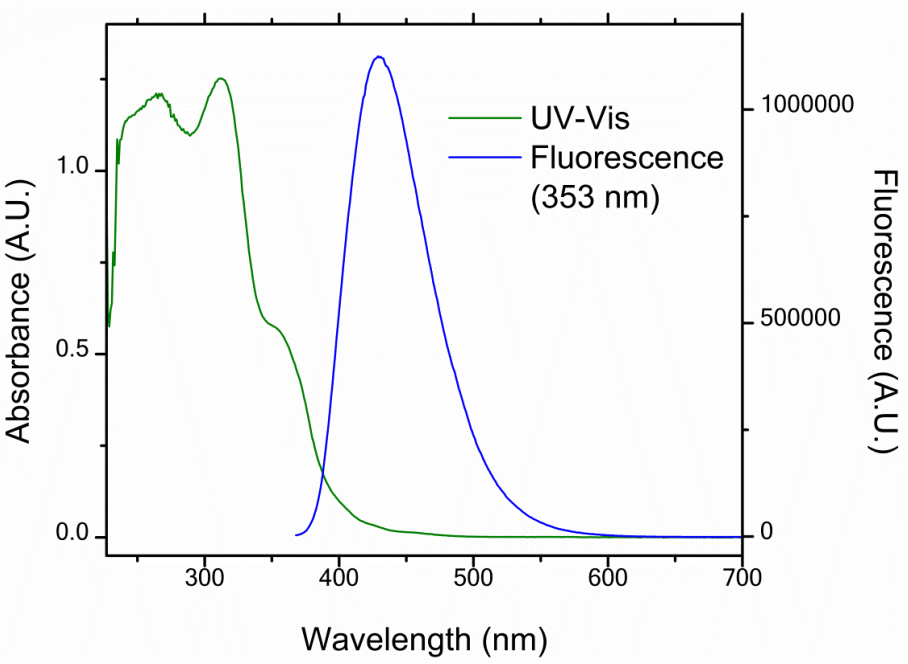

Figure 4.2: Electronic spectrum for a solution of H_4ttp in THF along with its fluorescence when excited at 353 nm.

The electronic spectrum of H_4ttp demonstrates that, like most organic compounds, it absorbs mainly UV light and marginally in the 400-500 nm range. Since the greatest absorption within the visible range occurs at 400 nm (violet), the electronic spectrum is consistent with the yellow appearance observed for H_4ttp. Using the absorption maxima at 353 nm, the fluorescence emission was measured. H_4ttp emits roughly between 375 nm and 575 nm, with a maxima at 429 nm.

Calorimetric experiments were also performed on H_4ttp (Figure 4.3). Both TGA and DSC experiments were performed in air with a heating rate

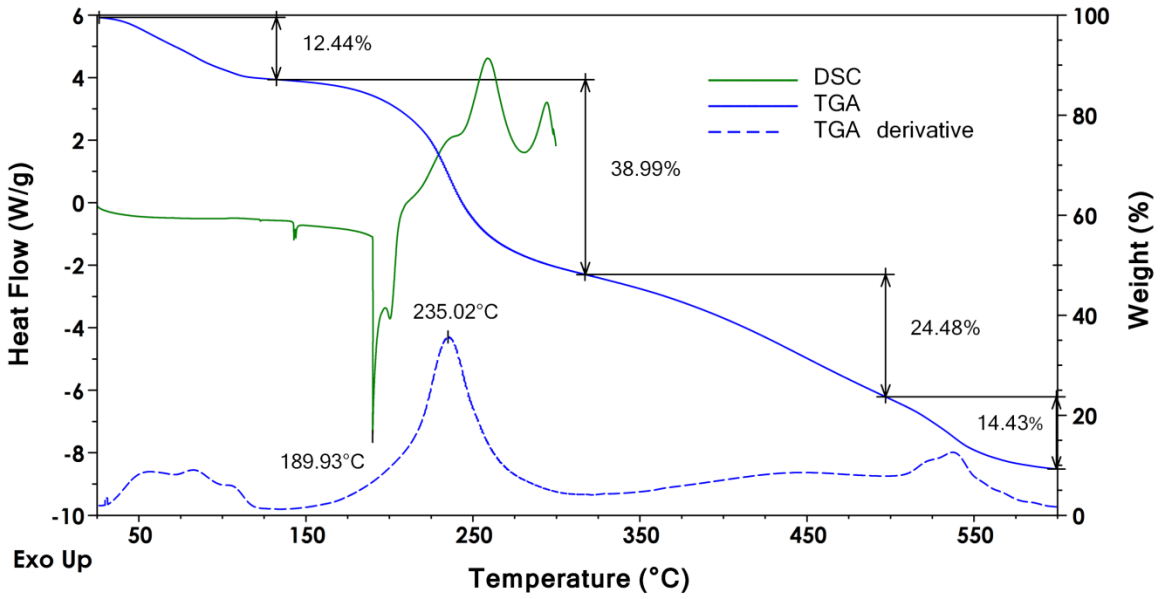

Figure 4.3: DSC and TGA plots of H_4ttp. Experiments were conducted at heating rates of 10 °Cmin^{-1} under oxidizing atmosphere.

of 10 °Cmin^{-1}. The TGA experiment demonstrates four major steps. The first step consists of the evolution of three components (12.44% of total mass) between room temperature and 125 °C. One of those components is thought to be water given that the sample was not dried under high vaccumm, but rather with a piab pump. At around 150 °C, the first decomposition step of the molecule is observed. Assuming that the first 12.44% is considered to be solvent and other impurities (H_4ttp is synthesized at 100 °C and was heated to 150 °C several times without any visual signs of decomposition), the second step accounts for a mass loss of 44.53%. This would accomodate for the loss of one N_2 gas molecule, and three HN_3 molecules; both common decomposition products of tetrazoles. The remaining fragment would have the empirical formula $C_8H_1N_7$. In continuation with the assumtion that the mass loss pertaining to H_4ttp commences at 87.56% of the sample mass, the third step sees a 27.96% mass loss of the molecule. This would be consistent with solely charcoal remaining within the sample. Since this experiment was

performed under air, the last step would be consistent with some of the carbon residue burning.

The pans employed for the DSC experiment were TA hermetically sealed aluminium pans. The first discrepancy between the TGA and DSC experiment is the apparent lack of DSC peak(s) corresponding to the evaporation of water below 125 °C. A small endothermic peak, occurring at 142.84 °C, coincides with the beginning of the decomposition step seen in the TGA thermogram. Integration of this peak gives 4.3 Jg^{-1}, which is most likely due to impurities melting. The second, significantly larger endothermic peak at 189.93 °C integrates to 299.6 Jg^{-1}, and is correlated to the melting point of H_4ttp. Past this point, the thermogram transitions to an exothermic regime which corresponds to the inflection point of the decomposition step in the TGA thermogram. From this it was concluded that H_4ttp decomposes in and around its melting point. It should be noted that the sample pan was recovered significantly distorted. Due to these distortions and the fact that the entirety of H_4ttp's decomposition occurred outside the limits of the hermetically sealed pans, the energy release could not be calculated. As such, the experiment needs to be repeated using TA High Pressure Pans, which would be more resistant to deformation, to determine this important parameter.

Re-crystallisation of the H_4ttp sample that was used to conduct the characterisation presented above was achieved using slow diffusion of diethyl ether into a solution of H_4ttp in DMF. Thin long yellow needles suitable for single crystal x-ray diffraction were obtained (Figure 4.4). As can be seen in the crystal structure representation, the sample was still contaminated with the HCl used for the acidic workup. The acidic proton hydrolysed DMF, creating a dimethylammonium chloride salt (DMACl), whose chloride ions is bound to the terpy-type coordination pocket. Studies have shown that the analogous

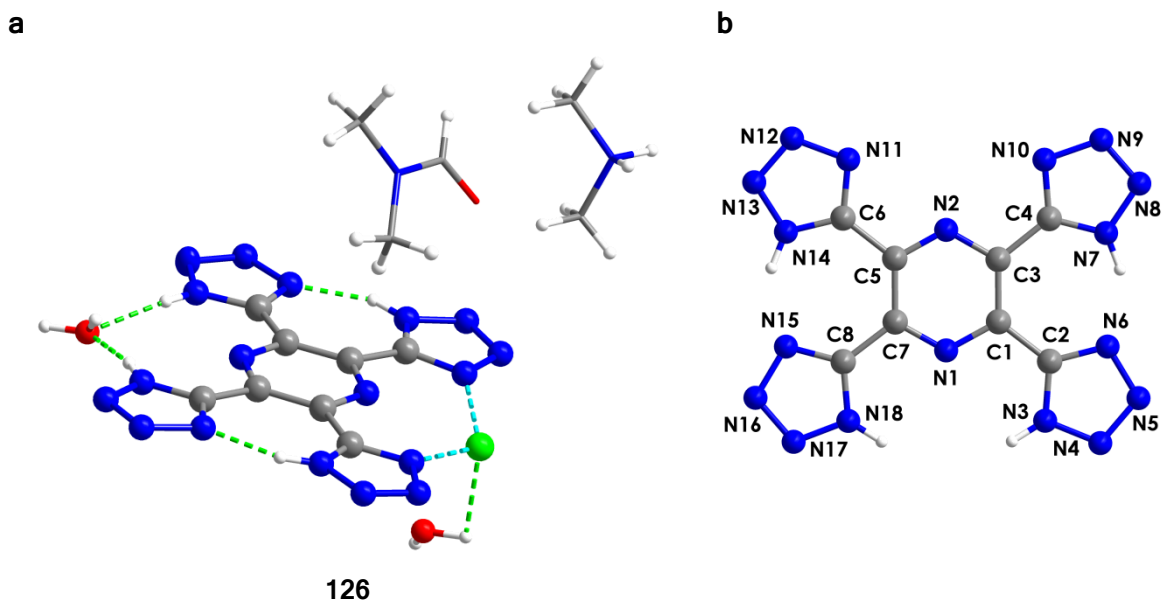

126

Figure 4.4: First crystal structure obtained for re-crystallisation of H_4ttp. a) Co-crystallisation of H_4ttp with dimethylammonium chloride, DMF, and water (H_4ttp·DMACl·2H_2O·DMF, **126**). b) Labelled atoms of H_4ttp. Ball and stick and wire frame representation. Colour code: grey (C), blue (N), red (O), white (H), lime green (Cl). Lime green dashed lines represent hydrogen bonds, while light blue dashed lines represent the tetrazole-chlorine binding affinity.

tetrazole-based coordination pocket, based on pyrrole centers, exhibit a great affinity for binding chloride anions.[42] The solvated co-crystallisation of H_4ttp with DMACl gives crystals with a triclinic crystal system and P–1 space group. H_4ttp molecules pack vertically in slightly staggered columns (Figure 4.5). The columns are separated by DMF and dimethylammonium ions along the *b* axis, while water and chloride ions separate the columns along the *c* axis. The chloride ions act as structural reinforcements for the H_4ttp columns, resulting in Cl–Cl distances within the same column of 6.45 Å. Chloride ions from the neighbouring columns pair up and are 4.40 Å apart. The tetrazole hydrogens are intra-hydrogen bonded to adjacent tetrazoles (1.75 Å, 1.79 Å) and inter-hydrogen bonded to a water molecule (1.93 Å, 2.00 Å). Water molecules are also hydrogen bonded to the chloride ions and DMA ions

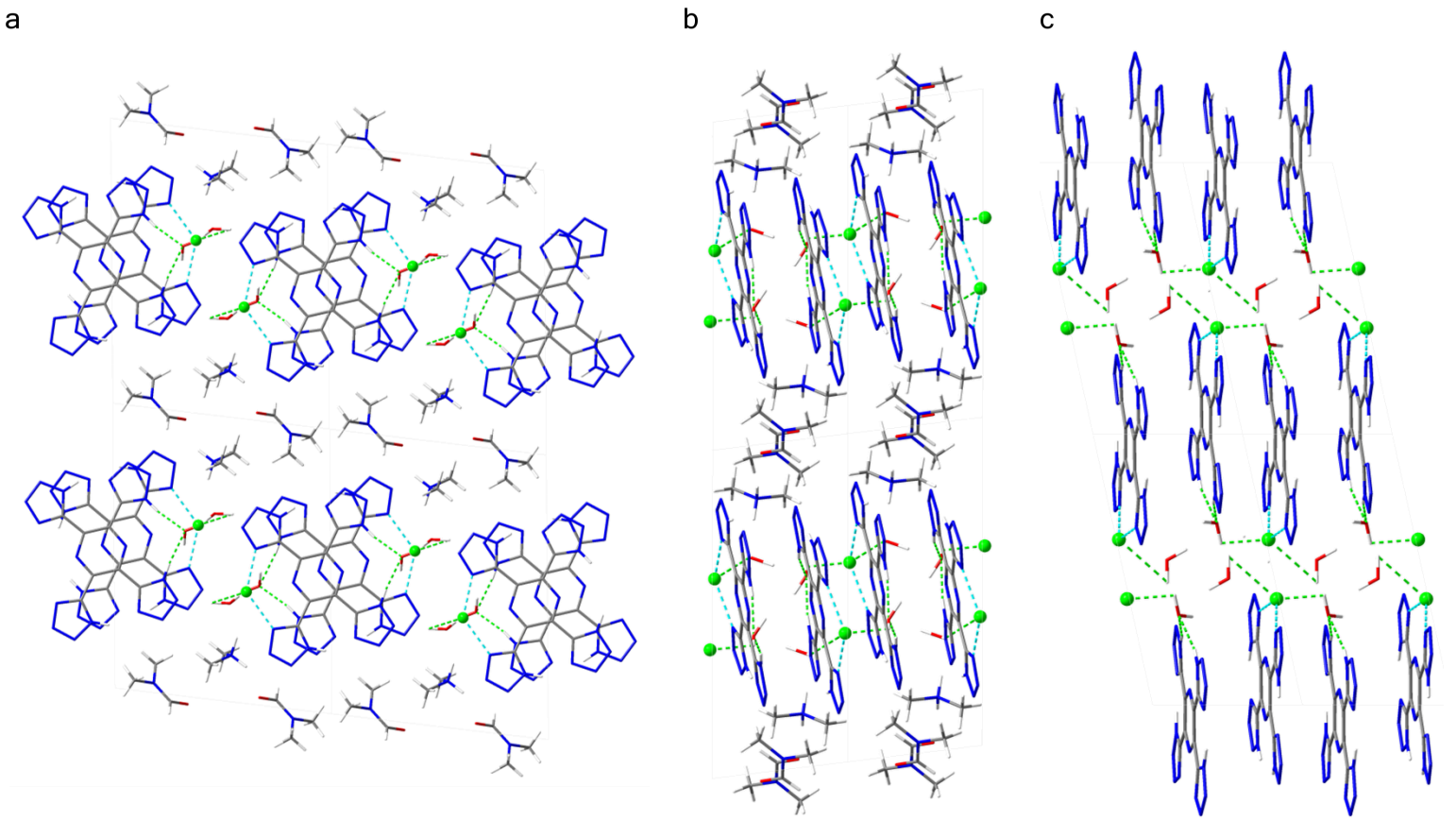

Figure 4.5: Packing for H_4ttp·DMACl·2H_2O·DMF (**126**). a) Viewed along axis *a*. b) Viewed along axis *b*. c) Viewed along axis *c*, with DMF and DMACl removed for clarity. Ball and stick representation for chloride ions and wire frame representation. Colour code: grey (C), blue (N), red (O), white (H), lime green (Cl). Lime green dashed lines represent hydrogen bonds, while light blue dashed lines represent the tetrazole-chlorine binding affinity.

(2.07 Å, 2.87 Å; 1.92 Å). Most remarkably, however, is how flat the H_4ttp molecule lies (Figure 4.6). The planarity of H_4ttp is attributed to the fact that it is comprised of five aromatic rings, providing it with five planar components, and hydrogen bonding between its tetrazole components (intramolecular), in addition to the lattice water molecule and chloride ion (intermolecular).

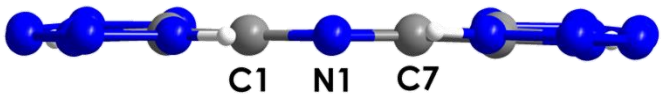

Figure 4.6: View of H_4ttp molecule, from H_4ttp·DMACl·2H_2O·DMF (**126**), along the plane of the pyrazine ring, demonstrating the planarity of the molecule. Ball and stick representation. Colour code: grey (C), blue (N), white (H).

In attempts to remove the DMF molecules and co-crystallised DMACl and isolate pure H_4ttp, crystals of **126** were soaked in ethyl acetate for a week. With unit cell check confirming that the dimensions had changed, a full collection was implemented. Instead of isolating pure H_4ttp, an H_2ttpDMA$_2$ salt was instead obtained (Figure 4.7). A proton was lost on each side of the pyrazine mirror plane of the H_4ttp molecule from **126**. The remaining

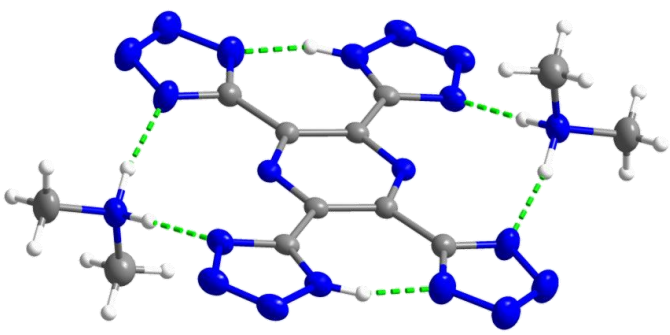

127

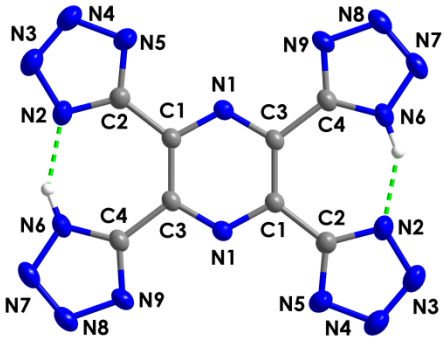

Figure 4.7: Molecular structure of dimethylammonium H_2ttp salt (H_2ttpDMA$_2$, **127**) obtained from soaking crystals of **126** (H_4ttp·DMACl·2H_2O·DMF) in ethyl acetate. Ellipsoid representation with 50%. Colour code: grey (C), blue (N), white (H), lime green dashed lines represent hydrogen bonds.

protonated tetrazoles hydrogen-bond to the deprotonated tetrazoles (1.75 Å). The charge is balanced with two dimethylammonium ions, each facing one of the terpy-type pockets (N1, N5, N9) which are directed by hydrogen-bonding (1.84 Å, 1.85 Å). The loss of two tetrazole protons had little to no effect on the planarity of the H_2ttp ion (Figure 4.8).

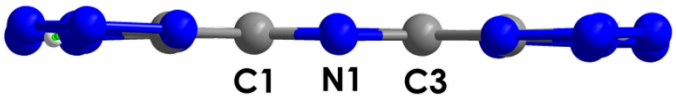

Figure 4.8: View of H_2ttp molecule, from H_2ttpDMA$_2$ (**127**), along the plane of the pyrazine ring, demonstrating the planarity of the molecule. Colour code: grey (C), blue (N), white (H).

Despite having no guest molecules within the crystal lattice, the density of this salt (1.49 gcm^{-3}) is lower than that of **126** (1.57 gcm^{-3}). The decrease in density is due to the herringbone packing pattern induced by the DMA cations (Figure 4.9). All the DMA cations form vertical pillars parallel to the *b* axis, and are arranged in a zigzag pattern (Figure 4.9b). Since one of the DMA ions lies above the plane of the H_2ttp ion, while the other lies below it, the zigzag pattern of the DMA columns creates the herringbone pattern. The shortest distance between parallel H_2ttp ions within the herringbone is 3.23 Å. Given that re-crystallisation failed to provide pure H_4ttp, attention was turned towards other strategies. The first strategy was to sublimate H_4ttp in order to remove the acid impurities. Unfortunately, several attempts, using two different methods: a sublimation apparatus with dry ice cold finger and sublimation tube furnace, were all unsuccessful. The limits of these sublimation attempts consisted of vacuum to the order of 10^{-6} mtorr and heating past H_4ttp's decomposition temperature (as high as 200 °C). The last attempt at sublimating H_4ttp in the tube furnace resulted in an energetic

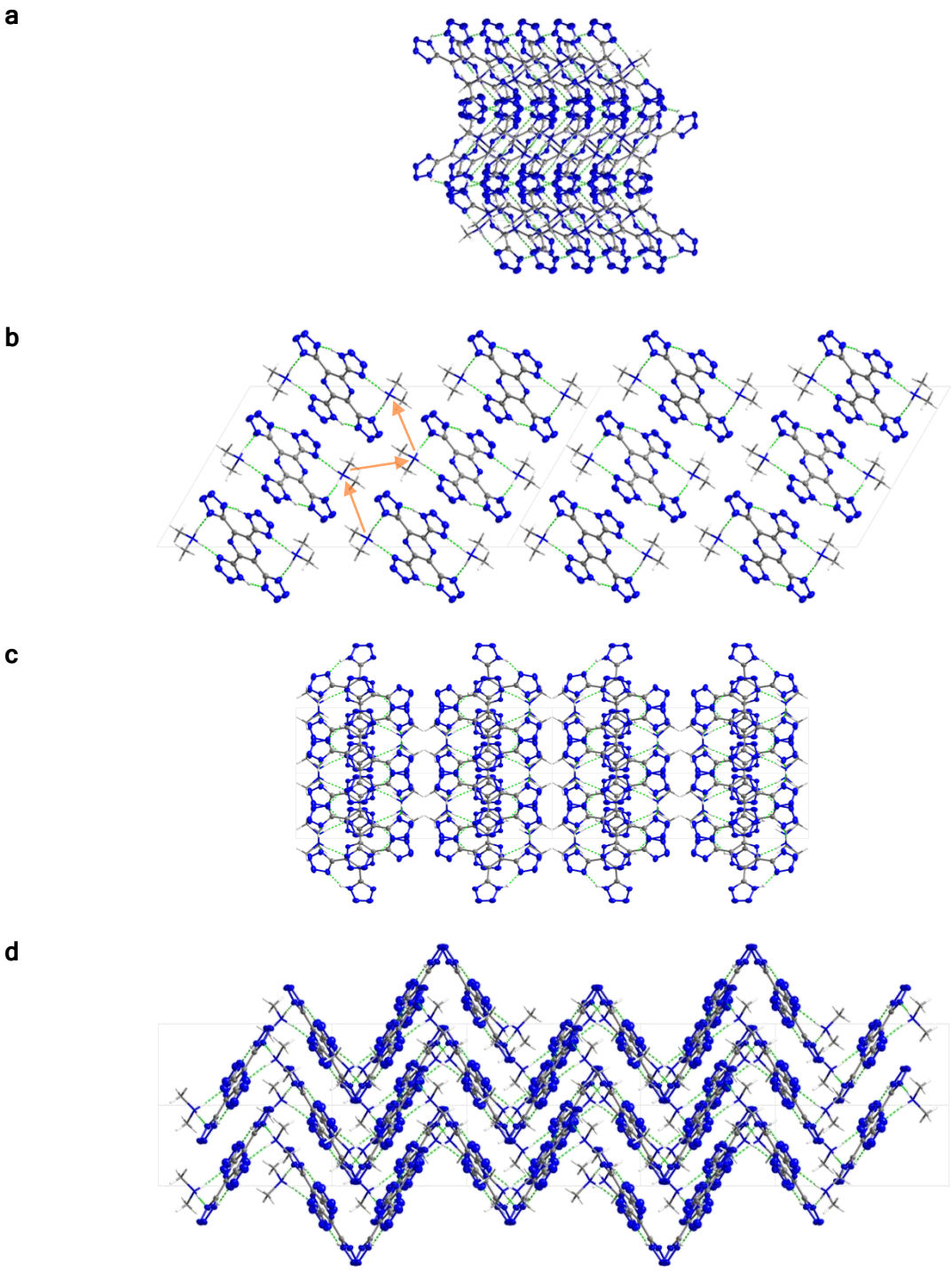

Figure 4.9: Packing for a 2x2x2 cell of H_2ttpDMA$_2$ (**127**). a) Viewed along axis *a*. b) Viewed along axis *b*, with orange arrows outlining zigzag placement of DMA pillars. c) Viewed along axis *c*. d) Viewed along y = 42, x = 0, z = 0 to show herringbone packing pattern. Ellipsoid representation for H_2ttp ions and wire frame representation for DMA ions. Colour code: grey (C), blue (N), white (H), lime green dashed lines represent hydrogen bonds.

event, either deflagration or detonation, which damaged the equipment. The next strategy was to avoid using an acid, for the acidic workup of the synthesis, which would interact with the tetrazole rings once protonated. Firstly, a trial using an organic acid was attempted. Trifluoroacetic acid (TFA) was selected because it is soluble in water, in addition to organic solvents within which H_4ttp is insoluble. Had residual TFA still been present in the sample, it could have been washed out with several organic solvents, leaving H_4ttp untouched. Unfortunately, TFA failed to protonate all the tetrazoles and no product precipitated out of the aqueous workup solution. Attempts to extract the residue proved ineffective and recovery of H_4ttp was only successfully accomplished by addition of concentrated HCl.

Focus was thus turned back towards the use of mineral acids, where HNO_3 was selected. Using HNO_3 rather than HCl for acidic workup was effective at protonating the tetrazoles. It had been thought that the nitrate ion would fail to bind to the tetrazoles as efficiently as the chloride ions. An IR comparison (Figure 4.10) of the residues recovered by both mineral acids shows very miner discrepancies between the two spectra. Two minor peaks in the 2500-3000 cm^{-1} range for the HCl sample, that had not been assigned above, are not visible in the HNO_3 sample, and could correspond to vibrations associated to the hydrochloride salt. A shoulder around 1680 cm^{-1} in the HCl sample becomes a proper peak in the HNO_3 sample. The two peaks 1538 cm^{-1} and 1557 cm^{-1}, assigned to C=C bond stretching, shift slightly and are more resolved in the HNO_3 sample. A broad shoulder between 1360 cm^{-1} and 1380 cm^{-1} becomes a defined peak at 1372 cm^{-1} in the HNO_3 sample. The shoulder at 1140 cm^{-1} becomes more pronounced in the HNO_3 sample. Since no knew peaks corresponding to nitrate ions appear in the HNO_3 sample, one would be lead to imply that no acidic impurities

are present within the sample. Unfortunately, re-crystallisation of HNO_3 generated samples failed to provide single crystals suitable for x-ray analysis.

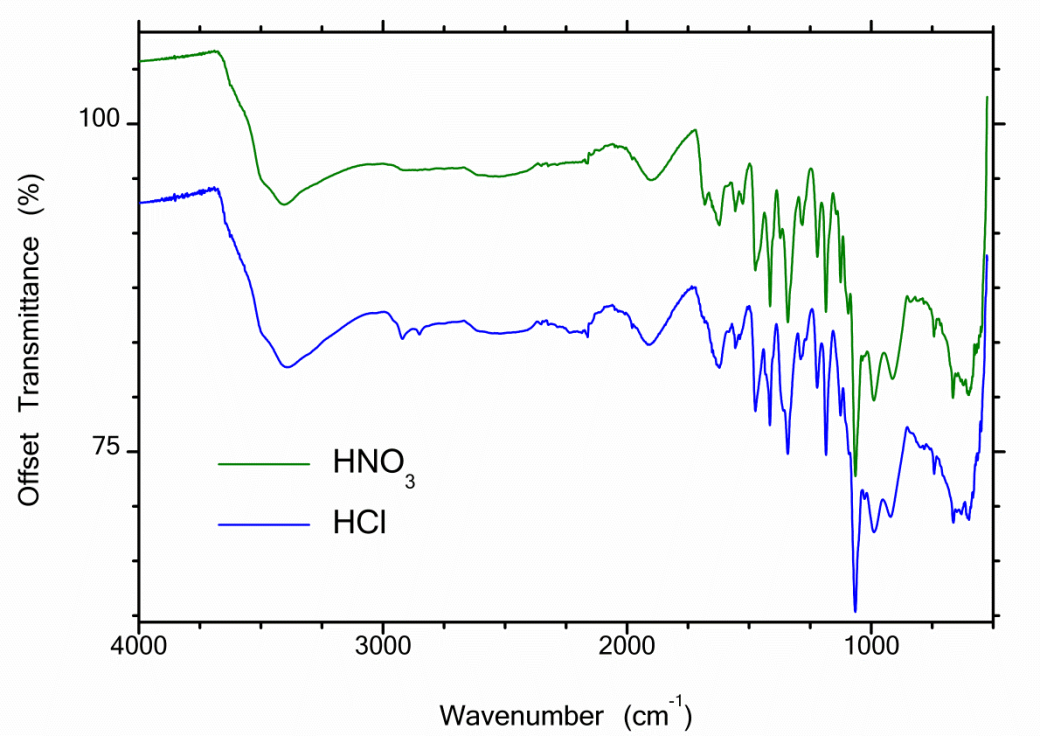

Figure 4.10: IR spectra of H_4ttp samples obtained by both HCl and HNO_3 acidic workups. The HNO_3 plot is offset by 10%.

4.2.2 Synthesis of ttp-based lanthanide complexes

First attempts at coordinating H_4ttp to various first row transition metal nitrates and perchlorates resulted in insoluble powders. Solvent systems consisting of varying ratios of DMF:CH_3CN and DMF:H_2O always resulted in insoluble powders which would crash out immediately. Even when the metal salts and ligand were layered with an additional intermediate layer in thin long test tubes for diffusion reactions, insoluble powders were obtained. Coordination attempts where base was used to deprotonate the ligand, forced the use of aqueous reaction media, as deprotonated ttp^{-4} is only soluble in water. However, even in aqueous media, only insoluble powders were obtained. Since polymeric phases for metal-tetrazole-based materials have been

reported to occur as insoluble polycrystalline powders,[25] it is very likely that this is what these coordination reactions were producing.

Difficulties in obtaining crystals for complexes of H_4ttp led to literature searches for complexes of comparable ligands (Scheme 4.2, page 118).[22-26,28-30,32,33,35] A notable trend for these complexed ligands was the use of solvothermal reactions. Since ligand **122** contains both the pyrazine component and half of the tetrazoles which constitute the H_4ttp ligand, an attempt at reproducing the conditions for the Zn MOF presented by Li *et al.* with H_4ttp was executed.[33] Two solvothermal reactions using $ZnCl_2$ and $Zn(NO_3)_2$ with H_4ttp using the procedure reported by Li *et al.* resulted once again in insoluble powders. Due to difficulties obtaining crystalline complexes using transition metals, which would be more cost effective for energetic applications, focus was turned towards the synthesis of lanthanide complexes. Though these metals would make very expensive energetic materials, complexes exhibiting luminescent or magnetic properties could find other applications.

4.2.2.1 Chain structures

4.2.2.1.1 $[La(H_2O)_8]_n([La(\mu\text{-}\kappa^3ttp)(H_2O)_4]_n)_3 \cdot (8H_2O)_n$

Qiao *et al.* presented uncoordinated Ln salts with ligand **117**,[25] whose structure is comparable to half of H_4ttp. Though this paper focused on the thermal stability of these complexes in reference to their water content (instead of properties, such as energetic performance, luminescence, or magnetism, which are of interest to our group), their synthetic preparation appeared promising. Using a 1:1 ratio of $LaCl_3$ and **117** suspended in water, the reaction mixture was sealed in a Teflon-lined steal bomb and heated to 160 °C for 72h. It was then cooled to room temperature at a rate of 10 °Ch^{-1}. Since this method used water as solvent in addition to a higher and

longer heating time than the procedure of Li *et al.*, this solvothermal reaction seemed a more plausible way to obtain a crystalline complex. Furthermore, it was anticipated that the addition of the terpyridine-type motif in H_4ttp would lead to coordinated ligand.

A suspension of two equivalents of $LaCl_3 \cdot 6H_2O$, one equivalent per pair of tetrazoles, for 15 mg of H_4ttp in 3 mL of distilled water was placed in a 25 mL Teflon bomb and heated according to the described procedure.[25] Upon completion, thin yellow needles suitable for X-ray analysis were recovered within the Teflon bomb. These proved to be an interesting linear chain complex (**128**) which is comprised of three chains of hydrated La^{3+} ions bridged by ttp ligands (Figure 4.11). Each repeating unit of $[La(\mu\text{-}\kappa^3\text{ttp})(H_2O)_4]^{-1}{}_n$ is counter balanced by a solvated $[La(H_2O)_8]^{+3}$ ion. Though the formula of each chain is identical, they are crystallographically unique due to distortions within the La coordination environment (Table 4.3). The coordination environment within all three chains (La1, La2, La3) consists of distorted, to varying degrees, bicapped square antiprism geometry (Figure 4.12). La-N distances range from 2.62 Å to 2.96 Å, with terpy-type coordination pocket bite angles ranging from 115.46° to 116.77°. These Ln-N bond lengths are longer than those generally obtained for tppz complexes.[71] This difference might simply be a result of inherent restriction caused by the 5-membered tetrazole rings with respects to the 6-membered pyridine rings in tppz.

As can be seen from Figure 4.11, The ttp bridging ligands are significantly distorted comparatively to the structures presented for **126** and **127** in all three chains. Although the tetrazoles remain fairly planar, deviations from planarity within the pyrazine rings range from 14.10° for the La1 chain to 9.23° for the La3 chain. Such distortions have been observed, to varying degrees, for the pyrazine core in tppz-based complexes.[5,11,13,14,72-74] In addition

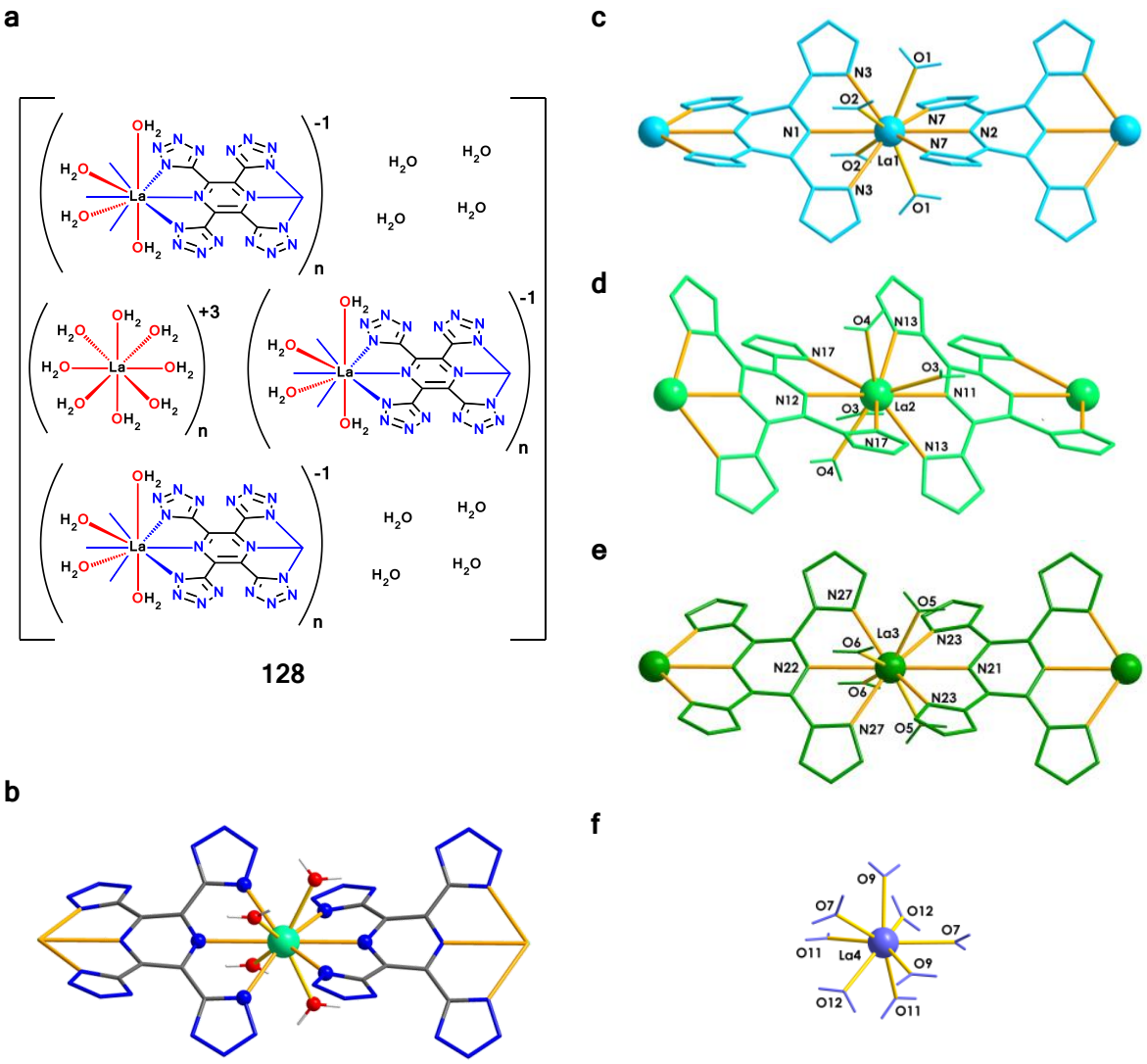

Figure 4.11: a) Diagram illustrating the chemical formula for complex **128**: $[La(H_2O)_8]_n([La(\mu\text{-}\kappa^3ttp)(H_2O)_4]_n)_3 \cdot (8H_2O)_n$. **128** consists of three crystallographically unique chains. The repeating unit within each chain has a charge of –1 and is associated with a solvated Ln^{+3} cation. b) Molecular structure of a chain fragment illustrating the generic lanthanum coordination environment for each chain. Ball and stick representation for coordination environment and wire frame representation for the rest of the fragment. Colour code: grey (C), blue (N), red (O), white (H), spring green (La). c) Labeled molecular structure of La1 chain fragment. d) Labeled molecular structure of La2 chain fragment. e) Labeled molecular structure of La3 chain. f) Labeled molecular structure of La4 solvated Ln^{+3} cation.

to the largest deviation from planarity, La1 chain ttp pyrazine cores have the longest bond lengths (N2–C3 1.31 Å, N1–C1 1.42 Å, C1–C3 1.46 Å) and the

largest difference in bond lengths. Given that the La2 chain has shorter bond lengths overall (N12–C7 1.28 Å, N11–C5 1.33 Å, C5–C7 1.39 Å), the La3 chain has the shortest difference in bond lengths (N22–C11 1.31 Å, N21–C9 1.40 Å, C9–C11 1.41 Å) and is more uniform overall. In addition to having the least distorted pyrazine core, the opposing terpy-type motifs coordinated to La3 are the closest to being planar (N23–La–N27 151.89°).

Table 4.3: Selected distances and angles for complex **128**

	Distances (Å)	**La1** Chain	**La2** Chain	**La3** Chain
La-N Tetrazole	La–N3, La–N13, La–N23	2.78 Å	2.66 Å	2.72 Å
	La–N7, La–N17, La–N27	2.66 Å	2.69 Å	2.62 Å
La-N Pyrazine	La–N1, La–N11, La–N21	2.88 Å	2.86 Å	2.82 Å
	La–N2, La–N12, La–N22	2.90 Å	2.92 Å	2.96 Å
La-OH_2	La–O1, La–O3, La–O5	2.55 Å	2.52 Å	2.55 Å
	La–O2, La–O4, La–O6	2.57 Å	2.59 Å	2.63 Å
Pyrazine	N1–C1, N11–C5, N21–C9	1.42 Å	1.33 Å	1.40 Å
	C1–C3, C5–C7, C9–C11	1.46 Å	1.39 Å	1.41 Å
	N2–C3, N12–C7, N22–C11	1.31 Å	1.28 Å	1.31 Å
	Angles (°)	**La1** Chain	**La2** Chain	**La3** Chain
Tetrazole N-bite	N3–La–N3, N13–La–N13, N23–La–N23	115.46	116.77	115.61
	N7–La–N7, N17–La–N17, N27–La–N27	116.39	116.02	116.52
Water	O1–La–O1, O3–La–O3, O5–La–O5	136.68	131.48	130.57
	O2–La–O2, O4–La–O4, O6–La–O6	126.87	130.40	133.25
Opposing tetrazole Ns	N3–La–N7, N13–La–N17, N23–La–N27	145.54	148.92	151.89
Opposing pyrazine Ns	N1–La–N2, N11–La–N12, N21–La–N22	180.00	180.00	180.00
Pyrazine distortion	C deviation from ring planarity	± 14.10	± 10.79	± 9.23

Deviation from ring planarity was established by first calculating a centroid between the pyrazine nitrogens, and then measuring the angle between opposing carbons within the ring. The value of that angle is subtracted from 180° to give the deviation from ring planarity.

In regards to the solvated La^{3+} ions (La4), La–O distances range from 2.37 Å to 2.62 Å. In addition to the variable La–O distances there is a considerable amount of disorder for the solvated La^{3+} ions (La4) throughout the lattice. The coordination geometry for this cation is best described as a severely distorted square antiprism. The square antiprism geometry has also been reported for solvated La^{3+} ions of complexes with ligand **117**.[24,25]

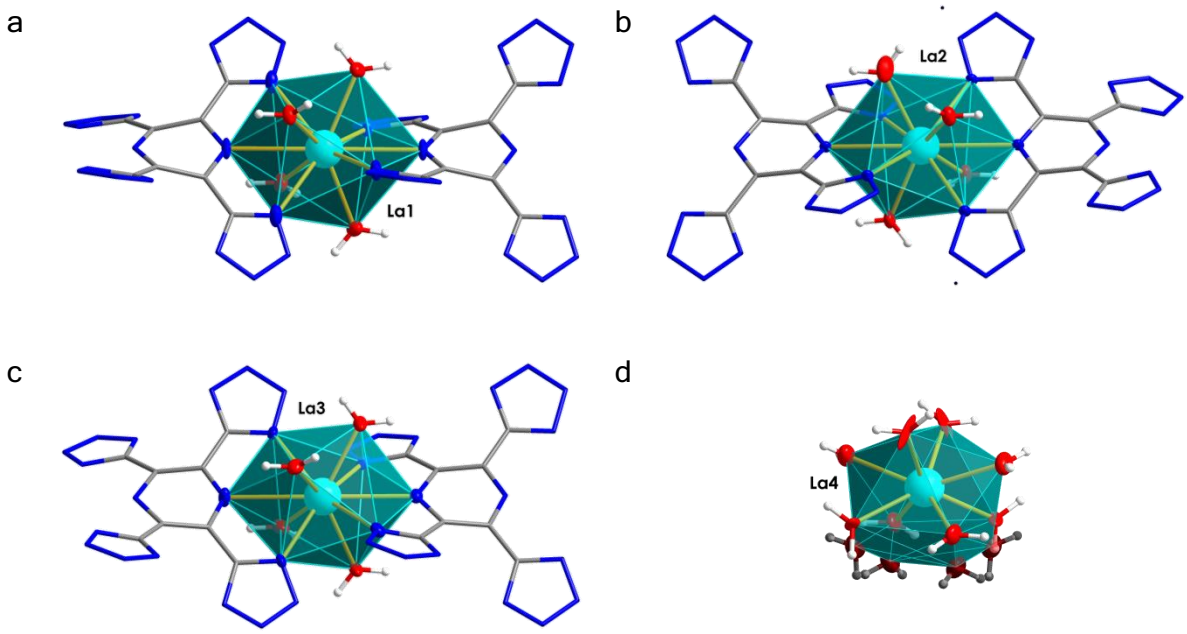

Figure 4.12: Coordination sphere polyhedra for complex **128**. a) coordination environment for La1. b) coordination environment for La2. c) coordination environment for La3. d) coordination environment for La4. Ellipsoid representation at 50% for coordinated atoms, ball and stick representation for the metal center, and wire frame representation for ttp ligand. Colour code: light blue (La), blue (N), red (O), grey (C), white (H).

Complex **128** crystallises in the monoclinic P2 space group. The La4 cations act as pillars around which all three chains align themselves (Figure 4.13). Though all chains run parallel to each other, the orientation of the ttp ligand within La1 chains are arranged pseudo-perpendicularly to the La2 and La3 chains along the *b* axis. La2 chains and La3 chains have the same general ttp ligand orientation, but run in opposite directions of each other, as can be

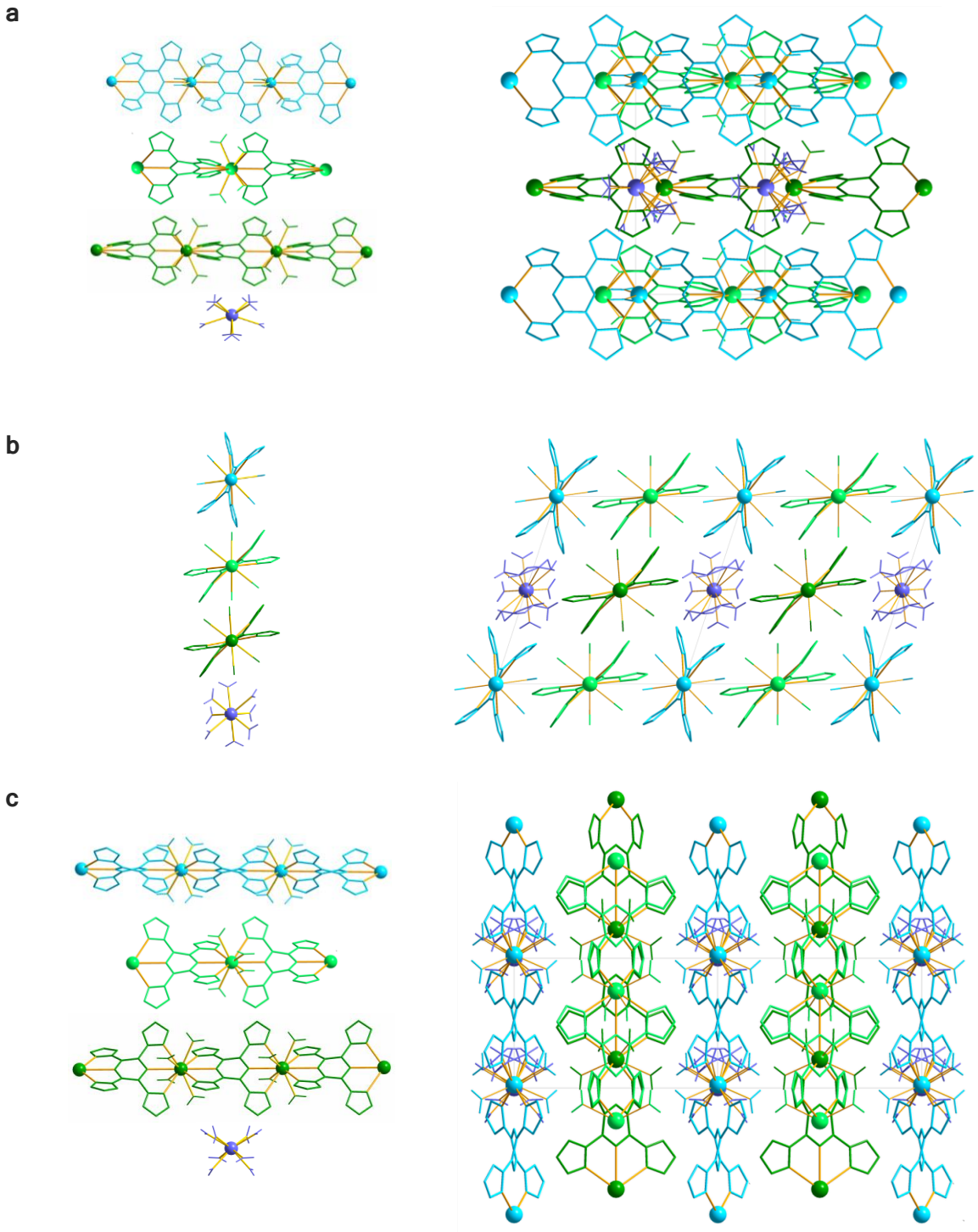

Figure 4.13: Packing for an extended 1x2x1 cell of complex **128**, with individual view of each chain for clarity and lattice water omitted for clarity. a) Viewed along axis *a*. b) Viewed along axis *b*. c) Viewed along axis *c*. Colour code: light blue (La1 chain), spring green (La2 chain), green (La3 chain), purple (La4 counter ion).

seen along the *a* and *c* axes. As a result, complex **128** has a density of 2.07 gcm^{-3}, which is an improvement on the densities obtained for compounds **126** and **127** (1.57 gcm^{-3} and 1.49 gcm^{-3} respectively). Furthermore, it is a significant improvement to the density of the 3D porous framework synthesised with **117** reported by Powell *et al.* (1.69 gcm^{-3}).[24] TGA studies were not undertaken for this complex as it was altered when the mother liquor was soiled during crystal selection and separation. Upon insertion of a rust free hand pick tool into the mother liquor, the solution turned purple around the pick. The pick was quickly removed, but the mother liquor was now a pinkish colour. Crystals were removed from the sample an examined by IR, which confirmed that complex **128** had also reacted and was now a different complex. This occurred before elemental analysis could also be performed.

4.2.2.1.2 $[Gd_2(\mu\text{-}OH)_{2x0.38}(\mu\text{-}HCO_2)_{2x0.62}(\mu\text{-}\kappa^3 ttp)(H_2O)_3]_n$, $[Dy_2(\mu\text{-}OH)_{2x0.65}(\mu\text{-}HCO_2)_{2x0.35}(\mu\text{-}\kappa^3 ttp)(H_2O)_3]_n$

With the procedure developed by Qiao *et al.*[25] proving to be an effective synthetic route in obtaining crystalline complexes for H_4tpp, further reactions with different lanthanide metals were undertaken. In the instance where the Teflon bombs were not washed by the general method (see section 4.3.4), thin yellow plates, whose twinning created rose-shaped clusters, were obtained for the $GdCl_3$ and $DyCl_3{\cdot}6H_2O$ precursors. X-ray diffraction of these plates revealed these complexes to be analogous dinuclear single chains: compounds **129** and **130** (Figure 4.14). Metal centers are bridged by a hydroxide ion to form a dinuclear metal cluster. These are further bridged by a κ^3-ttp ligand, with the remaining coordination sites on the metal centers occupied by three water molecules. As a result, these 8-coordinate metal centers exhibit a geometry that lies between a distorted cube and square

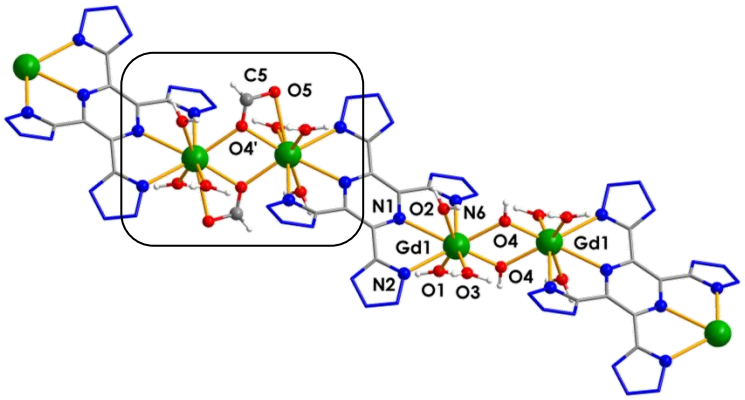

129

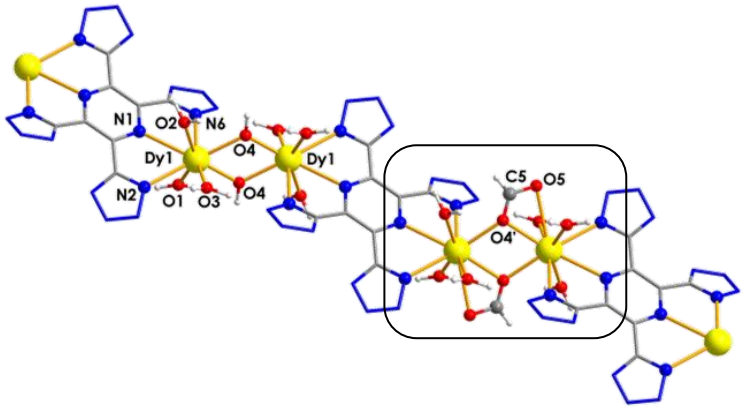

130

Figure 4.14: Labelled molecular structure of chain fragments for analogous dinuclear chain complexes of Gadolinium (**129**) and Dysprosium (**130**). There is a 62% replacement of the hydroxide bridge sites by formate anions for complex **129**, and a 35% replacement of the hydroxide bridge sites by formate anions for complex **130**; as highlighted by the black boxes. Colour code: green (Gd), yellow (Dy), blue (N), red (O), grey (C), white (H).

antiprism (Figure 4.15). Each complex, however, experiences a hydroxide bridge replacement by formate ions; 62% for the gadolinium and 35% for the dysprosium analog. The sites which experience hydroxide bridge replacement are in fact 9-coordinate, in which case the geometry consists of a mixture between a capped cube and a capped square antiprism. The intramolecular distances between hydroxide/formate bridged metal centers are 3.93 Å and 3.86 Å for gadolinium and dysprosium complexes respectively (Table 4.4).

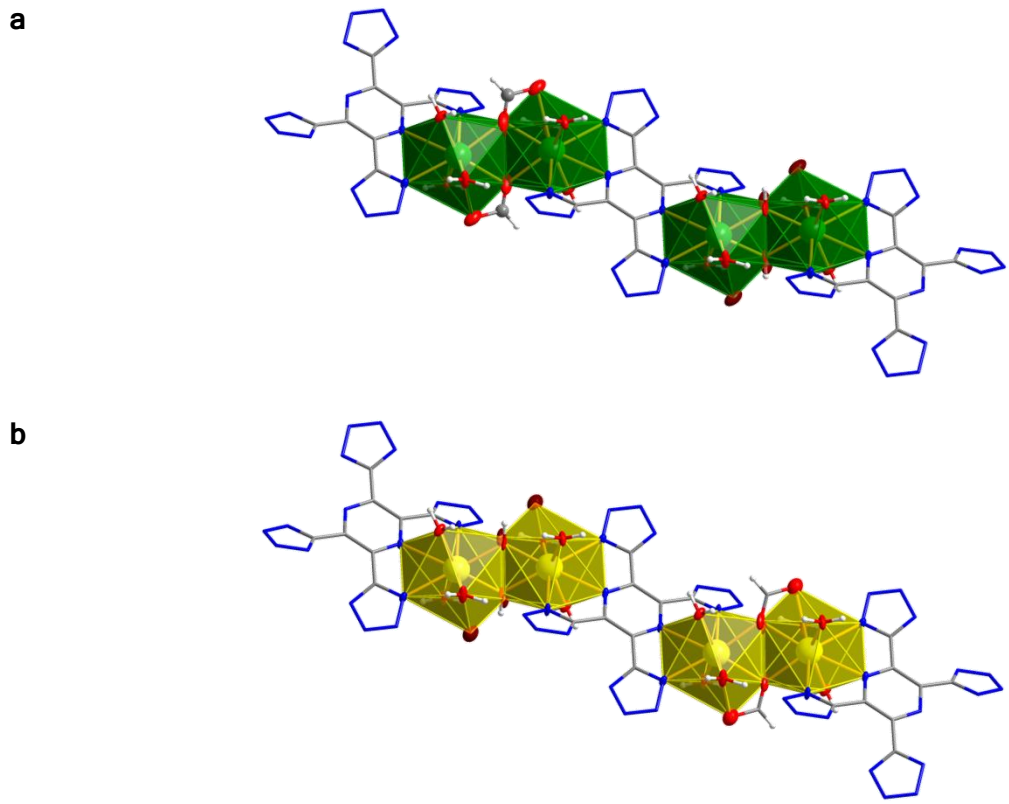

Figure 4.15: Coordination sphere polyhedra for analogous dinuclear chain complexes. a) Coordination sphere for complex **129**. b) Coordination sphere for complex **130**. Wire frame representation for organic ligands, ellipsoid representation (50%) for coordinated atoms, and ball and stick representation for metal centers and hydrogen atoms. Transparent oxygen atoms highlight where formate ions would be located over hydroxide bridge. Colour code: green (Gd), yellow (Dy), blue (N), red (O), grey (C), white (H).

The next closest metal-metal distance is the intermolecular distance between chains: 6.52 Å and 6.52 Å for complexes **129** and **130** respectively. The furthest metal-metal distance occurs through the ttp bridging ligand at 8.15 Å and 8.12 Å for complexes **129** and **130** respectively. This intramolecular distance is longer than the reported bridging distance for dinuclear dysprosium tppz complex reported by Long *et al.* (7.70 Å).[71] A notable trend in regards to distances presented in Table 4.4 is that the gadolinium analogue has longer bond distance than its dysprosium analogue with the exception of three bonds: one of the Ln–water bonds (Ln1–O3), and

Table 4.4: Selected angles for analogous dinuclear chain complexes **129** and **130**

	Angles (°)	**Gd 129**	**Dy 130**
Hydroxide bridge	Ln1–O4–Ln1	118.22	118.06
	O4–Ln1–O4	61.78	61.95
Formate bridge	Ln1–O4'–Ln1	109.42	108.12
	O4'–Ln1–O4'	70.58	71.88
TTP bite angle	N2–Ln1–N6	120.79	121.03
Water	O1–Ln1–O2	146.51	146.53
Tetrazole plane displacement	C2,N2,N3,N4,N5–C2,N2,N3,N4,N5	21.45	21.26
	C4,N6,N7,N8,N9–C4,N6,N7,N8,N9	65.05	56.96
	Distances (Å)	**Gd 129**	**Dy 130**
Ln-N pyrazine	Ln1–N1	2.72	2.71
Ln-N tetrazole	Ln1–N2	2.58	2.56
	Ln1–N6	2.55	2.51
Ln-O water	Ln1–O1	2.35	2.32
	Ln1–O2	2.41	2.33
	Ln1–O3	2.35	2.38
Ln-O hydroxide	Ln1–O4	2.25	2.19
		2.32	2.31
Ln-O formate	Ln1–O4'	2.40	2.32
		2.41	2.45
Bridged metal centers (OH^-)	Ln1–Ln1	3.93	3.86
Bridged metal centers (ttp^{4-})	Ln1–Ln1	8.15	8.12
Between chains	Ln1–Ln1	6.52	6.52
Between chains through pyrazine planes	N1,C1,C3,N1,C1,C3–N1,C1,C3,N1,C1,C3	3.95	3.96
Between chains through tetrazole planes (a ◤)	C2,N2,N3,N4,N5–C2,N2,N3,N4,N5	2.38	2.36
	C4,N6,N7,N8,N9–C4,N6,N7,N8,N9	5.91	5.89
Between chains through tetrazole centroids (c ◤)	C2,N2,N3,N4,N5–C2,N2,N3,N4,N5	6.52	6.52
	C4,N6,N7,N8,N9–C4,N6,N7,N8,N9	6.52	7.03
Parallel displacement of tetrazole (b ◤)	C2,N2,N3,N4,N5–C2,N2,N3,N4,N5	6.07	6.07
	C4,N6,N7,N8,N9–C4,N6,N7,N8,N9	2.75	3.83

◤ refers to the right angle triangle used to characterise parallel-displaced π–π interactions

one of the Ln–hydroxide/formate bridging bonds (Ln1–O4/Ln1–O4'). These longer bond distances are likely due to the fact that Gd^{III} is larger than Dy^{III}, and thus does not fit in the terpy-type pocket as tightly as dysprosium. The shorter Dy–ttp bond lengths also correspond to a wider ttp bite angle, further signifying that the dysprosium ions are closer to the ttp pocket. The cause of this trend could be confirmed by synthesizing another analogue with a smaller lanthanide ion.

The chains pack tightly together, in a slanted grid-like fashion within the triclinic P-1 space group (Figure 4.16 and Figure 4.17). The single chains extend to a 2D network, forming vertical sheets due to hydrogen bonding through the formate bridges. These vertical sheets are further reinforced by possible parallel-displaced π–π interactions between the C2,N2,N3,N4,N5 tetrazoles (2.38 Å with 6.07 Å parallel displacement, and 2.36 Å with 6.07 Å parallel displacement for **129** and **130** respectively) of vertically contiguous chains (d).[75,76] The distances between the pyrazine core of the ttp ligands lie outside of the accepted range for π–π interactions (3.3 – 3.8 Å).[75] Owing to the greater degree of hydroxide bridge replacement for complex **129** (62% versus 35% for **130**), its 2D network is undoubtedly more rigid than its dysprosium analog. The vertical sheets are slightly staggered such that the dinuclear clusters of one sheet are aligned next to the bridging ttp ligand of the sheets to the right and to the left (a).

TGA studies were undertaken for both complexes, for which similar profiles were obtained (Figure 4.18). Complexes **129** and **130** are thermally stable below 100 °C. At around 150 °C, TGA plots indicate that both complexes begin to decompose, with the first decomposition step having a maximum at 230.88 °C and 239.40 °C for **130** and **129** respectively. The lower decomposition temperature of **130** may be attributed to the smaller ratio

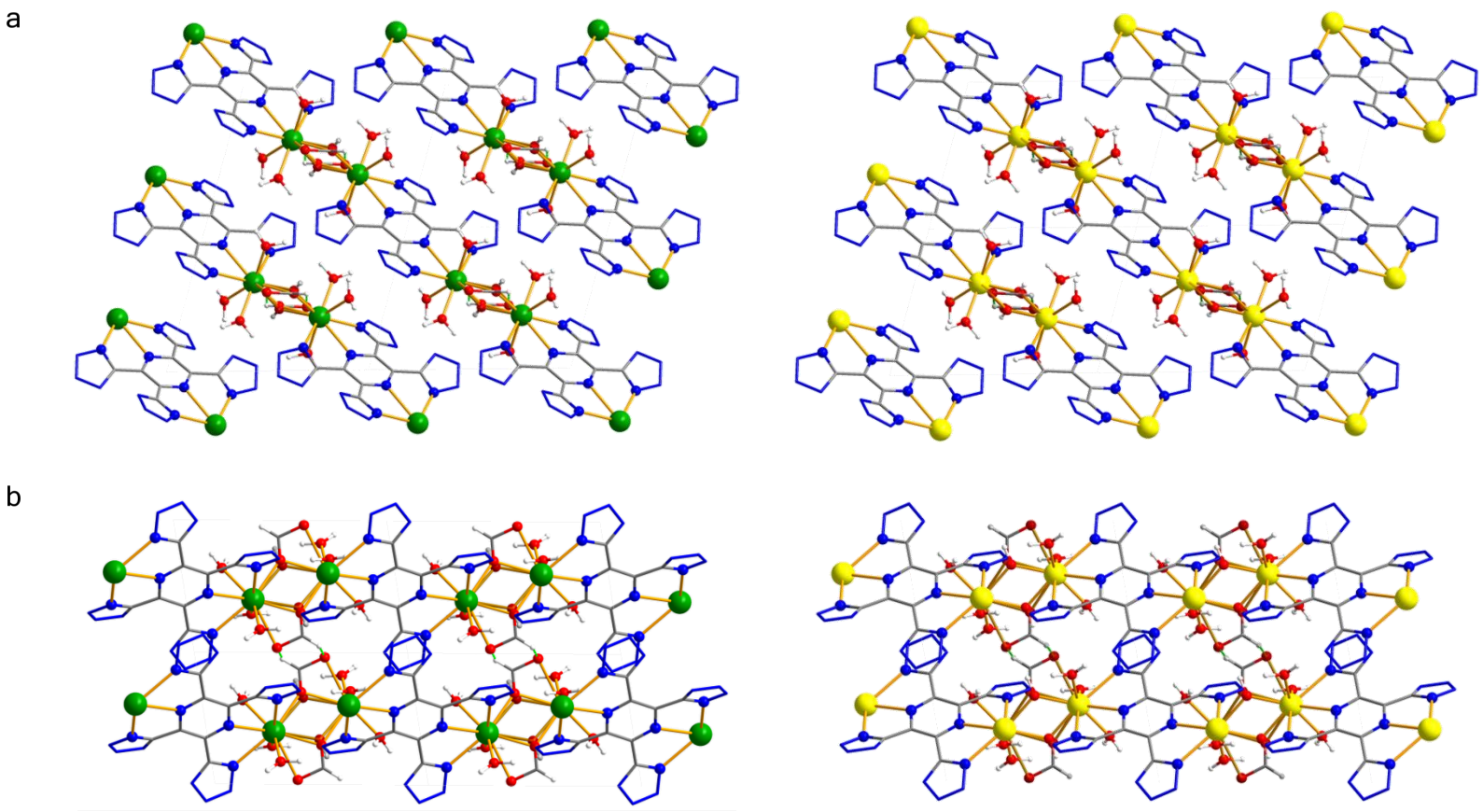

Figure 4.16: Packing for a 2x2x2 cell of complexes **129** (left) and **130** (right). a) Viewed along *a* axis. b) Viewed along *b* axis. Wire frame representation for organic ligands, and ball and stick representation for metal centers, coordinated atoms and hydrogen atoms. The least prominent bridging ions are shown as translucent. Colour code: green (Gd), yellow (Dy), blue (N), red (O), grey (C), white (H), lime green dashed lines represent hydrogen bonds.

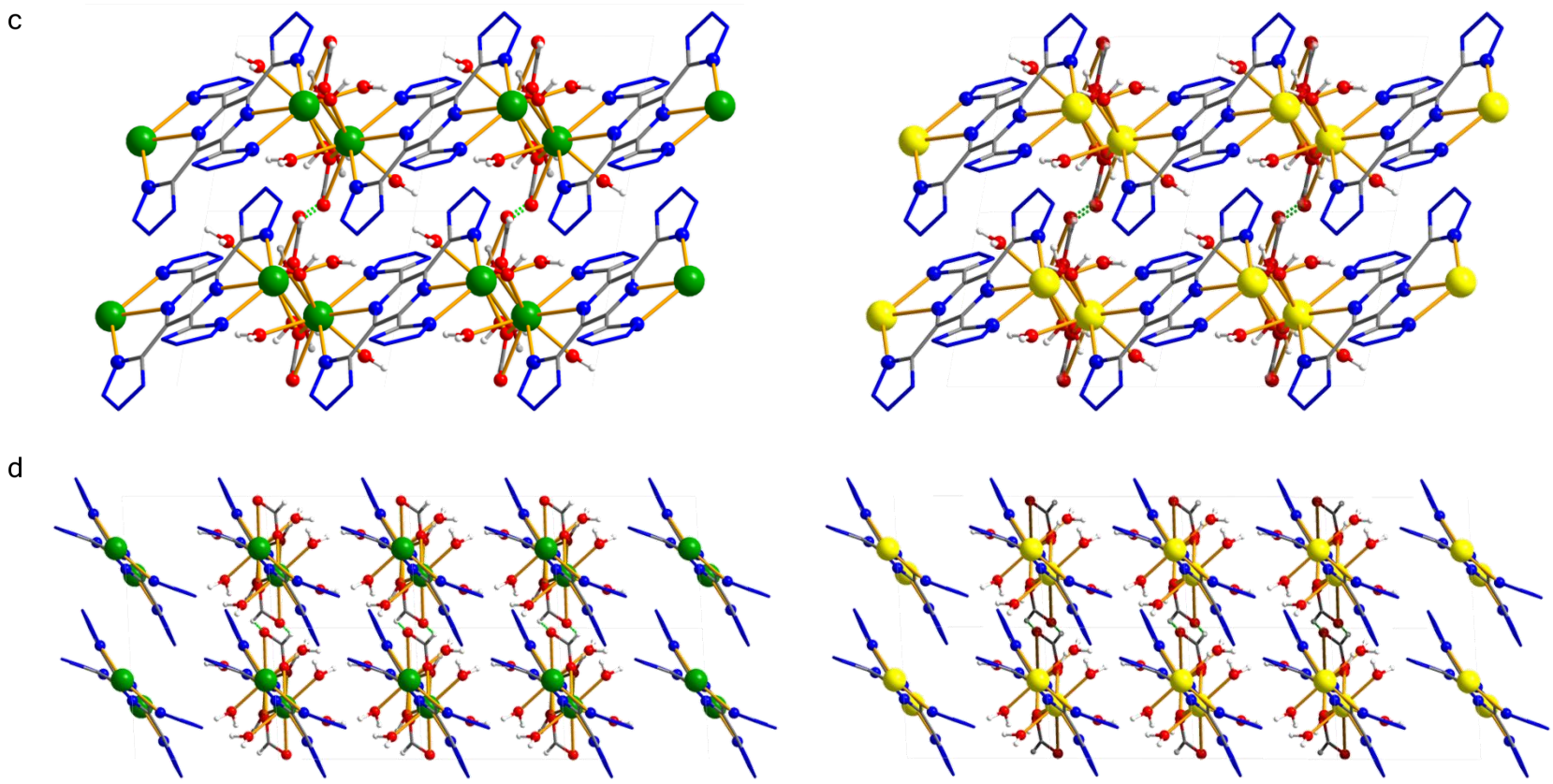

Figure 4.17: Packing for a 2x2x2 cell of complexes **129** (left) and **130** (right). c) Viewed along *c* axis. d) Viewed along x = 154.2, y = 11.9, z = -92.9. Wire frame representation for organic ligands, and ball and stick representation for metal centers, coordinated atoms and hydrogen atoms. The least prominent bridging ions are shown as translucent. Colour code: green (Gd), yellow (Dy), blue (N), red (O), grey (C), white (H), lime green dashed lines represent hydrogen bonds.

of formate bridges within the complex, comparatively to its gadolinium analog, and thus fewer stabilising hydrogen bonds. Though the second decomposition step maxima occur at the same temperature (297 °C), the completion of this step occurs at a higher temperature for **129**. The last step is considerably different for both complexes, with the gadolinium analog having a larger residual percent weight (+ 4.63%) at the end of the experiment. Since **129** has 0.80% more carbon content by weight than **130**, this larger residual weight cannot simply be explained by the additional hydroxide bridge replacement in **129.**

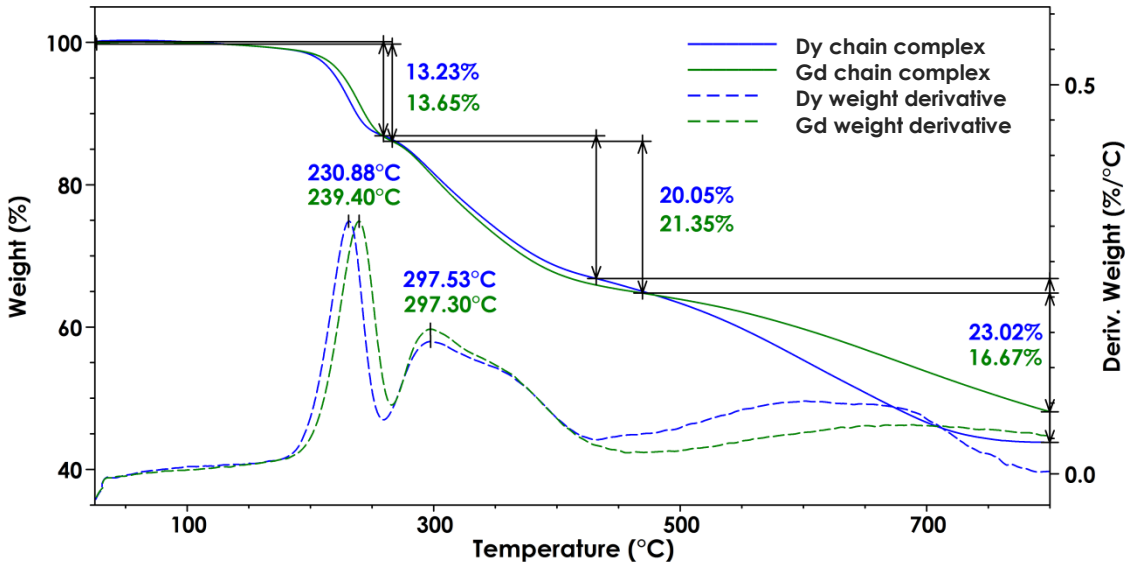

Figure 4.18: TGA plots for complex **129** (green) and **130** (blue). Experiments were conducted at heating rates of 10 °Cmin^{-1} under a nitrogen atmosphere. The samples sizes were 1.02 mg and 0.93 mg for complex **129** and **130** respectively.

4.2.2.2 Monomeric structures

4.2.2.2.1 [La(κ^{2}H$_2$ttp)(H$_2$O)$_7$] (H$_3$ttp) · 7H$_2$O

Since the scale used to synthesise complex **128** was fairly small and the synthesis requires four days including the cooling time, an attempt at doubling the scale (twice as many reactants, same Teflon bombs) was

executed, so as to provide more sample for analyses. Not surprisingly, as solvothermal reactions tend to be very sensitive to the reaction conditions, this lead to the synthesis of thin yellow plates rather than the yellow needles of **128**. X-ray diffraction of these plates revealed this compound to be the mononuclear salt $[La(\kappa^2H_2ttp)(H_2O)_7](H_3ttp)\cdot 7H_2O$ (**131**) (Figure 4.19). Unlike complexes **128**, **129**, and **130**, the coordinated H_2ttp ligand is only bound to the metal center by its tetrazoles. Comparatively to the other coordinated atoms, the pyrazine distance (La1–N1 3.12 Å) is too long to be considered a bond (Table 4.5). As a result, the planarity of the coordinated H_2ttp ligand is more comparable to compounds **126** and **127**, and lacks the distortions observed for complexes **128**, **129**, and **130**. Though terpy is generally a tridentate ligand (κ^3) there are documented examples of bidentate (κ^2) terpy complexes.[77] These κ^2 complexes occur when there are discrepancies between the geometries of the metal center and the ligand, and thus a compromise of the optimal geometry of both components is established.[77] It is therefore probable that the ttp ligand will display similar behaviour. The H_3ttp^{1-} counter ion is also quite planar, though one of the tetrazoles is slightly tilted up to form a hydrogen bond with the closest lattice water molecule.

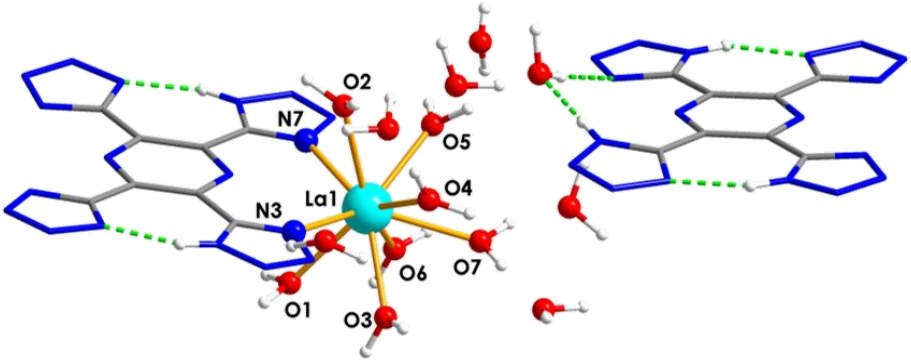

131

Figure 4.19: Labelled molecular structure of complex **131**. Colour code: light blue (Ln), blue (N), red (O), grey (C), white (H), lime green dashed lines represent hydrogen bonds.

Complex **131** is thus comprised of a 9-coordinate coordination sphere, whose geometry consists of a slightly distorted capped square antiprism (Figure 4.20). The complex exhibits longer La–N bonds comparatively to the La–O bonds at the base of the antiprism. Additionally, the cap is tilted slightly towards O3 (66.71°) and O4 (64.54°) rather than being centered between O3 and O5 at 67.60°, as well as O4 and O6 at 66.29°. The tip of the cap is also pointed 0.65° away from the plane of the H_2ttp ligand. This is most likely a result of the metal center lying 0.36° either above or below the plane of the H_2ttp ligand; depending on the orientation of the cation in the packing structure (Figure 4.21).

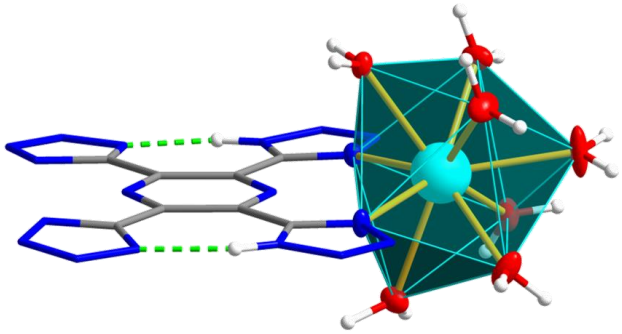

Figure 4.20: Coordination sphere polyhedra for complex **131**. Wire frame representation for organic ligands, ellipsoid representation (50%) for coordinated atoms, and ball and stick representation for the metal center and hydrogen atoms. Colour code: light blue (Ln), blue (N), red (O), grey (C), white (H), lime green dashed lines represent hydrogen bonds.

Complex **131** crystallises in the monoclinic $P2_1/c$ space group. The $[La(H_2ttp)(H_2O)_7]^+$ cations and H_3ttp^- anions are arranged in alternating vertical pillars along the *b* axis, with lattice water in between the cationic and anionic pillars. The cationic pillars are stacked with the H_2ttp ligands in the center and the orientation of the hydrated lanthanums alternating from one anionic pillar to the other. The H_3ttp^- ions in the anionic pillars are slanted with respects to the H_2ttp ligands and exhibit a slight staggering. In observing

Table 4.5: Selected angles for complex **131**

	Angles (°)	**131**
TTP bite angle	N3–La1–N7	108.69
	O1–La1–O2	76.23
	O3–La1–O5	135.20
Water	O4–La1–O6	132.58
	O3–La1–O7	66.71
	O4–La1–O7	64.54
Pyrazine plane displacement for H_3ttp anion	N19,C9,C11,N20,C15,C13–N19,C9,C11,N20,C15,C13	30.8 13.0
Pyrazine plane displacement for coordinated H_2ttp	N1,C1,C5,N2,C7,C3–N1,C1,C5,N2,C7,C3	53.9 13.8
	Distances (Å)	**131**
Ln-N pyrazine	La1–N1	3.12
Ln-N tetrazole	La1–N3	2.69
	La1–N7	2.71
Ln-O water	La1–O1	2.55
	La1–O2	2.63
	La1–O3	2.52
	La1–O4	2.58
	La1–O5	2.52
	La1–O6	2.54
	La1–O7	2.58
Between pyrazine planes for H_3ttp anion (a ◤)	N19,C9,C11,N20,C15,C13–N19,C9,C11,N20,C15,C13	3.2[a] 3.1[b]
Between pyrazine centroids for H_3ttp anion (c ◤)	N19,C9,C11,N20,C15,C13–N19,C9,C11,N20,C15,C13	4.47[a] 6.54[b]
Parallel displacement of pyrazine for H_3ttp anion (b ◤)	N19,C9,C11,N20,C15,C13–N19,C9,C11,N20,C15,C13	3.1[a] 5.7[b]
Between pyrazine planes for coordinated H_2ttp (a ◤)	N1,C1,C5,N2,C7,C3–N1,C1,C5,N2,C7,C3	3.2[a] 3.2[b]
Between pyrazine centroids for coordinated H_2ttp (c ◤)	N1,C1,C5,N2,C7,C3–N1,C1,C5,N2,C7,C3	3.56[a] 6.54[b]
Parallel displacement of pyrazine for coordinated H_2ttp (b ◤)	N1,C1,C5,N2,C7,C3–N1,C1,C5,N2,C7,C3	1.6[a] 5.7[b]

◤ refers to the right angle triangle used to characterise parallel-displaced π–π interactions
[a] measurements taken between AB H_3ttp planes or AB and CD H_2ttp planes.
[b] measurements taken between AA and BB H_3ttp planes or AD and BC H_2ttp planes.
See **Error! Reference source not found.** for clarification.

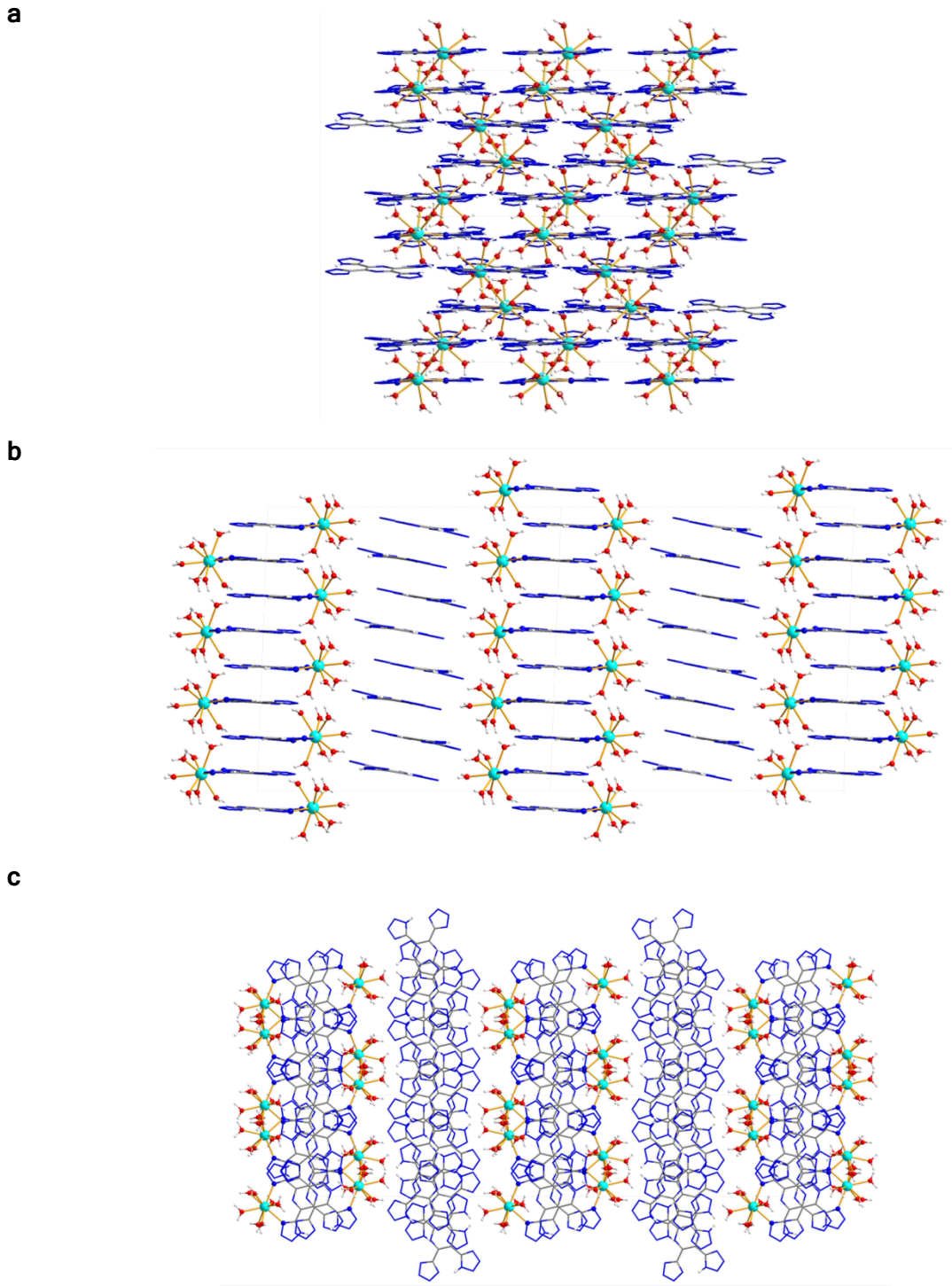

Figure 4.21: Packing for a 2x2x2 cell of complex **131**, with lattice water omitted for clarity. a) Viewed along axis *a*. b) Viewed along axis *b*. c) Viewed along axis *c*. Wire frame representation for organic ligands, and ball and stick representation for coordinated atoms, for metal centers and hydrogen atoms. Colour code: light blue (La), blue (N), red (O), grey (C), white (H).

the packing from the *a* and *c* axes, one can clearing see that both cationic and anionic pillars are layers, staggered in these directions. This packing pattern is similar to that of the $[Ln(H_2O)_x](m\text{-}BDTH)_3{\cdot}9(H_2O)$ (where Ln = Y, La, Pr, Gd, Ho, Er, Yb, or Lu, x = 8 or 9, and *m*-BDTH = 1,3-benzeneditetrazol-5-yl, ligand **117**) complexes obtained by Qiao *et al.*,[25] as well as by Powell *et al.*.[24] Unlike their complexes, however, in **131** the tpp ligand is bound to the hydrated metal center.

Another similarity between **131** and the published complexes by Qiao *et al.*[25] and Powell *et al.*[24] is the extensive hydrogen bonding and π–π interactions which makes **131** a 3D framework. While Powell *et al.*'s $[Pr(H_2O)_n](m\text{-}BDTH)_3{\cdot}9(H_2O)$ exhibited hydrogen bonding in the form of helices and cyclic pentamers between the $[Pr(H_2O)_9]^{3+}$ pillars, complex **131** appears to only exhibit helices which run parallel to the *c* axis (Figure 4.22).[24] When the H_2ttp ligand is taken into account, even more hydrogen bonding motifs are present, further reinforcing the pillars.

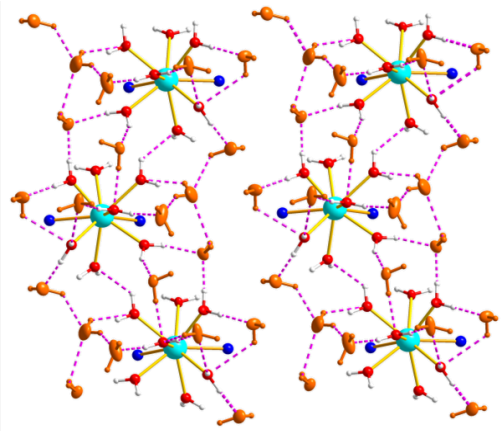

Figure 4.22: Hydrogen bonding between lattice water and cationic pillars of $[La(H_2ttp)(H_2O)_6]^+$ viewed along cell axis *a*. H_2ttp ligands are omitted for clarity, though the coordinated N atoms remain. The counter-anionic ligands are stacked in pillars in front and behind the La ions. Colour code: light blue (La), blue (N), red (O), grey (C), white (H), orange (lattice water in complex **131**). To be compared with the hydrogen bonding between lattice water and $[Pr(H_2O)_9]^{3+}$ pillars in $[Pr(H_2O)_n](m\text{-}BDTH)_3{\cdot}9(H_2O)$ viewed by cell axis *c* as presented by Powell *et al.*[24]

In examining **131** for π–π interactions, four distinctive parallel-displaced interactions are identified (Figure 4.23); two within both cationic and anionic pillars. The anionic pillars consist of two alternating layers of a AABBAA motif; wherein A (light blue) and B (turquoise) refer to the orientation of the H_3ttp^- anions. Since each anion was slightly slanted with respects to the anions in the layer below it, measuring the distance between planes for individual anions could not be achieved, as the planes were not parallel. Thus the planes were calculated using the average of three anions to establish the distance between the layers. Distances between the H_3ttp^- planes of the same orientation (AA or BB) were found to be 3.2 Å, while distances between planes of opposite orientation (AB) were found to be 3.1 Å. These distances are below the interplanar distances generally reported (3.3–3.8 Å),[75] though on par with what was reported by Powell *et al.* (3.26 Å).[24] Between AB planes, the H_3ttp^- anions are equally staggered, with a displacement angle of 13.0° and parallel displacement of 5.7 Å. However, H_3ttp^- anions are not evenly staggered between AA and BB planes and only one pair has parameters that fall within the excepted range: the pairs which have a displacement angle of 30.8° and parallel displacement of 3.1 Å (the pairs with centroid distances of 9.76 Å do not qualify).

The cationic pillars consist of four alternating layers conforming to the ABCDABCD motif; wherein AB (light blue) and CD (turquoise) refer to the orientation of the coordinated H_2ttp, and each letter differentiates between the orientations of the metal centers. Similar to the AB planes for the H_3ttp^- anions, the AD and BC planes for H_2ttp ligand are also equally staggered, with a displacement angle of 13.8° and parallel displacement of 5.7 Å. Between AB and CD planes, the H_2ttp ligands are not equally staggered. While one pair has a interplanar distance, centroid-centroid distance and

parallel displacement which all fit well within the normal ranges for π–π interactions (3.2 Å, 3.56 Å, and 1.6 Å respectively), its displacement angle of 53.9° lies outside the average range (16–40°).[75] This angle is, however, below the highest reported (60°).[75] As a result of the π–π interactions throughout both the anionic pillars and cationic pillars parallel to the *c* axis, and the hydrogen bonding parallel to the *c* axis and *a* axes, complex **131** does effectively form a 3D framework.

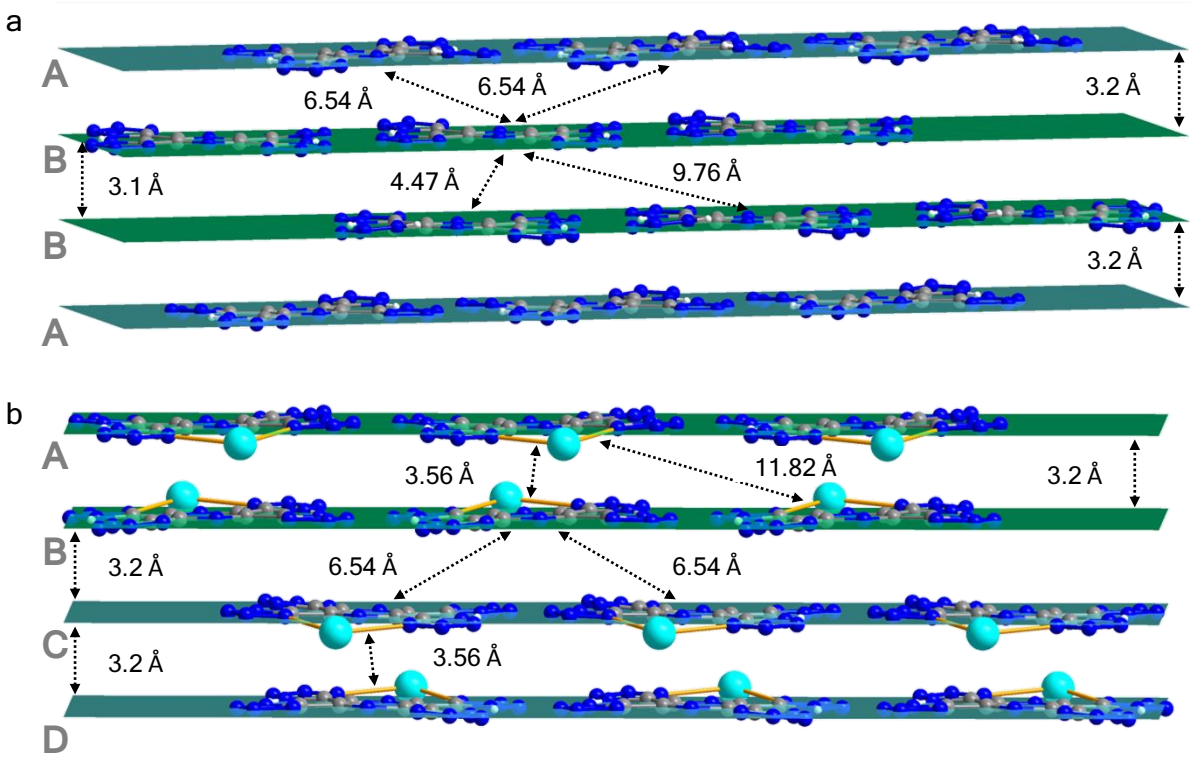

Figure 4.23: Distances used to determine π–π interactions in complex **131**. a) H_3ttp^- counter-ion layers. Colour code planes: light blue (A), turquoise (B). b) Coordinated H_2ttp ligand layers. Colour code planes: light blue (AB), turquoise (CD). Planes are coloured to indicate differences in orientation of H_3ttp^- counter ions and coordinated H_2ttp ligand. Ball and stick representation for all atoms. Colour code: light blue (Ln), blue (N), red (O), grey (C), white (H).

A TGA experiment, conducted under a nitrogen atmosphere, was performed for this complex (Figure 4.24). In comparing this TGA curve with those presented by Qiao *et al.*,[25] one can observe that the profiles for

$[Ln(H_2O_8](m\text{-}BDTH)_3 \cdot 9H_2O$ (where Ln = Lu, Yb, Er, Ho, and Y) are quite similar to **131**. Lattice and coordinated water molecules are lost below 200 °C. The mass loss from the three first steps (7.60%, 2.15%, and 8.30%) accounts for 78% of the water content within the complex. This suggests that three water molecules are still present. Qiao *et al.* had found through TGA and PXRD of the residues that their Ln^{III} metal centers were only partially dehydrated and that two water molecules remained bound to the metal centers.[25] Past 200 °C, the ttp molecules begin to decompose, with the first major decomposition step having a maximum at 250.68 °C, and continuing to just past 400 °C. The last decomposition step is much broader and appears to consist of several steps. The last two steps are consistent with the decomposition steps previously seen for ttp (Figure 4.3, Figure 4.18).

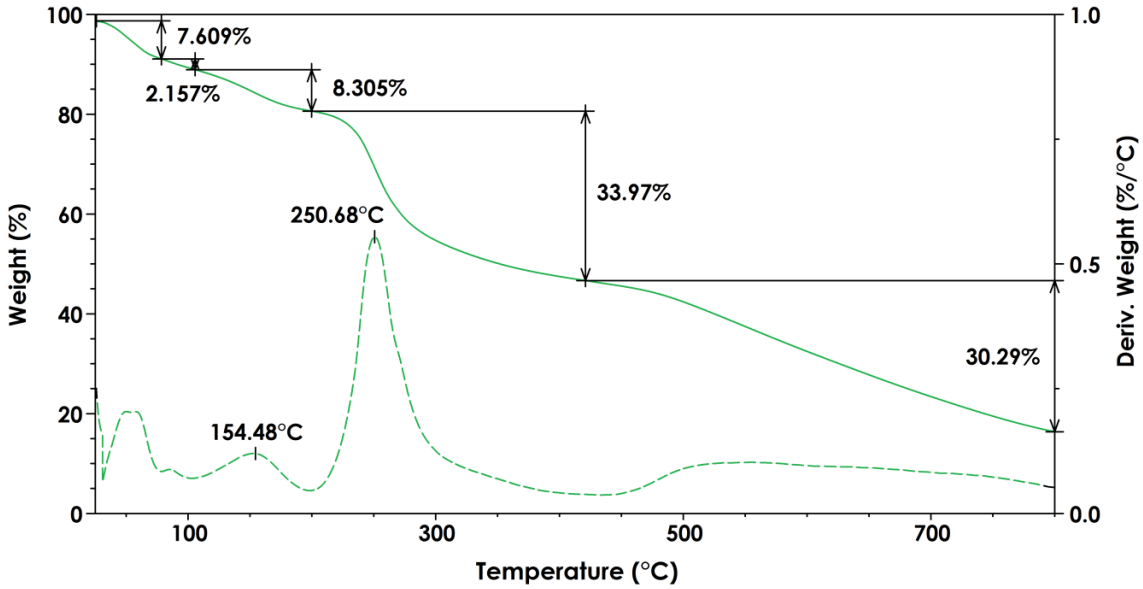

Figure 4.24: TGA plot for complex **131**. The experiment was conducted at a heating rate of 10 °Cmin^{-1} under a nitrogen atmosphere with a samples size of 3.268 mg.

4.2.2.2.2 Polymorphic mononuclear complexes $[Ln(\kappa^3H_2ttp)(H_2O)_6]_2$ $(H_2ttp)\cdot 12H_2O$, Ln = Gd, Dy, Er

Repeating the procedure used to synthesise **128** with the corresponding Gd, Dy and Er salts resulted in the growth of thin yellow plates suitable for x-ray diffraction: complexes **132**, **133**, and **134** for Gd, Dy and Er respectively. Unlike the chain structure of **128**, these complexes are mononuclear salts. Furthermore, these complexes did not adopt the bidentate coordination mode of the mononuclear **131**. Instead the tridentate coordination mode observed in all three chain complexes is present. Crystal structures of these compounds revealed sets of two hydrated lanthanide ions, each bound to one doubly deprotonated H_2ttp ligand, with a corresponding H_2ttp counter anion to balance the charge (Figure 4.25). All three complexes are triclinic and crystallise in the P-1 space group. These complexes are all isostructural, though the gadolinium analogue (**132**) experiences a higher degree of disorder. This disorder resulted in a doubled unit cell and identifying two spectroscopically unique metal centers in order to obtain a better fit (Figure 4.26).

All polymorphic analogs are 9-coordinate and exhibit distorted capped square antiprismatic geometry, with the planarity of the pseudo square bases differing by 6.45°, 1.94°, 2.85°, and 2.92° for Gd1, Gd2, Dy, and Er respectively. In comparing the bond lengths of coordinated atoms (Table 4.6), a notable trend is the decrease in bond lengths from complex **132** to **134**, with the exception of Gd1–N7. This trend is consistent with the decrease in ionic radii from Gd to Er due to the lanthanide contraction.[78] Consistent trends are harder to discern in regards to the complexes' angles (Table 4.7). Only the increasing bite angle of the H_2ttp ligand appears to conform to a plausible trend, where the bite angle experiences a minor increase with

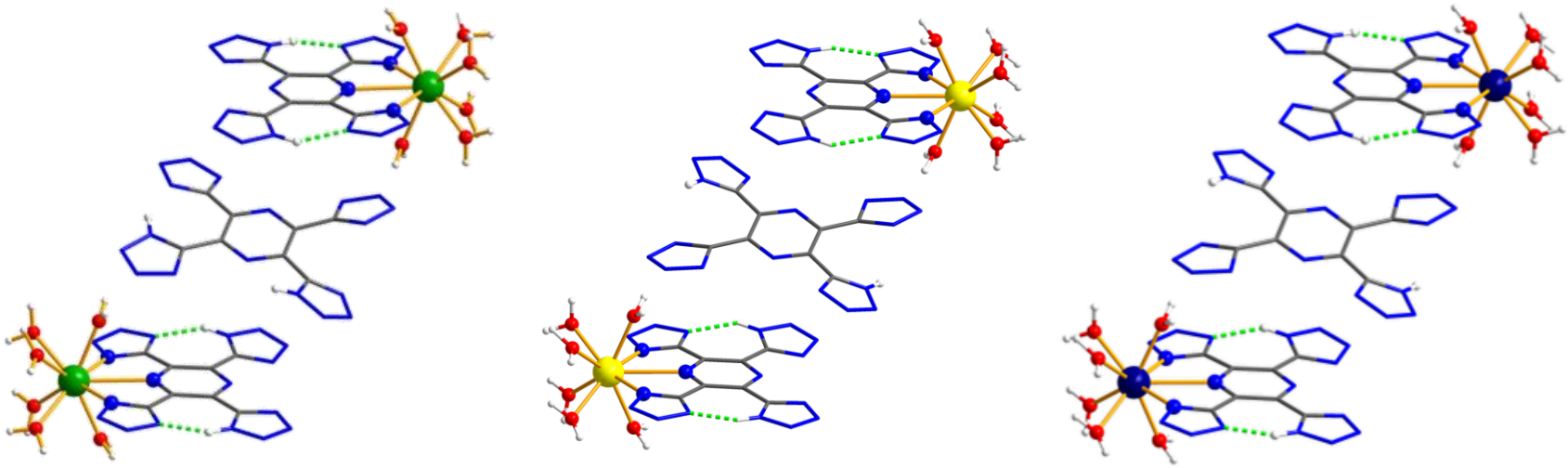

132 **133** **134**

Figure 4.25: Labeled molecular structures for polymorphic mononuclear analogs: $[Gd(H_2ttp)(H_2O)_6]_2$ $(H_2ttp) \cdot 12H_2O$ (**132**), $[Dy(H_2ttp)(H_2O)_6]_2$ $(H_2ttp) \cdot 12H_2O$ (**133**), $[Er(H_2ttp)(H_2O)_6]_2$ $(H_2ttp) \cdot 12H_2O$ (**134**). Ball and stick representation for the metal centers and coordinated atoms, wire frame representation for remaining organic components. Colour code: green (Gd), yellow (Dy), dark blue (Er), blue (N), red (O), grey (C), white (H), lime green dashed lines represent hydrogen bonds. Lattice water is omitted for clarity.

decreasing ionic radii (Gd2, Dy, Er). Gd1, however, has a significantly lower bite angle than the other three metal centers. When comparing its angles for oppositely placed coordinated water, along with the planarity of its pseudo square base to the other three metal centers, it is clear that Gd1 is significantly more distorted.

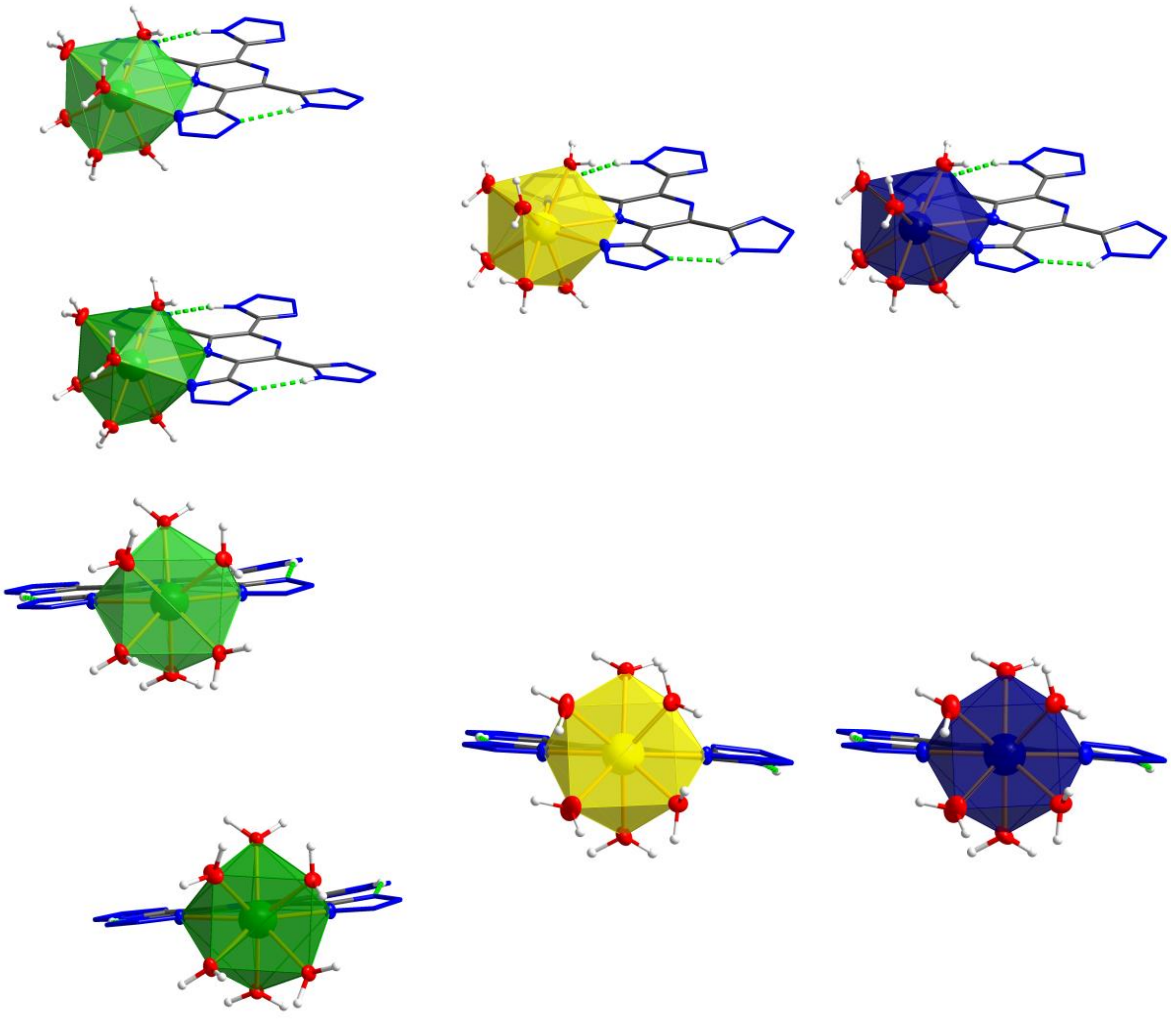

132 **133** **134**

Figure 4.26: Coordination sphere polyhedral for polymorphic mononuclear analogs: $[Gd(H_2ttp)(H_2O)_6]_2(H_2ttp)\cdot 12H_2O$ (**132**), $[Dy(H_2ttp)(H_2O)_6]_2(H_2ttp)\cdot 12H_2O$ (**133**), $[Er(H_2ttp)(H_2O)_6]_2(H_2ttp)\cdot 12H_2O$ (**134**). Colour code: green (Gd), yellow (Dy), dark blue (Er), blue (N), red (O), grey (C), white (H), lime green dashed lines represent hydrogen bonds.

Table 4.6: Coordination sphere distances for complexes **132**, **133**, **134**

	Distances (Å)	132 Gd	133 Dy	134 Er
Ln1 - N-Tetrazole	Ln1-N3	2.55	2.49	2.47
	Ln1-N7	2.52	2.52	2.49
Ln2 - N-Tetrazole	Ln2-N21	2.54	---	---
	Ln2-N25	2.52	---	---
Ln1 - N-Pyrazine	Ln1-N1	2.84	2.80	2.78
Ln2 - N-Pyrazine	Ln2-N19	2.81	---	---
Ln1 - O-Water	Ln1-O1	2.43	2.39	2.37
	Ln1-O2	2.41	2.37	2.35
	Ln1-O3	2.42	2.39	2.36
	Ln1-O4	2.40	2.38	2.38
	Ln1-O5	2.40	2.38	2.35
	Ln1-O6	2.40	2.37	2.34
Ln2 - O-Water	Ln2-O7	2.41	---	---
	Ln2-O8	2.43	---	---
	Ln2-O9	2.38	---	---
	Ln2-O10	2.42	---	---
	Ln2-O11	2.41	---	---
	Ln2-O12	2.43	---	---
Ln - Ln from opposing pillars	Ln1-Ln1	6.61	6.57	6.56
	Ln2-Ln2	6.60	---	---
Ln - Ln within the same pillar, same side	Ln1-Ln1	---	9.78	9.77
	Ln1-Ln2	9.68 9.93	---	---
Ln - Ln within the same pillar, opposite sides	Ln1-Ln1	10.16	10.12	10.08
	Ln2-Ln2	10.19	---	---

The coordinated H_2ttp ligands retain their planarity, with only a slight tilt away from the pyrazine plane noticeable for one of the non-coordinated tetrazoles. This was a surprising detail as more distortion was observed for previously described tridentate ttp ligand complexes (**128**, **129**, **130**). However for those examples the ttp ligand was the bridge which led to chain

Table 4.7: Selected angles for complexes **132**, **133**, **134**

	Angles (°)	132 Gd	133 Dy	134 Er
Ln1 - N-Tetrazole bite	N3-Ln1-N7	118.98	120.16	120.36
Ln2 - N-Tetrazole bite	N21-Ln2-25	120.08	---	---
Ln1 - O-Opposing Water	O1-Ln1-O6	133.38	134.41	134.21
	O2-Ln1-O5	114.63	112.01	111.46
	O3-Ln1-O4	107.99	109.64	109.29
Ln2 - O-Opposing Water	O7-Ln2-O12	135.38	---	---
	O8-Ln2-O11	111.84	---	---
	O9-Ln2-O10	109.08	---	---
Pyrazine plane displacement for H_2ttp cations	N1,C1,C5,N2,C7,C3–N1,C1,C5,N2,C7,C3	59.56	59.11	59.49
	N19,C9,C13,N20,C15,C11–N19,C9,C13,N20,C15,C11	58.55	---	---
Pyrazine plane displacement for H_2ttp cations and anions	N37,C17,C21,N38,C23,C19–N1,C1,C5,N2,C7,C3 **or** N19,C11,C9,N19,C11,C9–N1,C1,C5,N2,C7,C3	8.13 22.06	7.89 20.63 8.33 22.08	8.29 21.44
	N37,C17,C21,N38,C23,C19–N19,C9,C13,N20,C15,C11	20.74 8.61	---	---

structures. Complex **131** exhibits a planar H_2ttp ligand for a mononuclear complex but is coordinated to the metal center through a bidentate binding mode. The retained planarity of the H_2ttp ligand for complexes **132**, **133**, and **134** may be related to the lanthanide contraction; with Gd, Dy, and Er possessing ionic radii small enough to fit within the ttp coordination pocket, whereas La's ionic radius it too big to fit without inducing significant distortions. In measuring the distances between the bonded tetrazole N atoms (N3 and N7 / N21 and N25) in the terpy-type coordination pocket of the ttp ligand for complexes **131** through **134**, a decreasing trend is observed (4.39 Å, 4.37 Å, 4.38 Å, 4.34 Å, and 4.31 Å for complexes **131**, **132** Gd1, **132** Gd2, **133**, and **134** respectively). This trend is also consistent for the

distances between the metal centers and the pyrazine N atoms (Ln1–N1 / Ln2–N19) (Table 4.6). Thus it appears that the ionic radius of the coordinated metal center has a significant effect on the binding mode and planarity of the ttp ligand.

Rather than forming alternating cationic and anionic pillars, as in complex **131**, complexes **132**, **133**, and **134** consists of organic pillars which incorporate both the cation and anions (Figure 4.27). Between these pillars lie the solvated metal centers, in addition to the lattice water molecules which were omitted in the packing diagrams. The coordinate and lattice water molecules form a chain network of hydrogen bonding with connects the organic pillars together. In comparing Figure 4.27 to Figure 4.21, it appears as though the system was compressed such that the anionic pillars of complex **131** have been forced into the cationic pillars, to further bring the metal centers closer together. Furthermore, the tetrazoles of the H_2ttp anions (for complexes **132**, **133**, and **134**) do not lay flat within the plane of the pyrazine ring (as in **131**). The planes of the pyrazine rings are also angled at approximately 18° with respects to the cations' plane instead of approaching a parallel orientation. This, along with the observed increase in densities going from **131** to the polymorphic series, further supports the compressed analogy (1.24 gcm^{-3}, 1.95 gcm^{-3}, 1.97 gcm^{-3}, and 2.01 gcm^{-3} for complex **131**, **132**, **133**, and **134** respectively).

In observing complexes **132** from the *b* axis, as well as complexes **133**, and **134** from the *c* axis (Figure 4.28), one can notice that the pillars observed in Figure 4.27 also form layers. The consecutive cations from the pillars appear to form dimmers, which form double layers separated by slanted an anionic layer. The cations are also staggered with respects to their dimeric partner, though they remain in line with the other cationic

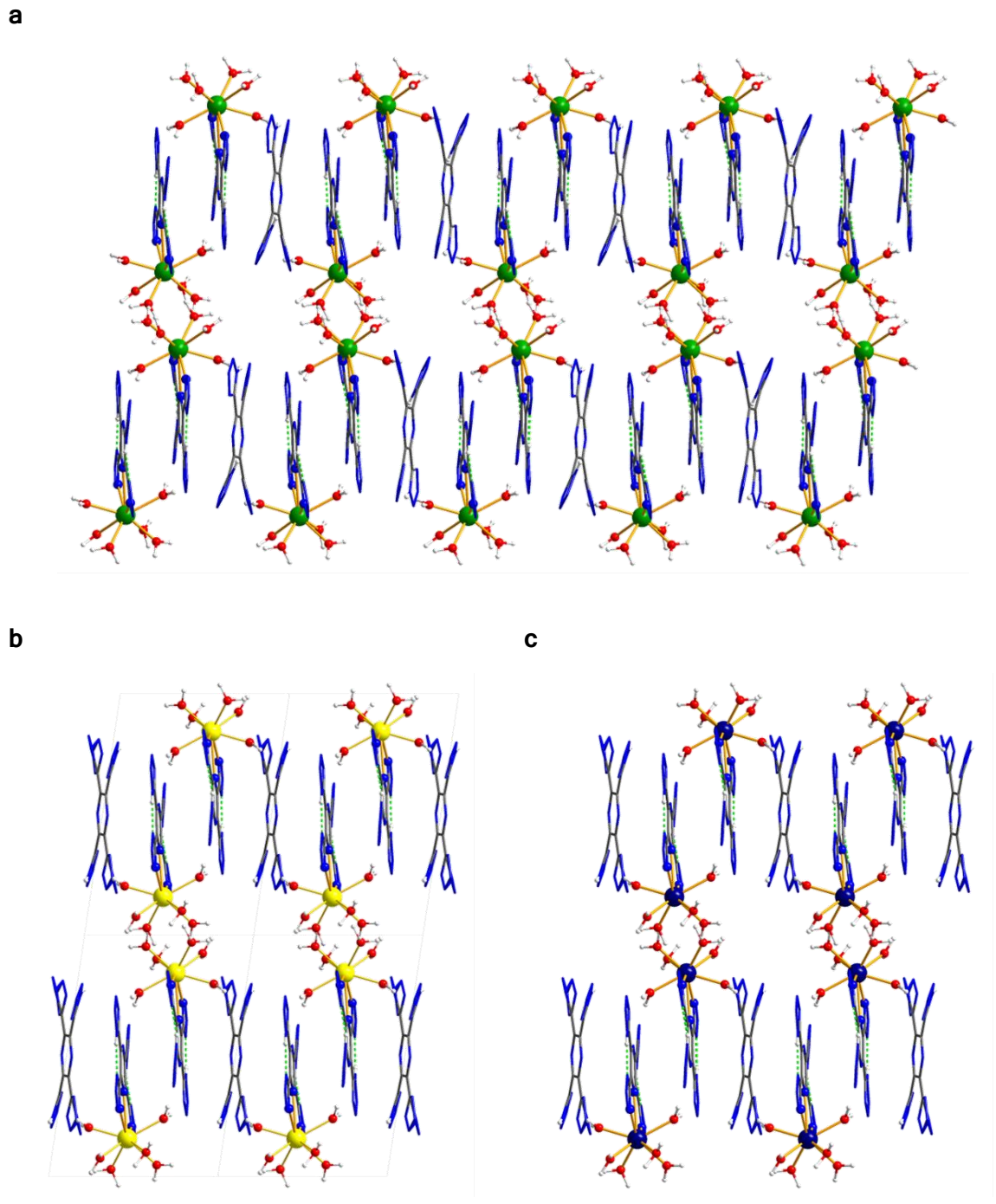

Figure 4.27: Packing for a 2x2x2 cell of complexes **132** (a), **133** (b), and **134** (c) along axis *a* and *b* for **132** as well as **133** and **134** respectively; with lattice water omitted for clarity. Wire frame representation for organic ligands, and ball and stick representation for coordinated atoms, for metal centers and hydrogen atoms. Colour code: green (Gd), yellow (Dy), dark blue (Er), blue (N), red (O), grey (C), white (H), lime green dashed lines represent hydrogen bonds.

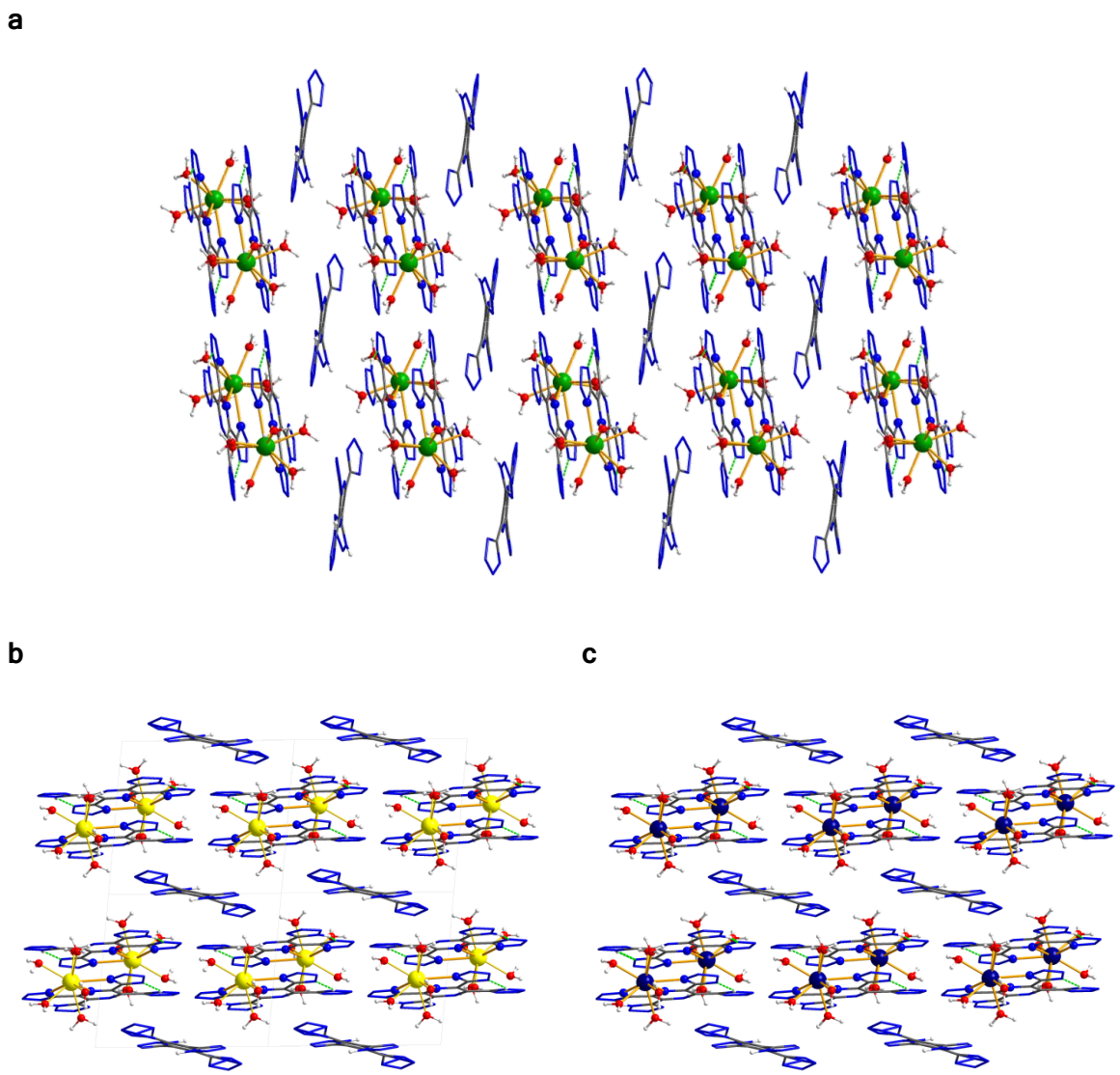

Figure 4.28: Packing for a 2x2x2 cell of complexes **132** (a), **133** (b), and **134** (c) along axis *b* and *c* for **132** as well as **133** and **134** respectively; with lattice water omitted for clarity. Wire frame representation for organic ligands, and ball and stick representation for coordinated atoms, for metal centers and hydrogen atoms. Colour code: green (Gd), yellow (Dy), dark blue (Er), blue (N), red (O), grey (C), white (H), lime green dashed lines represent hydrogen bonds.

layers. From this viewpoint, the anionic layers exhibit no visible staggering. However, in viewing complexes **132** from the *c* axis, as well as complexes **133**, and **134** from the *a* axis (Figure 4.29) one can observe that complex

132 does exhibit a slight staggering, while complexes **133**, and **134** do not. This, along with the other discrepancies in complex **132**, explains the need to double its unit cell. Another notable observation from Figure 4.29 is that instead of viewing four anions and six sets of cations for a 2x2x2 cell, as seen for complexes **133**, and **134**, the reverse is observed for complex **132**.

Similarly to complex **131**, several parallel-displaced π–π interactions can be identified for all three complexes (Table 4.7, Table 4.8). The layer of cationic pseudo dimmers (Figure 4.28) experiences π–π interactions between the dimers (interplanar distances: 3.32 Å, 3.31 Å, 3.30 Å, and 3.30 Å for **132** Gd2, **132** Gd1, **133**, and **134** respectively). While **133**, and **134** have the same interplanar distance, their parallel displacements are different (1.34 Å, and 1.32 Å for **133**, and **134** respectively). Parallel-displaced interactions are also present between the cations and anions. However, unlike complex **131** and the cationic interactions of this series, the plane–plane angle between the cationic pyrazine and anionic pyrazine for complexes **132**, **133**, and **134** is not close to zero, but rather approximately 18°. This angle, though scarcer than zero, still falls within reported norms.[75] Since the distance between the two planes could not be measured, the centroid of the anionic pyrazine was used to establish the distance between planes. It is interesting to note that the distances between the pyrazine centroids of two cations separated by anions, along with the pyrazine centroids of the two closest anions, forms a parallelogram for complex **134**, while complexes **132** and **133** form a non-regular quadrilateral. As such, there are two unique π–π interactions between cations and anions for complex **134** (interplanar distances of 2.60 Å and 3.71 Å), while four unique π–π interactions can be identified for complexes **132** (interplanar distances of 2.59 Å, 3.74 Å, 2.61 Å, and

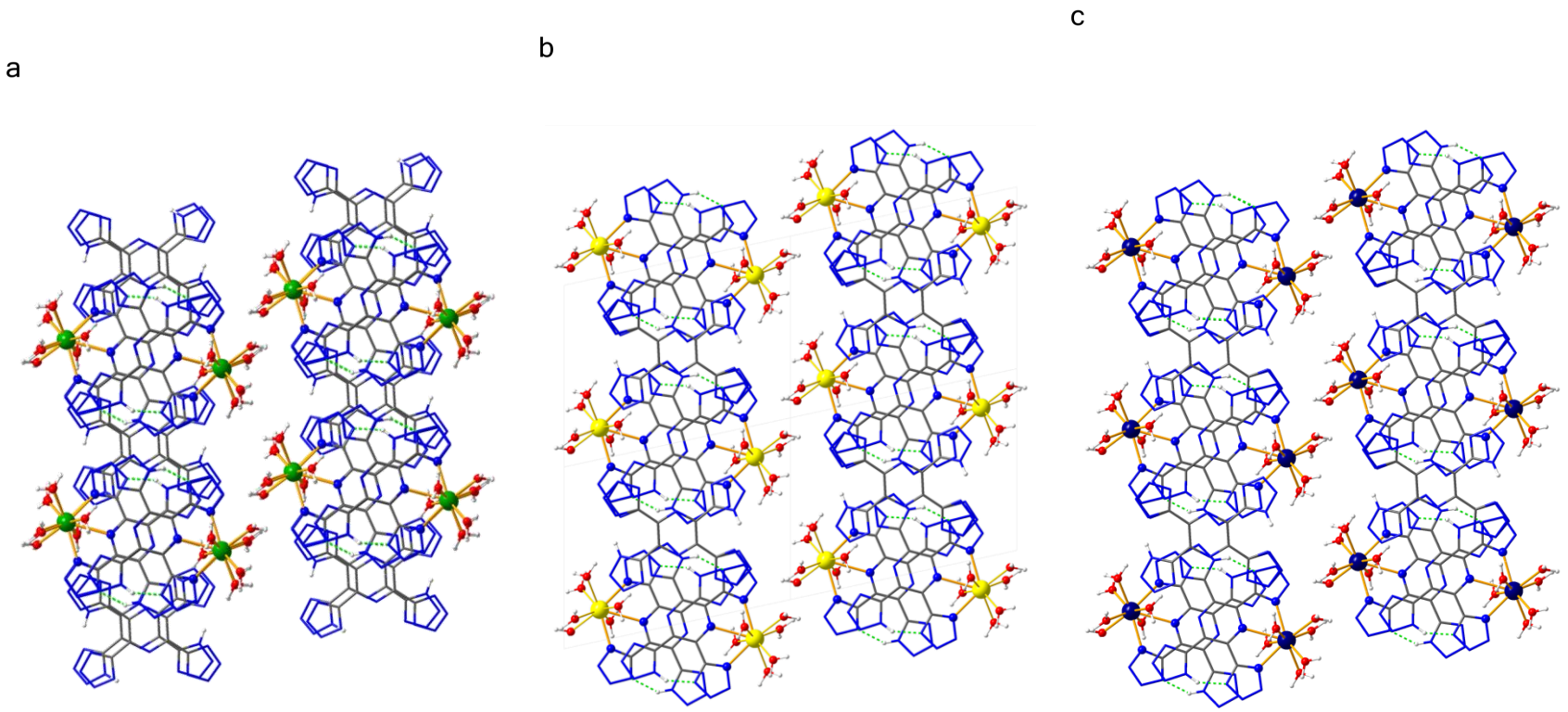

Figure 4.29: Packing for a 2x2x2 cell of complexes **132** (a), **133** (b), and **134** (c) along axis *c* and *a* for **132** as well as **133** and **134** respectively; with lattice water omitted for clarity. Wire frame representation for organic ligands, and ball and stick representation for coordinated atoms, for metal centers and hydrogen atoms. Colour code: green (Gd), yellow (Dy), dark blue (Er), blue (N), red (O), grey (C), white (H).

Table 4.8: Distances used to determine π–π interactions for complexes **132**, **133**, **134**

	Distances (Å)	132 Gd	133 Dy	134 Er
Between pyrazine planes for H_2ttp cations (a ◤)	N1,C1,C5,N2,C7,C3–N1,C1,C5,N2,C7,C3	3.31	3.30	3.30
	N19,C9,C11,N20,C15,C11–N19,C9,C11,N20,C15,C11	3.32	---	---
Parallel displacement of pyrazine for H_2ttp cations (b ◤)	N1,C1,C5,N2,C7,C3–N1,C1,C5,N2,C7,C3	1.32	1.34	1.32
	N19,C9,C11,N20,C15,C11–N19,C9,C11,N20,C15,C11	1.38	---	---
Between pyrazine centroids for H_2ttp cations (c ◤)	N1,C1,C5,N2,C7,C3–N1,C1,C5,N2,C7,C3	3.56	3.57	3.56
	N19,C9,C11,N20,C15,C11–N19,C9,C11,N20,C15,C11	3.60	---	---
Between pyrazine planes for H_2ttp anion and cation (a ◤)	N37,C17,C21,N38,C23,C19–N1,C1,C5,N2,C7,C3 **or** N19,C11,C9,N19,C11,C9–N1,C1,C5,N2,C7,C3	2.61 3.70	2.59 3.74 2.61 3.72	2.60 3.71
	N37,C17,C21,N38,C23,C19–N19,C9,C13,N20,C15,C11	3.73 2.64	---	---
Parallel displacement of pyrazine for H_2ttp anion and cation (b ◤)	N37,C17,C21,N38,C23,C19–N1,C1,C5,N2,C7,C3 **or** N19,C11,C9,N19,C11,C9–N1,C1,C5,N2,C7,C3	6.45 4.78	6.49 5.08 6.35 4.79	6.34 4.89
	N37,C17,C21,N38,C23,C19–N19,C9,C13,N20,C15,C11	5.04 6.30	---	---
Between pyrazine centroids for H_2ttp anion and cation (c ◤)	N37,C17,C21,N38,C23,C19–N1,C1,C5,N2,C7,C3 **or** N19,C11,C9,N19,C11,C9–N1,C1,C5,N2,C7,C3	6.05 6.96	6.99 3.31 6.86 6.07	6.85 6.14
	N37,C17,C21,N38,C23,C19–N19,C9,C13,N20,C15,C11	6.84 6.27		

Since H_2ttp anions were severely tilted with respects to the cation's pyrazine plane, the distance between these species (side a of the right angled triangle, ◤) was calculated using the centroid of the H_2ttp anions and the cation's pyrazine plane.

3.72 Å) and **133** (interplanar distances of 2.61 Å, 3.70 Å, 3.73 Å, and 2.64 Å). With the extensive π–π interactions and hydrogen bonding present within

these complexes, in addition to the extensive hydrogen bonding occurring through the coordinated and lattice water molecules, complexes **132**, **133**, and **134** all form 3D frameworks.

TGA experiments were carried out under nitrogen atmosphere for all three complexes (Figure 4.30). Although the general shapes of each profile are quite similar, they are all significantly different. Since complexes **133** and **134** loose 1-6% of their weight below 50 °C, it is likely that the samples were not adequately dried prior to starting the experiments. A small step, with inflection points at 86.50 °C and 68.29 °C, is observed for complexes **133** and **134** respectively. The first step for complex **132** has a shoulder which could be consistent with the small step observed for complexes **133** and **134**. In comparing with **Error! Reference source not found.**, a small step within the same range is also observed. As this step spans from room temperature to approximately 150 °C, it is consistent with the loss of water molecules. The next two

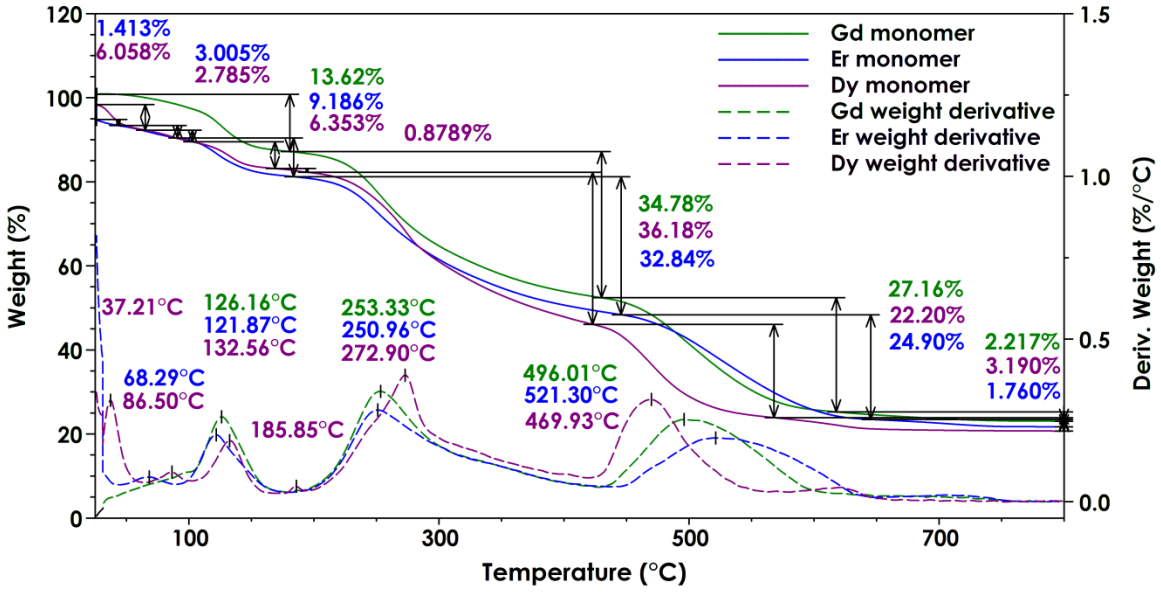

Figure 4.30: TGA plots for complex **132** (green), **134** (blue), and **133** (purple). Experiments were conducted at heating rates of 10 °Cmin^{-1} under a nitrogen

atmosphere. The samples sizes were 0.60 mg, 0.66 mg, and 1.07 mg for complexes **132**, **133**, and **134** respectively.

major steps for all three complexes are consistent with the decomposition of the ttp ligand. Overall, it appears the linear chain complexes **129** and **130** are more stable than all four of the mononuclear complexes.

4.2.3 Conclusion

The successful synthesis and characterisation of the new ligand H_4ttp was achieved. Two crystal structures were obtained (**126** and **127**), providing further insights, such as its planarity, into the molecule. H_4ttp was found to be relatively stable and safe to handle, considering its high nitrogen content of 71.58 mass %. There were, however, some difficulties in regards to its purification. Before assessing H_4ttp's full potential as and EM, the removal of residual workup reagents and solvents would have to be addressed. Future work on this compound should include obtaining an analytically pure sample for calorimetric characterisation and quantitative energetic sensitivity testing. The current synthetic preparation may also prove too costly for viable energetic applications. Efforts towards the development of a new synthetic route should be explored. Due to the aromatic nature and the planarity of this molecule, H_4ttp might also be a prime candidate for conductive organic materials. If this compound packs tightly in columns re-enforced by significant π–π interactions once purified, it may very well exhibit the properties of an organic semi-conductor. Tetrazole-based radical systems have also been shown to be stable under ambient conditions.[79] Future work should therefore also focus on electrochemistry and identifying whether H_4ttp can sustain a radical.

Coordination of H_4ttp with lanthanides lead to the synthesis of seven new complexes: three chains (complexes **128**, **129**, and **130**) and four mononuclear salts (complexes **131**, **132**, **133**, and **134**). These complexes

exhibited a higher degree of hydration than desired, though compounds **129** and **130** were a significant improvement over the bta-based complexes presented in Chapter 3. The lesser degree of hydration for compounds **129** and **130** reflects positively in their TGA thermograms; where the initial decomposition step occurs passed 200 °C (more thermally stable compound) and the overall steepness of the curve is improved (decomposes more quickly). This would suggest that the energetic performance of these two chain complexes may be better than the other tetrazole-based complexes presented. Further calorimetric experiments, such as DSC, would be required to confirm this. In addition to quantifying the potential energetic output of these complexes, further investigations should include electronic spectral studies and fluorescence studies, as well as magnetic measurements on the chain complexes. Lanthanide complexes have been known to exhibit interesting luminescent and/or magnetic properties. If one's aim was to produce materials comparable to those presented in Chapter 2, further efforts should also be aimed towards obtaining various transition metal complexes. Merging the two projects together, it would be interesting to the study the properties of chains such as complexes **129** and **130** bridged by hydrazines rather than the hydroxide/formate bridges. With regards to isolating monomeric complexes, a ttp molecule bridging two magnetically susceptible metal ions capped by bta ligands from Chapter 3 would also be a very interesting system to study, both magnetically and energetically. New complex motifs as well as expanding the breath of coordinated metals to include transition metals should all be pursued with this new ligand.

With the seven complexes presented within this chapter, H_4ttp has proven to be a versatile ligand, which has the ability to act as both a bidentate and tridentate ligand, as well as act as a bridge. Its binding mode

appears to be directly linked to the ionic radius of the metal center. Due to its ability to form numerous hydrogen bonds and extensive π–π stacking, this ligand lends itself well to form 3D-networks and is an excellent candidate for the development of new MOFs.

4.3 Experimental

4.3.1 Instrumentation

The ^{1}H and ^{13}C NMR spectra were acquired on a Bruker AVANCE 400 MHz NMR spectrometer in DMSO-d_6. A second ^{1}H NMR spectrum, as well as a ^{15}N NMR spectrum were acquired on a Bruker AVANCE 500 MHz Wide Bore NMR spectrometer in dry d_7-DMF; loaded in a glove box to avoid proton exchange with H_2O, and to improve solubility. The ^{13}C CPMAS and ^{15}N CPMAS spectra were acquired on a Bruker AVANCE III 200 NMR spectrometer. For the ^{15}N CPMAS experiment, the spectrometer was set to 20.28 MHz for ^{15}N, and was equipped with a 7 mm double resonance CPMAS probe with a zirconia rotor spinning at 4 kHz at the magic angle. The data were acquired with a 5 msec contact time using a rectangular ^{15}N pulse and a ramped ^{1}H pulse. The ^{1}H 90° pulse, recycle delay, and acquisition time were 5 μsec, 2 sec and 47 msec, respectively. High power CW ^{1}H decoupling was applied during the acquisition time. The spectrum represents approximately a 23 hour data collection time with 40874 scans. ^{1}H and ^{13}C experiments were referenced to TMS (at 0.00 ppm), while ^{15}N experiments were referenced to NH_4Cl, which was assigned a chemical shift of -341.2 ppm.[44]

Hydrothermal reactions were performed using 25 mL Teflon bombs in a Yamato Natural Convection (Gravity) oven, model DVS602. IR spectra were recorded using a Diamond ATR Thermo Scientific Nicolet 6700 spectrometer.

Raman scattering was induced using an argon ion laser (785 nm) with an estimated maximum power of 100 mW at the sample, and detected in near-backscattering geometry employing an Iridian Rayleigh scattering edge filter with an Andor 0.5 m spectrograph equipped with a Peltier-cooled charge-coupled device (CCD) detector. The spectral resolution of this setup was 1.7 cm^{-1} using an 1800 g/mm holographic diffraction grating. UV-Vis absorbance and fluorescence spectra were acquired using a Varian Cary 50 UV-visible spectrophotometer from Agilent Technologies as well as a Photon Technology International (PTI) spectrofluorimeter, using slit widths of 2 nm at the excitation source and 2 nm/5 nm at the detector, respectively. Mass spectrometry was performed using Micromass Q-TOF1, Accurate Mass ESI LC-MS spectrometer. Melting points and decomposition temperatures were determined using a TA Q2000 DSC (with hermetically sealed aluminium pans) and with a TA Q5000 TGA instrument. Single crystals x-ray diffraction data was collected using a Bruker AXS SMART single crystal diffractometer equipped with a sealed Mo tube APEX II CCD detector (Mo radiation wavelength of 0.71073 Å). Elemental analysis was performed by the University of Montreal which performs their analyses on either a Fisons EAS1108 S.p.A. instrument or a Costech ECS4010 instrument.

4.3.2 General considerations

Nitrogen-rich materials are potentially explosive and should be handled with care. The use of polycarbonate face shield, Kevlar sleeves, Kevlar gloves under thick leather gloves, ear protection, and blast shield (in addition to standard laboratory PPE such as lab coat and safety glasses), should be common practice when working with these materials. At the very least, rudimentary safety tests should be performed on all new nitrogen-rich compounds before further characterisations are performed.

The precursors used for the synthesis of H_4ttp are part of hydrogen cyanide chemistry. As such they can decompose back into hydrogen cyanide gas when exposed to acidic and basic media or, in the case of DISN, just water. It is recommended to ensure that the fume hood used is adequate to handle any accidental release of hydrogen cyanide gas. A hydrogen cyanide trap, consisting of an aqueous iron sulfate solution, can also be added to the Schenk line bubbler.

4.3.3 Ligand Synthesis

4.3.3.1 Reagents

Acetonitrile and *ethyl acetate* were purchased from Fisher Scientific. Both solvents were dried with activated molecular sieves and stored under nitrogen. *Trifluoroacetic acid* (TFA), *dimethyl sulfoxide* (DMSO), and *dimethyl formamide* (DMF) were also purchased from Fisher Scientific but used as received. *2,3-Dichloro-5,6-dicyano-1,4-benzoquinone* (DDQ) was purchased from Acros Organics, through Fisher Scientific, and used as received. If any product was unused when a fresh bottle was opened, the bottle would be flushed with nitrogen.

Diaminomaleonitrile (DAMN) was purchased from either Alfa Aesar or Acros Organics. DAMN from Alfa Aesar was received as a pungent light brown powder and required purification prior to use. This was achieved by first passing DAMN dissolved in acetonitrile over a short silica column 3 – 5 cm thick, which had been pre-treated with a 5% triethylamine in acetonitrile solution and subsequently rinsed thoroughly. A wide column is recommended for larger batches due to DAMN's limited solubility in acetonitrile. This removed a dark purple impurity, and produced a yellow-orange powder upon evaporation of acetonitrile. The recovered DAMN was then re-crystallised

according to literature procedures,[39] using a hot celite bed, boiling water, charcoal, and ice; producing an off white crystalline powder with a yield of 27%, though more DAMN could be retrieved from the filtrate. DAMN received from Acros Organics was a light beige crystalline powder and could be re-crystallised if desired. DAMN to be used for the synthesis of diiminosuccinonitrile, required being dried under vacuum with a P_2O_5 trap overnight.

4.3.3.2 Precursors

4.3.3.2.1 Diiminosuccinonitrile (DISN)

Diiminosuccinonitrile (DISN) was synthesised according to literature procedure.[39] Though DAMN is fairly stable, DISN, especially as a crude, is moisture sensitive and thus a Schlenk-line filtration apparatus (two Schlenk round bottom flasks separated by fine frit filter tube) was used for its preparation. DDQ (21.47 g, 94.6 mmol) was added to a stirring solution of DAMN (10.23 g, 94.6 mmol) in dry acetonitrile (120 mL) at room temperature. After 0.5h, the bright yellow DDQ suspension had become a beige colour, signalling its reduction. The solution was filtered and the beige DDQ washed with dry acetonitrile. The filtrate was then evaporated under reduced pressure to afford a crude brown residue of DISN (10.02 g, 99% yield). Sufficiently clean product was obtained by re-crystallisation in either dry acetonitrile or dry ethyl acetate (6.51g, 65% yield).[39]

4.3.3.2.2 Tetracyanopyrazine (TCP)

Tetracyanopyrazine (TCP) was prepared according to literature procedures.[40] A homogeneous mixture of DAMN (1.59 g, 14.7 mmol) and DISN (1.56 g, 14.7 mmol, 1 equiv.) was prepared with mortar and pestle. To avoid decomposition of DISN, a nitrogen stream was run above the mortar

throughout the manipulation. This mixture was added slowly to stirring trifluoroacetic acid (22.5 mL). The solution was then heated to 70°C and was filtered while hot. The resulting powder was washed with trifluoroacetic acid (1 mL) and ample water (10 mL twice). Contrary to what was reported in the referenced literature preparation, the recovered product contained a mixture of TCP as well as aminotricyanopyrazine (ATCP). Re-crystallisation of this crude product in benzene served to provide sufficiently clean TCP (0.82 g, yield 31.0%) for further reactions.

4.3.3.3 New ligand: 2,3,5,6-tetra(1*H*-tetrazol-5-yl)pyrazine (H_4ttp)

2,3,5,6-tetra(1*H*-tetrazol-5-yl)pyrazine (H_4ttp) was prepared according to the tetrazole synthesis presented by Dabiri *et al.*[43] TCP (0.49 g, 2.7 mmol) and sodium azide (2.13 g, 32.7 mmol) in a 1:12 mole ratio (1:3 per tetrazole) were added to DMSO and heated to 100°C in an oil bath for 3 days. While still heating at 100°C, DMSO was removed under reduced pressure. To ensure all the DMSO had been removed, the residue was re-dissolved in water and placed back under reduced pressure several times before it was stirred in acetone and filtered. Once dry and free of DMSO, an acidic workup was used to precipitate the product (H_4ttp) as a yellow powder. The powder was filtered, rinsed with water and dried. Using HCl for the acidic workup resulted in a hydrochloric salt (H_4ttp·xHCl·xH_2O) (0.96 g, yield 86.6 %). Recrystallising this product with DMF and slow diffusion of diethylether led to the hydrolysis of DMF molecules by HCl, giving thin yellow needles of H_4ttp-dimethylamonium chloride (**126**). Studies have shown tetrazoles to be efficient at binding to chloride ions.[42] Soaking H_4ttp-dimethylamonium chloride crystals in ethyl acetate for 1 week gave crystals of bis(dimethylamonium)H_2ttp (**127**). Acidic work ups were also successfully undertaken using HNO_3, with yields ranging from 14.9% to 70.7%. Re-crystallisation attempts of products

which had been worked up with HNO_3 failed to provide suitable crystals for X-ray analysis. Attempts to use organic acids, such as TFA, were unsuccessful at protonating Na_4ttp.

H_4ttp is soluble in DMF and DMSO. It is slightly soluble in THF and insoluble in dichloromethane, acetonitrile, water, chloroform, ethanol, methanol, acetone, and carbon tetrachloride. Small quantities of DMF or DMSO, renders H_4ttp soluble in the aforementioned insoluble solvents. Deprotonated ttp was found to be soluble only in water.

Cyclic voltammetry experiments were performed on H_4ttp dissolved in either DSMO or DMF. Electrolytes used for experiments were either tetrabutylammonium chloride or tetramethylammonium chloride, with ferrocene as reference. No redox processes were observed within the solvents' window.

^{1}H NMR in DMF-d_7: δ = 12.55 ppm (tetrazoyl H) *Note tetrazoyl protons are readily exchangeable. Any presence of water will drastically affect shift, which has been observed as low as 4 ppm. ; **^{13}C NMR** in DMSO-d_6: δ = 154.08 (tetrazoyl C), 140.50 (pyrazine C) ppm; **^{13}C CPMAS NMR**: δ = 153.01 (tetrazoyl C), 136.57 (pyrazine C) ppm; **^{15}N NMR** in DMF-d_7: δ = -3.93 (N1,N4 - tetrazoyl N), -48.92 (N5 - pyrazine N), -87.29 (N2,N3 - tetrazoyl N) ppm; **^{15}N CPMAS NMR**: δ = 7.12 (N3 - tetrazoyl N), -9.77 (N2 - tetrazoyl N), -58.34 (N5 - pyrazine N), -65.73 (N4 - tetrazoyl N), -142.81 (N1 - tetrazoyl N) ppm.

MS ESI$^+$ in DMF/CH_3CN (100 μL/1400 μL) m/z: 375.01 (M + Na), 376.01 (M isotope + Na),727.04 (Dimer + Na), 728.04 (Dimer isotope + Na), 1079.06 (Trimer + Na), 1080.06 (Trimer isotope + Na), 1431.10 (Tetramer + Na), 1432.10 (Tetramer isotope + Na), 1784.39 (Pentamer + Na).

EA calculated for sample of $C_8H_4N_{18}$ C27.28%, H1.14%, N71.58%. Found C25.37%, H2.39%, N55.74%. Calculated with DMSO and H_2O impurities $C_8H_4N_{18}\cdot 0.82C_2H_6OS \cdot 1.81H_2O$: C25.79%, H2.82%, N56.16%

Raman: ν = 3574.40, 2868.40, 2338.40, 1546.90, 1459.90, 1439.10, 1164.10, 1112.90, 1072.00, 1055.60, 1042.30, 817.10, 666.97, 527.24 cm^{-1}.

IR: ν = 3498.15, 3389.74, 2920.44, 2850.62, 2521.31, 2161.61, 1907.69, 1621.77, 1556.96, 1538.33, 1474.31, 1414.96, 1341.65, 1288.71, 1221.34, 1185.16, 1125.77, 1065.16, 1027.34, 988.56, 919.93, 782.99, 742.20, 663.34, 629.96, 599.11, 583.07, 563.87, 549.07 cm^{-1}.

4.3.4 Complex Synthesis

4.3.4.1 Reagents and Methods

Teflon bombs used for all complexation reactions, with the exception of **129** and **130**, were cleaned by heating 10 mL of 2M nitric acid at 120 °C for 12 h. For complexes **129** and **130**, the bombs were cleaned by a colleague who rinsed them with concentrated nitric acid, followed by ample water and finally acetone. H_4ttp ligand used for all complex syntheses was obtained using HNO_3 for the acidic workup.

4.3.4.2 Chain Structures

4.3.4.2.1 $([La(\mu\text{-ttp})(H_2O)_4]_n)_3\,[La(H_2O)_8]_n \cdot (8H_2O)_n$ - (128)

$LaCl_3\cdot 6H_2O$ (31.8 mg, 0.090 mmol) and $H_4ttp\cdot H_2O$ (15.3 mg, 0.041 mmol) were place in a 20 mL Teflon bomb with 3 mL of distilled water and heated at 160°C for 3 days, with 7.5°C/h cooling rate. This afforded thin yellow needles.

4.3.4.2.2 $[Gd_2(\mu\text{-}OH)_{2x0.38}(\mu\text{-}HCO_2)_{2x0.62}(\mu\text{-}ttp)(H_2O)_3]_n$ - (129)

$GdCl_3$ (22.6 mg, 0.086 mmol) and $H_4ttp{\cdot}H_2O$ (15.4 mg, 0.042 mmol) were place in a 20 mL Teflon bomb with 3 mL of distilled water and heated at 160°C for 3 days, with 7.5°C/h cooling rate. This afforded thin yellow-orange plates, whose twinning formed rose-like clusters (17.6 mg). EA of yellow plates: calculated C12.76%, H1.71%, N30.50%. Found C12.99%, H1.70%, N29.71%.

4.3.4.2.3 $[Dy_2(\mu\text{-}OH)_{2x0.65}(\mu\text{-}HCO_2)_{2x0.35}(\mu\text{-}ttp)(H_2O)_3]_n$ - (130)

$DyCl_3{\cdot}6H_2O$ (32.3 mg, 0.086 mmol) and $H_4ttp{\cdot}H_2O$ (15.0 mg, 0.041 mmol) were place in a 20 mL Teflon bomb with 3 mL of distilled water and heated at 160°C for 3 days, with 7.5°C/h cooling rate. This afforded thin yellow-orange plates, whose twinning formed rose-like clusters (19.5 mg). EA of yellow plates: calculated C12.52%, H1.69%, N30.20%. Found C12.67%, H1.65%, N29.05%.

4.3.4.3 Mononuclear Structures

4.3.4.3.1 $[La(H_2ttp)(H_2O)_6]\,(H_3ttp)\cdot 7H_2O$ - (131)

$LaCl_3{\cdot}6H_2O$ (61.5 mg, 0.174 mmol) and $H_4ttp{\cdot}H_2O$ (30.6 mg, 0.083 mmol) were place in a 20 mL Teflon bomb with 6 mL of distilled water and heated at 160 °C for 3 days, with 7.5 $°Ch^{-1}$ cooling rate. This afforded thin yellow plates (19.2 mg). EA of yellow plates: calculated C17.88%, H2.91%, N46.93%. Found C18.59%, H2.51%, N47.37%.

4.3.4.3.2 $[Gd(H_2ttp)(H_2O)_6]_2\,[H_2ttp]\cdot 12H_2O$ - (132)

$GdCl_3$ (22.6 mg, 0.086 mmol) and $H_4ttp{\cdot}H_2O$ (14.8 mg, 0.040 mmol) were place in a 20 mL Teflon bomb with 3 mL of distilled water and heated at 160 °C for 3 days, with 7.5 $°Ch^{-1}$ cooling rate. This afforded thin yellow plates (18.0 mg). The entire contents of the reaction product (yellow

plates and yellow powder were collected, crushed, and submitted for magnetic measurements. EA of submitted sample: calculated C8.77%, H6.99%, N23.02%. Found C18.48%, H2.02%, N46.33%.

4.3.4.3.3 $[Dy(H_2ttp)(H_2O)_6]_2$ (H_2ttp) · $12H_2O$ - (133)

$DyCl_3 \cdot 6H_2O$ (32.0 mg, 0.085 mmol) and $H_4ttp \cdot H_2O$ (14.8 mg, 0.040 mmol) were place in a 20 mL Teflon bomb with 3 mL of distilled water and heated at 160 °C for 3 days, with 7.5 $°Ch^{-1}$ cooling rate. This afforded thin yellow plates (12.2 mg). The entire contents of the reaction product (yellow plates and yellow powder were collected, crushed, and submitted for magnetic measurements. EA of submitted sample: calculated C8.75%, H6.98%, N22.96%. Found C17.51%, H2.13%, N44.10%.

4.3.4.3.4 $[Er(H_2ttp)(H_2O)_6]_2$ (H_2ttp) · $12H_2O$ - (134)

$ErCl_3 \cdot 6H_2O$ (32.0 mg, 0.084 mmol) and $H_4ttp \cdot H_2O$ (15.0 mg, 0.041 mmol) were place in a 20 mL Teflon bomb with 3 mL of distilled water and heated at 160 °C for 3 days, with 7.5 $°Ch^{-1}$ cooling rate. This afforded thin yellow plates (18.0 mg). The entire contents of the reaction product (yellow plates and yellow powder were collected, crushed, and submitted for magnetic measurements. EA of submitted sample: calculated C8.73%, H6.96%, N22.91%. Found C16.77%, H2.37%, N42.18%.

4.3.5 Supplemental Information

4.3.5.1 NMR Spectra

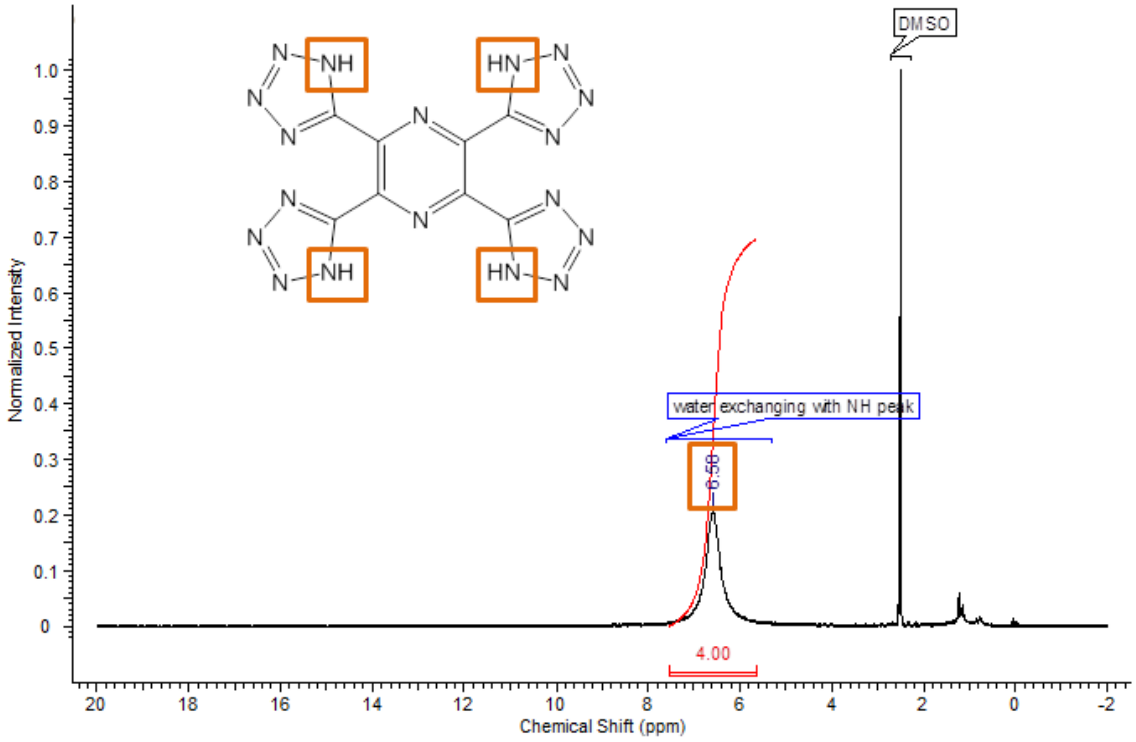

Figure 4.31: ^{1}H NMR spectra of H_4ttp dissolved in DMSO-d_6 and referenced externally to TMS. It was acquired on a Bruker AVANCE 400 MHz spectrophotometer. Due to hydrated product, and/or hydrated DMSO-d_6, a single peak is observed as the NH protons are exchanging rapidly with water.

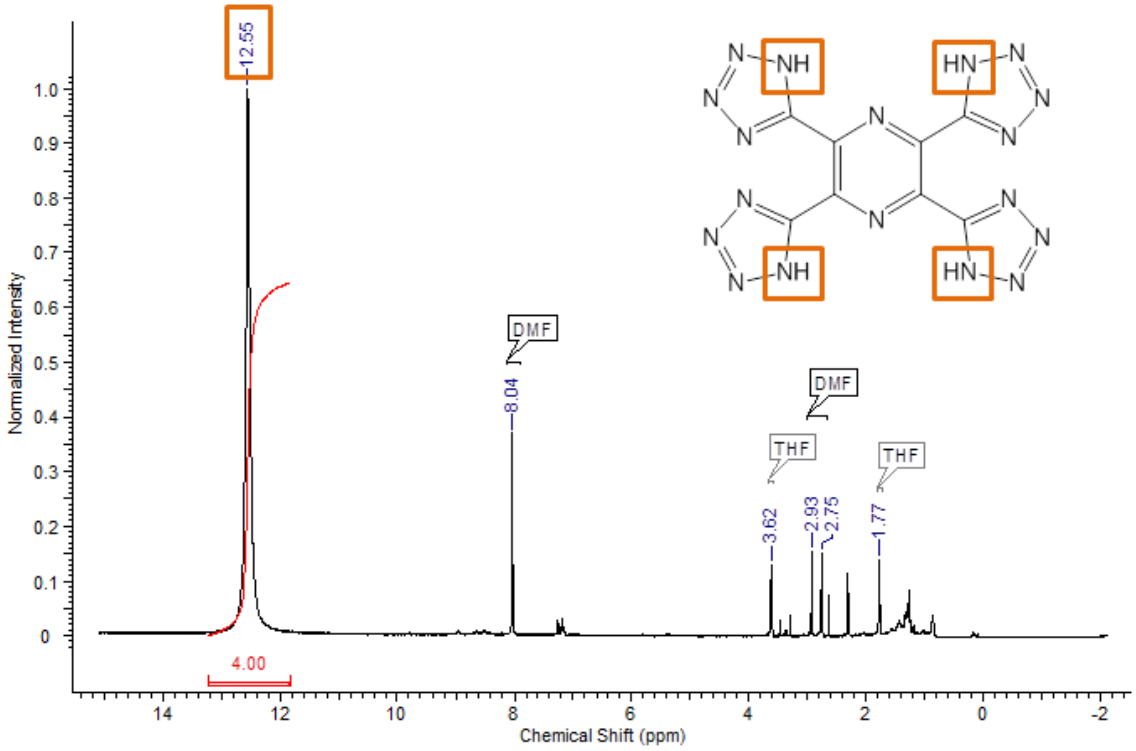

Figure 4.32: ^{1}H NMR spectra of H_4ttp dissolved in dry DMF-d_7 and referenced externally to TMS. It was acquired on a Bruker AVANCE 500 MHz Wide Bore spectrophotometer. An aliquot from the same batch as in Figure 4.31 was dried under vacuum for 2 days prior to being transferred to a glove box where the NMR sample was prepared, so as to ensure no presence of moisture. New contaminants (such as THF) were introduced in the glove box.

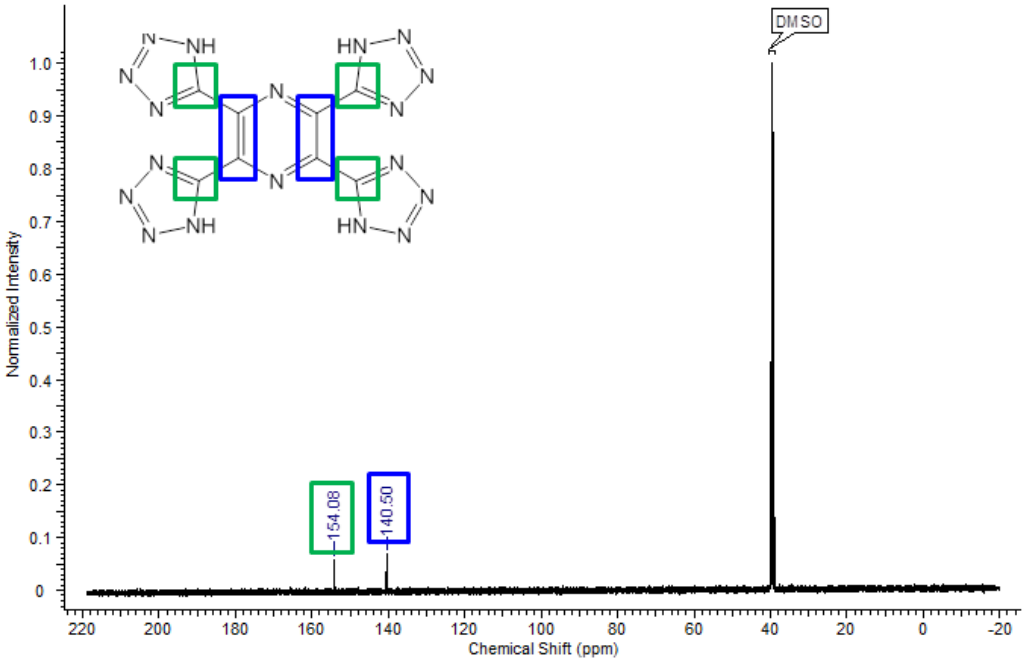

Figure 4.33: ^{13}C NMR spectra of H_4ttp dissolved in DMSO-d_6 and referenced externally to TMS. It was acquired on a Bruker AVANCE 400 MHz spectrophotometer.

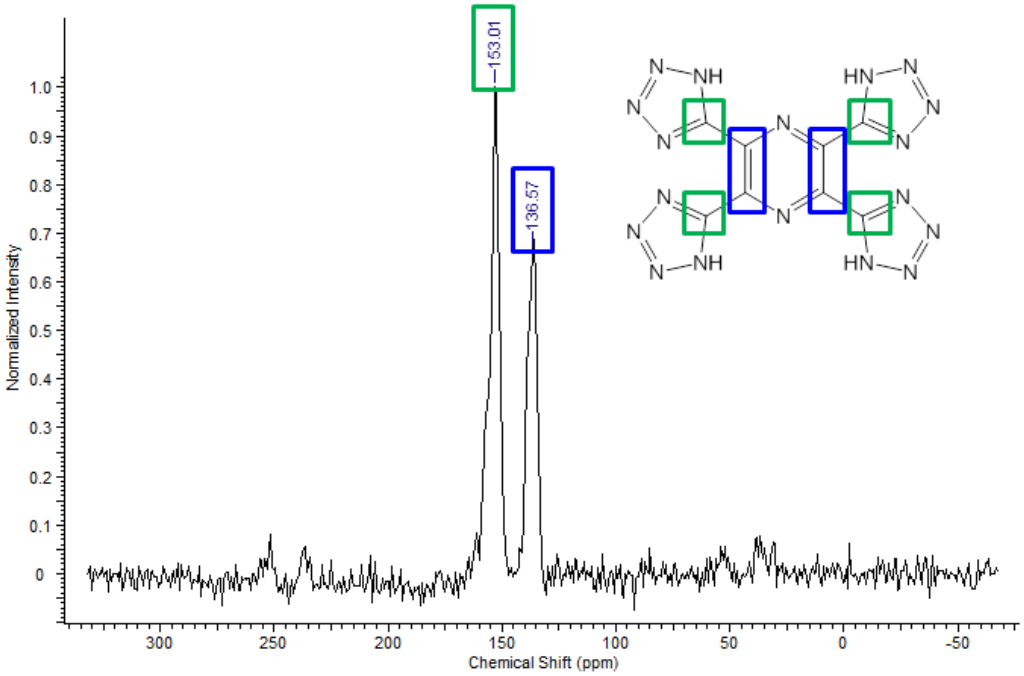

Figure 4.34: ^{13}C CPMAS spectra of H_4ttp referenced externally to TMS and acquired on a Bruker AVANCE III 200 NMR spectrometer.

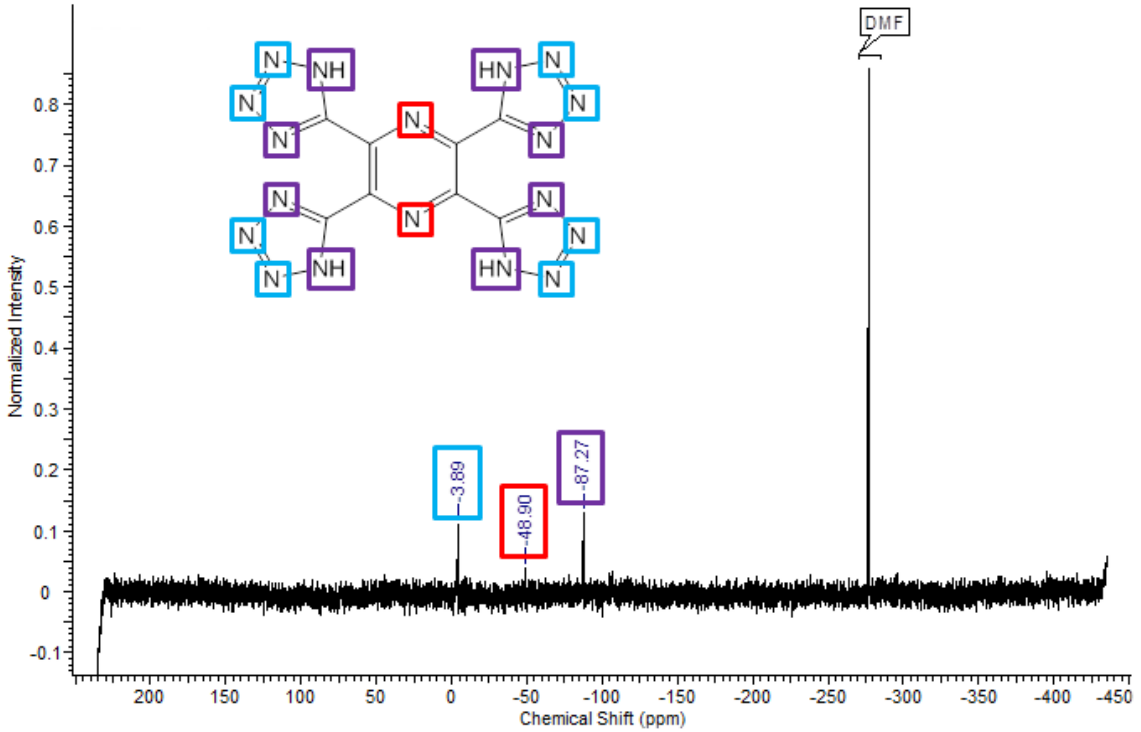

Figure 4.35: ^{15}N NMR spectra of H_4ttp dissolved in dry DMF-d_7 and referenced externally to $^{15}NH_4Cl$. It was acquired on a Bruker AVANCE 500 Wide Bore NMR spectrometer. This spectrum was subject to a 1 pts FID shift, in addition to baseline and phase corrections.

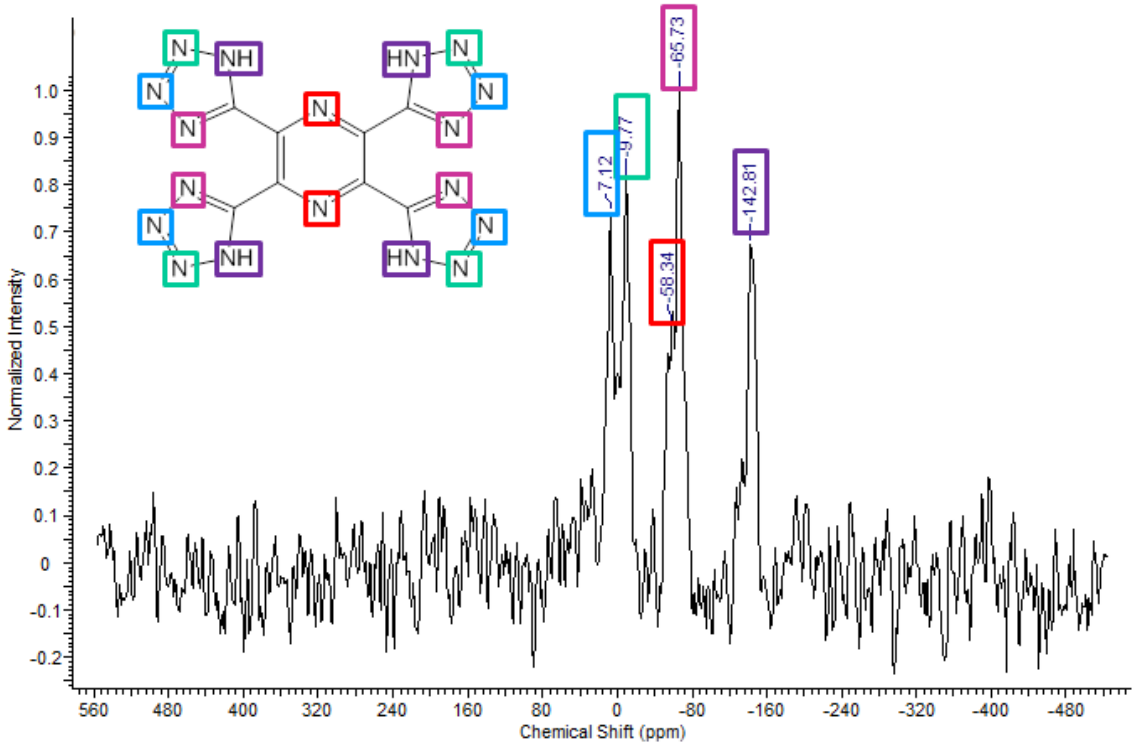

Figure 4.36: ^{15}N CPMAS NMR spectra of H_4ttp referenced externally to solid $^{15}NH_4Cl$, which was assigned a chemical shift of -341.2 ppm,[44] and acquired on a Bruker AVANCE III 200 NMR spectrometer operating at 20.28 MHz for ^{15}N. The spectrometer was equipped with a 7 mm double resonance CPMAS probe with a zirconia rotor spinning at 4 kHz at the magic angle. The data were acquired with a 5 ms contact time using a rectangular ^{15}N pulse and a ramped 1H pulse. The ^{1}H 90° pulse, recycle delay, and acquisition time were 5 μs, 2 sec and 47 ms, respectively. High power CW ^{1}H decoupling was applied during the acquisition time. The spectrum represents a ~23 hour data collection time with 40874 scans. The sample was dried under vacuum for 2 days prior to being transferred to a glove box where the sample was prepared. The spectrum was subject to a shifted squared sine bell multiplication apodization function and line broadening for clearer spectrum.

4.3.5.2 Ir Spectra for ttp-based complexes

4.3.5.2.1 Chain complexes

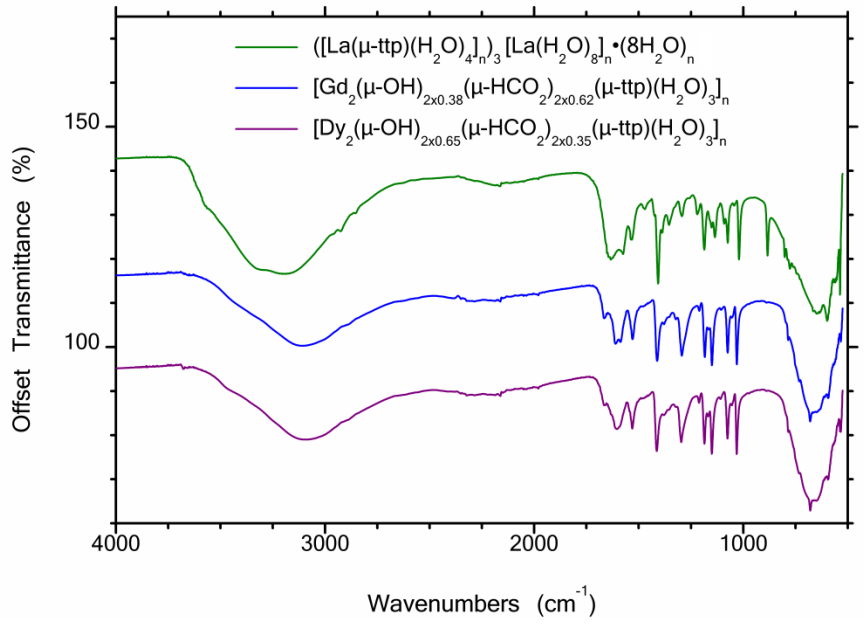

Figure 4.37: IR Spectra for ttp-based chain complexes.

4.3.5.2.2 Mononuclear complexes

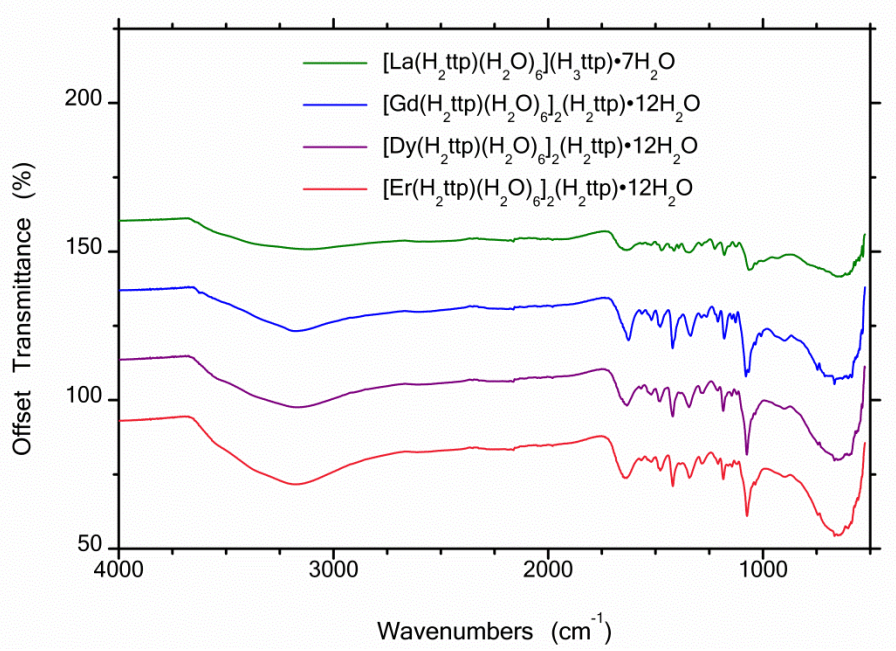

Figure 4.38: IR spectra for H_2ttp-based mononuclear complexes.

4.3.5.3 Crystallographic data tables for ttp- based compounds

4.3.5.3.1 Ligand crystals

Table 4.9: Crystallographic data for the re-crystallised ligand

Compound		126	127
Empirical formula		C_{13} H_{23} Cl N_{20} O_3	C_{24} H_{36} N_{40}
Formula weight (g/mol)		542.96	884.93
Space group		Triclinic	Monoclinic
Crystal system		P-1	C 2/c
Unit cell dimensions	**a (Å)**	6.459(2)	26.9265(16)
	b (Å)	11.953(4)	5.9264(3)
	c (Å)	15.342(5)	14.2525(8)
	α (°)	95.914(7)	90
	β (°)	95.652(7)	120.220(3)
	γ (°)	101.711(7)	90
V (Å^3)		1144.8(7)	1965.3(2)
Z		2	2
ρ_{calc} (g cm^{-3})		1.575	1.495
Absorption coefficient (mm^{-1})		0.233	0.110
F(000)		564	920
λ (Mo Kα) (Å)		0.71073	0.71073
Crystal size (mm)		0.21 x 0.06 x 0.02	0.19 x 0.17 x 0.15
θ Range (°)		2.34 - 21.40	3.40 - 28.25
Reflections collected		8800	8195
T_{min} / T_{max}		0.6115, 0.7449	0.7007, 0.7457
Goodness of fit		1.004	1.028
R1		0.0836	0.0373
wR2		0.1863	0.0957
Reflections with I>2σ(I)		1484	1986

These structures were collected at 200(2) K. Crystals were yellow needles.

4.3.5.3.2 Chain complex : $[La(H_2O)_8]_n([La(\mu ttp)(H_2O)_4]_n)_3 \cdot (8H_2O)_n$

Table 4.10: Crystallographic data for the chain complex **128**

Complex		**128**
Empirical formula		$C_{24}\ H_{56}\ La_4\ N_{54}\ O_{28}$
Formula weight (g/mol)		2104.86
Crystal system		P2
Space group		Monoclinic
Unit cell dimensions	**a (Å)**	14.0654(10)
	b (Å)	8.4975(6)
	c (Å)	14.7888(11)
	α (°)	90
	β (°)	107.877(3)
	γ (°)	90
V (Å^3)		1682.2(2)
Z		1
ρ_{calc} (g cm^{-3})		2.078
Absorption coefficient (mm^{-1})		2.608
F(000)		1030
λ (Mo Kα) (Å)		0.71073
Crystal size (mm)		0.18 x 0.10 x 0.08
θ Range (°)		2.80 - 28.36
Reflections collected		6407
T_{min} / T_{max}		0.381889, 0.745683
Goodness of fit		1.130
R1		0.0895
wR2		0.2377
Reflections with I>2σ(I)		4281

This structure was collected at 200(2) K. Crystals were pale yellow needles.

4.3.5.3.3 Chain complexes : $[Ln_2(\mu\text{-}OH)_{2x}(\mu\text{-}HCO_2)_{2y}(\mu\text{-}ttp)(H_2O)_3]_n$; Ln=Gd,Dy

Table 4.11: Crystallographic data for the chain complexes **129** and **130**.

Complex		129	130
Empirical formula		$C_{8.75}\ H_{14}\ Gd_2\ N_{18}\ O_{8.75}$	$C_{8.7}\ H_{14}\ Dy_2\ N_{18}\ O_{8.7}$
Formula weight (g/mol)		804.87	834.98
Crystal system		Triclinic	Triclinic
Space group		P-1	P-1
Unit cell dimensions	a (Å)	6.5239(2)	6.5214(2)
	b (Å)	7.8414(2)	7.8070(2)
	c (Å)	10.6792(3)	10.6509(3)
	α (°)	104.2714(12)	104.2559(12)
	β (°)	97.0307(14)	97.5429(14)
	γ (°)	97.8719(13)	98.3219(15)
V (Å^3)		517.48(3)	512.09(3)
Z		1	1
ρ_{calc} (g cm^{-3})		2.583	2.708
Absorption coefficient (mm^{-1})		6.438	7.332
F(000)		380	394
λ (Mo Kα) (Å)		0.71073	0.71073
Crystal size (mm)		0.17 x 0.12 x 0.10	0.18 x 0.10 x 0.08
θ Range (°)		2.72, 28.33	2.74, 28.31
Reflections collected		6019	5663
T_{min} / T_{max}		0.4985, 0.7457	0.5233, 0.7457
Goodness of fit		1.052	1.108
R1		0.0294	0.0243
wR2		0.0797	0.0559
Reflections with I>2σ(I)		2482	2408

These structures were collected at 200(2) K. All crystals were yellow-orange plates whose twinning formed rose-shaped agglomerations.

4.3.5.3.4 Monomeric complex: $[La(H_2ttp)(H_2O)_6](H_3ttp) \cdot 7H_2O$

Table 4.12: Crystallographic data for the monomeric complex **131**

Complex		**131**
Empirical formula		C16 H33 La N36 O14
Formula weight (g/mol)		1092.69
Crystal system		monoclinic
Space group		$P2_1/c$
Unit cell dimensions	**a (Å)**	26.5757(6)
	b (Å)	11.0294(2)
	c (Å)	12.8720(3)
	α (°)	90
	β (°)	92.1781(12)
	γ (°)	90
V (Å^3)		3770.24(14)
Z		4
ρ_{calc} (g cm^{-3})		1.925
Absorption coefficient (mm^{-1})		1.248
F(000)		2200.0
λ (Mo Kα) (Å)		0.71073
Crystal size (mm)		0.27 x 0.20 x 0.01
θ Range (°)		2.40 - 28.31
Reflections collected		47817
T_{min} / T_{max}		0.6409, 0.7457
Goodness of fit		1.004
R1		0.0317
wR2		0.0715
Reflections with I>2σ(I)		7821

This structure was collected at 200(2) K. Crystals were pale yellow plates.

4.3.5.3.5 Monomeric complexes: $[Ln(H_2ttp)(H_2O)_6]_2\,[H_2ttp]\cdot 12H_2O$; Ln=Gd, Dy, Er

Table 4.13: Polymorphic mononuclear complex analogs: **132**, **133**, **134**

Complex		132*	133	134
Empirical formula		$C_{24}\ H_{54}\ Gd_2\ N_{54}\ O_{24}$	$C_{12}\ H_{27}\ Dy\ N_{27}\ O_{12}$	$C_{12}\ H_{27}\ Er\ N_{27}\ O_{12}$
Formula weight (g/mol)		1797.71	904.10	908.86
Crystal system		Triclinic	Triclinic	Triclinic
Space group		P-1	P-1	P-1
Unit cell dimensions	**a (Å)**	11.2059(6)	9.7883(6)	9.7724(7)
	b (Å)	14.4149(7)	11.1740(6)	11.1551(9)
	c (Å)	19.6138(10)	14.3567(8)	14.2960(8)
	α (°)	97.8157(9)	101.599(3)	101.620(4)
	β (°)	93.9324(8)	97.500(3)	97.706(4)
	γ (°)	101.7444(8)	93.781(3)	93.931(5)
V (Å^3)		3057.9(3)	1518.14(15)	1505.36(19)
Z		2	2	2
ρ_{calc} (g cm^{-3})		1.952	1.978	2.005
Absorption coefficient (mm^{-1})		2.273	2.566	2.893
F(000)		1792	900.0	904.0
λ (Mo Kα) (Å)		0.71073	0.71073	0.71073
Crystal size (mm)		0.31 x 0.12 x 0.10	0.22 x 0.12 x 0.08	0.17 x 0.16 x 0.02
θ Range (°)		2.37 - 28.33	2.61 - 28.41	2.39 - 28.09
Reflections collected		29433	16933	12263
T_{min} / T_{max}		0.5945, 0.7457	0.5547, 0.7457	0.5551, 0.7457
Goodness of fit		1.016	1.023	1.037
R1		0.0277	0.0288	0.0504
wR2		0.0683	0.0714	0.1118
Reflections with I>2σ(I)		12915	6819	5325

All structures were collected at 200(2) K. All crystals were pale yellow plates. *Due to disorder within its structure, the Gd complex was refined with a unit cell double that of the Dy and Er complexes in order to obtain a better fit. However, it is essentially isostructural to the other complexes.

4.4 References

1. Hofmeier, H.; Schubert, U. S.; Chem. Soc. Rev. **2004**, 33, pp 373-399.
2. Cotton, S. A.; Annu. Rep. Prog. Chem., Sect. A: Inorg. Chem. **2003**, 99, pp 263-287.
3. Allis, D. G.; Rarig, R. S.; Burkholder, E.; Zubieta, J.; J. Mol. Struct. **2004**, 688, pp 11-31.
4. Hadadzadeh, H.; Rezvani, A. R.; Yap, G. P. A.; Crutchley, R. J.; Inorg. Chim. Acta **2005**, 358, pp 1289-1292.
5. Hsu, G.; Chen, C.; Cheng, S.; Lin, S.; Wei, H.; Lee, C.; Polyhedron **2005**, 24, pp 487-494.
6. Morsali, A.; Ramazani, A.; Z. Anorg. Allg. Chem. **2005**, pp 1759-1760.
7. Yuste, C.; Armentano, D.; Marino, N.; Cañadillas-Delgado, L.; Delgado, F. S.; Ruiz-Pérez, C.; Rillema, D. P.; Lloreta, F.; Julve, M.; Dalton Trans. **2008**, pp 1583-1596.
8. Jones, S.; Aldous, A.; Burkholder, E.; Zubieta, J.; Polyhedron **2013**, 52, pp 582-590.
9. Hartshorn, C. M.; Daire, N.; Tondreau, V.; Loeb, B.; Meyer, T. J.; White, P. S.; Inorg. Chem. **1999**, 38, pp 3200-3206.
10. Bera, J. K.; Campos-Fernández, C. S.; Rodolpheb, C.; Dunbar, K. R.; Chem. Commun. **2002**, pp 2536-2537.
11. Rocha, R.; Rein, F.; Jude, H.; Shreve, A.; Concepcion, J.; Meyer, T.; Angew. Chem., Int. Ed. **2008**, 47, pp 503-506.
12. Das, A. K.; Sarkar, B.; Fiedler, J.; Zális, S.; Hartenbach, I.; Strobel, S.; Lahiri, G. K.; Kaim, W. A; J. Am. Chem. Soc. **2009**, 131, pp 8895-8902.
13. Kundu, T.; Sarkar, B.; Mondal, T. K.; Fiedler, J.; Mobin, S. M.; Kaim, W.; Lahiri, G. K.; Inorg. Chem. **2010**, 49, pp 6565-6574.
14. Kundu, T.; Sarkar, B.; Mondal, T. K.; Mobin, S. M.; Urbanos, F. A.; Fiedler, J.; Jiménez-Aparicio, R.; Kaim, W.; Lahiri, G. K.; Inorg. Chem. **2011**, 50, pp 4753-4763.
15. Chen, W.; Rein, F. N.; Scott, B. L.; Rocha, R. C.; Chem. Eur. J. **2011**, 17, pp 5595-5604.
16. Kundu, T.; Schweinfurth, D.; Sarkar, B.; Mondal, T. K.; Fiedler, J.; Mobin, S. M.; Puranik, V. G.; Kaim, W.; Lahiri, G. K.; Dalton Trans. **2012**, 41, pp 13429-13440.
17. Aromí, G.; Barrios, L. A.; Roubeau, O.; Gamez, P.; Coord. Chem. Rev. **2011**, 255, pp 485-546.
18. Liang, L.; Peng, G.; Ma, L.; Sun, L.; Deng, H.; Li, H.; Li, W.; Cryst. Growth Des. **2012**, 12, pp 1151-1158.

19. Tao, J.; Ma, Z.; Huang, R.; Zheng, L.; Inorg. Chem. **2004**, 43, pp 6133-6135.

20. Kostakis, G. E.; Mondal, K. C.; Anson, C. E.; Powell, A. K.; Polyhedron **2010**, 29, pp 24-29.

21. Dincă, M.; Yu, A. F.; Long, J. R.; J. Am. Chem. Soc. **2006**, 128, pp 8904-8913.

22. Hill, M. S.; Mahon, M. F.; McGinley, J.; Molloy, K. C.; J. Chem. Soc. Dalton Trans. **1996**, pp 835-845.

23. Kostakis, G. E.; Abbas, G.; Anson, C. E.; Powell, A. K.; Cryst. Eng. Comm. **2009**, 11, pp 82-86.

24. Kostakis, G. E.; Abbas, G.; Anson, C. E.; Powell, A. K.; Cryst. Eng. Comm. **2008**, 10, pp 1117-1119.

25. Qiao, C.; Wei, Q.; Xia, Z.; Zhou, C.; Chen, S.; J. Therm. Anal. Calorim. **2012**, 107, pp 527-533.

26. Jiang, C.; Yu, Z.; Jiao, C.; Wang, S.; Li, J.; Wang, Z.; Cui, Y.; Euro. J. Inorg. Chem. **2004**, 2004, pp 4669-4674.

27. Dinca, M.; Dailly, A.; Liu, Y.; Brown, C. M.; Neumann, D. A.; Long, J. R.; J. Am. Chem. Soc. **2006**, 128, pp 16876-16883.

28. Wu, X.; Dong, P.; Yu, R.; Zhang, Q.; Kuang, X.; Chen, S.; Lin, Q.; Lu, C.; Cryst. Eng. Comm. **2011**, 13, pp 3686-3688.

29. Yao, R.; Qin, Y.; Ji, F.; Zhao, Y.; Zhang, X.; Dalton Trans. **2013**, 42, pp 6611-6618.

30. Andreiadis, E. S.; Imbert, D.; Pecaut, J.; Demadrille, R.; Mazzanti, M.; Dalton Trans. **2012**, 41, pp 1268-1277.

31. Rodriguez-Dieguez, A.; Palacios, M. A.; Sironi, A.; Colacio, E.; Dalton Trans. **2008**, pp 2887-2893.

32. Tao, Y.; Li, J.; Chang, Z.; Bu, X.; Cryst. Growth Des. **2010**, 10, pp 564-574.

33. Li, J.; Tao, Y.; Yu, Q.; Bu, X.; Sakamoto, H.; Kitagawa, S.; Chem. Eur. J. **2008**, 14, pp 2771-2776.

34. Li, Y.; Tao, Y.; Wang, L.; Hu, T.; Bu, X.; RSC Adv. **2012**, 2, pp 4348-4352.

35. Hu, T.; Tao, Y.; Chang, Z.; Bu, X.; Inorg. Chem. **2011**, 50, pp 10994-11003.

36. Steinhauser, G.; Klapötke, T. M.; Angew. Chem., Int. Ed. **2008**, 47, pp 3330-3347.

37. Zhao, H.; Ye, Q.; Wu, Q.; Song, Y.; Liu, Y.; Xiong, R.; Z. Anorg. Allg. Chem. **2004**, 360, pp 1367-1370.

38. Dinca, M.; Harris, T. D.; Iavarone, A. T.; Long, J. R.; J. Mol. Struct. **2008**, 890, pp 139-143.

39. Webster, O. W.; Hartter, D. R.; Begland, R. W.; Sheppard, W. A.; Cairncross, A.; J. Org. Chem. **1972**, 37, pp 4133-4136.

40. Begland, R. W.; Hartter, D. R.; Donald, D. S.; Cairncross, A.; Sheppard, W. A.; J. Org. Chem. **1974**, 39, pp 1235-1239.

41. Klapötke, T. M.; Mayer, P.; Stierstorfer, J.; Weigand, J. J.; J. Mater. Chem. **2008**, 18, pp 5248-5258.

42. Courtemanche, R. J. M.; Pinter, T.; Hof, F.; Chem. Commun. **2011**, 47, pp 12688-12690.

43. Tisseh, Z. N.; Dabiri, M.; Nobahar, M.; Soorki, A. A.; Bazgir, A.; Tetrahedron **2012**, 68, pp 3351-3356.

44. Aguilar-Parrilla, F.; Männle, F.; Limbach, H.; Elguero, J.; Jagerovic, N.; Magn. Reson. Chem. **1994**, 32, pp 669-702.

45. Andreiadis, E. S.; Demadrille, R.; Imbert, D.; Pecaut, J.; Mazzanti, M.; Chem. Eur. J. **2009**, 15, pp 9458-9476.

46. Sommer, H.; Bertram, H.; Krammer, G. E.; Schmidt, C. O.; Stumpe, W.; Werkhoff, P.; Zviely, M.; Magn. Reson. Chem. **2000**, 38, pp 907-917.

47. Guo, Y.; Tao, G.; Zeng, Z.; Gao, H.; Parrish, D. A.; Shreeve, J. M.; Chem. Eur. J. **2010**, 16, pp 3753-3762.

48. Eulgem, P. J.; Klein, A.; Maggiarosa, N.; Naumann, D.; Pohl, R. W. H.; Chem. Eur. J. **2008**, 14, pp 3727-3736.

49. Joo, Y.; Twamley, B.; Shreeve, J. M.; Chem. Eur. J. **2009**, 15, pp 9097-9104.

50. Gaponik, P. N.; Ivashkevich, O. A.; Chem. Prob. Dev. New Mater. Tech. **2003**, pp 193-233.

51. Klapötke, T. M.; Sproll, M.; Eur. J. Org. Chem. **2009**, pp 4284-4289.

52. Aridoss, G.; Laali, K. K.; Eur. J. Org. Chem. **2011**, pp6343-6355.

53. Tao, G.; Parrish, D. A.; Shreeve, J. M.; Inorg. Chem. **2012**, 51, pp 5305-5312.

54. Haiges, R.; Christe, K. O.; Inorg. Chem. **2013**, 52, pp 7249-7260.

55. Bethel, P. A.; Hill, M. S.; Mahon, M. F.; Molloy, K. C.; J. Chem. Soc., Perkin Trans. **1999**, pp 3507-3514.

56. Jaźwiński, J.; Kamieński, B.; Solid State Nucl. Magn. Reson. **2007**, 32, pp 25-33.

57. Koźmiński, W.; Aguilar-Parrilla, F.; Wawer, I.; Limbach, H.; Stefaniak, L.; Solid State Nucl. Magn. Reson. **1995**, 4, pp 121-124.

58. Witanowski, M.; Stefaniak, L.; Webb, G. A.; Annu. Rep. NMR Spectro. **1981**, 11B, pp 1-486.

59. Witanowski, M.; Stefaniak, L.; Webb, G. A.; Annu. Rep. NMR Spectro. **1987**, 18, pp 1-211.

60. Hubinger, S.; Hall, J. H.; Purcell, W. L.; Inorg. Chem. **1993**, 32, pp 2394-2398.

61. Witanowski, M.; Biedrzycka, Z.; Sicinska, W.; Grabowski, Z.; J. Magn. Reson. **1998**, 131, pp 54-60.

62. Jaźwiński, J.; Staszewska, O.; Stefaniak, L.; Araki, S.; Webb, G. A.; J. Mol. Struct. **2000**, 523, pp 103-107.

63. Aridoss, G.; Zhao, C.; Borosky, G. L.; Laali, K. K.; J. Org. Chem. **2012**, 77, pp 4152-4155.

64. Naumenko, V. N.; Koren, A. O.; Gaponik, P. N.; Magn. Reson. Chem. **1992**, 30, pp 558-564.

65. Martin, G. E.; Williams, A. J.; Annu. Rep. NMR Spectro. **2005**, 55, pp 1-119.

66. Sakuma, C.; Maeda, M.; Tabei, K.; Ohta, A.; Kerim, A.; Kurihara, T.; Magn. Reson. Chem. **1996**, 34, pp 567-570.

67. Stefaniak, L.; Roberts, J. D.; Witanowski, M.; Webb, G. A.; Org. Magn. Reson. **1984**, 22, pp 201-208.

68. Koldobskii, G. I.; Ostrovskii, V. A.; Popavskii, V. S.; Chem. Heterocycl. Compd. **1981**, 17, pp 965-988.

69. Gaire, J.; McGinley, J.; Fleming, A.; Kelleher, F.; Tetrahedron **2012**, 68, pp 5935-5941.

70. Endrédi, H.; Billes, F.; Holly, S.; J. Mol. Struct. THEOCHEM **2003**, 633, pp 73-82.

71. Demir, S.; Nippe, M.; Gonzalez, M. I.; Long, J. R.; Chem. Sci. **2014**, 5, pp 4701-4711.

72. Farràs, P.; Maji, S.; Benet-Buchholz, J.; Llobet, A.; Chem. Eur. J. **2013**, 19, pp 7162-7172.

73. Sakai, K.; Kurashima, M.; Acta Cryst. **2003**, E59, pp m411-m413.

74. Jude, H.; Scott, B. L.; Rocha, R. C.; Acta Cryst. **2013**, E69, pp m81-m82.

75. Janiak, C.; Dalton Trans. **2000**, pp 3885-3896.

76. Martinez, C. R.; Iverson, B. L.; Chem. Sci. **2012**, 3, pp 2191-2201.

77. Constable, E. C. in *The Coordination chemistry of 2,2':6',2''-Terpyridine and Higher Oligopyridines*; Advances in Inorganic Chemistry and Radiochemistry; Academic Press Inc.: **1986**; Vol. 30, pp 69-122.

78. Hutchings, A.; Habib, F.; Holmberg, R. J.; Korobkov, I.; Murugesu, M.; Inorg. Chem. **2014**, 53, pp 2102-2112.

79. Butler, R. N. in *Recent Advances in Tetrazole Chemistry; Advances in Heterocyclic Chemistry*, Academic Press: **1977**; Vol. 21, pp 323-437.